# Computationally Efficient Algorithms for Compressed Sensing in Image Processing



# Hassaan Haider 96-FET/PhDEE/F15

A dissertation submitted to IIUI in partial fulfilment of the requirements for the degree of

# **DOCTOR OF PHILOSOPHY**

Department of Electrical and Computer Engineering
Faculty of Engineering and Technology
International Islamic University,

Islamabad 2024



PhD 621-3822 HAC

compressed sensing. Wavelets
Signal processing. Wavelets
(Mathematics)
[mage processing]

4

Copyright © 2024 by Hassaan Haider

All rights reserved. Without the authors' permission, no portion of the content covered by this copyright notice may be duplicated or used in any electronic or mechanical form, including printing, recording, or any kind of storage and retrieval system.

£

# **DEDICATED TO**

My Parents, Teachers, Wife, Sisters, Son, Daughter, and Students

### **CERTIFICATE OF APPROVAL**

Title of Thesis: Computationally Efficient Algorithms for Compressed Sensing in Image

**Processing** 

Name of Student: HASSAAN HAIDER

Registration No: 96-FET/PHDEE/F15

Accepted by the Department of Electrical and Computer Engineering, Faculty of Engineering and Technology, International Islamic University (IIU), Islamabad, in partial fulfillment of the requirements for the Doctor of Philosophy degree in Electronic Engineering.

#### <u>Viva Voce committee:</u>

#### Dr. Jawad Ali Shah (Supervisor)

Assistant Professor, DECE, FET, IIU Islamabad.

### Dr. Umer Javed (Co-Supervisor)

Machine Learning Engineer, NSW, Australia.

### Dr. Abdul Basit (Internal)

Associate Professor, DECE, FET, IIU Islamabad.

### Dr. Hafiz Muhammad Faisal Zafar (External-I)

Chief Scientist, PAEC, Islamabad.

#### Dr. Tanveer Ahmed Cheema (External-II)

Professor, ISRA University, Islamabad.

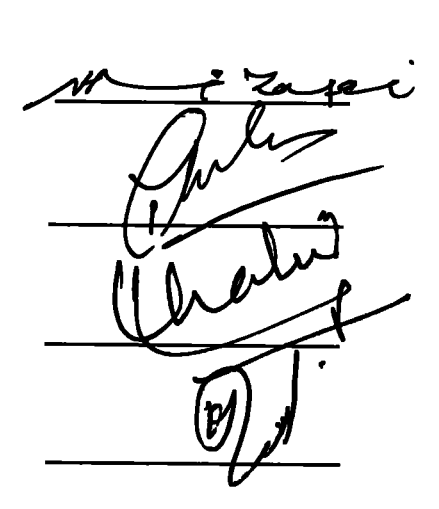
### Dr. Shahid Ikram (Chairman, DECE)

Assistant Professor, DECE, FET, IIU Islamabad.

### Prof. Dr. Khan Zaib Jadoon (Dean, FET)

Professor, DCE, FET, IIU Islamabad.

Jew Aller



### **ABSTRACT**

Compressed Sensing (CS) revolutionizes data acquisition by promising substantial reductions in acquisition time while preserving signal fidelity, particularly in Magnetic Resonance Imaging (MRI), where conventional techniques often encounter prolonged acquisition times and associated challenges. This thesis addresses these challenges by efficient CS MRI reconstruction methods, aiming to transform medical imaging through faster, more cost-effective, and artifact-free scans. We introduce a novel Kronecker Delta function for smooth  $l_0$  norm approximation, enhancing CS MRI and one-dimensional sparse signal recovery. Through a comprehensive comparative analysis, various Kronecker Delta functions are evaluated for their efficacy in signal reconstruction. Additionally, we propose a novel cost function combining  $l_0$  and  $l_1$ norms, significantly improving reconstruction efficiency from limited observations. Our method introduces a flexible approach for smooth  $l_1$  norm approximation and shrinkage using hyperbolic tangent, facilitating proficient recovery of sparse signals, MRI, and Cardiac Cine MRI from undersampled data. Furthermore, a Nature-Inspired Iterative Reweighted Shrinkage algorithm is proposed for MRI and sparse signal recovery, demonstrating substantial improvements over existing techniques. Leveraging the synergy between CS and deep learning, we propose a computationally efficient technique for CS MRI recovery, promising significant advancements in image acquisition and reconstruction. This thesis contributes novel, computationally efficient algorithms for CS recovery of one-dimensional sparse signals and their application in MRI, while also exploring the potential of deep learning in CS MRI recovery. These findings have the potential to propel CS MRI recovery forward, paving the way for more efficient and accurate imaging techniques in diverse applications, particularly in medical imaging. Additionally, the development of DISTA-CSNet showcases significant improvement in reducing MRI recovery time, underscoring the transformative potential of CS in medical imaging.

### List of Publications and Submissions

- [1]. Haider, Hassaan, Jawad Ali Shah, Sharjeel Abid Butt, Umer Javed and Kushsairy Kadir. 2024. DISTA-CSNet: Efficient Data Aware Deep Learning Model for CS MRI Recovery" in *IEEE Access (submitted)*.
- [2]. Haider, Hassaan, Jawad Ali Shah, Umer Javed and Kushsairy Kadir 2024 "Reconstruction of CS MRI with Heuristic Smooth Approximation of  $l_1$  norm", in MDPI Sensors (submitted).
- [3]. Haider, Hassaan, Jawad Ali Shah, Umer Javed and Kushsairy Kadir. 2024 "Nature Inspired Iterative Reweighted Least Square for CS MRI Recovery" in MDPI Journal of Sensor and Actuator Networks (submitted).
- [4]. Haider, Hassaan, Jawad Ali Shah, Kushsairy Kadir, and Umer Javed. 2024. "A Review and Comparative Analysis of Kronecker Delta Approximations of Smoothed 10 Norm for Recovery of Compressively Sampled MR Images", in The Scientific Bulletin Series C: Electrical Engineering and Computer Science (submitted).
- [5]. Haider, Hassaan, Jawad Ali Shah, Kushsairy Kadir, and Najeeb Khan. 2023. "Sparse Reconstruction Using Hyperbolic Tangent as Smooth li-Norm Approximation" MDPI Computation 11, no. 1: 7. https://doi.org/10.3390/computation11010007 (IF: 2.2)
- [6]. Haider, Hassaan, Jawad Ali Shah, Kushsairy Kadir, and Haidawati Nasir. "Recovery of Undersampled Sparse Signals using Combined Smoothed  $l_0 l_1$  Norm." In 2019 IEEE International Conference on Signal and Image Processing Applications (ICSIPA), pp. 249-253. IEEE, 2019.
- [7]. Haider, Hassaan, Jawad Ali Shah, Shahid Ikram, and Idris Abd Latif. "Sparse signal recovery from compressed measurements using hybrid particle swarm optimisation." in Signal and Image Processing Applications (ICSIPA), 2017 IEEE International Conference on, pp. 429-433. IEEE, 2017.
- [8]. Shah, Jawad Ali, Hassaan Haider, Kushsairy Abdul Kadir, and Sheroz Khan.

  "Sparse signal reconstruction of compressively sampled signals using smoothed

- E0-norm. Signal and Image Processing Applications (ICSIPA), 2017 IEEE International Conference on, pp. 61-65. IEEE, 2017.
- [9]. Haider, Hassaan, Jawad Ali Shah, Ijaz Mansoor Qureshi, Hammad Omer, and Kushsairy Kadir. "Compressively sampled MRI recovery using modified iterative-reweighted least square method." *Applied Magnetic Resonance* 47 (2016): 1033-1046. (IF: 1.0)
- [10]. Khan, Shafqat Ullah, Ijaz Mansoor Qureshi, Hassan Haider, Fawad Zaman, and Bilal Shoaib. "Diagnosis of Faulty Sensors in Phased Array Radar Using Compressed Sensing and Hybrid IRLS-SSF Algorithm." Wireless Personal Communications 91, no. 1 (2016): 383-402. (IF: 2.2)
- [11]. Hassaan Haider, Jawad Ali Shah, Usman Ali, "Comparative analysis of sparse signal recovery algorithms based on minimisation norms.", in Sustainable Technologies (WCST), 2014 World Congress on, pp. 72-76. IEEE, 2014.
- [12]. Hassaan Haider, Jawad Ali Shah, Usman Ali, I M Qureshi, Amir A Khaliq, "Recovery of Sparse Signal using Hybrid IRLS-SSF", MAGNT Research Report Journal, Vol 2(6), 2014.

This thesis covers research work based on publications mentioned from 1 to 8.

## **Awards and Grants**

- Awarded a six-month research fellowship as PhD Scholar by Universiti of Kaul Lumpur, British Malaysian Institute, (UniKL, BMI), Malaysia under the Student Mobility Program.
- Granted 15 months of Study Leave with full pay by International Islamic University, Islamabad, (IIUI), Pakistan.
- Merit-based full fee waiver from IIUI, Pakistan during entire studies.

### Acknowledgements

I am grateful to Almighty ALLAH SWT, for giving me the strength and courage to continue striving to complete my PhD. All the thoughts/ideas that come to complete research work are due to HIS blessings and nothing is possible without HIS consent.

Without the prayers of my parents and family, this could not have been possible. I am very fortunate to have my parents alive to see this day. They have sacrificed a lot for me and I am indebted to them. The continuous support of my sisters has made me determined to complete this uphill task. I am also thankful to my wife for her continuous encouragement and for helping me with her AutoCAD skills in making model diagrams for proposed algorithms.

I cannot thank my supervisor Dr Jawad Ali Shah enough, who has been fatherly and brotherly to me at the same time. Throughout my academic career as a faculty member at IIUI, he has been a great mentor, a source of inspiration and beacon of learning for me. He was the one who made it possible for me to join UniKL BMI, Malaysia under the student mobility program. He made me feel at home while being away from home during my entire stay in Malaysia. Provided more support to me than one can ask for. He kept believing in me even when I doubted myself throughout this journey. I hope to develop a lifelong relationship to keep learning and seek guidance from his wisdom even after completion of my PhD.

I would like to thank all my teachers for their guidance and dedication during my PhD coursework and research work especially Dr Ijaz Mansoor Qureshi (Late), who was my ideal teacher/mentor to admire. He taught us a Heuristic Techniques course that was very helpful in research work. Special thanks to Dr Syed Zubair for teaching state-of-the-art content in Machine Learning and Deep Neural Networks that opened a new research avenue. I would like to thank Dr Andrew Ng from Stanford University for creating such an interesting course series Deep Learning on the Coursera platform.

I would like to thank my Co-supervisor Dr Umer Javed for his guidance and teaching during coursework and research work. During coursework, he gave great insights into Computer Vision and Image Processing eventually leading to this research work. I admire him for his professionalism.

I would like to thank my friend, class fellow and colleague for his invaluable input and programming skills, which have helped me a lot. He was always there

to help whenever I got stuck. He is the true picture of a friend in need is the friend indeed.

I would like to thank UniKL BMI, Malaysia for providing an excellent environment and facilities to conduct my research work. I want to express my gratitude to Dr Kushsairy Kadir for providing state-of-the-art labs, and accommodation free and funding my research work throughout my degree program. I admire the beautiful surroundings of UniKL, BMI in Gombak, Malaysia. I would like to thank all my friends in UniKL, BMI, who played very competitive table tennis matches in the evening in such a friendly environment. Even made part of their team from UniKL, BMI an inter-university competition.

I would like to thank International Islamic University, Islamabad (IIUI) for providing me excellent research environment. Awarding me with the full fee waiver throughout my coursework and research phase of my PhD. IIUI allowed me study leave with full pay for 18 months to carry out my research work is a generous investment from IIUI for the development of their resource persons.

I would also like to acknowledge the Higher Education Commission (HEC) for the grant of funding under the National Research Program for Universities (NRPU). The grant of Rs. 7 million provided by HEC under Project No. 5797 having the title "Implementation of Recovery Techniques for Compressively Sampled Biomedical Images Using Graphical Processing Unit" allowed us to develop High-Performance Computing (HPC) Lab in the Department of Electrical and Computer Engineering, IIUI equipped with Lambda (λ) Quad AI Workstation with dual Nvidia GeForce RTX 3090 GPUs and HP Omen Desktop with Nvidia GeForce RTX 2080 Ti GPU. HEC offers free courses in Coursera that help students to learn state-of-the-art skills from the very best which enabled me to learn Deep Learning's latest techniques. Without these resources, this research would not have been possible.

(Hassaan Haider)

## **Table of Contents**

CERTIFICATE OF APPROVAL		
ABST	RAC"	Γ
List of	f Publ	ications and Submissions
		l Grantsv
		ements
		ntents
		resx
		PSX
		eviationsx
List of	Symi	oolsxx
СНА	PTER	1 INTRODUCTION
1.1	Mot	ivation for CS MRI
1.2		olem Statement
1.3	Rese	earch Objectives
1.4	Mai	n Contributions
1.5	The	sis Organization
СНАІ	PTER	2 COMPRESSED SENSING IN MRI10
2.1	Intro	duction1
2.2	Com	pressed Sampling12
2.3	Spar	sity12
2.4	Inco	herence15
2.5	Spar	se Signal Recovery Constraints16
<b>2</b> .	5. <i>1</i>	Restricted Isometric Property (RIP)16
<b>2</b> .	5. <i>2</i>	Minimum Sampling Frequency16
2.6	Intro	duction to MRI17
<i>2</i> .	6. I	Nuclear Magnetic Resonance (NMR)17
<b>2</b> .	6.2	Gradient Encoding and Signal Reception19
2	6.3	K-Space and Image Domain20
2.	6.4	Resolution vs FOV

	<i>2.6.5</i>	K-Space Sampling Patterns	. 22
	2.6.6	MRI Sparse Representations	. <i>22</i>
	2.67	Rapid MRI	. <i>25</i>
2.7	CS	MRI Recovery	. 26
	2.7 I	Linear Recovery Methods	. 26
	2.7.2	Projection onto Convex Set Method	. 27
	<b>2</b> .7.3	Iterative Reweighted Least Square (IRLS)	. 29
	2.7.4	Separable Surrogate Functionals	30
	<b>2</b> .7.5	Parallel Coordinate Descent (PCD)	30
	2.7.6	Fast Iterative Shrinkage Thresholding Algorithm (FISTA)	31
	2.7.7	Greedy Algorithms	31
2.8	Fusi	on of CS MRI with Machine Learning	32
2.9	Meti	rics for Performance Assessment	33
2	2. <i>9</i> .1	Structural Similarity Index (SSIM)	34
2	2. <i>9.2</i>	Artifact Power	34
2	2.9.3	Improved Signal-to-Noise Ratio (ISNR)	34
2	9.4	Peak Signal-10-Noise Ratio (PSNR)	34
2	2.9.5	Filness	35
2	2.9.6	Correlation	
2	2.9 7	Mean Square Error (MSE)	35
2	2.9.8	Signal-to-Noise Ratio (SNR)	
CHA	DTFD	3 SPARSE MRI RECOVERY BY SMOOTH APPROXIMATIONS OF <i>L</i> O NORM	
		S SPARSE MRI RECOVERY BY SMOUTH APPROXIMATIONS OF 10 NORM	
		duction to Norms	
	.1.1	l2-norm Based Recovery	
_	.1.2	lO-norm Based Recovery	
	.13	Lp-norm Based Recovery4	
3	.14	l1-norm Based Recovery4	
3.2		oth 10-norm Literature Review4	
3.3		e Signal Recovery by Smooth 10 norm4	
3.4	Delta	Approximations Functions for Smooth 104	4
3.5	Spars	e Signal Recovery Empirical Results and Discussion4	15
3.6		RI Recovery by Smooth 10 norm5	
3.7		RI Recovery Experimental Results and Discussion5	
3.8	Propo	sed Smooth 10 norm approximation5	9
3.9	Propo	sed Algorithms Experimental Results on k-Sparse Signal	2

3.10	Empirical Results for CS MRI Recovery	65
3.1	Conclusions	68
СНА	PTER 4 SPARSE RECOVERY USING HYPERBOLIC TANGENT BASED SMOOTH	L1
NOR	M AND SHRINKAGE	69
4.1	Introduction	60
4.2	Proposed Smooth l1-norm approximation by Hyperbolic Tangent	
4.3	Smooth l1 norm Error Bounds	
4.4	The MAP Estimation for Proposed Thresholding Mechanism	
4.5	Proposed Algorithms	82
4.6	Experimental Results and Discussions	82
4	.6.1 I-D Sparse Signal Recovery	82
4	.6.2 2-D CS MRI Recovery	<b>8</b> 5
4.	.63 CS Cardiac Cine MRI Recovery	89
4.7	Conclusion	96
CHAI	PTER 5 CS MRI RECOVERY USING COMBINED SMOOTH 10 AND 11 RECOVERY	,
		97
5.1	Introduction	97
5.2	Proposed SL01 Algorithm10	
5.3	Experimental Results and Discussion	)5
<b>5</b> .	3 1 Sparse Signal Recovery Application10	)6
<b>5</b> .	3.2 CS MRI Reconstruction Using Proposed Method10	18
5.4	Conclusions11	1
СНАР	TER 6 NATURE-INSPIRED IRLS FOR CS MRI RECOVERY11	.2
6.1	Nature-Inspired Algorithms	2
6.2	Particle Swarm Optimisation	
6.3	Iterative Reweighted Least Square (IRLS)	
6.4	Nature Inspired Iterative Reweighted Least Square (NI-IRLS)	
6.5	Experimental Results for Recovery of 1-D Signal	
6.6	Experimental Results and Discussion for CS MRI Recovery	0
6.7	Conclusions	6
CHAP	TER 7 CS MRI RECOVERY USING HEURISTIC APPROXIMATION OF <i>l</i> 1 NORM	
		8
7.1	Heuristic Algorithms	0
	11-norm Approximation by Hyperbolic Tengent	

7.3	Particle Swarm Optimisation (PSO)141
7.4	Heuristic Smooth Approximation of l1-norm (H-SL1)141
7.5	Experimental Results for Recovery of I-D Signal147
7.6	Experimental Results and Discussion for CS MRI Recovery
7.7	Conclusions
СНА	PTER 8 DISTA-CSNet: DEEP LEARNING-BASED CS MRI RECOVERY160
8.1	Introduction
8.2	Iterative Shrinkage Methods and Deep Learning162
8.3	DISTA-CSNet Model163
8.4	DISTA-CSNet Training Model165
8	.4.1 Training /Testing Datasets
8	4.2 Mote Carlo Dropouts167
8	.4.3 Soft Thresholding168
8	.4.4 Data Consistency Constraints
8	4.5 Convolution
8	4.6 Convolution Transpose
8	4.7 Rectified Linear Unit (ReLU)170
8	4.8 Xavier Initialisation171
8.	4.9 Adam optimizers171
<i>8</i> .	4.10 Cost Function171
8.5	DISTA-CSNet Testing Model173
8.6	DISTA-CSNet Model Testing Results and Discussion
8.7	Conclusions181
СНАР	TER 9 CONCLUSIONS182
9.1	Summary of Thesis
9.2	Future Directions
REFER	ENCES186

# List of Figures

Figure 2-1: Demonstrates the sparsity of signals when transformed on a suitable basis [5]	13
Figure 2-2: The three domains that attract interest in the field of Compressed Sensing	15
Figure 2-3: The magnetic and gradient fields utilized in MRI [16]	19
Figure 2-4: Recovery of an image by IFFT from it Fourier data [45]	21
Figure 2-5: The relationship between the field of view and resolution [45]	21
Figure 2-6: Patterns of sampling in the k-space domain	23
Figure 2-7: Applying sparsity-inducing transforms to various images [16]	23
Figure 2-8: Effect of undersampling in k-sparse [24]	24
Figure 2-9: Effect of sparse approximation on denoising [16]	25
Figure 2-10: Depicts the sampling pattern of the LR mask	27
Figure 3-1: Intersection of $lp$ ball and the set $Ax = y$ solved with various values of $p$ [21]	38
Figure 3-2: l2 norm-based signal recovery failure to achieve desired sparse solution	39
Figure 3-3: Effect of $\sigma$ on delta approximation function width	43
Figure 3-4: Delta Approximation Functions Width Matching	45
Figure 3-5 MSE vs change in σ with each iteration	47
Figure 3-6: SNR vs change in σ with each iteration	47
Figure 3-7. Computational Time vs Length of Signal	48
Figure 3-8: Effect of Change in Sparsity K on Recovered Signal MSE	48
Figure 3-9: Effect of change in Sparsity K on recovered signal SNR	49
Figure 3-10: Normalized successful recovery for different sparsity levels	49
Figure 3-11: Graphical Representation of SLO Algorithm	53
Figure 3-12: Image under-sampling mask and its domains	54
Figure 3-13: Reconstructed Images from different DA functions	55
Figure 3-14: ISNR variation with different values of $\sigma$	55
Figure 3-15: SNR against varying $\sigma$	56
Figure 3-16: PSNR verses $\sigma$	56
igure 3-17: Structural Similarity Index improvement with σ	57
igure 3-18: <i>Gγz</i> Behavior for different values of γ	60
Figure 3-19: Ground Truth "*" and Reconstructed Signal "o"	63
Figure 3-20: SNR versus iterations	. 64
Figure 3-21: MRI Recovery with PSL0 and Other Algorithms	.67
Figure 3-22: ISNR and SSIM attained by PSL0 and other Algorithms	
Figure 4-1: $l1$ norm approximation using the $tanh$ with varying values of $\gamma = (1, 4, 6, and 10)$	

Figure 4-2: Illustration of the bound for the error of the $l1$ norm approx. for $z > 0$
Figure 4-3: <i>l</i> 1 norm estimation bounds for the error while z < 078
Figure 4-4: Different curves for various values of $\alpha$
Figure 4-5: Fitness comparison of proposed and soft thresholding technique83
Figure 4-6: The effects of the sparsity of the proposed and soft thresholding technique84
Figure 4-7: The sparse signal recovered using the proposed algorithm and the soft thresholding method.
85
Figure 4-8: The SSIM between the soft-thresholding and proposed algorithm86
Figure 4-9: The correlation between the proposed tanh and the soft thresholding algorithm87
Figure 4-10: Depicts subjective analysis of MRI of recovered images88
Figure 4-11: Recovered cardiac cine MRI with different sparsifying transforms90
Figure 4-12: Cardiac Cine MRI using both algorithms93
Figure 4-13: SSIM attained by various techniques at different acceleration rates93
Figure 4-14: Fitness achieved by both methods for recovery of cardiac cine MRI94
Figure 4-15: Our method outperforms the soft thresholding method in terms of PSNR at all acceleration
rates94
Figure 4-16: In real vivo data simulation results95
Figure 5-1: Ground Truth 'o' and Reconstructed Signal '*'
Figure 5-2: Recovered signal SNR at each iteration
Figure 5-3: MSE of the recovered signal at each iteration
Figure 5-4: MSE and SNR curves for recovery of CS MRI
Figure 5-5: Illustration of proposed SL01 recovery from undersampled MRI (a) original and recovered
images (b) masks for undersampling (c) Magnified (difference error x 1000) between original
and recovered MRI
Figure 6-1: Basic PSO Flow Chart
Figure 6-2: Two Initial Inputs for NI-IRLS from ZF and LR and generated output from the proposed
algorithm119
Figure 6-3: Different domains used in the proposed algorithm120
Figure 6-4: k-Sparse Signal Recovered through LS
Figure 6-5: k-Sparse Signal Recovered through SSF
Figure 6-6: k-Sparse Signal Recovered through PCD125
Figure 6-7: k-Sparse Signal Recovered through PSO125
Figure 6-8: k-Sparse Signal Recovered through IRLS126
Figure 6-9: Recovered k-Sparse 1D Signal through Proposed Nature Inspired IRLS126
Figure 6-10: Cost Function minimisation by NI-IRLS vs other methods
Figure 6-11: MSE minimised by proposed NI-IRLS vs other techniques127
Figure 6-12: Maximum SNR achieved by proposed NI-IRLS vs other techniques

Figure 6-13: Results of increasing sparsity level achieved by NI-IRLS vs other methods128
Figure 6-14: Illustrates (a) Zoomed-in recovered phantom MRI, (b) Masks for Undersampling, (c)
Magnified Difference of Original and Recovered Phantom MRI132
Figure 6-15: ISNR, PSNR, SSIM and Fitness achieved by NI-IRLS vs. other Methods for recovery of
Phantom MRI132
Figure 6-16: Illustrates (a) Zoomed-in recovered Brain MRI, (b) Masks for Undersampling, (c)
Magnified Difference of Original and recovered Brain MRI Images
Figure 6-17: Comparison of ISNR, PSNR, SSIM and Fitness for recovery of CS Brain MRI at each
iteration
Figure 6-18: The SSIM achieved by varying compression ratio using NI-IRLS vs. other comparison
methods
Figure 6-19: The PSNR achieved by varying compression ratio using NI-IRLS vs. other comparison
methods
Figure 7-1: Two Initial Inputs for H-SL1 from ZF and LR and generated output from the proposed
algorithm143
Figure 7-2: Different domains used in the proposed algorithm143
Figure 7-3: Recovered ID k-sparse signal using LS
Figure 7-4: Recovered 1D k-sparse signal using SSF
Figure 7-5: Recovered 1D k-sparse signal using PCD
Figure 7-6: Recovered 1D k-sparse signal using PSO
Figure 7-7: Recovered 1D k-sparse signal using IRLS
Figure 7-8: Recovered 1D k-sparse signal by Heuristic SL1
Figure 7-9: Cost Function minimised by H-SL1 vs. other methods
Figure 7-10: SNR achieved by H-SL1 vs. other methods
Figure 7-11: MSE minimised by proposed H-SL1 vs. other methods
Figure 7-12: Normalized Success Rate by varying sparsity level
Figure 7-13: Illustrates (a) Zoomed-in recovered phantom MRI, (b) Masks for Undersampling, (c)
Magnified Difference of Original and Recovered Phantom MRI
Figure 7-14: ISNR, PSNR, SSIM and Fitness achieved by H-SL1 vs. other Methods for recovery of
Phantom MRI
Figure 7-15: Illustrates (a) Zoomed-in recovered Brain MRI, (b) Masks for Undersampling, (c)
Magnified Difference of Original and recovered Brain MRI Images
Figure 7-16: Comparison of ISNR, PSNR, SSIM and Fitness for recovery of CS Brain MRI at each
iteration
Figure 7-17: The SSIM achieved by varying compression ratio using H-SL1 vs. other comparison
methods
Figure 7-18: The PSNR achieved by varying compression ratio using H-SL1 vs. other comparison
methods

Figure 8-1: DISTA-CSNet Training Model	166
Figure 8-2: Loss functions vs Epochs for 5-fold compression of Brain and Knee MRIs	173
Figure 8-3: Loss functions vs Epochs for 2-fold compression of Brain and Knee MRIs	173
Figure 8-4: DISTA-CSNet Testing Model	174
Figure 8-5: Sample Recovered Images from Testing with Different Datasets	178
Figure 8-6: PSNR and SSIM for Brain MRI of 50 slices at a compression ratio of 20 %	180
Figure 8-7: PSNR and SSIM for Knee MR Images at 5-fold compression	180
Figure 8-8: PSNR and SSIM for Brain MRI with 123 slices with 5-fold compression	181

## List of Tables

Table 3-1: Value of $\sigma$ for matching of width for DA Functions	46
Table 3-2: Effects of MRI recovery on varying sampling ratio	58
Table 3-3: Values of MSE and SNR at Different Iterations	63
Table 4-1: Accuracy of recovery of 1-D sparse signal by the proposed method is evident	84
Table 4-2: The performance of both algorithms against varying CR	88
Table 4-3: The performance of various sparsity transforms is compared	
Table 4-4: Performance analysis of various sparsifying transform	
Table 4-5: The performance comparison of conventional IST with proposed in terms of RMSE	95
Table 8-1: Brain MRI with 50 Slices Testing Results	178
Fable 8-2: Knee MRI Dataset Testing Results with 21 MR Images	179
Table 8-3: Testing results of Brain MR images with 123 slices	
Table 9-1: Summary of SSIM attained proposed methods to recover CS MRI	102

### List of Abbreviations

CS Compressed Sensing or Compressive Sampling

MRI Magnetic Resonance Imaging

DCNN Deep Convolutional Neural Network

GPU Graphic processing unit

ReLU Rectified Linear Unit

POCS Projection onto convex set

IRLS Iterative Reweighted Least Square
SSF Separable Surrogate Functional
IST Iterative Shrinkage Thresholding

ZF Zero Filling

OMP Orthogonal Matching Pursuit
PCD Parallel Coordinate Descent
RIP Restricted Isometry Property

IST Iterative Shrinkage Thresholding

ST Soft Thresholding

DFT Discrete Fourier Transform
PSO Particle Swarm Optimisation

PDF Probability Distribution Function

SSIM Structural Similarity Index

MSE Mean Square Error
SNR Signal-to-Noise Ratio

ISNR Improved Signal-to-Noise Ratio

PSNR Peak Signal-to-Noise Ratio

NP Non-Deterministic Polynomial Time

MAP Maximum A posteriori Probability

CR Compression ration

CS MRI Compressively Sampled MRI in k-Space

RMSE Root Mean Square Error

DNN Deep Neural Network

LS Least Square

FDT Finite Difference Transform

FOV Field of View

FFT Fast Fourier transform

IFFT Inverse FFT

WT Wavelet Transform

CNN Convolution Neural Network

SL0 Smoothed approximation of  $l_0$  norm SL1 Smoothed approximation of  $l_1$  norm

SL01 Combined Smoothed  $l_0$  and  $l_1$  norm

DL Deep Learning

# **List of Symbols**

x	One-dimensional signal
X	Image
Z	One-dimensional sparse representation of the signal
Z	Sparse representation of the image
Ψ	Sparsifying transform, i.e., Wavelet
Φ	Compressed sensing matrix
Ω	Random sampling matrix
A	Measurement matrix
$\mathbf{A^T}$	Transpose of matrix A
A <sup>-1</sup>	Inverse of matrix A
b	Measurement noise
y	Observations
Y	Compressive sampled image
n	Length of signal
m	Number of observations
$\ \mathbf{x}\ _{\mathbf{p}}$	$l_p$ norm of vector <b>x</b>
x	Absolute of x
8	Estimate of x
F	Fourier transforms
F <sub>u</sub>	Undersampling in k - space data
M	Undersampling mask
λ	Thresholding parameter
α	Hyperbolic tangent parameter

### **CHAPTER 1**

#### INTRODUCTION

The conventional method of converting analog signals into digital systems involves sampling them at a frequency twice as high as the highest frequency component found in the continuous signal. This rate of sampling was established by the Nyquist criteria. The theorem demonstrated that sampling the continuous signal under the prescribed rate results in aliasing artefacts during the process of converting the sampled data back into an analog signal. These artefacts cause the loss of information contained in the original signal.

Since then, significant progress has been made to reduce the data volume in the digital domain by leveraging signal redundancy following data acquisition. One approach to achieve compression involves transforming a signal or image into a domain that highlights sparse information, where most of the signal's contents are concentrated. Compression can be accomplished by selectively discarding elements with less significant information while maintaining efficient signal reconstruction. For instance, commonly employed image compression standards like JPEG and JPEG 2000 use the DCT, and wavelet transforms, respectively, to use sparsity in images. These transformations allow for the retention of coefficients with the largest amplitudes while smaller coefficients are discarded. Remarkably, the image can still be reconstructed with minimal perceptible deviation from the ground truth image [1]. This method effectively decreases the storage requirements for a digital image. However, it's crucial to keep in mind that all pixels are collected in acquisition process, and disregarding this acquired data adds a processing burden and results in resource wastage.

Researchers have introduced a novel sampling theory known as Compressed Sensing (CS) that relies on signal sparsity instead of its maximum frequency. CS accurately reconstructs an image from a reduced set of incoherent measurements by taking advantage of its sparse nature, exceeding the requirements of the Nyquist sampling theorem. Unlike traditional approaches, CS achieves compression during the data acquisition stage itself,

instead of as a separate post-acquisition procedure. The samples obtained for a specific image depend on the amount of information it contains. In many cases, the information rate within an image is significantly lower than what is presented by its frequency content [2-5].

### 1.1 Motivation for CS MRI

Compressed Sensing (CS) finds its application in various domains such as data compression [6], noise removal [7], channel coding [8], radar array signal processing [9], data acquisition [10], and solving inverse problems [11]. Since the inception of CS theory, MRI has been recognized as a potential application. Two significant characteristics of MRI that make it well-suited for CS. Firstly, the data acquisition technique in MRI involves sampling in k-space rather than acquiring pixels individually. Secondly, MRIs naturally exhibit sparsity when represented in a suitable domain, i.e., the Wavelet domain.

MRI is a vital diagnostic technique in contemporary medical care, relying on the nuclear magnetic resonance phenomenon to provide high-quality soft tissue contrast in a non-invasive manner without ionizing radiation like X-rays and CT scans. MRI is particularly valuable for monitoring changes in oxygen saturation levels in the human brain, assessing blood flow velocity, and measuring body temperature.

Over the years, there have been significant improvements in the quality and speed of MRI. Research efforts have primarily focused on enhancing speed through hardware mechanisms. Faster data acquisition techniques and improved pulse sequences have contributed to increased imaging speed. Additionally, parallel imaging utilizing multiple coils has substantially reduced scanning times. Techniques such as leaving k-space encoding lines, although resulting in a reduced field of view (FOV) and decreased SNR, can speed up the scanning process. Another approach involves exploiting the conjugate symmetry in k-space through partial Fourier imaging. However, certain methods, such as employing high gradient amplitude with faster switching, may lead to undesirable nerve stimulation. However, due to physical limitations, hardware improvements have reached a point where further reduction of MRI scan time is challenging. Since the sampling rate during the data collection process directly relates to the amount of time an MRI scanner requires, CS can be a key factor in speeding up scans. Less samples were collected in k-

space, CS, in combination with non-linear reconstruction techniques, enabling high-quality MRI recovery while decreasing the overall scan time [12-28].

In recent times, there has been a surge of interest in employing deep learning methodologies to enhance the reconstruction of Compressively Sampled Magnetic Resonance Imaging (CS MRI) images from undersampled data. Convolutional Neural Networks (CNNs), as a form of deep learning models, exhibit promise in capturing intricate patterns and structures within images. This inherent capability proves beneficial for the reconstruction of high-quality MR images. Researchers have dedicated efforts to tailor deep learning architectures specifically for CS MRI reconstruction. These architectures undergo training to comprehend the mapping between undersampled k-space data and fully sampled MRI data. Through the utilization of extensive datasets comprising matched, undersampled, and fully-sampled data, these models strive to assimilate underlying image structures and enhance reconstruction accuracy [29-31].

Deep learning methodologies in CS MRI recovery commonly embrace an end-to-end learning framework. This implies that the network takes undersampled data as input and directly produces a fully sampled image as output, bypassing intermediate steps like iterative reconstruction. The adoption of an end-to-end learning approach not only enhances efficiency but also reduces computational complexity [32]. Researchers have delved into diverse data augmentation techniques to artificially enlarge the training dataset, addressing the challenge posed by limited training data. These techniques encompass random transformations, patch extraction, and simulated undersampling patterns. Moreover, regularization techniques, including the integration of sparsity or total variation constraints, have been implemented to refine the generalization and reconstruction quality of deep learning models [33, 34]. Transfer learning, an approach involving the fine-tuning of models pre-trained on extensive image datasets for CS MRI reconstruction, has been explored to counteract the limited availability of annotated training data. Pretraining CNN models on vast datasets of natural images, such as ImageNet, enables the capture of general image features that prove advantageous in CS MRI reconstruction tasks [35-37].

The advantages of deep learning for compressively sampled image recovery heralds a transformative approach, primarily through significantly improved reconstruction accuracy. These deep learning models excel in learning intricate patterns and features from the data, enabling a faithful recovery of compressed images. A notable advantage lies in

the reduction of sampling requirements; these models enable reliable reconstruction from substantially fewer measurements, potentially expediting the image acquisition process. The adaptability and generalization capabilities of these models across diverse imaging scenarios further solidify their advantages, ensuring robustness and high performance in various conditions. Furthermore, their ability to handle non-linear mappings between compressed measurements and the original image sets them apart from traditional methods, paving the way for more accurate and efficient image recovery without relying on handcrafted feature extraction.

However, the implementation of deep learning for compressively sampled image recovery isn't without challenges. One significant drawback pertains to the substantial computational complexity demanded during training, particularly when dealing with large datasets and complex network architectures. Moreover, the heavy reliance on large and diverse datasets for effective training could result in poor generalization if the data is insufficient or biased. Additionally, the lack of explanation in deep learning models poses a hurdle, as their operation often remains opaque, making it challenging to interpret the decision-making process during image recovery. Addressing issues such as overfitting and the sensitivity to hyperparameters is crucial to fully harness the potential of deep learning in compressively sampled image recovery applications.

#### 1.2 Problem Statement

In contemporary clinical disease diagnosis, Biomedical Imaging plays a pivotal role, with MRI and CT scans being increasingly relied upon by physicians. Despite their effectiveness in detecting conditions such as tumours, heart weaknesses, and bone fractures, these imaging techniques come with drawbacks. CT scans expose patients to potentially harmful electromagnetic radiation, while Dynamic MRIs necessitate lengthy image acquisition times, inducing patient anxiety and claustrophobia. To ensure clear final MR images and minimize artefacts caused by breathing and respiratory motion, patients often must remain motionless and hold their breath during scans, necessitating sedation for children and uncooperative patients. Compressed Sensing (CS) has emerged as a promising solution for expediting image acquisition, generating high-quality images with fewer measurements, thus reducing patient exposure to radiation and scan duration. However, the computational complexity of recovering images from fewer measurements presents challenges,

particularly in the nonlinear optimization involved in CS-based biomedical imaging reconstruction. Conventional CS-based reconstruction algorithms are not optimized for large datasets, exacerbating computational intensity and time consumption. This research aims to enhance the efficiency of CS-based biomedical imaging reconstruction by leveraging data parallelism and exploiting processor hardware architecture. Efficient utilization of computational resources, including parallel processing and optimization techniques, is essential to address these challenges and effectively recover compressively sampled MRI using deep neural networks.

### 1.3 Research Objectives

The following are the objectives of the research work:

- Develop novel compressed sensing recovery algorithms that enhance the efficiency
  of recovering compressively sampled biomedical images such as MRI and 1D
  sparse signals.
- Investigate the performance of combining the l<sub>0</sub> and l<sub>1</sub> norm with regularized smooth approximations to accelerate the recovery process compared to existing cost functions of algorithms used in compressed sensing recovery.
- Explore improved smooth approximations of the l<sub>0</sub> and l<sub>1</sub> norm to enable the
  application of gradient-based algorithms for finding optimal sparse solutions in the
  compressed sensing recovery framework.
- Investigate the heuristic algorithms combined with a smooth approximation of l<sub>1</sub>
   norm for the reconstruction of CS MRI and undersampled 1D sparse signal.
- Investigate and develop the nature-inspired algorithms in combination with Iterative Shrinkage Algorithms for recovery of CS MRI and limited observations of 1D sparse signal.
- Modify Iterative Shrinkage Algorithms (ISA) to optimise their suitability for graphical processing units (GPUs) by utilizing parallel processing techniques that can be applied in Deep Neural Networks CS MRI recovery context.
- Explore and develop deep neural network architectures specifically tailored for compressive sensing recovery, aiming to enhance the efficiency and accuracy of image reconstruction from compressed measurements.

### 1.4 Main Contributions

The motivation behind this work is to introduce efficient reconstruction methods for compressively sampled biomedical images, i.e., MRI, and to be able to use these algorithms in the context of Machine Learning based CS MRI reconstruction. The proposed recovery algorithms rely on iterative shrinkage methods based on smooth approximations of sparsity-promoting norms such as  $l_0$  and  $l_1$  norm, which are particularly suitable for high dimensional signals.

The following are the key contributions to our research work:

- This dissertation proposed a novel Kronecker Delta function for smooth approximation of  $l_0$  norm that efficiently recovers the undersampled 1D signal sparse signal and CS-MRI compared to previous techniques.
- In depth, performance analysis of different Kronecker Delta functions to approximate sparsity promoting  $l_0$  norm for recovery of CS MRI and undersampled 1D sparse signal.
- The introduced novel cost function that combines smooth approximations of  $l_0$  and  $l_1$  norm for recovery of undersampled 1D sparse signal and MRI from fewer observations in K-space.
- A novel method that approximates l<sub>1</sub> norm with smooth hyperbolic tangent function. The smooth approximation in loss function allows us to apply gradient descent-based optimisation techniques to find near-optimal solution of the inverse problem posed by CS MRI recovery efficiently.
- The nature-inspired algorithm i.e., PSO has been combined with Iterative Reweighted Least Square (IRLS) method to recover CS MRI from undersampled k-space data and 1D sparse signal from fewer observations. The proposed method was evaluated with comprehensive experiments to recover 1D sparse signal and MRI accurately from undersampled data as compared to existing techniques.
- The heuristic smooth approximation of  $l_1$  norm is proposed to recover CS MRI from undersampled k-space data and 1D sparse signal. The proposed method was assessed with extensive experimentation to recover 1D sparse signal and MRI accurately from undersampled data compared to existing techniques.

• The major contribution of this thesis is developing a novel deep neural network dubbed as DISTA-CSNet that efficiently trains the model to efficiently recover MRI from undersampled k-space date in significantly reduced time compared to state-of-the-art methods in literature. The dropouts introduced in the proposed DNN as a regularization method made the trained model more robust to different datasets while testing it to three different datasets. The DISTA-CSNet not only recovered MR images more efficiently in the testing phase, but also improved the accuracy of the recovered CS MRI.

### 1.5 Thesis Organization

The rest of the thesis is organized as follows:

In Chapter 2, introduce compressed sensing and their sparsifying domains, with a specific emphasis on their application in biomedical imaging, such as MRI. This chapter presents an overview of existing deep-learning methods for recovering CS MRI from fewer samples k-space. Furthermore, a concise overview of the relevant literature is presented, followed by an explanation of the quantitative measures employed in the recovery algorithms for compressed sensing.

Chapter 3 reviews the existing Kronecker Delta smooth approximations of  $l_0$  norm and proposes a novel smooth approximation of  $l_0$  norm. Since solving the  $l_0$  norm minimisation is a challenging combinatorial problem, researchers have proposed nonlinear recovery methods that employ smoothed approximations of the  $l_0$  norm, which offers computational efficiency. This chapter conducts an in-depth comparative analysis of five versions of smoothed  $l_0$ -norm functions. The existing smoothed  $l_0$ -norm-based recovery algorithm is modified and applied to reconstruct CS MRI using these approximation functions. The performance of each smoothed  $l_0$  norm approximation is extensively evaluated for reconstructing compressively sampled 1D sparse signals and 2D MRI (Brain) data across various sampling rates.

Chapter 4 aims to overcome the non-differentiable nature of the  $l_1$  norm and the inapplicability of gradient-based minimization algorithms, there arises a necessity to approximate the  $l_1$  norm using a smooth approximation. IST algorithms offer a proficient approach to minimise  $l_1$  regularized LS optimization problems while inducing sparsity in the solutions that is required in compressive sensing (CS) recovery. This chapter presents

a novel recovery method that utilizes the tanh to reconstruct undersampled signals/images within the CS framework. The proposed approximates the  $l_1$  norm and soft thresholding using hyperbolic tangent functions. We also evaluate bounds for the error of the proposed  $l_1$  norm smooth approximation. To assess the efficiency of the proposed method, the datasets used consists of 1-D sparse signals, CS MRI, and Cardiac Cine MRI.

Chapter 5 proposes a non-linear reconstruction technique based on smoothed approximations of  $l_0$  and  $l_1$  norms, which have been demonstrated to be computationally efficient. This technique is proposed for recovering sparse signals by combining the  $l_0$  and  $l_1$  norms, enabling accurate reconstruction of CS sparse signals. Empirical results indicate that the proposed method outperforms traditional smooth approximations of the  $l_0$  and  $l_1$  norms in terms of efficiency.

Chapter 6 proposed a novel method for recovery of CS MRI and 1D sparse signal using nature-inspired iterative reweighted least square. This method combines the PSO with the IRLS method. Through extensive experimentation, the performance of proposed algorithm was evaluated, demonstrating its ability to accurately recover both 1D sparse signals and MRI from undersampled data. The evaluation results revealed superior performance compared to existing techniques for CS recovery.

In Chapter 7 we have proposed the novel heuristic smooth approximation of the  $l_1$  norm is introduced in this study for the recovery of CS MRI from undersampled k-space data and 1D sparse signals. The proposed method was thoroughly evaluated through extensive experimentation to accurately recover both 1D sparse signals and MRI from undersampled data. The assessment demonstrated the advantage of the above-mentioned technique over existing methods in terms of achieving accurate recovery in the context of CS.

In Chapter 8, a novel deep neural network called DISTA-CSNet is introduced, which is specifically designed to efficiently train the model for the recovery of MRI from undersampled k-space data in a considerably reduced time relevant to existing state-of-the-art algorithms. DISTA-CSNet demonstrates improved efficiency in the testing phase by efficiently recovering MR images and enhancing the accuracy of the recovered CS MRI.

The thesis concludes in *Chapter 9*, summarizing the key findings and contributions in CS MRI recovery. Potential future directions for further exploration and advancement in this field are discussed. This includes identifying areas for improvement, potential

extensions of existing techniques, and emerging research trends that could shape the future of CS MRI recovery. By highlighting these future directions, the thesis aims to inspire and guide future research endeavours in advancing the field of CS MRI recovery and its applications in medical imaging.

#### **CHAPTER 2**

### **COMPRESSED SENSING IN MRI**

Recently, significant advancement in sampling rates of modern analogue-to-digital converters. This has led to the realization that the data obtained from sampling natural analogue signals is superfluous and can be compressed without a noticeable loss of quality. Researchers have exploited this redundancy and developed various effective data compression techniques, enabling efficient storage capacity and bandwidth utilization. Many compression methods, such as JPEG and JPEG 2000, leverage signal and image sparsity in specific domains. More recently, the emergence of CS theory suggests that the data sampling process can achieve compression itself, rather than relying solely on postacquisition compression. CS finds application in scenarios where each measurement is costly, sensor limitations exist, measurements take a long time (e.g., in MRI), and power constraints are crucial, particularly in battery-powered devices. DNN has also shown promise in the recovery of compressively sampled MRI from fewer samples in k-space. These networks can effectively reconstruct superior MRI from sparse measurements by leveraging their powerful learning capabilities. This approach offers potential advancements in efficient and accurate MRI recovery, leading to improved diagnostic capabilities and reduced scanning time. This chapter provides a detailed description of CS MRI theory, and its applicability in the DNN framework.

#### 2.1 Introduction

Compressed sensing revolutionizes traditional signal processing by introducing a novel approach to signal acquisition. It exploits the well-known fact that many signals possess sparsity in a suitable domain, allowing for effective compression during the data acquisition process. The conventional sampling method follows the Nyquist criteria [38], which needs a sampling frequency exceeding two times the maximum frequency component present in the signal. However, to lower the sample rate without compromising the accuracy of the restored data, researchers have looked for solutions. In a breakthrough paper in 1967 [39], it was proposed that signals exhibiting sparsity after Fourier

transformation can be accurately sampled at a significantly lower rate using arbitrary sampling schemes, deviating from the uniform sampling suggested by Nyquist.

Practical applications in fields such as image processing, geophysics, and seismic wave detection often involve signals that exhibit sparsity in specific bases. For instance, modern cameras capture millions of pixels in digital acquisition, which can be efficiently transformed into the wavelet domain. A few significant coefficients can accurately reconstruct the image without noticeable quality loss in this domain. This example highlights that the required information to portray an image is much lower than its apparent bandwidth suggests.

Compressed sensing brings about a paradigm shift in signal acquisition by linking the required number of measurements to the information rate instead of its bandwidth alone. This innovative approach involves non-adaptive measurement acquisition, where correlations are established between the signal and random vectors like Fourier or Gaussian distributed matrices. When a signal exhibits sparsity in a known transform and the undersampling process introduces noise-like aliasing artefacts, it becomes possible to recover the signal using a reduced number of measurements faithfully. Nonlinear recovery techniques encourage sparsity and ensure coherence with the acquired data, thereby enhancing the efficiency and effectiveness of compressed sensing methods.

By leveraging the integral sparsity or compression of signals, CS techniques have revolutionized signal acquisition and recovery, making them more efficient and resource-friendly. CS eliminates the need for excessive measurements, reducing acquisition time and lowering data storage requirements. This makes CS particularly valuable in situations where traditional Nyquist-based sampling approaches are impractical or resource-intensive.

The CS techniques are applied in various fields, including in the context of compressed sensing MRI (CS MRI), which has opened new possibilities in various domains. CS MRI allows for efficient and accurate recovery of MRI from fewer measurements, reducing scan times and improving overall efficiency. Machine learning techniques have been integrated with CS MRI to enhance performance. By incorporating machine learning algorithms, CS MRI can effectively learn the underlying structures and patterns in the acquired samples, resulting in improved reconstruction quality and faster processing.

The integration of CS MRI with machine learning holds great promise in advancing medical imaging, wireless communications, and sensor networks. By combining the benefits of compressed sensing with the capabilities of machine learning, we can achieve more accurate and efficient signal recovery, leading to improved diagnoses, faster wireless data transmission, and enhanced performance of sensor networks in various applications. The utilization of machine learning in CS MRI paves the way for further advancements and breakthroughs in these fields [4, 15, 19].

## 2.2 Compressed Sampling

We are interested in determining a solution x of length n for the generic system of linear equations denoted by Eq. (2.1) given system coefficient matrix  $\Phi$  and measurements vector y of length m.

$$\mathbf{\Phi}\mathbf{x} = \mathbf{y} \tag{2.1}$$

In CS, the term x is described as the signal of interest to be retrieved, given that we have a set of measurements y and the sensing matrix  $\Phi$ . As expressed in Eq. (2.2), each measurement in vector y is produced by signal x and the vectors in the sensing matrix  $\Phi$ , where  $y_i$  is each entry of vector y and  $a_i$  are the columns in the sensing matrix  $\Phi$ .

$$\mathbf{y}_{l} = \langle \mathbf{x}, \mathbf{a}_{l} \rangle \tag{2.2}$$

For a matrix  $\Phi$  to qualify as an orthogonal matrix, it must fulfil the condition specified in the given Eq. (2.3).

$$\mathbf{\Phi}^T = \mathbf{\Phi}^{-1} \tag{2.3}$$

When the matrix  $\Phi$  meets the condition stated in Eq. (2.3) and vectors are normalized as unit vectors, it is referred to as an ortho-normal matrix. Furthermore, the orthonormal matrix satisfies Eq. (2.4).

$$\mathbf{\Phi}^{T}\mathbf{\Phi}^{-1} = \mathbf{I} \tag{2.4}$$

When the matrix  $\Phi$  is square, indicating that measurements are equal to the length of the signal, the vector  $\mathbf{x}$  can be retrieved straightforwardly using Eq. (2.5).

$$\mathbf{x} = \mathbf{\Phi}^{\mathsf{T}} \mathbf{y} \tag{2.5}$$

$$y = \Phi x$$

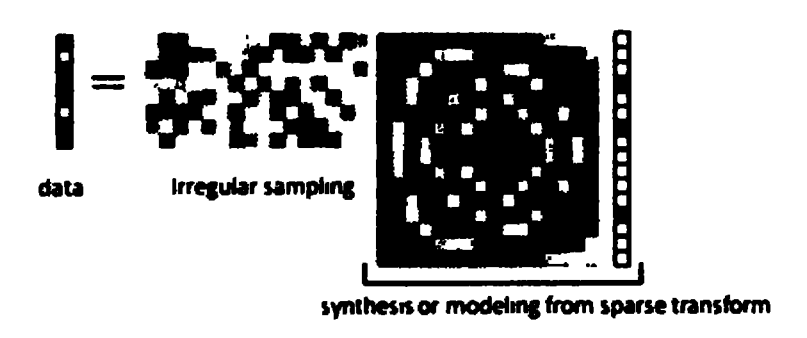


Figure 2-1: Demonstrates the sparsity of signals when transformed on a suitable basis [5]

where, m is the number of measurements that surpasses the length of the signal (n), i.e., m > n, an exact solution may not exist. However, the signal can still be estimated using the least squares method, as defined in Eq. (2.6).

$$\hat{\mathbf{x}} = (\mathbf{\Phi}^{\mathsf{T}}\mathbf{\Phi})^{-1}\mathbf{\Phi}^{\mathsf{T}}\mathbf{y} \tag{2.6}$$

Compressed sensing (CS) operates under the assumption that measurements (m) are significantly less as compared to signal length (n), denoted as  $m \ll n$ . Eq. (2.1) represents an under-determined linear equation system in CS. For a full-rank matrix  $\Phi$ , there can be infinite possible solutions. To obtain the optimal solution, additional constraints are necessary, typically in the form of sparsity constraints. CS proposes that if the signal x has only a few non-zero elements relative to its length and the sensing matrix  $\Phi$  satisfies certain conditions, it is possible to accurately retrieve the signal x from limited observations.

A straightforward approach to consider the feasibility of reconstructing a signal x from limited observations is to assume knowledge of the signal support. If there are only s non-zero elements in a signal of length n, we only need to identify and recover those s elements instead of the entire signal. Consequently, with s elements in the signal x, only s measurements are required, as defined by Eq. (2.7). This approach highlights the potential for accurate signal recovery using fewer measurements, leveraging the sparsity of the signal.

$$y = \Phi_{\rm e} x_{\rm s} \tag{2.7}$$

Indeed, in practical scenarios, the support of the original signal is typically unknown. Therefore, relying solely on s measurements is insufficient. Instead, we require m measurements, where s < m < n. The objective is to recover the actual signal by finding the sparsest possible estimate. By leveraging additional measurements beyond the number of non-zero elements (s), we aim to capture enough information to accurately recover the actual signal, even without prior knowledge of its support. The recovery process involves finding a solution that minimizes the sparsity while satisfying the measurement constraints, enabling the retrieval of the actual signal. Figure 2-1 depicts the illustration of taking measurements as a sparse representation of signal x.

#### 2.3 Sparsity

Compressed sensing operates effectively with a special class of sparse signals. These signals possess most of their elements with closer-to-zero amplitudes, while few elements have non-zero values. The sparsity of a signal allows for the possibility of discarding or ignoring the coefficients with negligible amplitudes without perceptual loss in signal quality.

However, signals with less sparsity can still have sparsifying representations in other domains. The information in a signal is often concentrated in just a limited number of coefficients, while the remaining coefficients can be discarded. The choice of the sparsity domain depends on the signal characteristics. For example, piecewise constant signals can be sparsified using the FDT, while some images can be sparsified using DCT, a widely used technique in image compression. Another popular approach is wavelet transform, as employed in JPEG-2000, which enables sparsification and compression of images by a factor of up to 10 times their original size. Hence, no single transforms applies to all signals, and the suitable sparse transformation is subject to the signal's characteristics and the specific application.

The transformation of a signal that facilitates sparsity is referred to as the sparsifying transform  $\Psi$ . Eq. (2.8) represents the signal transformation x into its sparse representation z.

$$z = \Psi x \tag{2.8}$$

Compressed sensing focuses on three distinct signal domains, as depicted in Figure 2-2. The sparsity domain, denoted as z, represents the signal with fewer non-zero components. The signal domain, represented by x, is where the signal is observed and analyzed. It is the primary domain of interest for understanding the signal's characteristics. Lastly, the sampling domain is where measurements of the signal are obtained. This domain captures the specific locations and values of the acquired measurements.

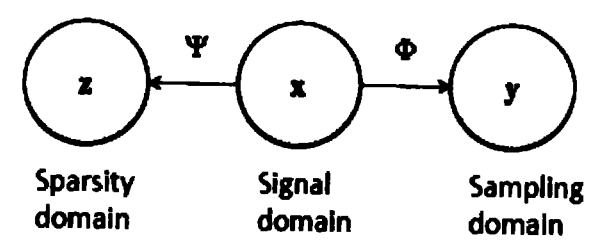


Figure 2-2: The three domains that attract interest in the field of Compressed Sensing

#### 2.4 Incoherence

In compressed sensing, incoherence is a crucial factor that must be considered. It refers to the desired low coherence between the sparsity basis and the measurement basis. When considering a sparsifying matrix  $\Psi$  and a sensing matrix  $\Phi$  with orthonormal bases in  $\mathbb{R}^n$ , the coherence can be defined as the highest inner product of two vectors from the matrices defined by Eq. (2.9). Ensuring a low coherence value is important for the success of compressed sensing techniques.

$$\mu(\mathbf{\Phi}, \mathbf{\Psi}) = \sqrt{n} \max_{i \le k, j \le n} |\langle \varphi_k, \psi_j \rangle| \tag{2.9}$$

The value of  $\mu$  represents a correlation of the bases of the two matrices. Each vector is normalized to a magnitude of one, and the normalization factor  $\sqrt{n}$  ensures that  $\mu$  falls within the range of 1 to  $\sqrt{n}$ . In compressed sensing, a low coherence between the two domains is desirable. Incoherence guarantees that the signal is dense in the sampling domain, allowing for flexibility in selecting any set of samples during under-sampling [40].

Compressed sensing techniques often employ random matrices, i.e., random Gaussian and Bernoulli measurement matrices. This is because these matrices have less coherence to sparse basis  $\Psi$ . However, the application of the above-mentioned matrices has certain drawbacks. These matrices can have high computational costs and may not be suitable for handling large datasets, such as high-resolution images. In such cases, alternative options

like the Fourier and Wavelet bases prove to be advantageous. These bases exhibit high incoherence with the canonical basis [41], making them viable alternatives in scenarios where random matrices are less feasible.

### 2.5 Sparse Signal Recovery Constraints

To faithfully reconstruct a sparse signal, two conditions must be satisfied. Firstly, the measurement matrix must adhere to the RIP, ensuring accurate recovery of a signal. Secondly, the minimum sampling rate required for precise recovery must be determined. These conditions will be elaborated upon in the following discussion.

### 2.5.1 Restricted Isometric Property (RIP)

The faithful recovery of sparse signals relies on the adherence of the sampling matrix to the RIP. In the case, where signals represented in an orthogonal basis are sparse, the recovery of its sparse representation (z) is like the recovery of the actual signal (x). This can be achieved by employing the matrix  $\mathbf{A} = \mathbf{\Phi} \mathbf{\Psi}^{\mathrm{T}}$ , where  $\mathbf{\Phi}_{m \times n}$  and  $\mathbf{\Psi}_{n \times n}$  are orthonormal matrices that map the sparse coefficients to a set of observations. The concept of RIP was initially introduced by Candes and Tao [42], to assess the effectiveness of the sampling matrix. The RIP constant, denoted as  $\delta_s$ , is the smallest quantity specified in Eq. (2.10).

$$(1 - \delta_s) \|\mathbf{z}\|_2^2 \le \|\mathbf{A}\mathbf{z}\|_2^2 \le (1 + \delta_s) \|\mathbf{z}\|_2^2 \tag{2.10}$$

The sparse signal z,  $\delta_s$  is preferred to be closer to zero with a well-performing matrix A, a smaller  $\delta_s$  indicates a reduced likelihood of z falling within the null space of A. Additionally, when matrix A satisfies the RIP, the energy of signal (z) is preserved following the transformation Az. Moreover, the RIP guarantees that any subset of the matrix A maintains an orthonormal property.

#### 2.5.2 Minimum Sampling Frequency

CS provides the capability to recover a sparse signal x from a significantly reduced number of measurements (m) compared to what is traditionally suggested by the Nyquist sampling theorem. However, a crucial question remains: How far can we push the limits of undersampling while still achieving accurate signal recovery? The minimum number of samples

required is defined by Theorem 2.1, which establishes the lower bound for reliable signal reconstruction.

**Theorem 2.1:** Let's consider a signal  $x \in \mathbb{R}^n$  that is s sparse in  $\Psi$  basis and select m measurements at random in  $\Phi$  domain. If

$$m \ge c.\mu^2(\mathbf{\Phi}, \mathbf{\Psi}).s.\log(n/k)$$
 (2.11)

for constant c > 0, the vector x, there is a high chance of its recovery, ensuring exact reconstruction.

The significance of coherence in determining the required number of samples is evident from Eq. (2.11). Greater incoherence within systems allows for accurate recovery even with a smaller number of samples. By acquiring m measurements, which can be significantly fewer than the signal length (n), no information is lost in the signal. If the coherence  $\mu(\Phi, \Psi)$  closer to one, the required observations can be reduced to s.log(n/k) instead of the traditionally used n measurements [4].

Practically, numerous researchers adhere to a commonly followed guideline known as the "4 to 1" rule. According to this rule, it is recommended to have four incoherent measurements for every unit of unknown nonzero element in the sparsifying domain[43].

#### 2.6 Introduction to MRI

MRI has emerged as a prominent domain for implementing compressed sensing (CS) techniques. In the early stages of CS theory, the research community recognized MRI as a promising application for CS. The fundamental principles of MRI and how MR images can exhibit sparsity through various sparsifying transforms. Furthermore, the chapter delves into the potential of CS in reducing the scan time required for MRI procedures.

#### 2.6.1 Nuclear Magnetic Resonance (NMR)

The phenomenon of NMR finds its most accurate description in the realm of quantum mechanics. However, at the microscopic level, classical physics can also provide an accurate representation [16, 44, 45]. In the context of MR imaging, the signals originate from the protons found within water molecules present in the body. These protons become polarized by a strong magnetic field,  $B_0$ , resulting in a magnetic moment aligned with the static field. The NMR signals are generated by this magnetic moment. The longitudinal

direction refers to the orientation of the field, while the transverse plane represents the vertical plane to the direction of the field.

Bloch Eq. (2.12) establishes the connection between magnetic field B and the magnetic property M.

$$\frac{dM}{dt} = M + \gamma B + \frac{M_0 - M_z}{T_1} + \frac{M_{xy}}{T_2} \tag{2.12}$$

In this equation,  $M_{xy}$  represents the transverse magnetization,  $M_0$  represents the equilibrium magnetization, and  $M_z$  represents the longitudinal magnetization. The constants  $T_1$ ,  $T_2$ , and  $\gamma$  depend on the specific characteristics of the tissues and materials involved.

When a Radio Frequency (RF) is applied to the  $B_1$  field, the net magnetic field becomes distributed, resulting in the generation of the magnetization component  $M_{xy}$ . The equation describes the characteristic frequency produced by this magnetization process.

$$f_0 = \frac{\gamma B_0}{2\pi} \tag{2.13}$$

The equation introduces the procession frequency, denoted as  $f_0$ , which relates to the static field  $B_0$ , with the constant  $\frac{\gamma}{2\pi}$ . For a typical 1.5T MR scanner, the frequency is approximately 64 MHz. The coil that receives the signal generated by the transverse magnetization component,  $M_{xy}$ . By capturing the spatial spreading of this magnetization, the MR image is obtained.

The relaxation of magnetization in the transverse plane occurs over some time period  $\tau$ . The longitudinal component experiences an exponential recovery described by:  $M_0\left(1-e^{-\frac{\tau}{T_1}}\right)+M_z(t)$ , where  $T_1$  represents the time constant. Instead, the transverse component declines exponentially as  $M_{xy}(t+\tau)=M_{xy}(t)e^{-t/T_2}$ , with  $T_2$  as the time constant. These relaxation time constants,  $T_1$  and  $T_2$ , are crucial for capturing image contrast, and different tissues within the body may exhibit varying relaxation parameters [44, 45].

Figure 2-3 depicts the magnetic fields employed in magnetic resonance imaging (MRI). The primary static field, denoted as  $B_0$ , establishes the net magnetization within the imaging subject. It creates a stable magnetic field aligning the nuclear spins in atoms of the tissue.

To initiate the imaging process, a transverse RF field, known as  $B_1$ , is applied. This RF field acts as an excitation source, perturbing the equilibrium of the nuclear spins and causing them to process around the  $B_0$  field. By manipulating the parameters of the  $B_1$  field, such as its frequency and duration, specific regions of the subject can be selectively excited for imaging.

In addition to the primary static and RF fields, gradient fields are employed to facilitate spatial encoding. One of these gradient fields, represented as  $G_x$ , is responsible for generating spatial variations in the magnetic field. By changing the  $G_x$  gradient field, different regions of the subject experience varying B strengths. This spatial encoding enables capturing the spatial distribution of magnetization, which is essential for producing detailed and localized images.

Overall, the combination of the primary static field  $(B_0)$ , the transverse RF field  $(B_1)$ , and the gradient field  $(G_x)$ , allows for the precise manipulation and capturing of the magnetization within the subject, forming the foundation of magnetic resonance imaging.

Magnetic fields used in MRI are shown in Figure 2-3. The net magnetization is generated by the main static field,  $B_0$ . The gradient field,  $G_x$ , generates spatial encoding while the transverse RF field,  $B_1$ , generates magnetization, allowing for the spatial distribution of magnetization to be recorded [16].

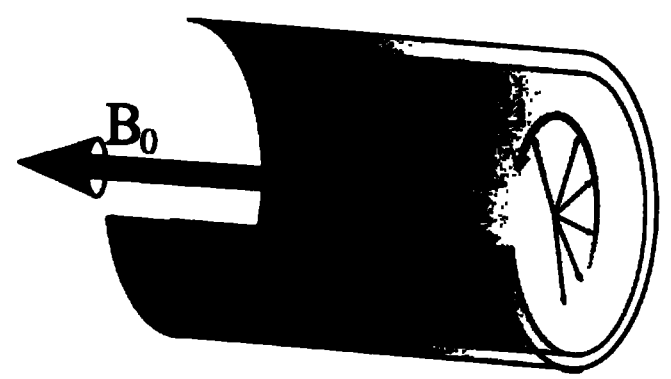


Figure 2-3: The magnetic and gradient fields utilized in MRI [16]

#### 2.6.2 Gradient Encoding and Signal Reception

The use of RF energy to stimulate magnetization results in a change in magnetic flux, which alters the voltage at the receiving coil. Voltage represents the sum of the observations from all stimulated sources and serves as the signal for MR imaging. The signal that was received is intricate and appears as a harmonic frequency.

To capture spatial k-space data, three-dimensional fields are employed. The coils  $G_x$ ,  $G_y$ , and  $G_z$  detect changes in the B concerning spatial location. For instance, when  $G_x$  is used, the B variation relative to the position is represented as  $B(x) = |B_0| + G_x x$ . The change in RF magnetization is proportional to the applied gradient field, establishing the basis for spatial distribution characterization [44, 45].

#### 2.6.3 K-Space and Image Domain

To depict the received magnetic resonance signal and the magnetization distribution have a Fourier association, and the magnetization distribution goes through spectral decomposition. The induced gradient produces a variation in precession frequency, leading to a phase shift. The frequency contribution induced by the gradient is as follows:

$$f_0 = \frac{\gamma G(t).r}{2\pi} \tag{2.14}$$

Here, the amplitude of the gradient is denoted by G(t). The phases of magnetization are defined by the integration of frequency.

$$\phi(r,t) = 2\pi \int_0^t \frac{\gamma}{2\pi} G(s).r \, ds = 2\pi.r.k(t) \tag{2.15}$$

where k(t) can be defined by

$$k(t) = \frac{\gamma}{2\pi} \int_0^t G(s) \, ds \tag{2.16}$$

The signal produced by the received coil can be defined by Eq. (2.17)

$$s(t) = \int m(r)e^{-i2\pi k(t)r}dr \tag{2.17}$$

The signal in MRI is defined by Eq. (2.17), where the signal at a given time t is obtained as the  $F_u$  of the magnetization distribution, m(r), which is acquired in the spatial representation of the Fourier domain represented by k(t). It is important to note that MR imaging techniques differ from pixel-by-pixel optical imaging modalities.

The gradient waveform, G(t), is used in the MR system to acquire the MR image. The RF pulses and gradient waveforms are combined to generate magnetization, referred to as the pulse sequence. The trajectory, k(t), in spatial frequency space (also known as k-space), is determined by integrating the G(t) waveforms. The MR image can be visualized by IFFT to the acquired k-space samples, as depicted in Figure 2-4 [44, 45].

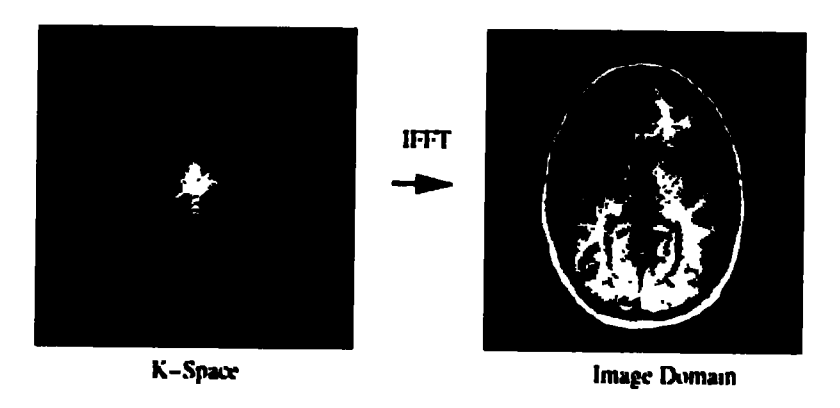


Figure 2-4: Recovery of an image by IFFT from it Fourier data [45]

#### 2.6.4 Resolution vs FOV

The conventional approach to k-space sampling follows the Nyquist criteria, which considers both the FOV and its resolution. The resolution is determined by the extent of the data acquisition area in k-space, with a larger sampling region corresponding to higher resolutions. The FOV can be established by the density of sampling within that area, with bigger objects requiring a higher density of sampling to adequately capture the details.

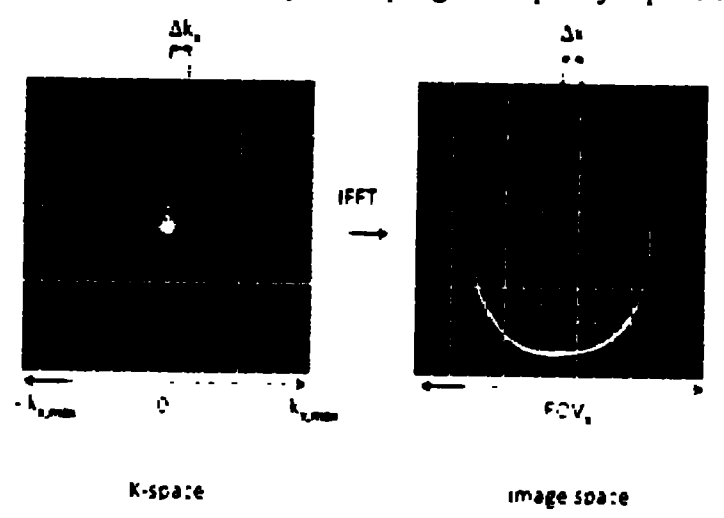


Figure 2-5: The relationship between the field of view and resolution [45]

When departing from the Nyquist sampling rate, artefacts can arise in the image, and the specific characteristics of these artefacts can vary depending on the chosen sampling patterns [45]. The relationship between k-space sampling and FOV is defined by Eq. (2.18), and the connection between resolution and k-space is illustrated in Figure 2-5[16].

$$FOV \alpha \frac{1}{\Delta k} \tag{2.18}$$

#### 2.6.5 K-Space Sampling Patterns

The popular k-space sampling technique for MRI is Cartesian sampling, which adheres to the Nyquist sampling criterion. With Cartesian sampling, the image may be straightforwardly reconstructed using an IFFT. This method is perfect against system shortcomings. However, a downside to Cartesian sampling is that it requires many samples to satisfy the Nyquist limit, which is time-consuming given the inherently slow data acquisition speed in MRI. This motivates the exploration of alternative non-Cartesian sampling methods that can accelerate image acquisition.

In addition to the above, non-Cartesian sampling in k-space has also acquired popularity, especially for accelerated undersampled MRI acquisition. Radial sampling, where k-space is sampled along radial spokes, is a common non-Cartesian technique [46]. Radial sampling patterns have the benefit of over-sampling to the centre of k-space, providing robustness against the motion and flow artefacts [47]. Spiral sampling is another popular approach, with possible variations [48]. The Propeller technique combines aspects of radial and Cartesian sampling for motion correction [49]. Random or stochastic trajectories are also utilized, with compact data acquisition closer to the centre of the k-space and sparse sampling farther out. Stochastic sampling is advantageous for compressed sensing as it introduces noise-like artefacts [14, 15, 50]. Other non-Cartesian patterns like rosette [51] and Lissajou [52] sampling have also been explored. The best-suited sampling method is subject to the application and types of artefacts needing correction [53]. Figure 2-6 illustrates several k-space sampling trajectories.

#### 2.6.6 MRI Sparse Representations

In applying compressed sensing (CS) to MRI, the first step entails undersampling the k-space using different sampling patterns, as explained in the preceding section. Achieving an accurate recovery of the original MR image from the under-sampled k-space data is

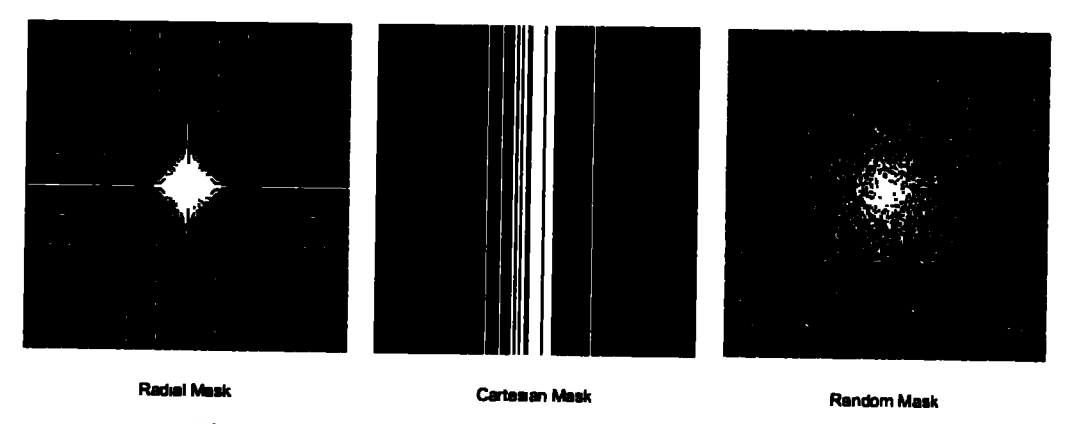


Figure 2-6: Patterns of sampling in the k-space domain

contingent upon the MRI signal demonstrating sparsity, either in the image domain directly or after undergoing a well-defined transformation. Fortunately, numerous MRIs has inherent sparsity in a specific domain, such as MR angiogram images, enabling direct application of CS without requiring additional sparsifying transforms. However, with most MR images, achieving sparsity necessitates employing a specific sparsifying transform, such as the finite difference and Wavelet transforms.

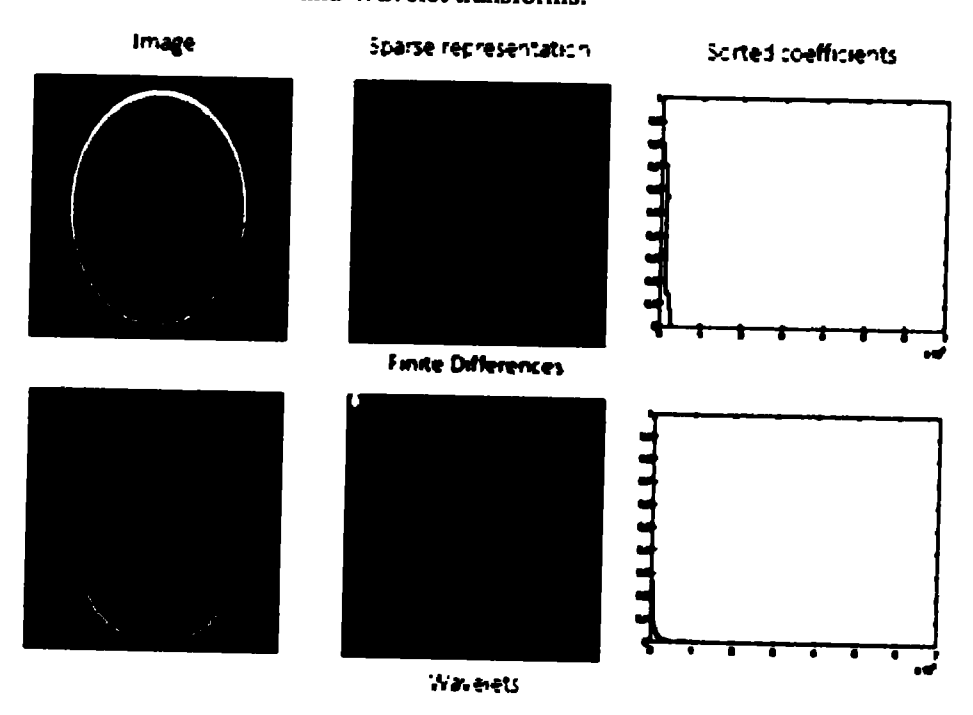


Figure 2-7: Applying sparsity-inducing transforms to various images [16]

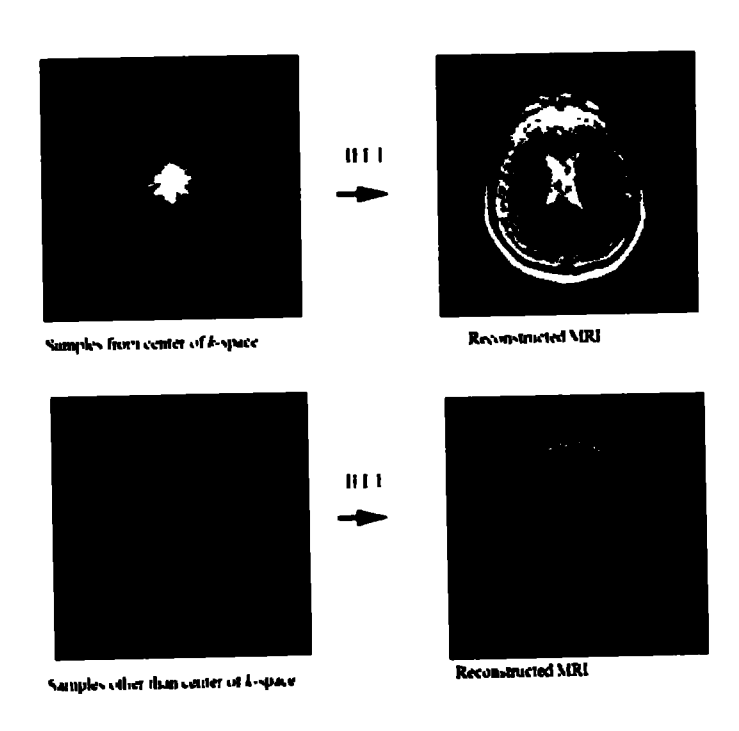


Figure 2-8: Effect of undersampling in k-sparse [24]

The finite difference transform offers an exceptionally sparse representation for images exhibiting piece-wise constancy. Moreover, different wavelet transforms are beneficial for some sets of MR images. Figure 2-7 visually illustrates the sparsity of a Shepp-Logan phantom image using the FDT and an MRI using the WT. Figure 2-7 shows that approximately ten-fold compression in sampling can be reduced in WT without loss of information [54].

Figure 2-8 shows the effect of taking samples from the centre of the k-space and away from the centre. The central part of k-space got the details of a smooth region while outside the central region edge information is stored. So, to get a complete picture we need some samples from both the central part and away from the central part. In some cases, the sparsity of an image can be influenced by the presence of noise. Through sparse approximation, where coefficients with very small amplitudes are set to zero, the image can undergo denoising. This denoising effect is established in the accompanying Figure 2-9 [16].

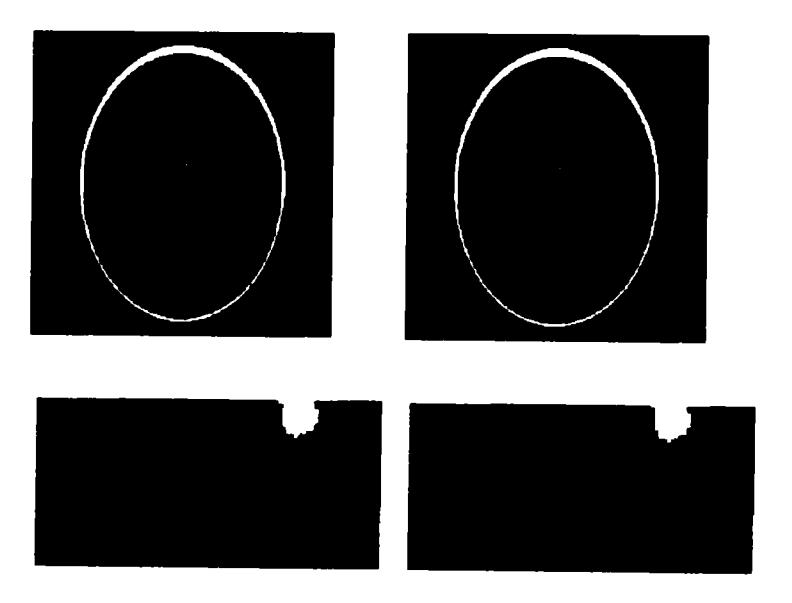


Figure 2-9: Effect of sparse approximation on denoising [16]

#### 2.6.7 Rapid MRI

Recently, progress in improving the quality with speed of MRI. The research focuses primarily on accelerating the speed of MRI through hardware advancements. Faster data acquisition techniques have been crucial in achieving improved acquisition speed. The scanning duration to acquire an MRI relies on the repetition duration  $(T_R)$  multiplied by the amount of RF excitations. One phase in the encoding line is typically obtained from one RF excitement. To estimate the total scanning duration for acquiring a 3D MR image, Eq. (2.19) can be used.

$$T_{acquisition} = N_y N_z N_a T_R \tag{2.19}$$

Here,  $N_y$  represents the phases-encoding lines in the y direction,  $N_z$  indicates the total phases-encoding lines in the z direction, and,  $N_a$  corresponds to the number of averages.

Improving the speed of MR scanning attained by reducing the  $T_R$  according to the equation. The duration of  $T_R$  relies on the applied gradients, and to maintain a constant FOV and resolution, higher gradient amplitudes are necessary for shorter  $T_R$ . However, this approach can lead to unwanted nerve stimulation, making it an undesirable method [55].

Another strategy to increase scanning speed involves employing alternative acquisition methods, such as acquiring multiple sampling lines for one RF excitement. For example, Echo Planar Imaging (EPI), when every piece of data is gathered at once [56]. Furthermore, developing improved pulse sequences and utilizing parallel imaging techniques with

multiple coils have also contributed to significant reductions in scanning times [57]. Skipping encoding lines in k-space is another approach to expedite the scanning process, although it produces less FOV and reduces the SNR. Undersampling in k-space can exploit the symmetry in k-space to address this challenge [58].

The progress in MRI hardware has reached a stage where physical limitations restrict the potential for reducing scan time. As the scan time of MRI is related to the sampling rate during scanning, compressed sensing (CS) has emerged as a valuable approach for reducing this scan time. CS allows for the scanning of a reduced number of samples in the k-space domain while still enabling high-quality MRI recovery through non-linear reconstruction techniques. By leveraging the inherent sparsity or compressibility of MRI signals, CS enables efficient data acquisition and reconstruction, resulting in significant time savings without compromising image quality [12-28].

### 2.7 CS MRI Recovery

Various recovery methods are developed for MRI from undersampled k-space data. These reconstruction techniques can differ in terms of the computational approach taken to recover the image and the k-space sampling methods used during accelerated acquisition.

#### 2.7.1 Linear Recovery Methods

The most straightforward method for recovering a signal or image is the inverse fast Fourier transform (IFFT). However, applying IFFT to undersampled signals can introduce aliasing artefacts that distort the image. To mitigate these artefacts, two techniques are commonly employed:

#### 2.7.1.1 Zero Filling (ZF)

ZF is a simple approach for reconstructing magnetic resonance (MR) images. In ZF, any sampling pattern could be employed for undersampling in k-space. ZF fills the un-sampled k-space data with zeros, essentially extending the acquired data to a fully sampled k-space. While ZF alone does not exploit the compressibility or sparsity of MR images, it serves as a useful initialization step for more advanced compressed sensing (CS) MRI recovery techniques. By starting with ZF reconstruction, CS MRI algorithms can build upon this initial estimate and refine it further to achieve high-quality image reconstructions.

Therefore, ZF is a valuable starting point for CS MRI recovery, setting the stage for subsequent iterative algorithms to enhance the final image reconstruction quality [15].

#### 2.7.1.2 Low Resolution

Another linear reconstruction method using undersampled data and a distinctive sampling pattern is called Low Resolution (LR). The image is reconstructed using IFFT after just the k-space data is entirely sampled from the k-space's centre. This method is quite effective at recovering smooth regions in images, but it cannot restore sharp edges [15]. Figure 2-10 depicts the sampling pattern for the LR recovery technique.

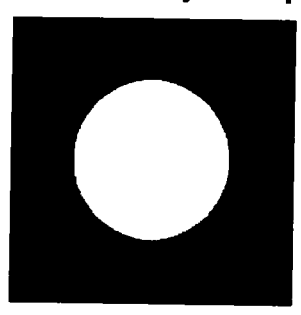


Figure 2-10: Depicts the sampling pattern of the LR mask

#### 2.7.2 Projection onto Convex Set Method

The Projection Onto Convex Sets (POCS) algorithm is an iterative reconstruction approach for undersampled MRI that casts the image recovery problem as finding the intersection of a priori- constraint defined convex sets [59]. In POCS, the known constraints on the desired MR image, such as spatial smoothness, sparsity, and data consistency with the acquired k-space samples, are each represented as a convex set in Hilbert space containing all images satisfying that constraint. The algorithm finds the image at the intersection of these sets through sequential projections. While simple to implement, POCS provides an effective framework for minimizing the mixed  $l_1 - l_2$  convex optimization objective function in Eq. (2.20) for constrained MR reconstruction.

$$\widehat{x} = \underset{x}{\operatorname{argmin}} \|\Psi x\|_{1} \text{ subject to } \|F_{u}x - y\|_{2}^{2} < \varepsilon$$
 (2.20)

In Eq. (2.20),  $\Psi$  represents a sparsifying representation such as a WT or FDT applied to the target image x to be recovered.  $\mathbf{F}_u$  denotes the FFT relating the image to undersampled k-space measurements y.  $\|\Psi x\|_1 = \sum_l |\psi_l x_l|$  is the  $l_1$ norm which promotes sparsity in

the reconstructed image. A modified POCS algorithm for undersampled MRI reconstruction is proposed in [13] that incorporates sparsity-promoting regularization into the iterative projection framework. This allows improved image recovery from limited k-space data by leveraging transform-domain sparsity constraints The enhanced POCS technique employs full-resolution phase estimations, alternating between acquired k-space halves in time series or multi-echo acquisitions. This process allows the calculation of full-resolution phase estimations for each volume/echo, subsequently integrated into the POCS framework [60]. Lately modified POCS has been applied for CS MRI recovery in [61, 62].

The POCS method for Compressively Sampled MRI recovery offers computational efficiency and simplicity through iterative projection onto sets enforcing data fidelity and prior knowledge, enabling easy integration of constraints. However, it can struggle with complex image structures and noise, potentially limiting its ability to capture fine details accurately. The method's performance hinges on the chosen sets and their interaction, impacting convergence and final image quality, posing challenges when these sets don't fully encapsulate the image structure.

Algorithm 2.1: Steps involved in the POCS algorithm.

```
Task: Find the value of x that minimises the objective function: \widehat{x} = \operatorname{argmin} \|\Psi x\|_1 \text{ subject to } \|F_u x - y\|_2^2 < \varepsilon
```

Inputs:

 $Y = F_u X$  (Undersampled k – space data)

 $\lambda = Thresholding parameter$ 

 $\Psi = Sparsifying transform$ 

Output:

 $\mathbf{\hat{X}} = recovered image$ 

**POCS Algorithm:** 

Initialization:  $X_0 = 0, y_0 = y, i = 1$ 

Iterations:

1.  $X_i = F_u^{-1}(y_i)$ ; *IFFT* 

2.  $X_l = \Psi^{-1}\{S_{\lambda}(\Psi X_l)\}$ ; Shrinkage  $(S_{\lambda})$  in sparsifying domain

3. Data Consistency Constraint

3a. 
$$Y_l[j] = F_u(X_l)$$
  
3b.  $Y_l[j] = \begin{cases} y_l[j] & \text{if } y[j] = 0 \\ y[j] & \text{otherwise} \end{cases}$ 

4. Increment i by 1 & repeat 1 — 3 until stopping criteria are met

Output:  $\hat{x} = \mathbf{F_u}^{-1}(y_i)$ 

### 2.7.3 Iterative Reweighted Least Square (IRLS)

IRLS explores using an overcomplete complex wavelet transform to obtain sparse representations of natural images for efficient compression [23]. Conventional image coders use an orthogonal DWT that cannot well model the heavy-tailed non-Gaussian marginal distributions of wavelet coefficients. The authors propose modelling the coefficients with a complex generalized Gaussian distribution with shape parameter p < 2 this non-Gaussian behaviour accurately. They estimate the distribution parameters from training data. An overcomplete complex wavelet provides more flexibility to adapt to image characteristics than an orthonormal DWT. For a given level of sparsity, the overcomplete representation has lower modelling error resulting in lower reconstruction distortion. The authors also present an efficient way to implement the overcomplete transform using a tree-structured filter bank, requiring only 14% more computations than an orthogonal DWT. The overcomplete complex wavelet representation concentrates more signal energy in fewer large coefficients. Encoding these coefficients shows improved rate-distortion performance compared to baseline DWT-based image coders.

Modified IRLS was also presented in [12], where it is applied to efficiently recover compressively sampled MR images. Recently, enhanced versions of IRLS algorithms are used in many applications related to MRI recovery from compressively sampled k-space data [63-65].

The IRLS method excels in recovering sparse signals, particularly in MRI applications, by iteratively updating estimates through weighted least squares solutions, promoting accurate image reconstruction. However, its reliance on prior information about signal sparsity and limitations in handling highly dynamic or non-sparse signals might affect its accuracy, making its success heavily reliant on the appropriateness of assumed sparsity levels and potentially limiting its adaptability to diverse MRI scenarios.

#### 2.7.4 Separable Surrogate Functionals

The Separable Surrogate Functionals (SSF) algorithm proposed by Daubechies et al. [66]. is an iterative shrinkage-based approach for solving inverse problems with objectives containing smooth and non-smooth convex terms. It constructs an SSF that upper bounds the objective using quadratic surrogates for the smooth terms and linear surrogates for the non-smooth terms. Minimizing this separable surrogate reduces the actual objective. This leads to an iterative algorithm with parallelable shrinkage-like updates applied to the nonsmooth terms, providing an efficient solver that leverages problem structure and is guaranteed to converge. SSF has been used successfully to inverse problems like CS MRI reconstruction. Its modified version for efficient recovery of CS MRI has also been developed recently [25]. Recently, SSF is used for recovery of free undersampled breathing Cardiac Cine MRI [67]. The SSF offers quick computation and the ability to incorporate constraints effectively, enhancing reconstruction quality. Yet, its reliance on precise modelling and parameter selection presents challenges, as inaccuracies in the surrogate functional might lead to suboptimal results. The method's performance heavily relies on the choice of the surrogate functional, impacting its ability to accurately capture image features and potentially limiting its effectiveness in specific imaging scenarios.

## 2.7.5 Parallel Coordinate Descent (PCD)

The PCD algorithm by Michael Elad in 2007 is an iterative thresholding approach for recovering sparse signals from incomplete information [68]. It decomposes the full problem into smaller dimensional subproblems, each involving a single component or block of components, that can be solved in parallel. Each subproblem applies a soft-thresholding operator to the residual from the previous iteration to identify the support set. The PCD algorithm leverages block sparsity and parallelization to achieve fast convergence for large-scale sparse coding problems like compressed sensing and CS MRI recovery. A parallel variant of coordinate descent, and provides rigorous theoretical bounds on achievable parallelism. These bounds assist in optimizing the level of parallelism to achieve efficient and effective parallel optimization [69]. Recently, PCD algorithm is modified to be utilized for various applications of biomedical imaging [70, 71]. The PCD offers faster convergence and efficient computation through parallelization, allowing effective integration of constraints. However, its performance hinges on convergence rates

and chosen parameters, potentially affecting the quality of reconstruction. In situations with correlated features, PCD might encounter slower convergence, limiting its ability to capture fine image details, which could pose challenges in certain MRI reconstruction tasks.

## 2.7.6 Fast Iterative Shrinkage Thresholding Algorithm (FISTA)

The ISTA is an iterative optimization algorithm used for solving sparse signal recovery and compressed sensing problems by Daubechies et al. [20]. ISTA targets to reconstruct a sparse signal using an under-determined system of linear equations or observations. It works by iteratively updating the signal estimate using a soft thresholding operator. At each iteration, ISTA performs a gradient descent step followed by soft thresholding, where coefficients less than the threshold are zeroed. This thresholding operation promotes sparsity in the signal estimate. The algorithm iterates until convergence, and the final estimate provides a sparse approximation of the original signal.

FISTA is an accelerated version of ISTA introduced by Beck and Teboulle [72]. FISTA improves the convergence speed of ISTA by incorporating Nesterov's acceleration technique. It achieves this acceleration by introducing an additional momentum term in the gradient descent step. This momentum term helps in making larger steps towards the optimum solution. FISTA retains the same thresholding step as ISTA, but its convergence rate is significantly improved. By exploiting the momentum term, FISTA achieves faster convergence compared to ISTA, making it more efficient for large-scale sparse signal recovery problems. While FISTA often converges faster compared to other algorithms, it may face challenges in handling certain image structures or textures due to its reliance on sparsity constraints. Additionally, FISTA's performance can be sensitive to parameter tuning, where improper choices might lead to suboptimal reconstructions. Furthermore, in scenarios with high noise levels or incomplete sampling, FISTA might struggle to achieve accurate reconstructions, impacting its effectiveness in those specific conditions. Recently, efficient variants of FISTA are employed for recovery of Compressively Sampled MRI recovery in [73-76].

#### 2.7.7 Greedy Algorithms

The greedy algorithms employ projections and least squares to compute the inner product of a signal and the columns of matrix A. These algorithms, including MP [77], OMP [78],

stOMP [79], ROMP [80], and CoSaMP [81], SRR [82], SPAMP [83] come in various variants. The primary objective of greedy algorithms is to iteratively determine the signal support  $\Omega$ . Once  $\Omega$  is identified, the next step involves estimating the signal amplitudes by the LS method. The amplitudes can be easily calculated by taking the pseudo inverse of the submatrix  $\mathbf{A}_{\Omega}$ , which comprises only those columns associated with the support  $\Omega$ , along with the measurements vector  $\mathbf{y}$  in Eq. (2.21).

$$\hat{\mathbf{z}} = \mathbf{A}_{\mathbf{\Omega}}^{\mathsf{T}} (\mathbf{A}_{\mathbf{\Omega}} \mathbf{A}_{\mathbf{\Omega}}^{\mathsf{T}})^{-1} \mathbf{y} \tag{2.21}$$

Greedy methods like .ROMP [80] and CoSaMP [81], offer advantages such as computational simplicity and rapid convergence, making them appealing for real-time applications. These methods efficiently handle sparse signal recovery and are relatively straightforward to implement. However, their performance heavily relies on sparsity assumptions, which might limit their effectiveness in scenarios with less sparse or non-sparse signals. Additionally, their greedy nature might struggle to capture complex image structures or textures, potentially leading to suboptimal reconstructions in such cases. Moreover, in the presence of noise or incomplete measurements, these methods might face challenges in achieving accurate image recovery.

Recently, various variants of Greedy Algorithms are proposed for the recovery of biomedical images from their undersampled k-space data [84-86]. FPGA based implementation of OMP for recovery of CS MRI is described in [87].

# 2.8 Fusion of CS MRI with Machine Learning

The deep learning methods to improve the reconstruction of compressively sampled MRI (CS MRI) images from undersampled data have gained significant attention in recent years. CNN is a deep learning method, that has shown its potential in capturing intricate image patterns and structures, thereby aiding in the recovery of near-perfect MRI. Specifically, tailored deep learning architectures have been developed exclusively for CS MRI reconstruction. These architectures are trained to map undersampled input data to a fully-sampled MRI. By leveraging large datasets containing paired undersampled and fully sampled MR images, these models strive to acquire knowledge about the underlying image structures and enhance reconstruction accuracy [29-31].

Deep learning methods applied to CS MRI recovery frequently embrace an end-to-end learning paradigm. In this paradigm, the network accepts the undersampled data as input

and directly generates the fully sampled image as output, bypassing the need for intermediate steps like iterative reconstruction. Adopting of an end-to-end learning framework offers improved efficiency and reduced computational complexity [32].

Researchers have investigated diverse approaches for augmenting the available dataset artificially to tackle insufficient training data. Various data augmentation techniques have been explored, such as employing random transformations, extracting patches, and simulating undersampling patterns. Additionally, regularization techniques, including the integration of sparsity or total variation constraints, have been employed to enhance the generalization capability and reconstruction quality of deep learning models [33, 34].

Researchers have investigated transfer learning as a strategy for compressively sampled MRI (CS MRI) reconstruction to overcome the scarcity of labelled training data. In this approach, models that have been pre-trained on extensive image datasets are fine-tuned specifically for CS MRI reconstruction tasks. By initially training convolutional neural network (CNN) models on vast natural image datasets like ImageNet, valuable general image features are learned, which can be leveraged to enhance CS MRI reconstruction [35-37, 76].

Leveraging deep learning for compressively sampled image recovery brings substantial advancements, notably in vastly improved reconstruction accuracy and reduced sampling requirements, expediting image acquisition. The models' adaptability and capacity for non-linear mappings across varied imaging scenarios enhance robustness. However, challenges arise from the substantial computational complexity in training, reliance on large and diverse datasets, and the models' lack of explanation, potentially impacting generalization, and interpretability in image recovery. Overcoming issues like overfitting and hyperparameter sensitivity is crucial to fully utilize deep learning's potential in this field.

### 2.9 Metrics for Performance Assessment

An objective analysis of algorithm performance is done using various image comparison metrics. The performance of different algorithms can be objectively assessed by comparing the original image X with the recovered image  $\widehat{X}$  using the following performance parameters:

### 2.9.1 Structural Similarity Index (SSIM)

The SSIM, proposed by Zhou Wang et al. [56], addresses the limitation of MSE by considering the quality differences between images with the same MSE. The SSIM index exhibits a more comprehensive indication of image similarity. A higher SSIM index value indicates a closer match between the two images, while a lower SSIM index value indicates a poorer match for the recovered image. Eq. (2.22) depicts the mathematical equation of SSIM.

SSIM = 
$$\frac{(2\mu_{\sigma_l}\mu_{\bar{\sigma}_l} + C_1)(2\delta_{\sigma_l\bar{\sigma}_l} + C_2)}{(\mu_{\sigma_l}^2 + \mu_{\bar{\sigma}_l}^2 + C_1)(\delta_{\sigma_l}^2 + \delta_{\bar{\sigma}_l}^2 + C_2)}$$
(2.22)

Calculating  $(\mu_{\sigma_l}^2 \text{ and } \mu_{\widehat{\sigma_l}}^2)$  is the mean, variance  $(\delta_{\sigma_l}^2 \text{ and } \delta_{\widehat{\sigma_l}}^2)$ , and covariance  $(\delta_{\sigma_l \widehat{\sigma_l}})$  between actual and recovered images.

#### 2.9.2 Artifact Power

Artifact Power (AP) provides a mathematical measurement of the accuracy of a recovered image. It is calculated using the equation for square difference error, shown in Eq. (2.23). Lower AP values indicate the recovered image is of higher quality.

$$AP = \frac{\sum_{i} |X(i) - \hat{X}(i)|^{2}}{\sum_{i} |X(i)|^{2}}$$
 (2.23)

### 2.9.3 Improved Signal-to-Noise Ratio (ISNR)

The ISNR serves as an additional metric for judging the worth of a reconstructed image [88]. The ISNR is determined using Eq. (2.24), where higher ISNR values indicate superior image recovery. This metric quantifies the improvement in the SNR achieved by the reconstruction process. The ISNR is calculated as:

$$ISNR = 10 \cdot \log_{10} \left\{ \frac{\|X - |F_{\mathbf{u}}X|\|_{2}^{2}}{\|\widehat{X} - X\|_{2}^{2}} \right\} [dB]$$
 (2.24)

## 2.9.4 Peak Signal-to-Noise Ratio (PSNR)

PSNR is a popular metric to measure image fidelity and quality [89]. It is calculated as the ratio of the maximum value of a pixel in the image and the mean squared error power attained by the reconstructed image, as shown in Eq. (2.25). Higher PSNR values indicate

better recovery of the original image, with a higher PSNR corresponding to a higher-quality reconstructed image.

$$PSNR = 20 \cdot \log_{10}\{Max(X)\} - 10 \cdot \log_{10}\left\{\frac{1}{mn}\sum_{i}\sum_{j}(X(i,j) - \bar{X}(i,j))^{2}\right\}$$
(2.25)

#### 2.9.5 Fitness

Fitness provides another metric to assess the quality of a recovered image. At each iteration, fitness can be calculated using either  $\|\mathbf{F}_{\mathbf{u}}\mathbf{X}_k - \mathbf{y}\|_2^2$  or  $\|\mathbf{X}_k - \mathbf{X}_{k-1}\|_2^2$ . A lower fitness value a higher efficiency of the recovered image. This is because fitness represents the deviation between the recovered image and the original image - so minimized fitness corresponds to an image that more closely matches the original.

#### 2.9.6 Correlation

Correlation provides a statistical measurement of the relationship between the actual and reconstructed images. It is calculated using equation (2.24), where  $\rho$  is the correlation,  $cov(X, \hat{X})$  is the covariance between the original image X and recovered image  $\hat{X}$ , and  $\sigma_{\hat{X}}$  are the standard deviations of X and  $\hat{X}$  respectively.

$$\rho_{X,\bar{X}} = \frac{cov(X,\bar{X})}{\sigma_X \sigma_{\bar{X}}} \tag{2.26}$$

Correlation ranges from -1 to 1. Here, 1 shows a perfectly positive correlation, meaning the original and recovered images match exactly. A correlation approaching 1 indicates the two images are very similar. Values near 0 denote little relationship, while -1 is a perfect negative correlation, meaning the images are inverses of each other. Thus, a correlation value closer to 1 signifies that the reconstructed image accurately reflects the actual image.

#### 2.9.7 Mean Square Error (MSE)

The MSE is a widely used to quantify the difference between an original image f and a recovered image g. As shown in Eq. (2.27), MSE is the calculated average of the squared differences in pixel values between the two images. Lower MSE values indicate less deviation between X and  $\hat{X}$ . An MSE approaching zero signifies that the recovered image  $\hat{X}$  is close to a perfect reconstruction of the original image X. Thus, MSE provides a simple way to measure how well X matches  $\hat{X}$  with smaller values denoting better recovery quality.

$$\frac{\left\|\mathbf{X} - \mathbf{\hat{X}}\right\|_{2}^{2}}{\left\|\mathbf{X}\right\|_{2}^{2}} \tag{2.27}$$

### 2.9.8 Signal-to-Noise Ratio (SNR)

SNR is a widely used performance metric in various signal processing applications, including sparse signal recovery. SNR measures the quality of a signal by quantifying the ratio of signal power to noise power present in the signal. It provides a quantitative assessment of how well the signal of interest can be distinguished from the background noise.

In sparse signal recovery, SNR is commonly used to evaluate the accuracy and fidelity of the reconstructed signal. A higher SNR indicates a higher level of signal power relative to the noise power, suggesting a better-quality reconstruction. Conversely, a lower SNR indicates a greater influence of noise and potential distortion in the reconstructed signal. It is measured in decibels (dB) for easier interpretation. A higher SNR value indicates a stronger, clearer signal with less noise interference, while a lower SNR value indicates a weaker, noisier signal.

When comparing different algorithms or techniques for sparse signal recovery, the one that yields a higher SNR is considered to provide a better reconstruction. SNR is a useful metric for the performance evaluation of sparse signal recovery algorithms and comparing their effectiveness in handling noise and reconstructing the original signal accurately.

$$SNR = 10 \cdot \log_{10} \left\{ \frac{\|\mathbf{X}_0\|_2^2}{\|\hat{\mathbf{X}} - \mathbf{X}_0\|_2^2} \right\} [dB]$$
 (2.28)

#### **CHAPTER 3**

#### SPARSE MRI RECOVERY BY SMOOTH

### APPROXIMATIONS OF $l_0$ NORM

This chapter discusses the primary approach for reconstructing sparse signals, which involves minimizing the  $l_0$  -norm, aiming to find a suitable solution with the minimum non-zero elements. However, due to the combinatorial nature of the problem, finding the exact solution to  $l_0$ -norm minimization is computationally challenging. To address this, the literature proposes non-linear reconstruction techniques that utilise smoothed  $l_0$ -norm approximations. These approaches have been proven to be computationally efficient, offering practical solutions for sparse signal reconstruction. A novel smooth approximation of  $l_0$ -norm is proposed and an analysis of five different versions of smoothed  $l_0$ -norm functions is also presented. The existing smoothed  $l_0$  norm-based recovery algorithm is then modified and applied to reconstruct compressively sampled magnetic resonance images using five different approximation functions. To justify a comparison, the widths of the approximation functions were cross-matched, keeping other adjustable parameters of the algorithm identical. The performance of each smoothed  $l_0$ -norm approximation reconstructing compressively sampled 1D sparse signal and 2D MRI (Brain) against different sampling rates have also been surveyed.

### 3.1 Introduction to Norms

The objective of sparse signal recovery algorithms (decoder) is to reconstruct a signal  $x \in \mathbb{R}^n$  or its corresponding s-sparse coefficients of vector z from a few numbers of m incoherent random samples. These samples are obtained using a known sparse basis  $\Psi$  and sensing matrix  $\Phi$ . The task at hand involves solving the following under-determined system of linear Eq. (3.1).

$$\mathbf{y} = \mathbf{A}\mathbf{z} \tag{3.1}$$

Here  $A \in \mathbb{R}^{n \times m}$ ,  $y \in \mathbb{R}^n$  is the s-sparse corresponding vector and  $m \ll n$ .

The objective of sparse signal reconstruction is to estimate of a signal, denoted as z, that possesses sparsity properties. This estimation is derived from measurements y and a rectangular matrix A. Since matrix A contains fewer equations than unknowns, Eq. (3.1) has infinitely many solutions. To address this, the problem can be approached as a constraint optimization problem that promotes sparsity in the solution while satisfying the constraints defined by Eq. (3.1). In general, this optimization is defined below:

$$(P_p)$$
  $\hat{z} = \underset{z}{\operatorname{argmin}} ||z||_p, \quad subject \ to \ ||y - Az||_2 = 0$  (3.2)

where  $\|\mathbf{z}\|_p$  defines the  $p^{th}$  norm of  $\mathbf{z}$  and it may be calculated as

$$\|\mathbf{z}\|_{p} = \left(\sum_{i} |\mathbf{z}[i]|^{p}\right)^{1/p}$$
 (3.3)

When the  $l_p$  norm ball is expanded to intersect with the feasible solution set, certain characteristics emerge. Figure 3-1 depicts the  $l_p$  norm ball for different values of p. For p=0.7 and p=1, the intersection points occur at the corners of the ball along the axes, causing two out of three coordinate values to become zero. This leads to a sparse solution; fewer coordinates have non-zero values. Conversely, for p=1.5 and p=2, the point of intersection results in non-zero values for all three coordinates, yielding a non-sparse solution. The choice of p determines the sparsity level of the solution, with smaller p values promoting sparsity and larger p values favouring non-sparse solutions [21].

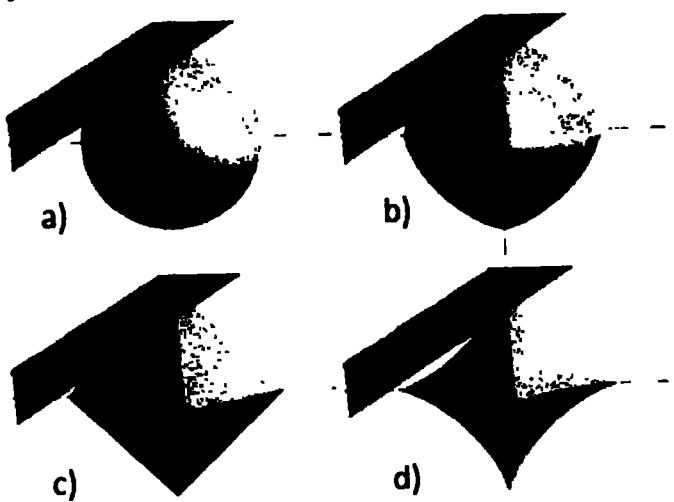


Figure 3-1: Intersection of  $l_p$  ball and the set Ax = y solved with various values of p [21]

#### 3.1.1 $l_2$ -norm Based Recovery

Eq. (3.2) can be solved linearly by minimising the  $l_2$  norm. This approach, commonly referred to as  $l_2$  norm minimisation leads to the solution dubbed as the LS solution that minimises error energy. The approximated solution can be easily obtained by applying Eq.(3.3).

$$(P_2) \ \ \hat{z} = A^{T} (AA^{T})^{-1} y \tag{3.4}$$

The utilization of the least square approach offers the advantage of yielding a unique solution. However, the  $l_2$  norm minimised solution disperses its energy across many elements, resulting in a dense solution. Consequently, this approach is not suitable for obtaining an s-sparse solution, where only a few elements should have non-zero values. Figure 3-2 depicts the solution by 'o' of a sparse signal indicated by '\*'. The resulting least square estimated solution failed to achieve the sparsity level in the desired signal.

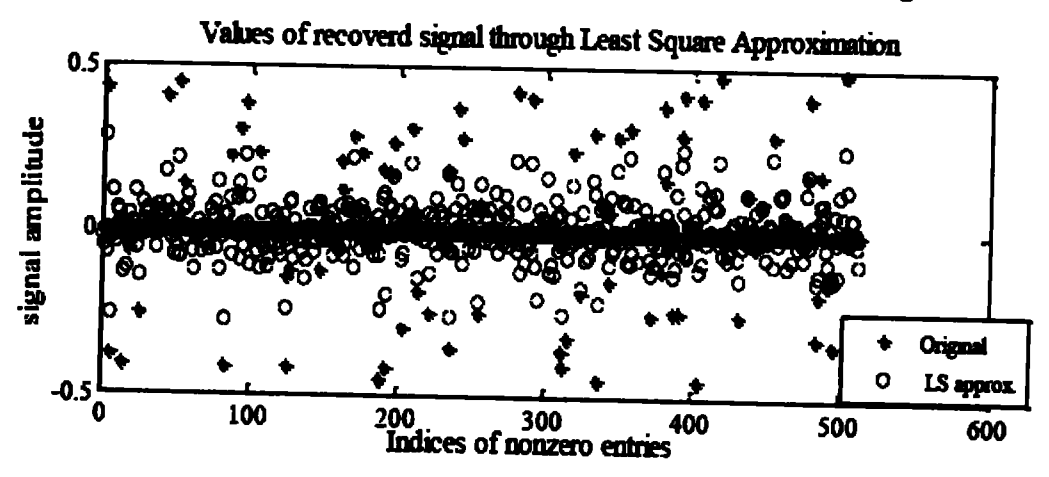


Figure 3-2:  $l_2$  norm-based signal recovery failure to achieve desired sparse solution

### 3.1.2 *l*<sub>0</sub>-norm Based Recovery

The  $l_2$  norm measures the energy or magnitude of error in a signal recovery, measuring the signals' overall strength. On the other hand, the  $l_0$  norm is utilised to quantify the sparsity of a signal. The  $l_0$  norm, as defined by Eq. (3.5), counts the number of non-zero entries in a vector, denoted as  $\mathbf{z}$ . If the vector  $\mathbf{z}$  is s-sparse, meaning it has only s non-zero entries, then its  $l_0$  norm will be equal to s.

The  $l_0$  norm is a useful tool for assessing the sparsity level of a signal by counting the number of non-zero elements. It indicates of how concentrated or spread out the signals' non-zero entries are. If the signal has a small  $l_0$  norm, it suggests a high sparsity level,

indicating that only a few elements significantly contribute to the signal. Conversely, a large  $l_0$  norm indicates a less sparse signal, with a greater number of non-zero elements contributing to its overall structure.

$$\|\mathbf{z}\|_{0} = \lim_{p \to 0} \sum_{i} |x_{i}|^{p} \tag{3.5}$$

The  $l_0$  norm minimum solution can be formulated as  $P_0$ .

$$(P_0)$$
  $\hat{z} = \underset{z}{\operatorname{argmin}} ||z||_0$ , subject to  $||y - Az||_2 = 0$  (3.6)

The  $l_0$  norm can exhibit significant changes in the presence of noise, affecting its reliability as a measure of sparsity. To address this issue, the equality constraint can be relaxed. Consequently, the original problem defined as the  $P_0$  problem can be reformulated as the  $P_{0,\varepsilon}$  problem, where  $\varepsilon$  represents a small threshold or tolerance level. This relaxation allows for a more robust and stable estimation of sparsity, accommodating the effects of noise in the signal as defined by Eq. (3.7).

$$(P_{o,\varepsilon}) \hat{z} = \underset{z}{\operatorname{argmin}} ||z||_{0}, \quad subject \ to \ ||y - Az||_{2} < \varepsilon \tag{3.7}$$

To obtain the near-perfect solution for the constraint optimisation problem in Eq. (3.7), it is necessary to explore the best s vectors in matrix A, which defines the observations vector y. This implies that the optimal solution needs searching through  $\binom{n}{s}$  possible basis can occur, potentially resulting in a unique solution. However, this search is an NP-hard problem  $\binom{n}{s}$ , it is not possible practically to find a solution through the combinatorial problem. Furthermore, the formulation presented in Eq. (3.7) is not convex, which poses challenges for optimisation methods that involve calculating derivatives. Due to the non-convex nature of the problem, gradient-based methods may struggle to find a globally optimal solution, making the optimisation process difficult and potentially leading to suboptimal results. Alternative approaches, such as greedy algorithms, heuristics, or relaxations, are often employed to tackle the complexity and intractability of the problem, offering more practical and efficient solutions.

An alternative approximation to the  $l_0$  norm involves replacing it with a smoothed function [90]. Smoothed  $l_0$  functions, such as the zero mean Gaussian  $exp(-\frac{x^2}{2\sigma^2})$ , provide a means for gradient-based methods to be applied while offering immunity to noise by adjusting the  $\sigma^2$  parameter of the Gaussian function. This smoothing approach allows for

more tractable optimisation using gradient-based techniques and provides flexibility to control the trade-off of sparsity and noise resilience by adjusting the smoothing parameter  $\sigma^2$ .

### 3.1.3 $l_p$ -norm Based Recovery

Practical implementations of variants for the  $l_0$  norm exist, with one notable example being FOCUSS [91]. In FOCUSS, the  $l_p$  norm replaces the  $l_0$  norm, typically selecting a value of p between 0 and 1 [24]. FOCUSS builds upon the concept of Iterative Reweighted Least Squares (IRLS) [23], which utilises the  $l_p$ -norm as a weighting mechanism. By incorporating the  $l_p$  norm in FOCUSS, the algorithm aims to promote sparsity and achieve accurate signal reconstruction computationally efficiently.

#### 3.1.4 *l*<sub>1</sub>-norm Based Recovery

The  $l_0$  norm is defined by Eq. (3.6) and Eq. (3.7) in problems  $P_0$  and  $P_{0,\epsilon}$  can be relaxed by minimising the  $l_1$  norm used in Basis Pursuit [92].

$$(P_1) \quad \hat{z} = \underset{z}{\operatorname{argmin}} ||z||_1, \quad subject \ to \ ||y - Az||_2 = 0$$
(3.8)

$$(P_{1,\varepsilon})$$
  $\hat{z} = \underset{z}{\operatorname{argmin}} ||z||_1$ , subject to  $||y - Az||_2 < \varepsilon$  (3.9)

Eq. (3.8) and Eq. (3.9) reformulate the problems presented in Eq. (3.6) and (3.7) as convex optimisation problems, which are solved using linear programming and  $2^{nd}$ -order cone programming, respectively [93]. Minimising the  $l_1$  norm is often effective in finding the sparsest solution, especially when the measurement matrix A has a small RIP constant and the target signal is sparse [41] [94]. The optimisation based on the  $l_1$  norm provides robustness against noise and ensures stability. However, the high computational cost of  $l_1$  norm minimisation, it is not efficient for large-scale applications such as medical imaging.

## 3.2 Smooth $l_0$ -norm Literature Review

The  $l_0$  norm has an appealing mathematical property in sparse signal recovery, as it counts the non-zero elements in a signal. However, optimising this norm is non-convex and computationally challenging due to its combinatorial nature. To overcome these limitations, the smoothed  $l_0$  norm approximation algorithm was proposed [90]. This paper modifies [90] and proposes weighted methods [95] and [96] replaces the Steepest Descent

method with the Quasi-Newton method. SL0 was further extended to handle complex valued sparse signals [97]. This algorithm has significantly reduced the computational cost, leading to widespread adoption in various sparse signal recovery applications.

The SL0 algorithm has been successfully applied in image smoothing [98] [30], image denoising [99], dictionary learning [100], estimating the direction of arrival in radar [101], compressed image recovery [95], sparse channel estimation [102], hyperspectral image unmixing [103], and various image-restoration techniques such as de-mosaicking, super-resolution, and in-painting [104]. Moreover, SL0 has demonstrated its effectiveness in the recovery of compressed speech signals [105], and compressively sampled functional MRI (FMRI) data [106]. Overall, SL0 has emerged as a powerful tool in sparse signal recovery, enabling efficient and accurate recovery of signals from compressed or under-sampled measurements.

# 3.3 Sparse Signal Recovery by Smooth $l_0$ norm

Finding the sparsest solution of a signal by minimising the  $l_0$  norm is a computationally challenging NP-hard problem because of discontinuity in the norm. To address this, a smoothed  $l_0$  norm approximation was proposed in [90], where the original discontinuous function is replaced with a continuous and smooth function. The optimal solution is then obtained by finding the sparsest solution of this approximated function, which can be interpreted as approximating the Kronecker delta function defined by Eq. (3.10). This smoothing technique enables a more tractable optimisation problem while still aiming to achieve sparsity in the solution.

$$\delta(\mathbf{z}_i) = \begin{cases} 1, & \text{if } \mathbf{z}_j = 0 \\ 0, & \text{if } \mathbf{z}_j \neq 0 \end{cases} \quad i = 1, 2, ..., n$$
 (3.10)

Correspondingly  $l_0$  norm can be defined by Eq. (3.11).

$$\|\mathbf{z}\|_{0} = \sum_{i=1}^{n} \{1 - \delta(\mathbf{z}_{i})\}$$
(3.11)

The  $l_0$  norm is estimated by Delta Approximating (DA) smooth function, i.e.,  $F_{\sigma}(z) = \sum_{i=1}^{n} f_{\sigma}(z_i)$ . This smooth approximation function must hold the characteristics defined by Eq. (3.12).

$$\lim_{\sigma \to 0} f_{\sigma}(z_i) = \begin{cases} 1, & \text{if } z_j = 0 \\ 0, & \text{if } z_j \neq 0 \end{cases}$$
(3.12)

From Eq. (3.11) and Eq. (3.12), the approximation of the  $l_0$  norm can be defined by Eq. (3.13)

$$\|\mathbf{z}\|_{0} \approx \lim_{\sigma \to 0} \sum_{i=1}^{n} (1 - f_{\sigma}(\mathbf{z}_{i})) = n - F_{\sigma}(\mathbf{z})$$
 (3.13)

The value of  $\sigma$  plays a significant role in sparse signal recovery. It represents the trade-off between the smoothness and accuracy of the estimated solution. The smaller  $\sigma$  results in a more accurate but non-smooth approximate solution whereas the larger value of  $\sigma$  leads to a smoother but less accurate solution. The width of the DA function is controlled by varying  $\sigma$ . The larger  $\sigma$  results in a wider DA function that gives a smoother but poor estimation of the Kronecker Delta. The smaller  $\sigma$  results in a smaller width that yields an accurate Kronecker Delta but a less smooth approximation. This phenomenon is further illustrated

Figure 3-3

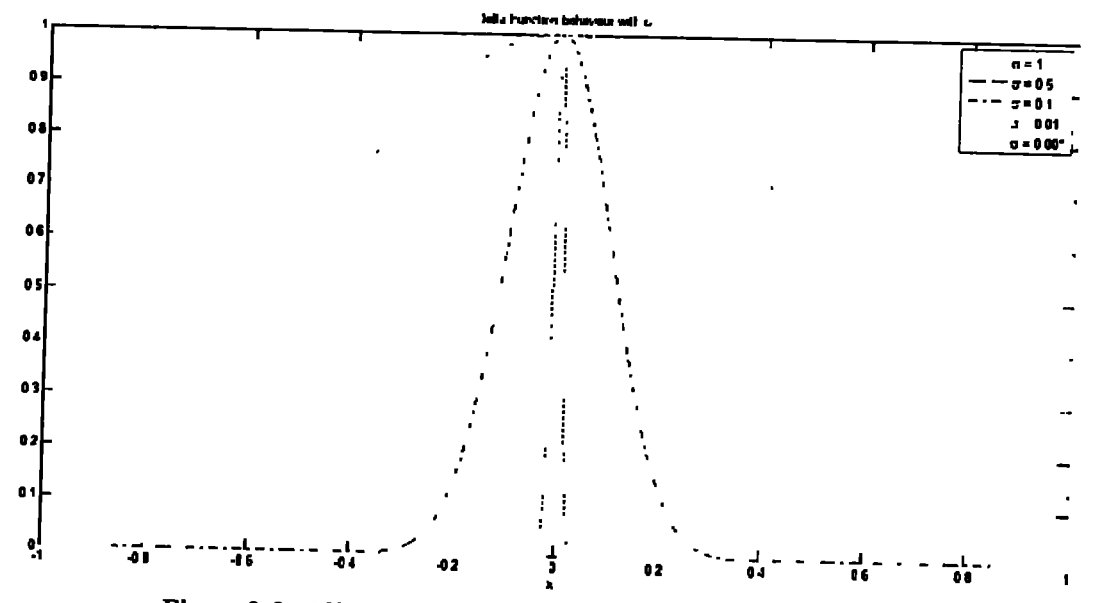


Figure 3-3: Effect of  $\sigma$  on delta approximation function width

Algorithm 3.1. 1D Sparse Signal Recovery by Smoothed  $l_0$  Norm

Initialise:

- 1. Initialise  $z_0$  by  $l_2$  norm solution of  $z_0 = \Phi^T (\Phi \Phi^T)^{-1} y$
- 2. Set  $\sigma$  as decreasing sequence for  $\sigma = [\sigma_1, \sigma_2, ..., \sigma_n]$  for i = 1, 2, ..., P:
- 1. Set  $\sigma = \sigma_i$

- 2. Find Maxima for  $F_{\sigma}(x)$  in m iterations of the steepest ascent algorithm.
  - a. Initialise:  $\mathbf{z} = \mathbf{z}_{i-1}$
  - b. For j = 1, 2, ..., Q

i. Set 
$$\Delta z = [x_1 f_{\sigma_i}(x_1), ..., x_n f_{\sigma_i}(x_n)]^T$$

- ii. Set  $z \leftarrow z \mu \Delta z$
- iii. Project z back as  $z \leftarrow z \phi^T (\phi \phi^T)^{-1} (\phi z y)$
- 3. Set  $x_i = x$

Final solution:  $\mathbf{x} = \mathbf{x}_P$ 

 $F_{\sigma}(z)$  can be assumed as the measure of sparsity in an estimated solution, where the larger value of  $F_{\sigma}(z)$  means a sparser solution and smaller values of  $F_{\sigma}(z)$  will result in a denser solution. In terms of the optimisation problem defined by Eq. (3.7), the maxima of  $F_{\sigma}(z)$  yields the sparsest and optimal solution.

For smaller values of  $\sigma$ ,  $F_{\sigma}(z)$  will have lots of local maxima, therefore, an initially large value of  $\sigma$  is used to avoid local maxima, and then iteratively  $\sigma$  is decreased to find the optimal solution [90]. Steepest ascent or Quasi-Newton methods can be used to find the maxima of  $F_{\sigma}(z)$  for each value of  $\sigma$ . The smoothed  $l_0$  norm algorithm for recovery of the sparse 1D signal is presented as: Algorithm 3.1.

# 3.4 Delta Approximations Functions for Smooth $l_0$

The efficiency of five proposed state-of-the-art DA functions is compared for smoothed  $l_0$  norm. All the functions are symmetric functions that are f(x) = f(-x), here vector  $x = x_i \ \forall \ i = 1,2,3,...,n$ . The delta approximation functions are defined below:

The Gaussian Function (GF) defined by (11) [90]:

$$f_{\sigma}(x_i) = \exp\left(-\frac{x_i^2}{2\sigma^2}\right) \tag{3.14}$$

The Reciprocal Square Function (RSF) defined by (12) [107]

$$f_{\gamma}(x_i) = \frac{1}{1 + (\gamma \pi x_i)^2} \tag{3.15}$$

Composite Trigonometric Function (CTF) defined by (13) in [96]

$$f_{\sigma}(x_l) = \sin\left(\arctan\left(\frac{ax_l^2}{\sigma^2}\right)\right)$$
 (3.16)

The Laplacian Kernel Function (LKF) is defined by (14) and the Laplacian kernel approximation by Hyperbolic Cosine Function (HCF) is defined by (15) [106]

$$f_{\sigma}(x_l) = exp\left(-\frac{|x_l|}{\sigma}\right) \tag{3.17}$$

$$f_{\sigma c}(x_i) = \cosh (\beta s)^{-1/(\beta \sigma c)}$$
(3.18)

# 3.5 Sparse Signal Recovery Empirical Results and Discussion

The performance of all the delta approximation functions defined in Section 3.4 is compared for their efficiency in recovering a random 1D sparse signal. To justify fair comparison for all the proposed DA functions, the variance (width) of functions is matched against each value of  $\sigma$ . Figure 3-4 shows the width matching results with different values of  $\sigma$  for all the functions defined by Eq. (3.14) to Eq. (3.18). The values of  $\sigma$  are empirically fixed for all the smoothed  $l_0$  norm approximations. The resultant values of  $\sigma$  from this experiment are presented in Table 3-1. This will justify the fair comparison for all approximation functions.

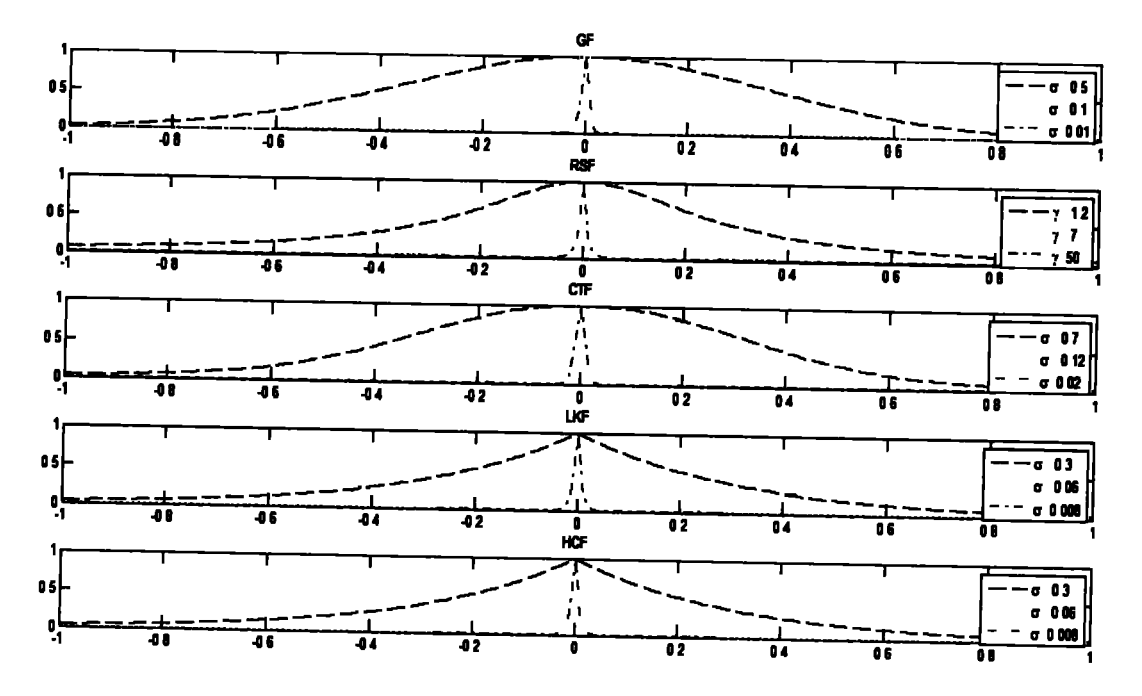


Figure 3-4: Delta Approximation Functions Width Matching

Table 3-1: Value of  $\sigma$  for matching of width for DA Functions

<b>Functions</b> GF	Values of $\sigma$						
	1	0.5	0.2	0.1	0.05	0.02	0.01
RSF	0.45	1.2	5	7	20	30	50
CTF	1.2	0.7	0.25	0.12	0.07	0.03	0.02
LKF	0.8	0.3	0.1	0.06	0.025	0.01	0.008
HCF	1	0.3	0.1	0.06	0.025	0.01	0.008

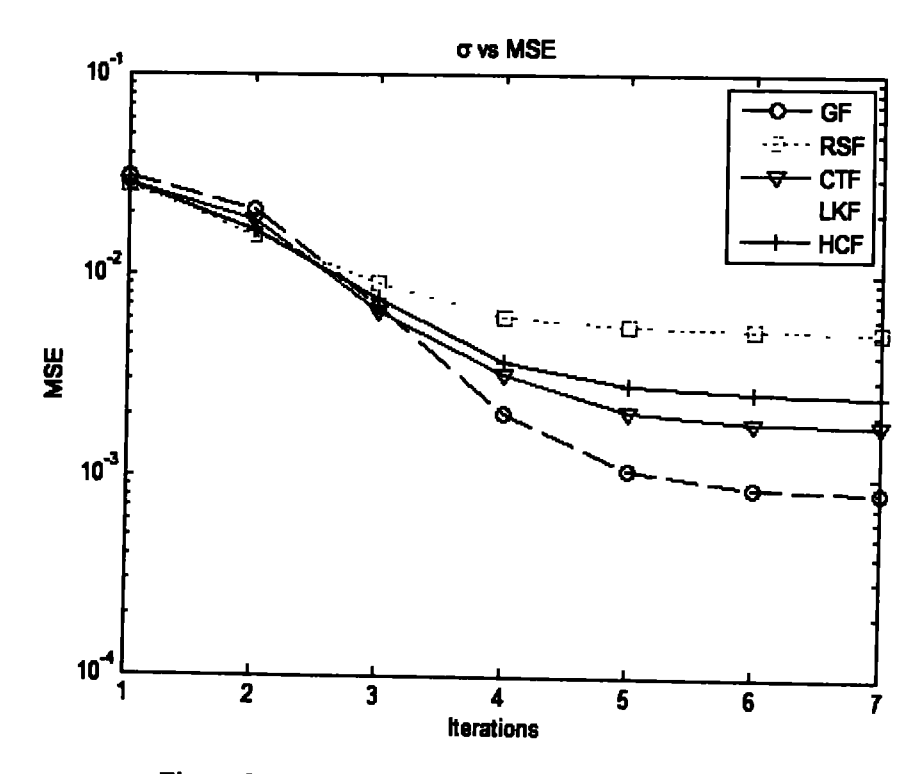


Figure 3-5 MSE vs change in  $\sigma$  with each iteration

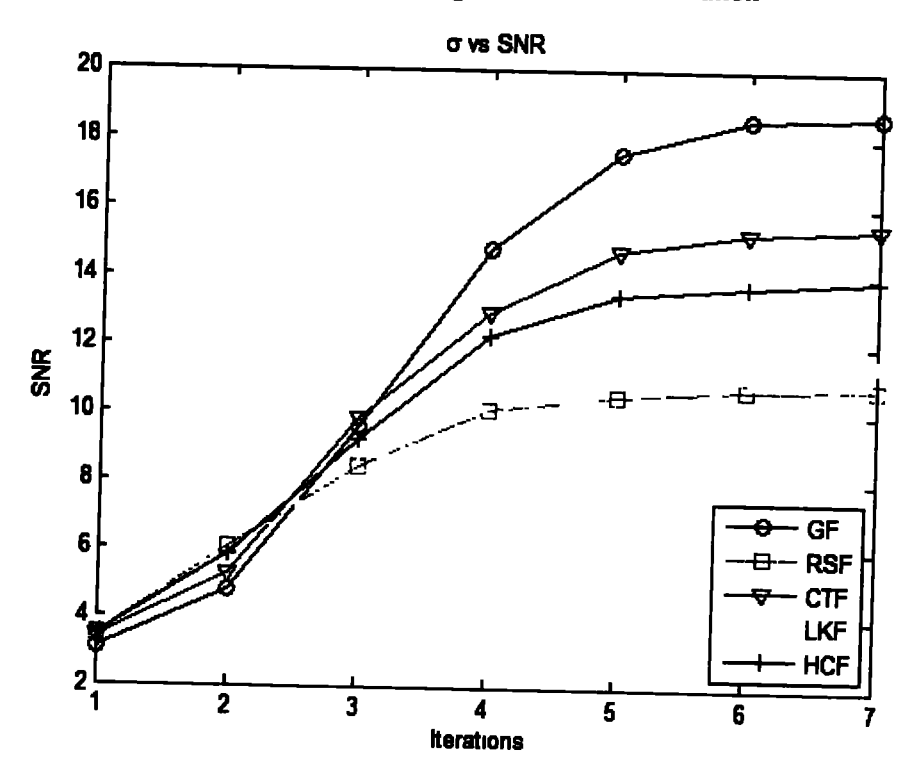


Figure 3-6: SNR vs change in  $\sigma$  with each iteration

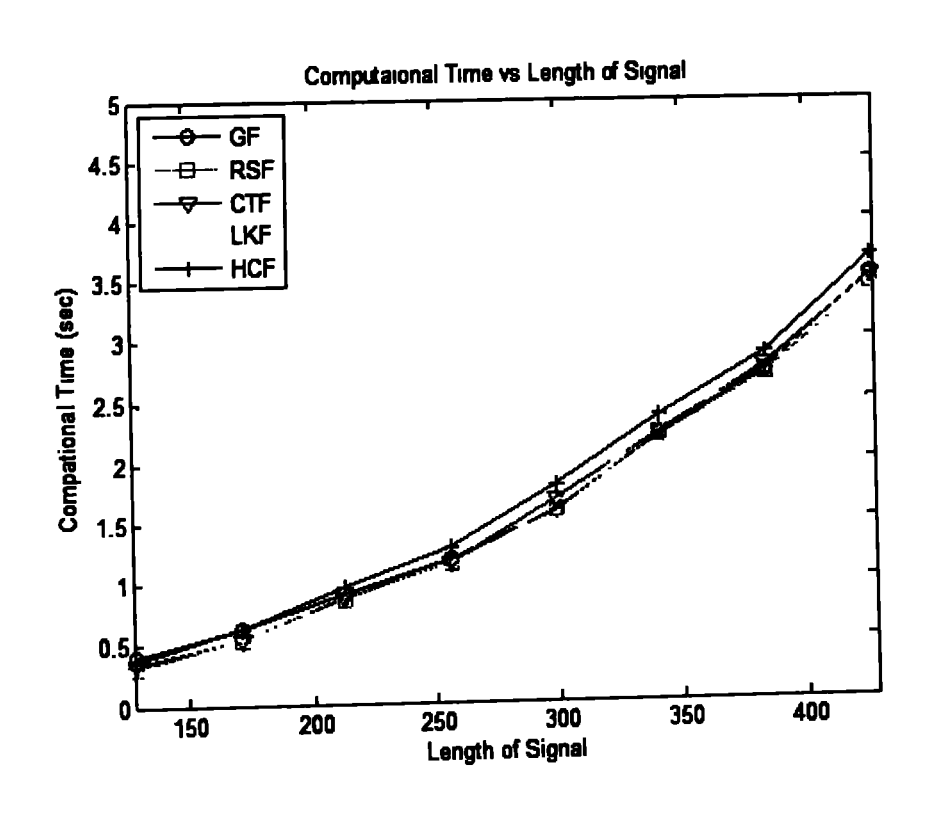


Figure 3-7. Computational Time vs Length of Signal

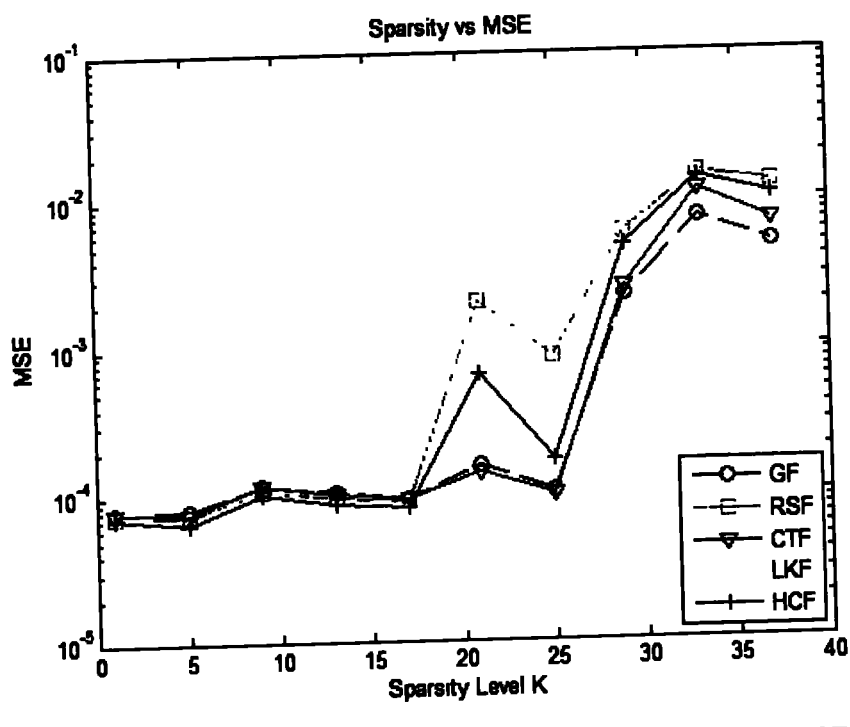


Figure 3-8: Effect of Change in Sparsity K on Recovered Signal MSE

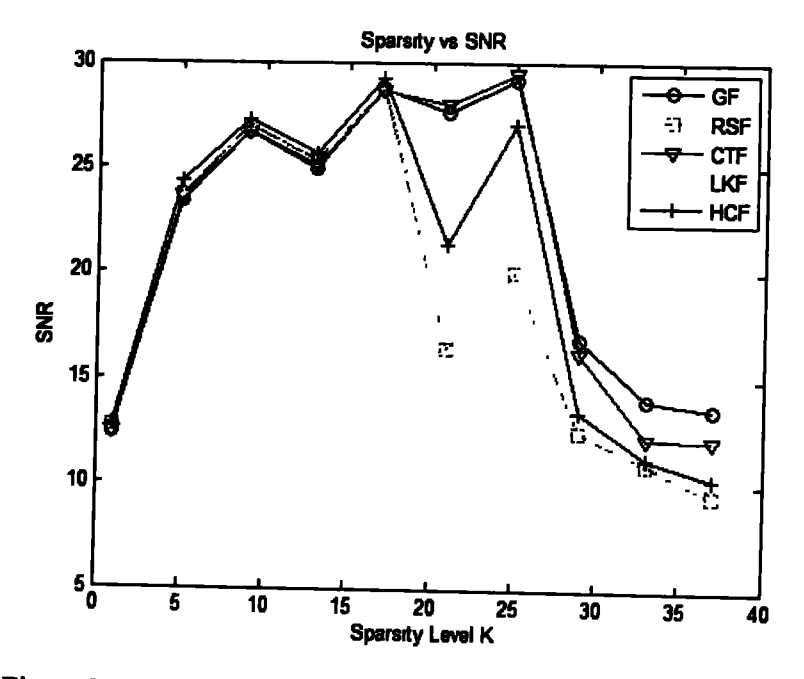


Figure 3-9: Effect of change in Sparsity K on recovered signal SNR

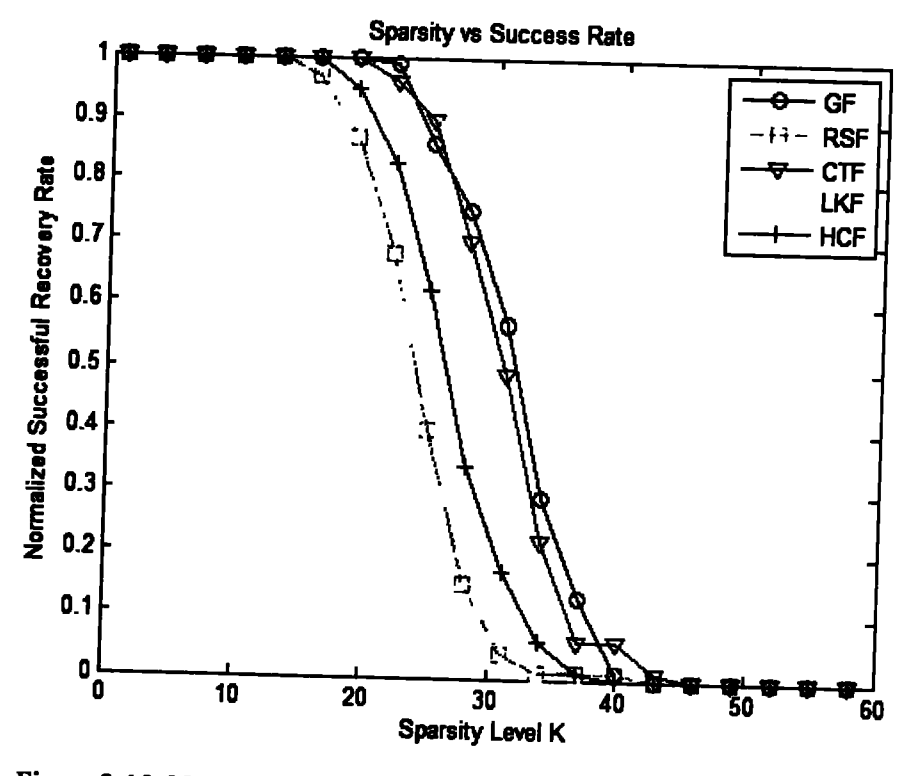


Figure 3-10: Normalized successful recovery for different sparsity levels

To test the performance of each delta approximation function, we generated a random 1D sparse signal that has a length of n=256, total measurements taken during the process of CS are m=100. The step size for the steepest-descent algorithm (SDA) is set as  $\mu=2$  and the total number of internal iterations for the SDA is Q=3. The external iterations were set to P=7 with different values of  $\sigma$ , as shown in Table 3-1.

In Figure 3-5, the performance of each DA function in terms of MSE is calculated for all values of  $\sigma$  in Table 3-1.

. It can be concluded that GF has achieved the least MSE therefore, it has the best recovery of a sparse signal. The RSF has achieved poor recovery with the highest MSE. The MSE performance of each DA function can be seen in Figure 3-5. Similarly, the SNR of each smoothed  $l_0$  approximation is evaluated in Figure 3-6. Based on the SNR of the recovered sparse signal it is visible that GF has shown the best performance with the highest SNR and the RSF has the lowest SNR, resulting in a poor recovery. The rest of the function's performance can be viewed from Figure 3-6.

The important parameter for the recovering a sparse signal is its computational efficiency. The recovery time depends on the length of the signal to be recovered. The efficiency of each smoothed  $l_0$  approximation function has been measured by varying the length of a sparse signal in Figure 3-7. The length of a signal is varied from 128 to 450 elements and the number of measurements m is taken as half of the length of the signal n and the corresponding sparsity level k is set to half of the measurements. The computational time was calculated by MATLAB tic/toc commands using MATLAB R2014a on a Core i5, 2.4 GHz Processor with 6GB RAM. The computational time HCF takes is the highest and thus it is computationally inefficient. The RSF is found to be a computationally efficient function, while the rest of the function's computational time is very close to each other.

The performance of the algorithm for recovering sparse signals can be evaluated based on its capability to recover a sparse signal at varying sparsity levels. The sparser signal will require a lesser number of measurements to successfully recover it. Figure 3-8 shows the MSE in the recovery of a sparse signal with fixed length n = 256 elements and a fixed number of measurements m = 100. The sparsity k of a signal is varied from 1 to 35. The Gaussian approximation function is found the most efficient with the least MSE and the

CTF performed very close to each other. The DA functions RSF and LKF have shown comparatively poor results, while CTF performance lies in the middle. Figure 3-9 shows the SNR achieved by each smoothed  $l_0$  norm function. The GF performed the best in terms of SNR of the recovered signal with the highest SNR and CTF performed the second best. RSF and CTF have shown comparatively poor results.

Figure 3-10 depicts the normalized successful recovery achieved by each delta function, with the success threshold set at  $10^{-3}$ . Each algorithm runs for 30 iterations and successes are counted at each sparsity level and then divided by the number of iterations. In this context, successful recovery refers to the accurate reconstruction or approximation of the original signal using the respective delta function. The figure showcases the effectiveness of the different delta functions in achieving successful signal recovery, demonstrating their ability to accurately represent and capture the essential characteristics of the signal.

# 3.6 CS MRI Recovery by Smooth $l_0$ norm

The smoothed  $l_0$  norm (SL0) algorithm has been modified to achieve computationally efficient recovery of Compressively Sampled MRI. The fully sampled human brain MR image X is compressed by the non-uniform random undersampling mask (M) in the Fourier domain represented by  $F_u$ , the resultant undersampled image is a non-sparse image with a noise-like artefacts. To sparsify the image, it is transformed in the Wavelet domain. Data consistency is maintained in the Fourier domain  $(F_u)$  for faster convergence to the optimal solution. The proposed modified smoothed  $l_0$  norm algorithm is described in Algorithm 3.2. Figure 2 shows the graphical representation of Algorithm 3.2.

#### Initialise:

- 1. Initialise  $X_0 = F_u^{-1}(Y)$ , where Y is undersampled k-space data
- 2. Set  $\sigma$  as decreasing sequence for  $\sigma = [\sigma_1, \sigma_2, ..., \sigma_n]$

for i = 1, 2, ..., P:

- 3. Set  $\sigma = \sigma_l$
- 4. Find the Maxima for  $F_{\sigma}(x)$  in m iterations of SDA.
  - a. Initialise:  $X = X_{l-1}$
  - b. For j = 1, 2, ..., Q
    - i.  $X_{sparse} = \Omega(X)$
    - ii. Set  $\Delta X_{sparse} = X_{sparse}^T * f_{\sigma_l}(X_{sparse})$
    - iii. Set  $X_{sparse} = X_{sparse} \mu \Delta X_{sparse}$ , where  $\mu$  is a step size
    - iv.  $X = \Omega^{-1}(X_{sparse})$
    - v. Data consistency:  $X \leftarrow F_u^{-1}(F_u(X) * (1 M) + Y)$ , where M represents the undersampling mask.
- 5. Set  $X_i = X$

Final solution:  $X = X_P$ .

# 3.7 CS MRI Recovery Experimental Results and Discussion

The MR image is a fully sampled k-space, as shown in Figure 3-12 (a). The fully sampled MR image was undersampled by acquiring a compression ratio of 25% in k-space using a non-uniform random sampling mask, as shown in Figure 3-12 (b). The random undersampled image has noise-like artefacts that are depicted in Figure 3-12 (c). As the scanned MR image is not sparse in the spatial domain, we have transformed it to its sparse representation in the Wavelet domain shown in Figure 3-12 (d).

The MR image was recovered by all the smoothed  $l_0$  norm approximation functions defined in Eq. (3.14) to Eq. (3.18). All DA functions successfully recovered the MR image as shown in Figure 3-13. However, LKF was found to be the most accurate among all the functions whereas, RSF showed relatively poor MR image recovery from compressively sampled MRI.

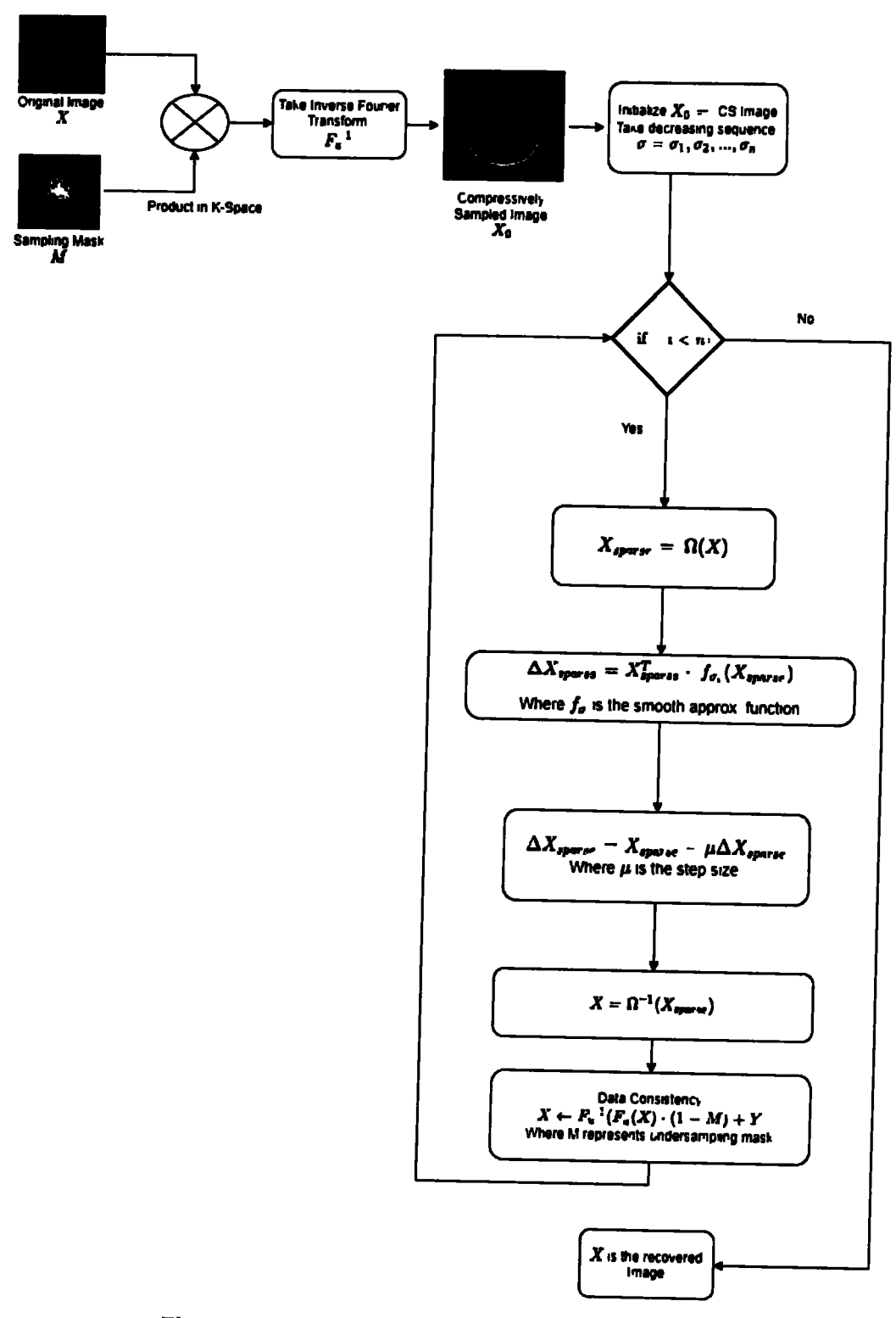


Figure 3-11: Graphical Representation of SLO Algorithm

The performance metrics used to authenticate the results are SNR, ISNR, PSNR [89], and SSIM [56].

The LKF achieves the best ISNR, while RSF showed the least efficiency with the minimum ISNR. GF and CTF also improved ISNR as shown in Figure 3-14. In terms of SNR performance metrics, LKF and CTF achieved the best SNR as shown in Figure 3-15. LKF accomplished the best PSNR, whereas GF also performed well in terms of PSNR. The PSNR achieved by each DA function is shown in Figure 3-16. The SSIM is another important parameter for the accuracy of the recovered images. LKF achieved the best SSIM index. The GF also attained better SSIM compared to the rest of the DA functions as shown in Figure 3-17.

The performance of each smoothed  $l_0$  approximation function was evaluated by varying the sparsity level of MRI from 5% samples to 90% samples, as shown in Table 3-2. The performance measures such as PSNR, ISNR, SSIM, SNR, and MSE are evaluated against different sampling ratios. The Laplacian kernel delta approximation function has performed the best among all the functions under varying sampling rates.

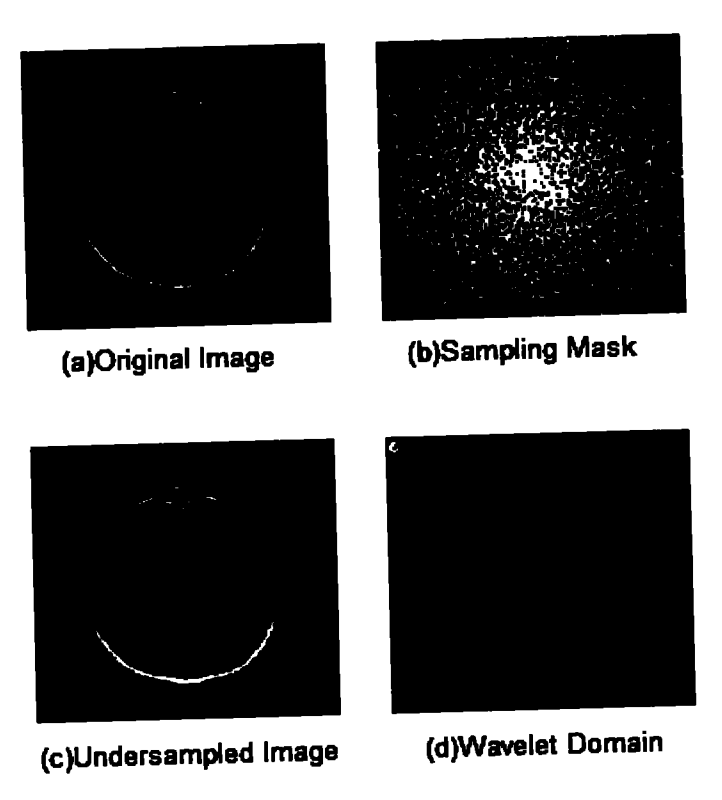


Figure 3-12: Image under-sampling mask and its domains

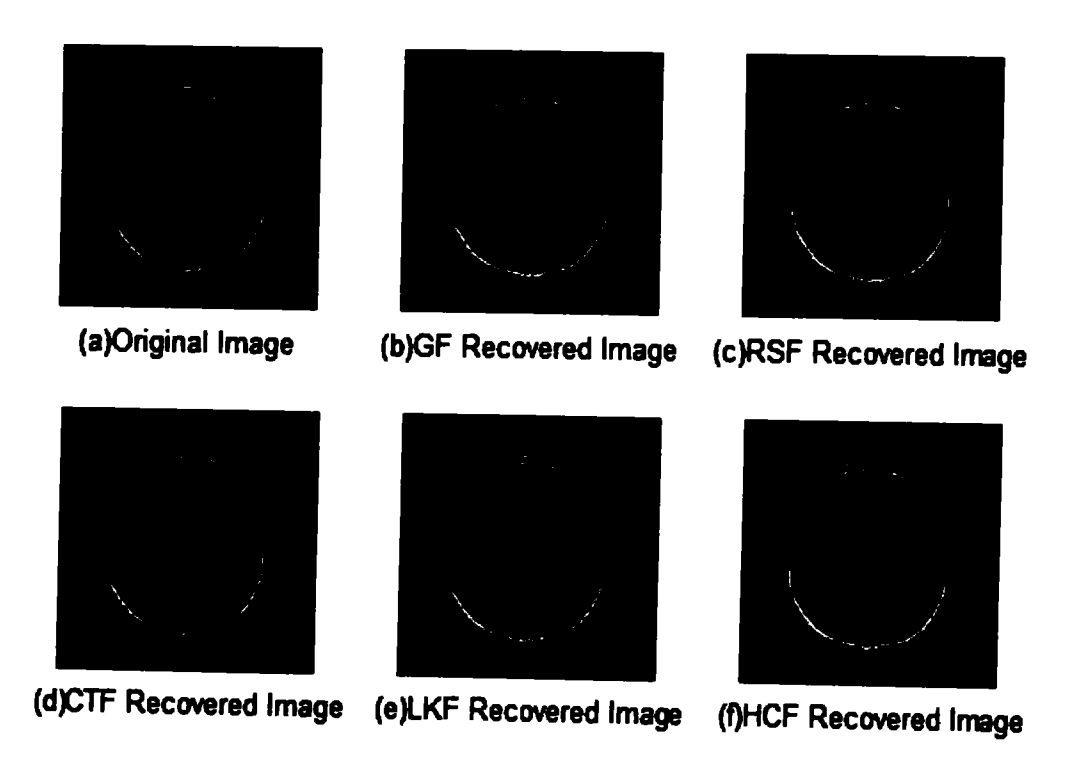


Figure 3-13: Reconstructed Images from different DA functions.

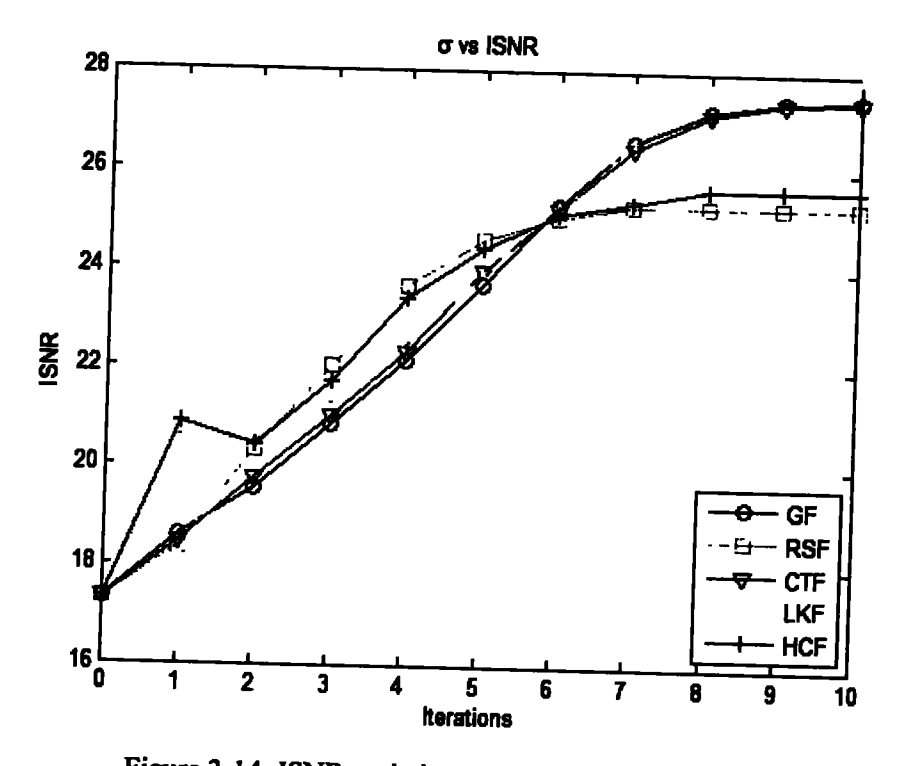


Figure 3-14: ISNR variation with different values of  $\sigma$ 

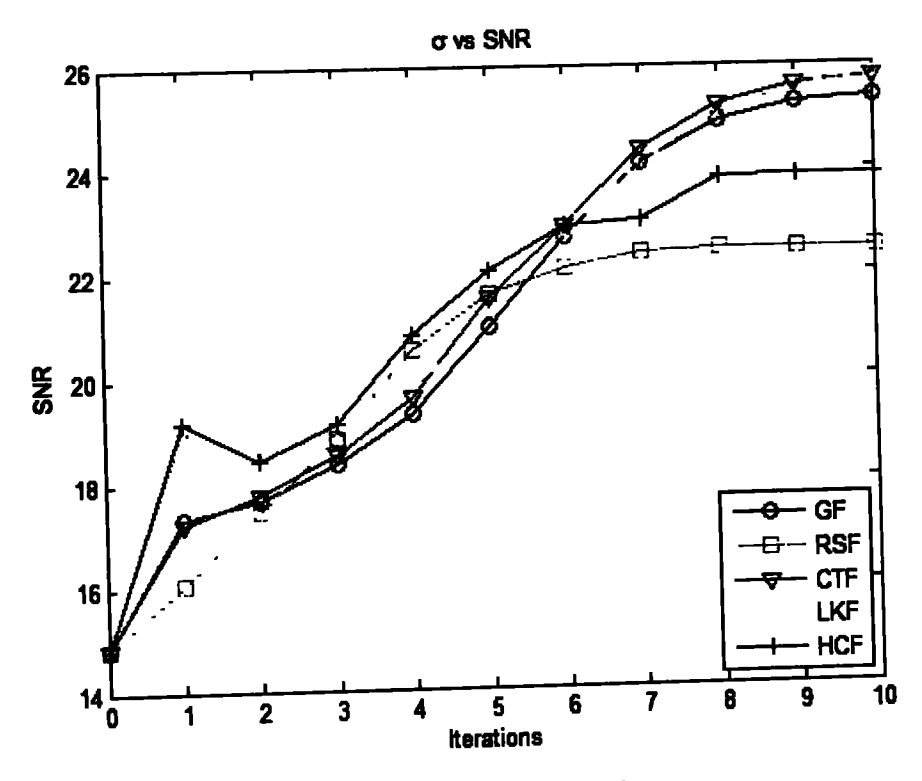


Figure 3-15: SNR against varying  $\sigma$ 

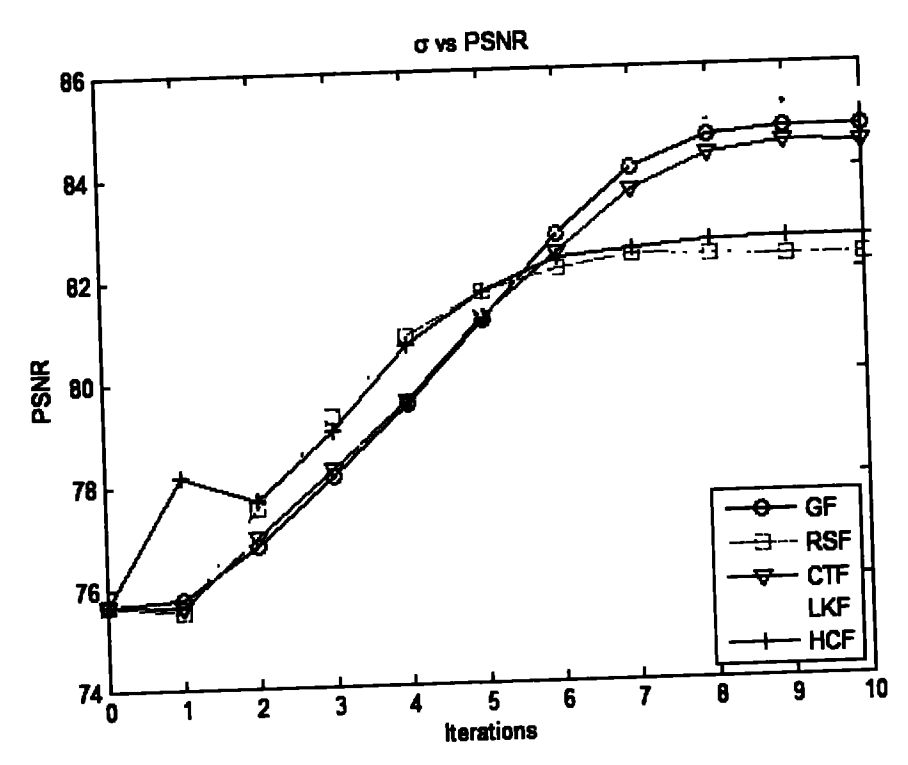


Figure 3-16: PSNR verses  $\sigma$ 

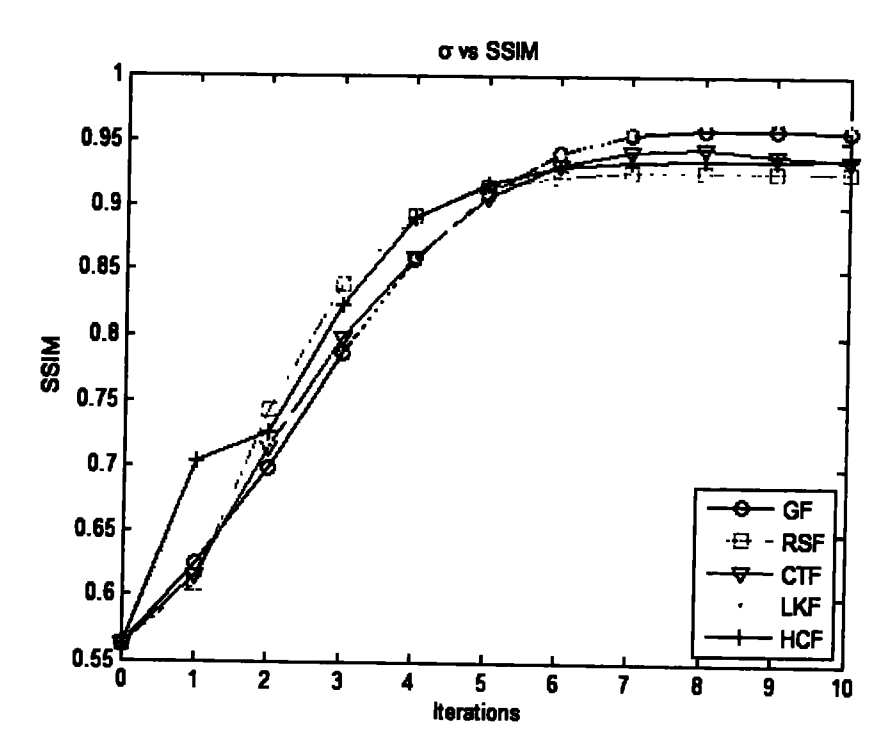


Figure 3-17: Structural Similarity Index improvement with  $\sigma$ 

Table 3-2: Effects of MRI recovery on varying sampling ratio

Samplin	g %	5%	10%	20%	30%	40%	50%	60%	70%	80%	90%
SNR	GF	13 67	16 08	20 09	26.84	32.13	49.18	43.02	47 14	51 30	57 14
	RSF	11.96	12 46	16.82	23 03	26 50	38.04	32.86	36.38	40.18	45 60
	CTF	14.18	17 05	20.99	27.49	32.68	48.87	42 89	46.82	50.92	56 08
	LKF	13.81	16.35	20.76	27.51	32.82	49 14	43.16	47.09	51.27	57.24
	HCF	13.27	15 55	18 61	25.06	25.73	41 15	35.43	39.30	43 55	49.74
PSNR	GF	74 35	77 03	80 17	86.05	90 40	105.2	99 71	103 4	106.9	111.8
	RSF	71.54	71 71	75.69	82.65	86.14	96.49	91 82	94.93	98.44	103 5
	CTF	73 01	76.37	79.91	86.04	90.55	103.4	98 83	101.9	105.0	109.5
	LKF	74 59	77 37	80 81	86.75	91 15	105 1	99.94	103.3	106.8	111.6
	HCF	73 53	75 69	77 58	83 60	86 33	96.79	92 48	95.36	98.54	103.2
ISNR	GF	16 41	19 38	22 77	28 84	33.33	48.53	42.85	46 65	50 41	55 52
	RSF	14.10	14 60	18 82	25.88	29.26	40.11	35.22	38 48	42.16	47.55
	CTF	15.62	19 19	22 86	29 02	33.56	47.18	42 19	45 48	48.86	53.59
	LKF	16 65	19 72	23.41	29 48	34 02	48.42	43 04	46.58	50.26	55 43
	HCF	15 71	18.26	20.59	26 71	29.65	40.36	35.79	38.84	42.21	47.23
MSE	GF	2 09e-3	1 09e-3	5 03e-4	1 21e-4	0 44e-4	1 31e-6	4 91e-6	2 03e-6	8 52e-7	2 60e-7
	RSF	1 49e-3	6 5e-4	2 39e-4	1 19e-4	6 9e-5	3 69e-6	1 44e-5	5 8e-6	2 05e-6	3 90e-7
	CTF	2 28e-3	i 12e-3	5 12e-4	1 26e-4	4 3e-5	1 79e-6	5 7e-6	2 65e-6	1 21e-6	4 06e-
	LKF	1 70e-3	8 48e-4	3 33e-4	8 17e-5	2 64e-5	6 98e-7	2 79e-6	1.13e-6	4 11e-7	8 99e-
	HCF	1 81e-3	9 52e-4	4 09e-4	1.19e-4	5.70e-5	3 66e-6	1 33e-5	5 72e-6	<b></b>	4 30e-
SSIM	GF	0 6652	0 8074	0.8858	0.9670	0.9853	0 9991	0 9973	0.9986	0.9994	0 999
	RSF	0 5396	0 5099	0 7459	0 9400	0 9694	0.9954	0.9889	0.9938	<del></del>	0.998
	CTF	0 5261	0 7203	0.8236	0 9509	0 9800	0.9987	0.9966		<del> </del>	0.999
	LKF	0 6823	0 8246	0 9019	0.9722	0.987	0 9990	0 9974			<del> </del>
	HCI	F 0.5916	0 7215	0.7921	0 9513	0.969	0.995	0.9901	0 9942	0 9968	0.998

# 3.8 Proposed Smooth $l_0$ norm approximation

A novel smoothed approx. of the  $l_0$  norm, known for its discrete and discontinuous nature. The proposed approximation provides a smooth and differentiable alternative to the original function defined by Eq. (3.10). Building upon this approximation, a comprehensive algorithm is developed for sparse signal recovery. By replacing the discontinuous function with the smooth and differentiable approximation, the algorithm enables more efficient and effective gradient-based recovery of sparse signals.

$$g_{\gamma}(z_j) = \frac{1}{1 + (\gamma \pi z_j)^2}$$
 (3.19)

The parameter  $\gamma$  in the proposed function is important in controlling the width of the function. In the extreme case, the function defined in Eq. (3.19)can be utilised as an inverse of the indicator function, offering a useful mathematical tool for handling sparse signal recovery.

$$\lim_{\gamma \to \infty} g_{\gamma}(z_j) = \begin{cases} 1 & z_j = 0 \\ 0 & z_j \neq 0 \end{cases}$$
(3.20)

To use  $g_{\gamma}(z_j)$  approx.  $l_0$ -norm, we consider two properties:

Property-I:

$$\lim_{\gamma \to \infty} g_{\gamma}(z_j) = 1 - q(z_j) \tag{3.21}$$

Where  $q(x_i)$  is given by (3).

Property-II: Define  $G_{\nu}(z)$  as:

$$G_{\gamma}(\mathbf{z}) = \sum_{j=1}^{n} g_{\gamma}(\mathbf{z}_{j})$$
(3.22)

Then,

$$\lim_{\gamma \to \infty} G_{\gamma}(z) = \sum_{j=1}^{n} (1 - q(z_j))$$

$$= n - \|z\|_{0}$$
(3.23)

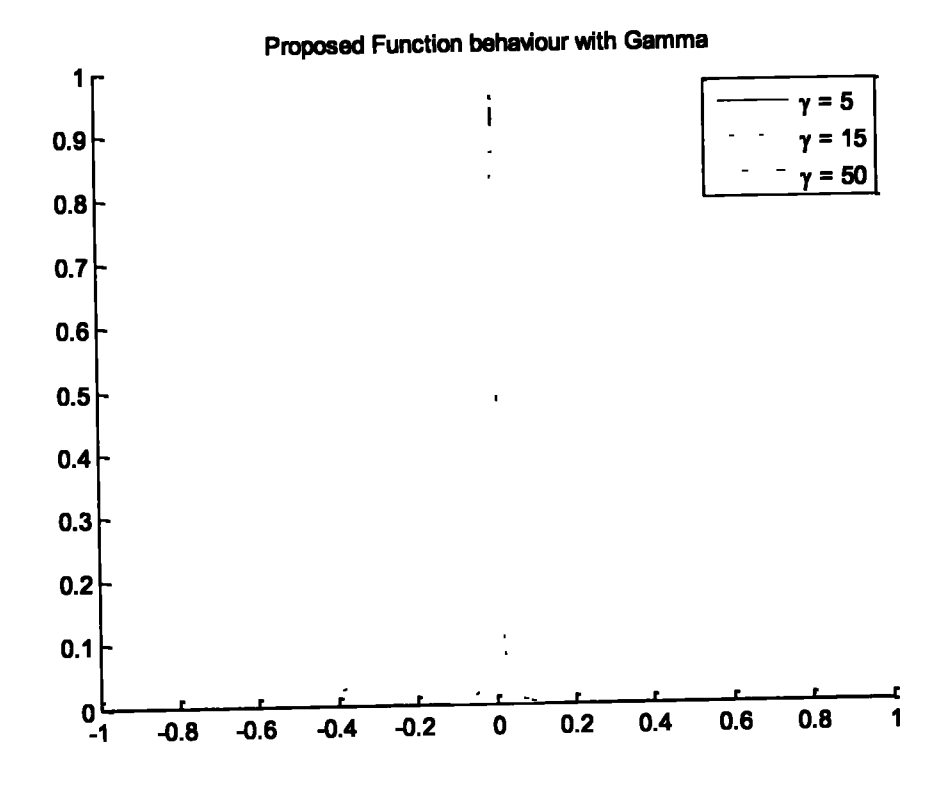


Figure 3-18:  $G_{\gamma}(z)$  Behavior for different values of  $\gamma$ 

Thus,  $||z||_0$  can be approximated as:

$$\|\mathbf{z}\|_0 \cong n - \lim_{\gamma \to \infty} G_{\gamma}(\mathbf{z}) \tag{3.24}$$

Eq. (3.24) introduces the parameter  $\gamma$ , which serves as a balance between the smoothness and accuracy of the estimated solution. By adjusting the value of  $\gamma$ , one can control the compromise between the two factors. Larger values of  $\gamma$  lead to a more accurate approximation, capturing finer details of the solution. Conversely, smaller values of  $\gamma$  result in a smoother approximation, sacrificing some precision but providing a more generalized representation of the problem defined in Eq. (3.7). Therefore, the choice of  $\gamma$  depends on certain requirements and priorities of the problem at hand.

The minimisation problem based on the  $l_0$  norm in Eq. (3.7) can be reformulated as a maximization problem of the function  $G_{\gamma}$ , particularly for larger values of  $\gamma$ . However, when  $\gamma$  is large,  $G_{\gamma}$  may exhibit non-smooth characteristics, leading to multiple local maxima. In contrast, for smaller values of  $\gamma$ ,  $G_{\gamma}$  becomes smoother, minimising the

likelihood of becoming trapped in the local maxima. Thus, the main idea is to initiate the optimisation process with a small  $\gamma$  value to side-step local maxima to increase  $\gamma$  gradually to achieve an optimal sparse solution problem in Eq. (3.7). This approach enables a balance between accuracy and sparsity while mitigating the risk of getting stuck in suboptimal solutions.

Figure 3-18 illustrates the function  $G_{\gamma}(.)$  behaviour across different values of  $\gamma$ . As  $\gamma$  increases, the function progressively approaches a better approximation of the  $l_0$  norm. Particularly for smaller  $\gamma$ , the behaviour of the  $G_{\gamma}(.)$  appears to be smooth, indicating a smoother approximation. The  $G_{\gamma}(.)$  can be interpreted as a measure of the level of sparsity in the solution, especially for larger values of  $\gamma$ . Maximizing  $G_{\gamma}(.)$  yields the sparsest solution, providing a valuable metric for evaluating the sparsity of the solution.

The development of the sparse signal recovery algorithm depends on the estimate provided by  $G_{\gamma}(.)$ , the steepest ascent algorithm is employed to maximize the function  $G_{\gamma}(.)$ . In the iteration of the SDA, the solution is updated using the gradient, which enables the algorithm to move towards the maximum of the function. This iterative process allows for the refinement of the solution, iteratively improving its sparsity based on the maximization of  $G_{\gamma}(.)$ .

By utilising the steepest ascent algorithm and the gradient-based updates, the proposed sparse signal reconstruction algorithm effectively explores the solution space to achieve higher levels of sparsity. The algorithm capitalizes on the insights provided by the behaviour of the function  $G_{\gamma}(x)$  and leverages the gradient information to guide the iterative optimisation process, enabling the recovery of sparse signals from limited and noisy observations.

$$\mathbf{z}_{k+1} \leftarrow \mathbf{z}_k + \mu_k \nabla G_{\gamma}(\mathbf{z}_k) \tag{3.25}$$

The proposed sparse signal reconstruction algorithm incorporates gradient descent optimisation with an adaptive step size  $\mu_k$ , which decreases with each iteration to ensure stability and convergence. For larger values of  $\gamma$ , a small step size is suggested to accommodate the fluctuating nature of the function  $G_{\gamma}$  and maintain stability. The approx. solution is further improved using back-projection, enhancing the accuracy of the reconstructed signal. Algorithm 3.3 is described below, illustrating the iterative process

that combines gradient descent, step size adaptation, and back projection to achieve accurate and sparse signal recovery from limited and noisy measurements.

Algorithm 3.2: Proposed Smoothed  $l_0$  Norm Approximation

```
Initialisation:

1. Initialise z_0 by l_2 approximate solution of \Phi z = y.

2. Set sequence of increasing \gamma, [\gamma_1, \gamma_2, ..., \gamma_N]

for k = 1, 2, ..., N:

1. Set \gamma = \gamma_k.

2. Maximise G_{\gamma} using M iterations of th steepest ascent algorithm.

a. Initialise: z = q_{k-1}

b. For i = 1, 2, ..., M

i. Set \Delta z = \left[z_1 g_{\gamma_k}(z_1), ..., z_n g_{\gamma_k}(z_n)\right]^T

ii. Set z \leftarrow z - \mu \Delta z

iii. Project z back as z = z - \Phi^T(\Phi \Phi^T)^{-1}(\Phi z - y)

3. Set q_k = x

Final solution: z = q_N.
```

# 3.9 Proposed Algorithms Experimental Results on k-Sparse Signal

The efficiency of the proposed method is empirically validated through MATLAB. In the experiments, a 1-D sparse signal is sampled using a random Gaussian matrix  $\Phi_{m\times n}$ , where m=400 are observations and n=1000 is a k-sparse signal length that needs to be recovered. To ensure consistency, every column of the matrix  $\Phi$  is normalized to unity. The measurements are taken based on a noisy model y=Ax+w, here w denotes white Gaussian noise (WGN).

The proposed algorithm incorporates an inner loop using gradient descent, which is executed three times (N=3) for each value of  $\gamma$ . This iterative process allows for fine-tuning and refinement of the reconstructed signal by iteratively updating the solution. The algorithm's robustness and effectiveness are evaluated under different conditions and scenarios by systematically varying  $\gamma$  and conducting multiple iterations

The experimental validation using MATLAB simulations provides quantitative insights into the algorithm's performance and demonstrates its ability to recover sparse signals from noisy observations accurately. The choice of specific parameters ensures a

comprehensive evaluation of the algorithm's performance and robustness. The proficiency of the proposed method is examined by MSE and SNR, where the proposed algorithm recovers the sparse signal more accurately than the base SL0 algorithm defined by [90].

Table 3-3: Values of MSE and SNR at Different Iterations

Iteration	Prop	osed Algori	SLO Algorithms		
	γ	MSE	SNR	MSE	SNR
1	0.45	2.75e — 2	6.70	3.75e - 2	2.88
2	0.90	1.26e - 2	10.10	2.19e – 2	5.21
3	1.80	5.50e — 3	13.70	4.28e - 3	12.29
4	3.60	1.44e - 3	19.53	1.67e - 3	16.37
5	7.20	3.43e - 4	25.74	6.18e - 4	20.71
6	14.4	7.66e — 5	32.26	1.91e - 4	25.80
7	28.8	1.87e — 5	38.38	1.87e - 4	25.89
8	57.6	4.78e — 5	43.38	1.72e – 4	26.15
9	115.2	1.48e — 6	48.61	1.53e - 4	27.97
10	230.4	8.42e - 7	51.52	1.59e — 4	28.80

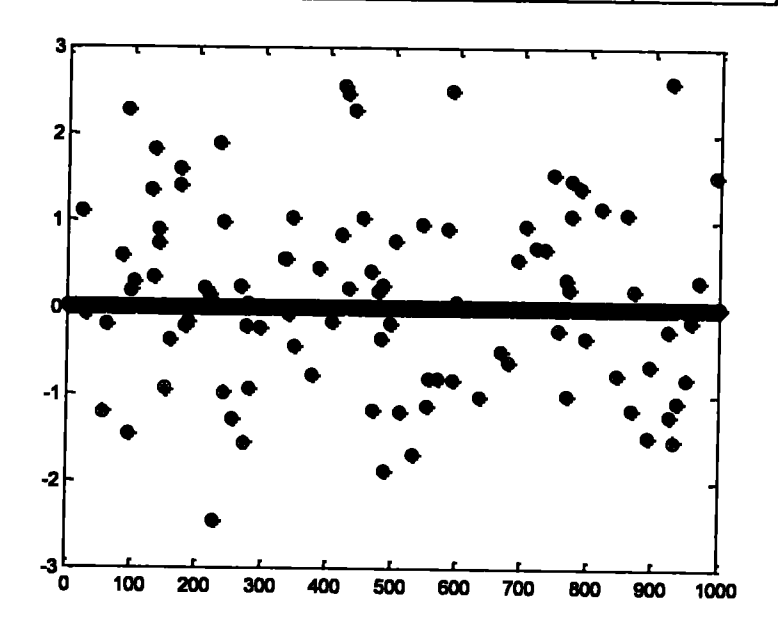


Figure 3-19: Ground Truth "\*" and Reconstructed Signal "o"

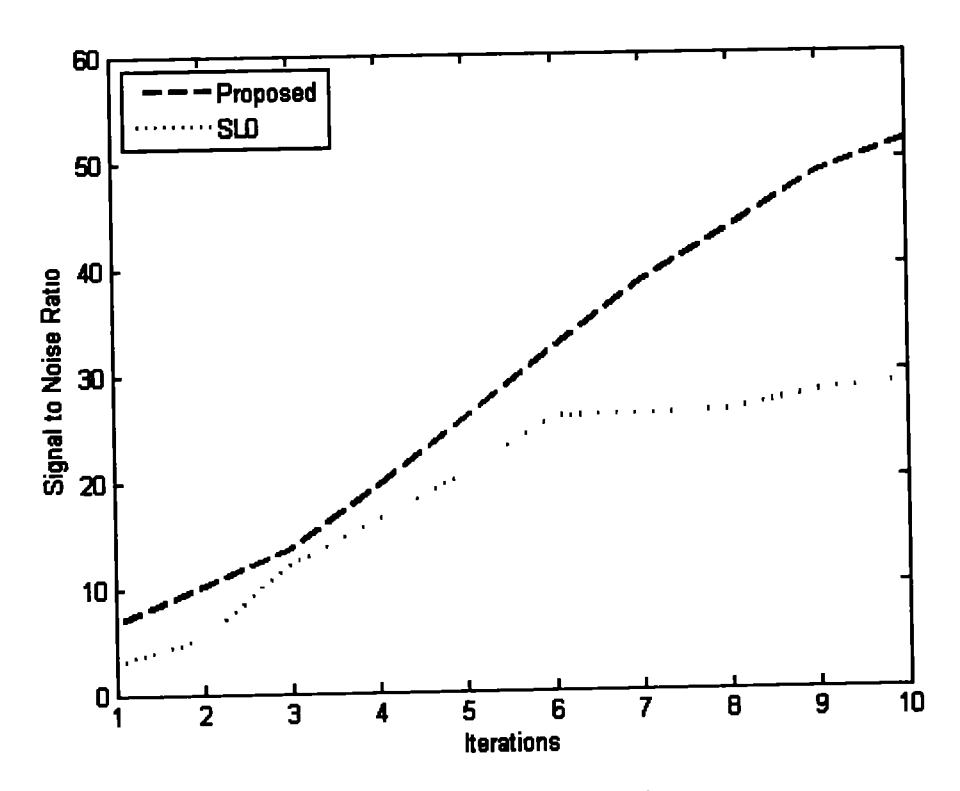


Figure 3-20: SNR versus iterations

The proposed algorithm is compared with the baseline SL0 algorithm, as presented in shown in experimental results. The results in Table-1 highlight that the novel function proposed in this section outperforms the SL0 algorithm by achieving significantly improved SNR values. The proposed method achieves SNR values of up to 51.52 dB, while the SL0 algorithm achieves only 28.80 dB. Moreover, the MSE of the estimated signal by the proposed method lies in the vicinity of zero, indicating a highly accurate reconstruction.

Figure 3-19 visually demonstrates the reconstructed signal alongside the actual signal. The non-zero elements of the actual sparse signal are marked with '\*', while the non-zero values of the estimated signal are marked with 'o'. The perfect alignment of these markers indicates the nearly perfect reconstruction achieved by the proposed algorithm, as the non-zero values of the recovered signal perfectly overlap with those of the original signal.

Furthermore, Figure 3-20 illustrates the enhancement in SNR by proposed algorithms. This comparison allows for a visual assessment of the performance improvement over the iterations. The figure shows the clear advantage of the proposed algorithm, which consistently exhibits superior SNR improvement compared to the conventional SL0 algorithm.

Collectively, the experimental results provide strong evidence of the superior performance of the proposed method by reconstruction accuracy and consistency throughout the iterations. The proposed algorithm offers significant advancements in sparse signal recovery, achieving high-quality reconstructions with improved fidelity compared to existing approaches.

## 3.10 Empirical Results for CS MRI Recovery

The proposed smooth approximation of the  $l_0$  norm (PSL0) technique is applied to recover of MRI from its undersampled k-space data. Drawing a comparison between CS encoding and noisy images, compressed sensing recovery fundamentally transforms into an image-denoising task. Estimating the noise, done using the maximum a posteriori (MAP) estimator, is the first step in recovering the original image. A 2-D compressively sampled genuine human brain MR picture with dimensions of 256 x 256 is recovered using the suggested approach. The original human brain MR image was obtained utilising a 1.5 Tesla GE-HDxt-MRI scanner using Gradient Echo (GE) sequence and 8-channel head coils. This scan was fully sampled. At St. Mary's Hospital in London, England. The MR image is compressively extracted in this instance by acquiring only 25% of the samples using a random mask.

Figure 3-21 presents the recovery of CS MRI data under-sampled using a variable density random sampling scheme. In Figure 3-21 (a), the recovery results of the MRI using different algorithms, namely ZF, LR, SSF, IRLS, POCS, MIRLS, and the proposed method (PSL01), are displayed. Subjectively, the image recovered by the proposed method exhibits better visual quality compared to the other recovered images, indicating the effectiveness of the proposed algorithm.

Figure 3-21 (b) illustrates the sampling pattern utilised by each algorithm. It visually represents how the different algorithms capture the under-sampled data. The sampling pattern reflects the spatial distribution of acquired measurements, which is crucial for accurate recovery.

Furthermore, Figure 3-21 (c) focuses on the magnified difference between the original and recovered images. The Zero Filling approach performs poorly, as the difference between the original and recovered images is more pronounced. On the other hand, the SSF and IRLS algorithms exhibit higher error levels than the PSL0. The error in the proposed

method is considerably lower than that of the other methods, indicating its superiority in terms of achieving more accurate and faithful image recovery.

Figure 3-22 provides a quantitative comparison of the proposed algorithm PSL0 performance with PSO, POCS, and MIRLS algorithms when applied to under-sampled MR data. The under-sampling process is conducted using a variable-density random sampling pattern.

Figure 3-22 (a) depicts the improvement in ISNR achieved by the proposed algorithm is depicted. It showcases the superiority of the proposed algorithm in terms of achieving higher ISNR values compared to other methods. The higher SNR values indicate better quality and fidelity in the recovered MRI.

Figure 3-22 (b) illustrates the reduction in SSIM achieved by the PSL0. A higher SSIM value indicates a closer match between the recovered MRI and the actual image. The significant improvement in SSIM achieved by the PSL0 indicates its ability to achieve more accurate and reliable results compared to the other algorithms.

Overall, these comparisons highlight the quantitative advantages of the proposed algorithm PSL0 over other methods, as evidenced by the improvement in SSIM and ISNR. These results further validate the effectiveness of the proposed algorithm for recovering under-sampled MR data.

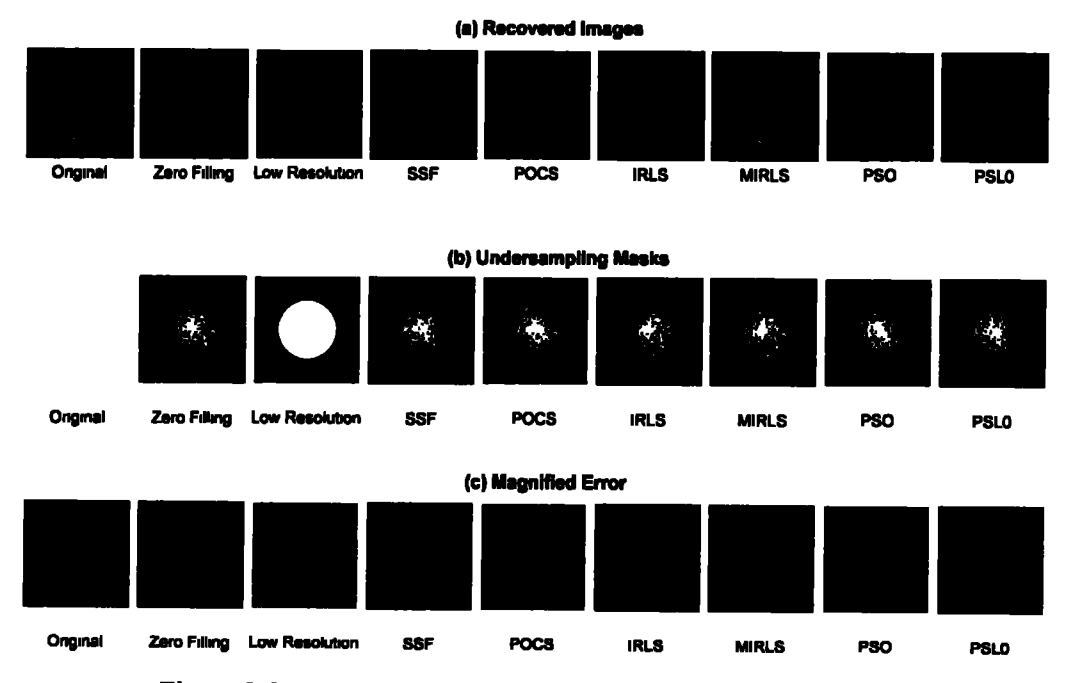


Figure 3-21: MRI Recovery with PSL0 and Other Algorithms

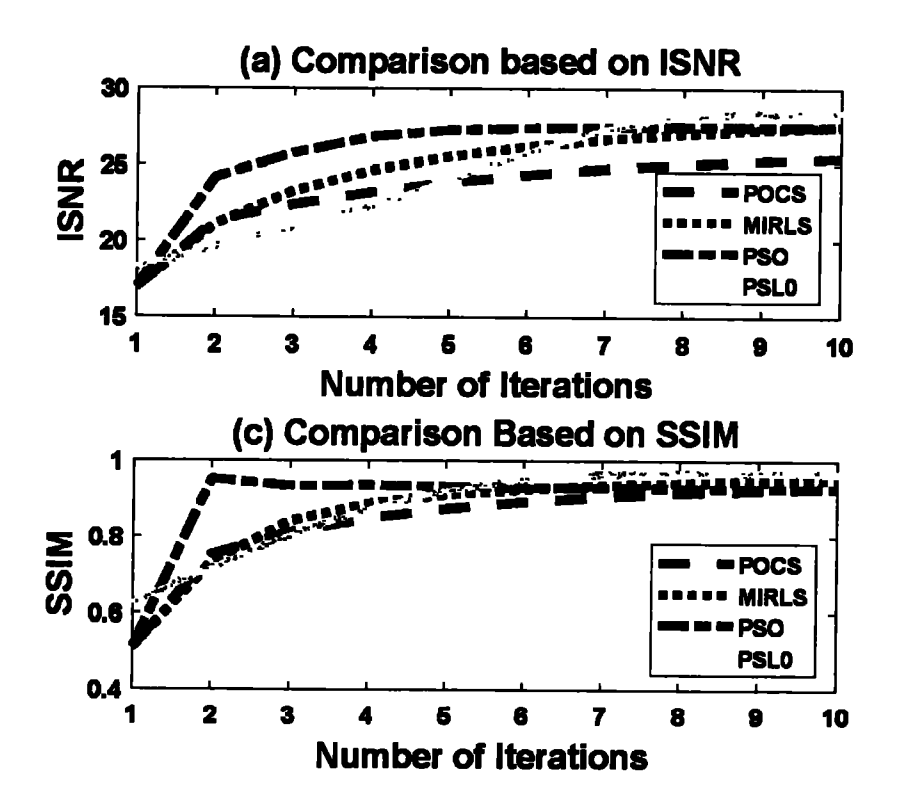


Figure 3-22: ISNR and SSIM attained by PSL0 and other Algorithms

#### 3.11 Conclusions

In conclusion, the precise reconstruction of sparse signals from limited observations poses significant computational challenges. This chapter has presented a novel technique to address this issue and reconstruct a sparse signal by the reduced number of observations. The proposed algorithm has been compared to the conventional SL0 algorithm in terms of MSE and SNR. The empirical findings have demonstrated that the proposed technique surpasses existing smooth approx. methods of the  $l_0$  norm in terms of accuracy and performance. This signifies the efficacy of the proposed algorithm in recovering sparse signals from limited measurements.

This chapter has also presented a comprehensive analysis of various smoothed  $l_0$  norm approximation functions found in the literature, ensuring fair comparison by matching the width of each function. The performance of these functions was evaluated for 1D sparse signal recovery, considering metrics, such as SNR and MSE. Among the tested functions, the Gaussian Function (GF) demonstrated the best efficiency in terms of signal recovery accuracy, while the Reciprocal Smoothed Function (RSF) exhibited the least computational cost.

Furthermore, the smoothed  $l_0$  norm approximations were applied to the reconstruction of compressively sampled MRI images. Performance measures including SNR, Improved ISNR, PSNR, and SSIM were utilised to evaluate the efficiency of the reconstructed images. The empirical results revealed that the Laplacian kernel function yielded the most accurate reconstruction of CS 2D MRI. The accuracy of each smoothed  $l_0$  norm approximation was assessed across varying levels of MRI compression, and it was concluded that the Laplacian function is the most efficient choice for the recovery of CS MRI.

These findings highlight the significance of selecting appropriate smoothed  $l_0$  norm approximation functions for different signal recovery scenarios. The Gaussian Function proved to be highly effective in 1D sparse signal recovery, while the Laplacian kernel function demonstrated superior performance in compressively sampled MRI reconstruction. The outcomes of this study contribute to the advancement of sparse signal recovery techniques, providing valuable insights into the selection and application of smoothed  $l_0$  norm approximation functions in practical signal processing applications.

## **CHAPTER 4**

# SPARSE RECOVERY USING HYPERBOLIC TANGENT BASED SMOOTH L1 NORM AND SHRINKAGE

In this chapter, a novel reconstruction algorithm utilizing the hyperbolic tangent function (tanh) to reconstruct signals and images within the Compressed Sensing (CS) framework. The proposed approach involves approximating the  $l_1$  norm and soft thresholding using the tanh. This chapter also presented criteria for optimising tuning parameters to achieve nearperfect results. The proposed  $l_1$  norm approx. error bounds have been examined. To assess the proficiency of the proposed technique, we have used datasets consisting of 1-D k-sparse signals, CS MRI, and cardiac cine MRI (CC-MRI), which is crucial for evaluating cardiac vascular function. CC-MRI provides valuable information, such as ejection fraction and cardiac output, but its slow acquisition process hinders its efficiency. Therefore, there is a need to expedite the scanning methods to exploit the advantages of CC-MRI fully. Empirical findings using efficiency evaluation measures i.e., including SSIM, PSNR, and RMSE demonstrate that the suggested CS recovery method based on the tanh outperforms traditional IST recovery methods, providing significantly improved performance in reconstructing undersampled signals and images.

#### 4.1 Introduction

In the CS framework, the under-determined system of linear equations may have infinitely many solutions. However, the objective is to find the sparsest possible solution, which involves minimising the  $l_0$  norm. Unfortunately, finding an  $l_0$  norm solution is a non-convex and NP-hard optimisation problem, given the infinitely many possible solutions. To address this, the  $l_1$  norm has been established as a suitable approximation for the  $l_0$  norm, transforming the non-convex problem into a convex one[94]. However, the non-differentiability of the  $l_1$  norm and the inability to apply gradient-based minimisation algorithms necessitate smooth approximations for the  $l_1$  norm. Iterative shrinkage algorithms have proven to be efficient in numerically minimising the  $l_1$ -regularised least

squares optimisation problem [23], but they require inducing sparsity in the solutions to fulfil the requirements of CS reconstruction. CS is a sampling technique, that enables the retrieval of a signal using only limited observations, provided that the signal exhibits sparsity in a specific domain and the observations are incoherent with that domain. However, many existing reconstruction methods for CS signals have high computational costs and rely on non-linear techniques. These limitations have motivated the need for more efficient and computationally feasible approaches to signal reconstruction in CS [2, 5, 40]. A novel recovery method is introduced that employs the *tanh* to reconstruct undersampled signals and images within the CS framework.

CC-MRI is a valuable tool for assessing cardiac-vascular disease by providing detailed information about cardiac wall thickness, motion, and functional parameters like ejection fraction and cardiac output [108-111]. However, the traditional scanning methods of CC-MRI are time-consuming and require patients to hold their breath multiple times during the scan, leading to patient discomfort and limited scan efficiency.

Researchers are exploring techniques to reduce scanning time in CC-MRI to address these challenges. One approach is to use fast pulse sequences that allow for quicker image acquisition. Another approach is to reduce the sampling frequency during data acquisition, which can be achieved through CS techniques. CS benefits from the inherent sparsity of cardiac cine MRI data in the temporal dimension. By exploiting the fact that only a few significant changes occur between consecutive frames of a cardiac cycle, CS enables accurate reconstruction of the entire sequence from a smaller number of acquired samples [14, 112]. This reduction in the number of samples leads to shorter acquisition times and increased patient comfort. Researchers in medical imaging, particularly in the field of MRI, are actively working on improving the speed and efficiency of CS-based reconstruction methods. These methods involve non-linear reconstruction algorithms that can effectively exploit the sparsity of the cardiac cine MRI data. Additionally, incoherent undersampling techniques, such as random sampling, produce noise-like aliasing artefacts during the reconstruction process, further enhancing the efficiency of CS in cardiac cine MRI [113, 114]. Continual advancements in CS techniques hold great promise for improving the speed, efficiency, and diagnostic capabilities of cardiac cine MRI. By leveraging the principles of sparsity, non-linear reconstruction, and incoherent undersampling,

researchers aim to develop more efficient CS algorithms to accelerate image acquisition, reduce patient burden, and improve the overall quality of cardiac cine MRI examinations.

In MRI, sparsity can be achieved by finding a suitable sparsifying transform for its sparse representation, while incoherent sampling is fulfilled by using various undersampling patterns such as radial lines or variable density sampling [14]. Non-linear recovery methods based on  $l_1$ -norm regularisation have commonly solved the problem by finding the sparse estimated solutions to the LS. While the  $l_2$ -norm employs a simple solution, it dispenses the error energy across all solutions, resulting in non-sparse solutions that do not fit well within the CS framework. On the other hand,  $l_p$ -norm regularisation with  $1 tends to penalise only the largest parameters, leading to less sparse solutions. Thus, <math>l_1$ -norm regularisation is preferred as it promotes sparsity, making it suitable for the CS framework [2, 5, 40].

However, the  $l_1$  norm penalty is non-differentiable, making it challenging to apply efficient optimisation methods that rely on derivatives. To address this, different methods have been suggested to solve the  $l_1$  norm penalty problem. The IST algorithm has been successfully used for efficient image reconstruction from under-sampled data in the CS framework [15, 115]. Another approach is the iterative hard thresholding-based recovery method, although under-performed as compared to soft thresholding-based methods. Several algorithms, such as random filters for CS [116], Bregman algorithms for [117], and weighted  $l_1$  norm reconstruction method [118], have been suggested to address the CS reconstruction problem.

Recently, a smooth  $l_1$ -norm regularisation CS recovery method using a tanh has emerged. This technique has shown promise in reconstructing under-sampled MR images from fewer samples, enabling fast scanning with no compromise on spatial resolution. It has been demonstrated that the tanh performs better in signal reconstruction compared to (soft and hard) thresholding and Garrote thresholding methods [119, 120]. Researchers have also explored the implementation of wavelet thresholding using tanh, which has been found to provide more precise recovery results than IST techniques [121-123].

These developments in approximating the  $l_1$ -norm using the tanh have opened new possibilities for improved signal recovery in under-sampled MR imaging. Experimental evidence supports the effectiveness of this approach in achieving better reconstruction

compared to traditional thresholding methods. By leveraging the advantages of the tanh, researchers are advancing the field of CS image restoration for MR imaging.

This chapter explores the application of CS to reduce MRI data acquisition time by leveraging the sparsity in MRI signals in k-space. A novel CS reconstruction method is suggested that employs tanh, which provides a more efficient approximation of the  $l_1$ -norm and enables accurate recovery of compressively sampled sparse signals, MR images, and cardiac cine MRI. The proposed algorithm utilises the steepest descent algorithm for objective function minimisation and incorporates the IST technique based on the tanh, inspired by the MAP noise predictor. The efficient criteria for tuning the parameters are also suggested. Empirical results are evaluated through simulations involving the recovery of random 1-D sparse signal, 2-D MRI, and clinical CC-MRI. Quantitative performance measures, including MSE, RMSE, SNR, PSNR, ISNR, correlation, SSIM and, fitness was employed to demonstrate the superiority of our suggested algorithm over existing reconstruction methods.

# 4.2 Proposed Smooth $l_1$ -norm approximation by Hyperbolic Tangent

Reconstructing an undersampled signal using CS is an optimisation problem that minimises the  $l_1$  norm in the solution. This penalty is sparsity-promoting mechanism in the solution, so only a few elements of the solution are nonzero. This is useful for reconstructing naturally sparse signals, such as MRI images on an appropriate basis.

Consider a signal represented as a vector  $x \in \mathbb{R}^n$ . Let  $y \in \mathbb{C}^m$  limited observations of the signal. The CS reconstruction can be expressed as follows:

$$f(x) = \frac{1}{2} \| y - \Phi \Psi^{H} x \|_{2}^{2} + \lambda \| x \|_{1}$$
 (4.1)

Here,  $\Phi$  defines the sampling matrix for signal x, while  $\Psi$  is the sparsifying domain. The parameter  $\lambda$  in Eq. (4.1) crucial for the trade-off between fidelity and sparsity. The effectiveness of our algorithm depends on choosing the right threshold level. Depending on the signal size and its noise variance, we used the fixed value expression. [115].

$$\lambda = \sigma_v \sqrt{2 \ln{(n)}} \tag{4.2}$$

The noise standard variance is denoted by  $\sigma_v$ , and sparse signal length is denoted by n. The tanh has several properties, including non-convex, odd function, differentiable, bounded function, and monotonically increasing. You can also adjust the curve of the function at its

point of origin to any desired value [123]. This is why we propose to use the tanh as an approximation for the  $l_1$ -norm in Eq. (4.1). The approximation is defined as follows:

$$\|\mathbf{z}\|_{1} \cong \sum_{i=1}^{n} z_{i} tanh(\gamma z_{i})$$
(4.3)

As the tanh serves as a differentiable function to approx.  $l_1$ -norm, we select a relatively high value for the parameter  $\gamma$  to bring it closer to the  $l_1$ -norm, as depicted in Figure 4-1. In Figure 4-1  $l_1$  norm approximation using the tanh with varying values of  $\gamma = (1, 4, 6, and 10)$ . As  $\gamma$  increases, the approximation becomes closer to the true  $l_1$  norm but also becomes less smooth. The proposed technique offers a trade-off between smoothness and accuracy, allowing flexibility in choosing the desired level of approximation.

This choice allows us to leverage the advantages of smoothness and differentiability. Consequently, Eq. (4.1) can be expressed as follows:

$$f(z) = \frac{1}{2} \| y - \Phi \Psi^{H} z \|_{2}^{2} + \lambda \sum_{i=1}^{n} z_{i} \tanh(\gamma z_{i})$$
(4.4)

To accommodate the steepest descent algorithm, vector differentiation is not applicable. Therefore, it becomes necessary to rewrite it in element form, as shown in Eq. (4.4), compute the partial derivatives. By introducing the notation,  $\mathbf{A} = \mathbf{\Phi} \mathbf{\Psi}^{H}$ , we can express the element-wise equation as follows:

$$f(z) = \frac{1}{2} \sum_{i} (Az - y)_{i} (Az - y)_{i} + \lambda z_{i} \tanh(\gamma z_{i})$$
(4.5)

By introducing the notation  $A = \phi \Psi^H$ , we can formulate the gradient of Eq. (4.4) in the form of the element as follows. This formulation allows us to calculate the derivatives regarding each element individually:

$$\frac{\partial f(z)}{\partial z_l} = \sum_{ij} A_{ij} A_{il} z_j - \sum_{l} y_l A_{ll} + \lambda \left( \tanh(\gamma z_l) + z_l \gamma (1 - \tanh^2(\gamma z_l)) \right)$$
(4.6)

So, the proposed steepest descent algorithm scheme can be defined as for its  $l^{th}$  update is:

$$(\Delta z)_l = -\eta \frac{\partial f(z)}{\partial z_l} \tag{4.7}$$

The SDA is employed to find a solution using Eq. (4.7). This equation provides a framework for iteratively updating the solution by taking steps toward the steepest descent.

The algorithm aims to minimise the loss function by adjusting the solution according to the gradient information provided by Eq. (4.7).

# 4.3 Smooth $l_1$ norm Error Bounds

In this section, bounds for error are examined for smooth  $l_1$  norm, as described by Eq. (4.2) [124]. The  $l_1$  norm is approximated using two fundamental rules, which serve as the foundation for its effectiveness are defined below:

- 1.  $|z| = (z)_+ + (-z)_+$ , where  $(z)_+ = \max[z, 0]$  is the plus function.
- 2. The above-mentioned plus function is redefined by the smooth approximation as:

$$(z)_{+} \approx p(z, \gamma) = \frac{1}{2}[z + z. \tanh(\gamma z)]$$
 (4.8)

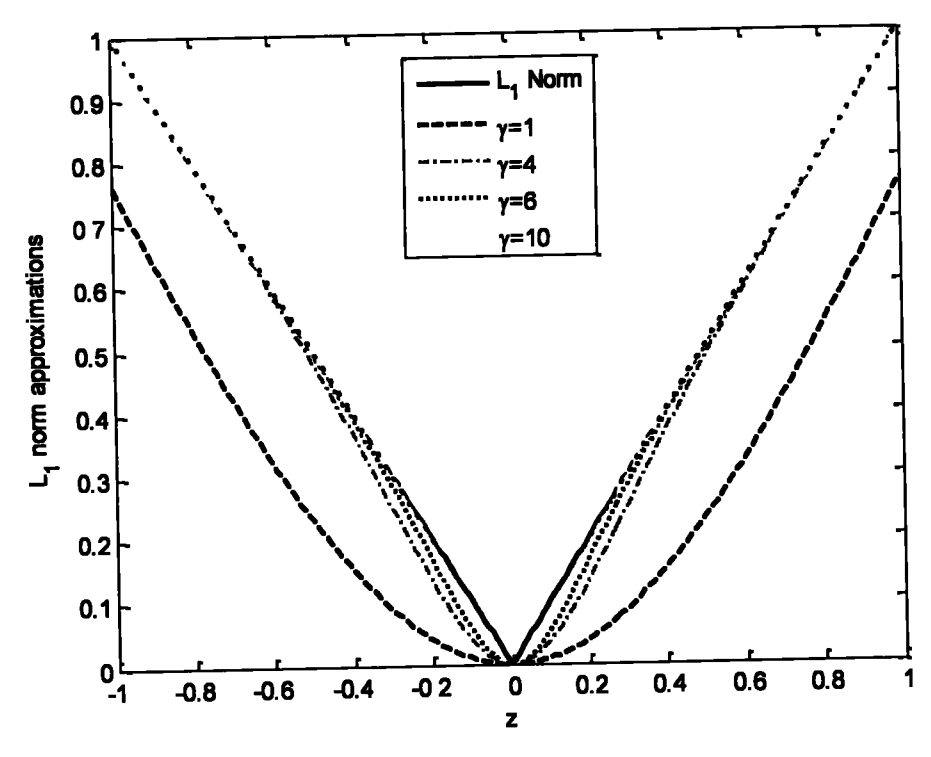


Figure 4-1:  $l_1$  norm approximation using the tanh with varying values of  $\gamma = (1, 4, 6, and 10)$ .

From Eq. (4.8), we can write a smooth approximation of  $l_1$ norm:

$$||z||_{1} = (z)_{+} + (-z)_{+} \approx p(z,\gamma) + p(-z,\gamma)$$

$$= \frac{z}{2} [1 + \tanh(\gamma z)] - \frac{z}{2} [1 + \tanh(-\gamma z)]$$
(4.9)

$$= \frac{z}{2} \tanh(\gamma z) + \frac{z}{2} \tanh(\gamma z)$$
$$= z \tanh(\gamma z)$$
$$= ||z||_{\gamma}$$

In contrast to the  $l_1$  norm, the proposed approximation allows for applying unconstrained optimisation techniques, as it is twice differentiable. The first-order gradient of the proposed  $l_1$  norm can be calculated using Eq. (10), while the second-order gradient can be obtained using Eq. (11). This differentiability property enables the use of gradient-base optimisation algorithms to efficiently solve the optimisation problem associated with the proposed approximation.

$$\nabla(||z||) \approx \tanh(\gamma z) - \gamma z \left(\tanh(\gamma z)^2 - 1\right) \tag{4.10}$$

$$\nabla^2(||z||) \approx 2\gamma(\gamma z \tanh(\gamma z) - 1)(\tanh(\gamma z)^2 - 1) \tag{4.11}$$

The value of  $\gamma$  approaches infinity and the difference between  $||z||_1$  and  $||z||_{\gamma}$  becomes negligible. In this study, we introduce a straightforward lemma to establish error boundaries for  $||z||_1$  and  $||z||_{\gamma}$ . This lemma provides a useful framework for understanding the relationship between the two norms and quantifying the approximation error as  $\gamma$  increases.

**Lemma 1:** The smooth function proposed for the  $l_1$  norm,  $f(z) = z \tanh(\gamma z)$ , satisfies both the necessary and sufficient convexity condition within the interval  $z \in [-1, 1]$ . This can be observed through its monotonically non-decreasing derivative, f'(z), as defined by Eq. (4.10), and its nonnegative second derivative, f''(z), as defined by Eq. (4.11), for  $0 < \gamma \le 1$ . These properties ensure that the proposed function is convex and suitable for approximating the  $l_1$  norm.

**Lemma 2:**  $l_1$ -norm based approx. error is bound for any  $z \in \mathbb{R}^n$  and  $\gamma > 0$ 

$$|||z||_1 - ||z||_{\gamma}| \le \frac{1}{2\gamma} \tag{4.12}$$

#### Proof:

Let's consider two cases, the first case for z > 0,

$$p(z,\gamma) - (z)_{+} = \frac{z}{2}(1 + \tanh(\gamma z)) - z$$

$$= \frac{z}{2}\tanh(\gamma z) - \frac{z}{2}$$
(4.13)

$$=\frac{z}{2}(\tanh(\gamma z)-1)$$

To determine the upper bound for Eq. (13), we can find the highest value of  $\tanh(\gamma z)$ . It is well-known that the highest  $\tanh(\gamma z)$  value is 1. Therefore, this is expressed as follows:

$$maxima\ tanh\ (\gamma z) = \frac{e^{\gamma z} - e^{-\gamma z}}{e^{\gamma z} + e^{-\gamma z}} = 1$$
 (4.14)

By Eq. (4.14), The relationship between  $\gamma$  and z can be readily derived as follows:

$$z = \frac{1}{2\gamma} \tag{4.15}$$

By inserting the value of z from Eq. (4.15) in Eq. (4.14)

$$p(\mathbf{z}, \gamma) - (\mathbf{z})_{+} \le \frac{1}{4\gamma} \tag{4.16}$$

For  $z \leq 0$ ,

$$0 \le p(z,\gamma) - (z)_{+} = p(z,\gamma) \le p(0,\gamma)$$

$$= \frac{z}{2} \left( \tanh(\gamma z) - 1 \right) \le 0$$

$$= \frac{1}{4\nu}$$

$$(4.17)$$

Here p is the monotonically increasing. So, from Eq. (4.17) and Eq. (18),  $p(z, \gamma)$  will dominate  $(z)_+$ , so

$$|p(z,\gamma)-(z)_{+}| \leq \frac{1}{4\gamma}$$
 (4.18)

From Eq. (4.12), we can insert  $||z|| = (z)_+ + (-z)_+$ 

$$\begin{aligned} \left| \|z\|_{1} - \|z\|_{\gamma} \right| &= |p(z,\gamma) + p(-z,\gamma) - ((z)_{+} + (-z)_{+})| \\ &\leq |p(z,\gamma) - (z)_{+}| + |p(-z,\gamma) - (-z)_{+}| \\ &\leq \frac{1}{4\gamma} + \frac{1}{4\gamma} = \frac{1}{2\gamma} \end{aligned}$$

$$(4.19)$$

Let's define  $||z||_{(1,\gamma)}$  as a smooth estimate of  $l_1$  norm function  $||z||_1$  for a vector  $z \in \mathbb{R}^n$  as:

$$\|\mathbf{z}\|_{(1,\gamma)} = \sum_{i}^{n} \|\mathbf{z}_{i}\|_{\gamma}$$

$$\|\mathbf{z}\|_{(1,\gamma)} - \|\mathbf{z}\|_{1} \le 2n \frac{1}{4\gamma} = \frac{n}{2\gamma}$$
(4.20)

Hence, we can conclude that:

$$\lim_{\gamma \to \infty} ||z||_{(1,\gamma)} = ||z||_1 \ \forall z \in \mathbb{R}^n \tag{4.21}$$

Let  $L: \mathbb{R}^n \to \mathbb{R}$  by any continuous loss function that is defined as  $f(z) = L(z) + ||z||_1$  and  $f_{\gamma}(z) = L(z) + ||z||_{(1,\gamma)}$ . If we define,  $\bar{z} = \underset{z}{\operatorname{argmin}} f(z)$  and  $\bar{z}_{\gamma} = \underset{z}{\operatorname{argmin}} f_{\gamma}(z)$ . By definition of f and  $f_{\gamma}$  and from Eq. (20), it can be concluded that.

$$\lim_{\gamma \to \infty} f_{\gamma}(\mathbf{z}) = f(\mathbf{z}) \ \forall \mathbf{z} \in \mathbb{R}^n$$
(4.22)

Using the fact  $f(\bar{z}) \le f(z) \forall z$ . In particular  $f(\bar{z}) \le f(\bar{z}_v)$ , then:

$$f(\bar{z}) \leq f(\bar{z}_{\gamma}) = L(\bar{z}_{\gamma}) + \|\bar{z}_{\gamma}\|_{1}$$

$$= L(\bar{z}_{\gamma}) + \|\bar{z}_{\gamma}\|_{1} + \|\bar{z}_{\gamma}\|_{(1,\gamma)} - \|\bar{z}_{\gamma}\|_{(1,\gamma)}$$

$$= (L(\bar{z}_{\gamma}) + \|\bar{z}_{\gamma}\|_{(1,\gamma)}) + (\|\bar{z}_{\gamma}\|_{1} - \|\bar{z}_{\gamma}\|_{(1,\gamma)})$$

$$= f_{\gamma}(\bar{z}_{\gamma}) + (\|\bar{z}_{\gamma}\|_{1} - \|\bar{z}_{\gamma}\|_{(1,\gamma)})$$

$$(4.23)$$

This implies that  $f(\bar{z}) - f_{\gamma}(\bar{z}_{\gamma}) \ge -\frac{n}{2\gamma}$  from Eq. (21), similarly  $(\bar{z}) - f_{\gamma}(\bar{z}_{\gamma}) \le \frac{n}{2\gamma}$ , hence proved that  $\lim_{\gamma \to \infty} f_{\gamma}(\bar{z}) = f(\bar{z})$ .

This can be elaborated further:

$$|f(\bar{z}_{\gamma}) - f(\bar{z})| = |f(\bar{z}_{\gamma}) - f(\bar{z}) - f_{\gamma}(\bar{z}_{\gamma}) + f_{\gamma}(\bar{z}_{\gamma})|$$

$$\leq |f(\bar{z}_{\gamma}) - f_{\gamma}(\bar{z}_{\gamma})| + |f_{\gamma}(\bar{z}_{\gamma}) - f(\bar{z})|$$

$$(4.24)$$

Hence it proved that  $\lim_{\gamma \to \infty} f(\bar{z}_{\gamma}) = f(\bar{z})$ . Furthermore, the L is strictly convex, it's proved that:  $\lim_{\gamma \to \infty} z_{\gamma} = \bar{z}$ .

Figure 4-2 Illustration of the error bounds of the  $l_1$  norm approximation for z > 0. The green line represents the mathematically proven upper boundary as defined in Eq. (4.16), while the dotted red line represents the real error between tanh and the discontinuous  $l_1$  norm. The error is highest near zero and diminishes as  $\gamma$  approaches infinity.

In Figure 4-3, the  $l_1$  norm estimated bounds for error while z < 0 the green line depicts the higher boundary as shown in Eq. (4.24), while, the dotted red line illustrates the original difference between the suggested  $l_1$  norm approx. and actual  $l_1$  norm. The error is highest near zero and diminishes as  $y \to \infty$ .

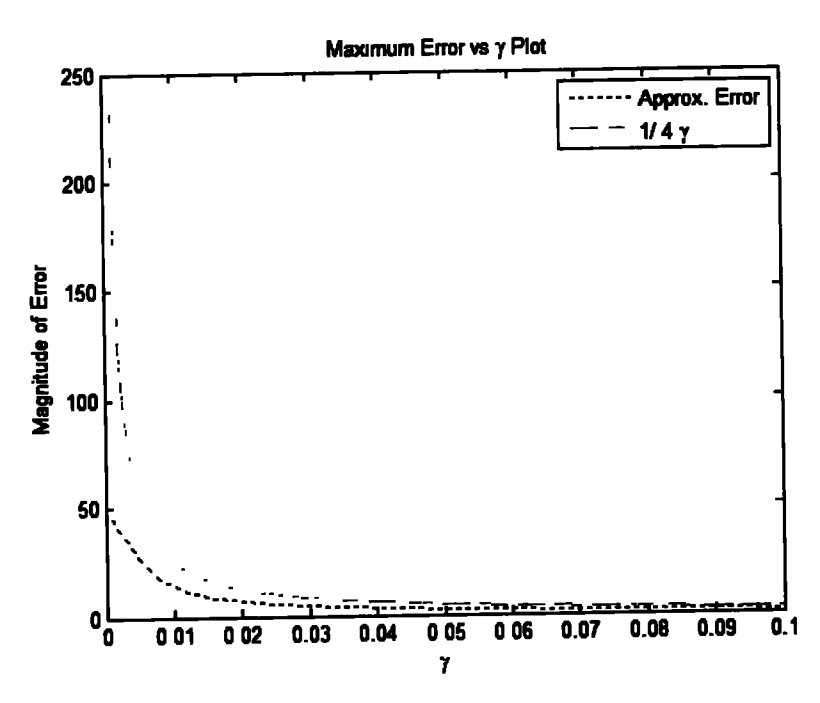


Figure 4-2: Illustration of the bound for the error of the  $l_1$  norm approx. for z > 0.

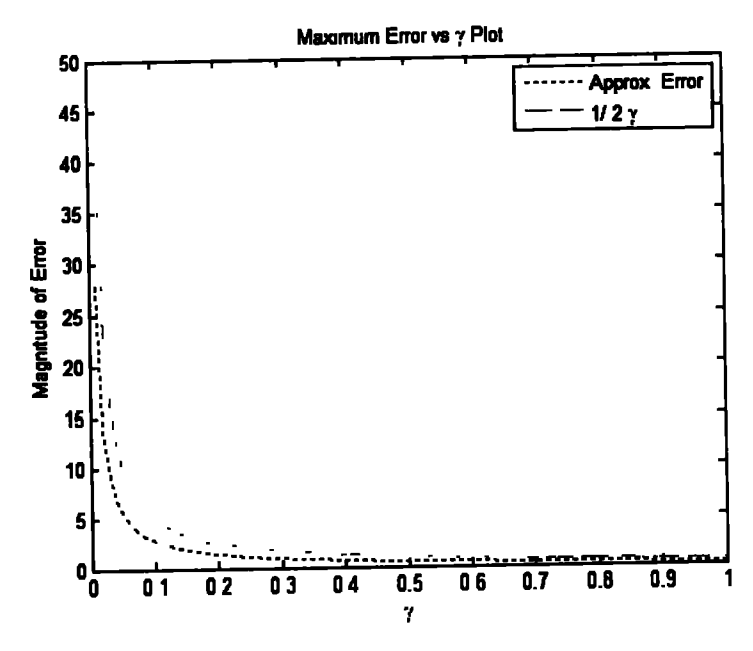


Figure 4-3:  $l_1$  norm estimation bounds for the error while z < 0.

## 4.4 The MAP Estimation for Proposed Thresholding Mechanism

The traditional approach of minimising the  $l_1$ -norm incorporates intrinsic soft thresholding [115]. However, the  $l_1$ -norm estimate using the tanh, thresholding process is not performed intrinsically. In [125], an alternative hard thresholding operator is introduced, which can be defined as follows:

$$S_{\beta}(z) = \begin{cases} z & |z| > \beta \\ 0 & otherwise \end{cases}$$
 (4.25)

In our approach, a novel thresholding function is employed that utilises the tanh. Consequently, the parameter  $\beta$  is important in managing the Gaussian distribution of the under-sampling noise [123]. The determination of the optimal value for  $\beta$  relies on the characteristics of the undersampling noise. Hence, we utilise the data-driven thresholding parameter  $\beta$ , as indicated by references [115, 126].

$$\beta = \frac{\sigma_v^2}{\sigma_z} \tag{4.26}$$

Assuming  $\sigma_z$  represents the standard deviation of the sparse signal and  $\sigma_v$  represents the standard deviation of the random noise due to undersampling.

To improve efficiency in various situations, various thresholding operators are presented by researchers [127-129]. The fundamental concept behind these operators is to map values near the origin to zero, while values farther apart from the origin are gradually reduced to zero.

The primary objective of the denoising technique is to obtain an estimation of the actual image based on a set of perturbed measurements, as illustrated in Eq. (4.27).

$$y = z + v \tag{4.27}$$

Here,  $y \in \mathbb{R}^n$  represents the image with noise,  $z \in \mathbb{R}^n$  is the actual signal and v is zero mean Gaussian noise with pdf described below:

$$p_{\boldsymbol{v}}(\theta) = \frac{1}{\sqrt{2\pi\sigma_{\boldsymbol{v}}^2}} exp\left(\frac{\|\theta\|_2^2}{2\sigma_{\boldsymbol{v}}^2}\right)$$
(4.28)

By taking the Wavelet transform of Eq. (4.27), we get:

$$q = s + v \tag{4.29}$$

Here, we have  $q = \Psi y$  representing the sparsity-promoting transform for the noisy image, and  $s = \Psi z$  representing the sparsifying domain for the actual image. Since the WT fulfils

the linearity property, the zero-mean Gaussian noise v, in WT, will remain unchanged. The MAP predictor of the random signal s is given by the following equation:

$$\hat{\mathbf{s}} = \max_{\mathbf{s} \in \mathbb{R}^n} p(\mathbf{s}|\mathbf{q}) \tag{4.30}$$

Applying Bayes' rule allows us to disregard p(q) since it is independent of s. Therefore, the MAP predictor can be expressed as follows:

$$\hat{\mathbf{s}} = \max_{\mathbf{s} \in \mathbb{R}^n} p(\mathbf{q}|\mathbf{s}) p_{\mathbf{s}}(\mathbf{s}) \tag{4.31}$$

The problem in Eq. (4.31) can be simplified further by taking  $p(q|s) = p_v(q-s)$ :

$$\hat{s} = \max_{s} [p_{v}(q-s)]p_{s}(s)$$

$$= \max_{s} [\ln p_{v}(q-s) + \ln p_{s}(s)]$$

$$= \max_{s} \left[ \ln \left\{ \frac{1}{\sqrt{2\pi\sigma_{v}^{2}}} exp\left( -\frac{\|q-s\|_{2}^{2}}{2\sigma_{v}^{2}} \right) \right\} + \ln p_{s}(s) \right]$$

$$= \max_{s} \left[ \ln \left\{ \left( \frac{1}{\sqrt{2\pi\sigma_{v}^{2}}} \right)^{n} exp\left( -\frac{\|q-s\|_{2}^{2}}{2\sigma_{v}^{2}} \right) \right\} + \ln p_{s}(s) \right]$$

$$= \max_{s} \left[ -\frac{\|q-s\|_{2}^{2}}{2\sigma_{v}^{2}} + f(s) \right]$$

Where  $f(s) = \ln p_s(s)$ . By differentiating the argument of Eq. (4.32) regarding s and setting the obtained value as 0, the MAP predictor can be estimated for the Wavelet contents for the noise-free signal by:

$$\frac{(q_i - \hat{s}_i)}{\sigma_v^2} + f'(\hat{s}_i) = 0, \quad 1 \le i \le n$$
 (4.33)

The PDF of biomedical images exhibits a higher concentration of values around the centre compared to a Gaussian distribution. As a result, the Laplacian distribution is more effective in estimating the distribution of Wavelet domain coefficients.

$$p_s(s_l) = \frac{1}{\sqrt{2}\sigma_v} exp\left(\frac{\sqrt{2}}{\sigma_v}|s_l|\right)$$
 (4.34)

gives  $f'(\hat{s}_i) = -\frac{\sqrt{2}}{\sigma} sig(\hat{s}_i)$ . Solving Eq. (4.34) results in

$$q_i = \hat{\mathbf{s}}_i + \sqrt{2}\,\operatorname{sig}(\hat{\mathbf{s}}_i) \tag{4.35}$$

Let  $\beta = \sqrt{2}\sigma_v^2$  and solve Eq. (4.35) for  $\hat{s}_i$  by formulating the nonlinear shrinkage:

$$\hat{s}_i = S_{\beta}(q) = max\{|q| - \beta, 0\}. sig(q)$$
 (4.36)

Eq. (4.36) can be further explained as:

$$S_{\beta}(q) \cong \begin{cases} sgn(q)(|q| - \beta) & |q| > \beta \\ 0 & otherwise \end{cases}$$
 (4.37)

This chapter presents a thresholding approach that is estimated by tanh. The tanh offers the advantage of the adjustable slope near the origin and is a function that is bounded, making it a preferable choice as an estimation for soft thresholding (ST). Consequently, the mathematical description of tanh-based ST is represented as:

$$S_{\alpha,\beta}(q) \cong \begin{cases} cz(\tanh(\alpha(|q|-\beta))) & |q| > \beta \\ 0 & \text{otherwise} \end{cases}$$
 (4.38)

The equation above includes a thresholding parameter,  $\beta$ , and a parameter  $\alpha$  that controls the shape of the tanh. When  $\alpha$  is closer to zero, Eq. (4.38) approximates the behaviour of a soft thresholding function. As  $\alpha$  approaches infinity, Eq. (4.38) transforms into a hard thresholding (HT) function, as depicted in Figure 4-4. The proposed algorithm initially employs an ST function that gradually transitions to an HT at higher iterations. This approach yields improved recovery in compared to traditional ST techniques [123]. In Figure 4-4 tanh-based thresholding, different values of  $\alpha$ , specifically  $\alpha = (2,4,8,16)$  are chosen. The choice of  $\alpha$  controls the trajectory of the ST curves. The suggested technique allows flexibility to change the slope as per the need of the certain application.

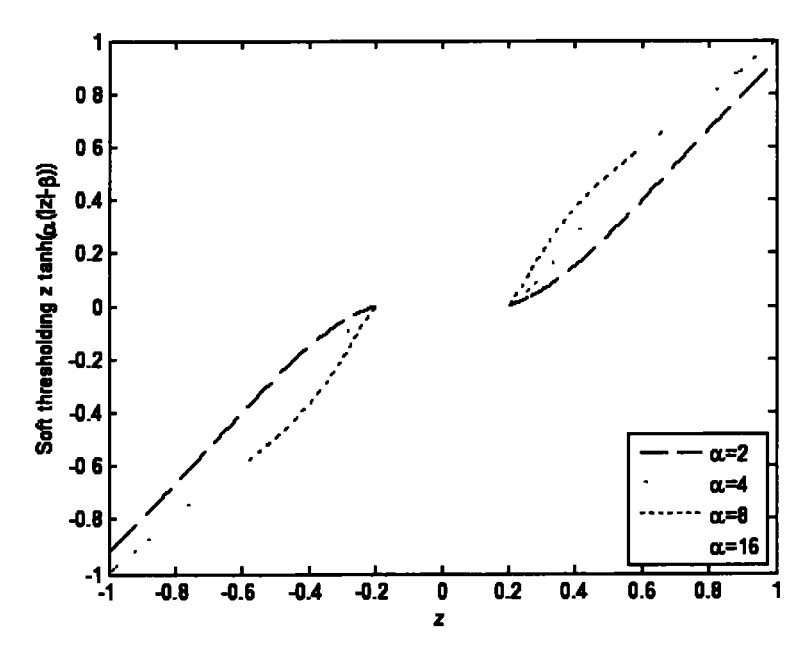


Figure 4-4: Different curves for various values of  $\alpha$ 

## 4.5 Proposed Algorithms

The proposed algorithm is described as Algorithm 4.1.

Algorithm 4.1: Recovery of k-sparse signal by proposed algorithm

```
Input:

Sensing matrix \mathcal{F}_u, measurement vector \mathbf{y} \in \mathbb{C}^m, parameters \gamma, \lambda and \beta
Initialise: A k — sparse vector \mathbf{\hat{x}} \in R^n as \mathbf{x}_0

for i=1,2,...,P:

Step No 1 (Sparse Transformation): \mathbf{z}_i = \Psi \mathbf{x}_i

Step No 2 (Gradient Computation): Evaluate \nabla f(\mathbf{z}_i) by Eq. (4.6)

Step No 3 (Solution Update): Calculate the update using Eq. (4.7).

Step No 4 (Shrinkage): Shrink by Eq. (4.38) i.e., \mathbf{\hat{z}}_{i+1} = S_{\beta}(\mathbf{z}_{i+1})

Step No 5 (Repeat): If the stopping criterion is met (stop), else go to step 1
```

## 4.6 Experimental Results and Discussions

To assess the effectiveness of our suggested method, experiments on three different types of data: 1-D k-sparse signals, CS MRI, and CC-MRI. In evaluating the algorithm's performance in the field of CC-MRI, we utilised the MRXCAT simulator. Quantitative and qualitative assessments were carried out to gauge the performance of our technique.

For quantitative evaluation, we employed several performance measures in this research article. First, we visually depicted the under-sampling artefacts to observe the improvement achieved by our algorithm. Additionally, we utilised the SSIM index to measure the similarity between the recovered images and the ground truth. The PSNR and RMSE were also calculated to provide further quantitative insights into the quality of the recovered images. By employing this comprehensive set of performance measures, we could thoroughly evaluate and demonstrate the efficacy of our proposed technique in various scenarios.

#### 4.6.1 1-D Sparse Signal Recovery

The suggested method is employed to recovers a 1-D k-sparse signal (z). In this experiment, a random k-sparse signal of length n = 512 is generated in MATLAB, where non-zero elements are randomly generated with K = 85. To compressively sample the z,

a random measurement matrix  $A \in \mathbb{R}^{256x512}$  is used, resulting in only m = 256 measurements.

Figure 4-5 illustrates the achieved fitness of IST techniques and the suggested method. The proposed method demonstrates a fast decrease in loss function in comparison with IST.

Figure 4-6 showcases the impact of sparsity on reconstruction success by both the IST method and the suggested method. Remarkably, the suggested method outperforms the soft thresholding technique even at higher sparsity levels.

In Figure 4-7, the effectiveness of the proposed method in accurately recovering the sparse signal is evident, while the soft thresholding technique struggles to achieve the same level of accuracy.

To further evaluate the accuracy, metrics like SNR, MSE, and correlation were used, as presented in Table 4-1. The suggested method performs more in all these measures than the IST method. In terms of computation time, the proposed algorithm takes 1.57 seconds, slightly longer than the conventional IST method, which takes 1.34 seconds.

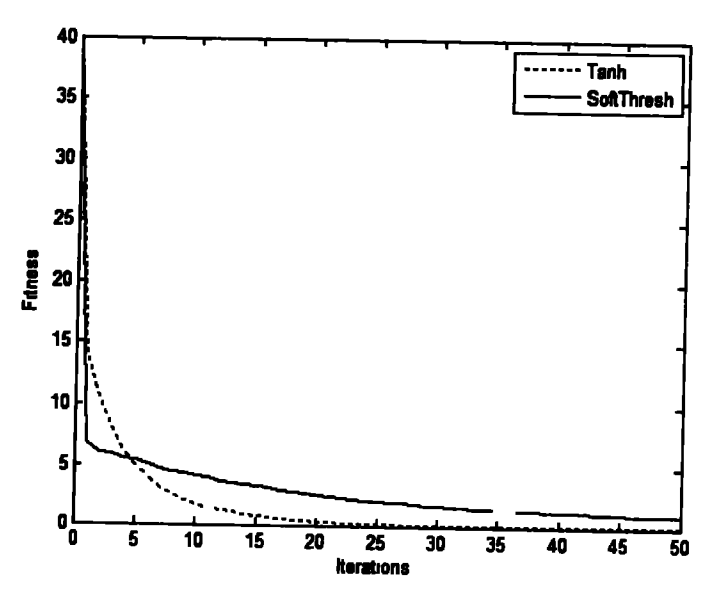


Figure 4-5: Fitness comparison of proposed and soft thresholding technique.

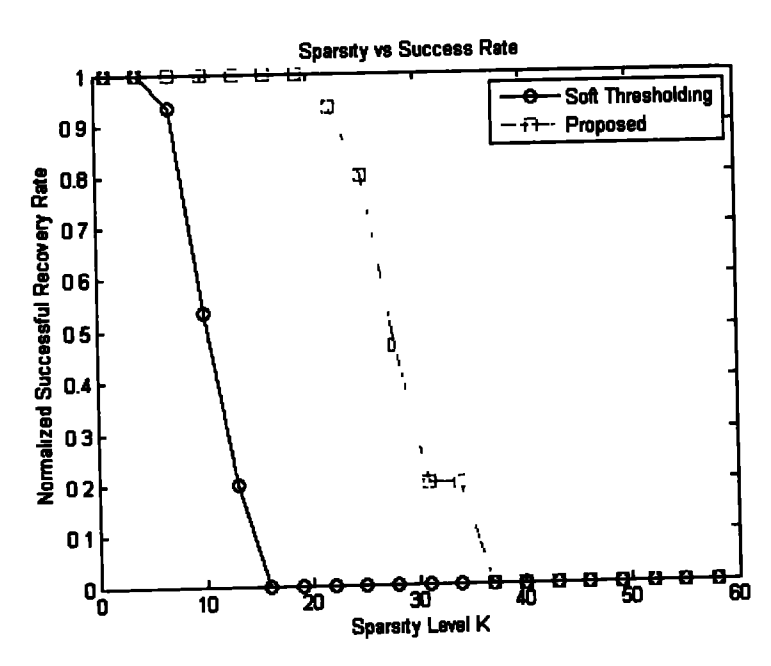


Figure 4-6: The effects of the sparsity of the proposed and soft thresholding technique.

Table 4-1: Accuracy of recovery of 1-D sparse signal by the proposed method is evident

<b>Performance Metrics</b>	Soft Thresholding	Proposed Algorithm
MSE	1.00 x 10 - 2	1.61 x 10 - 4
Fitness	0.8664	0.0224
SNR	12.6712	30.6259
Correlation	0.9787	0.9995

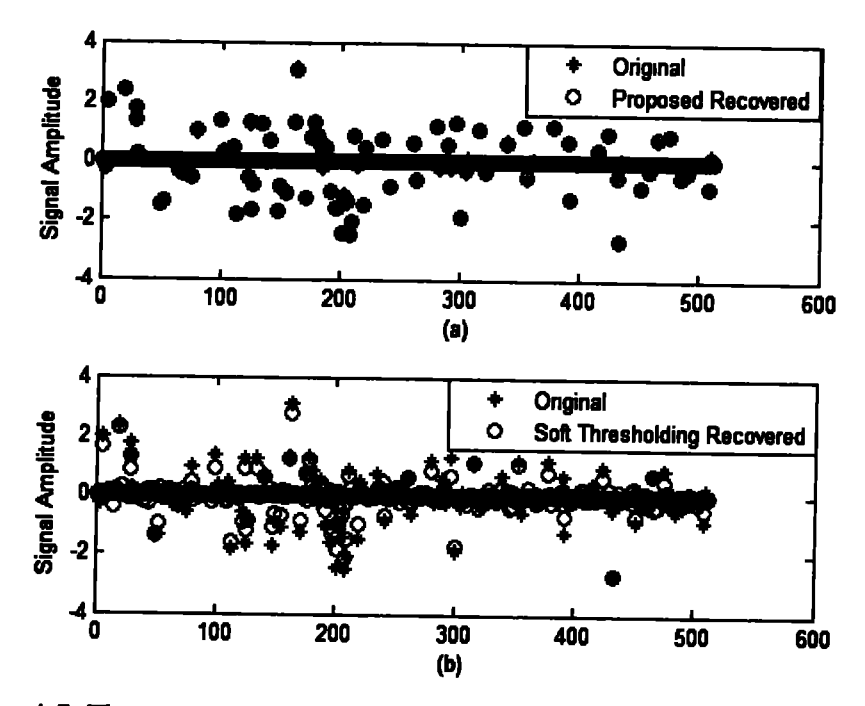


Figure 4-7: The sparse signal recovered using the proposed algorithm and the soft thresholding method.

## 4.6.2 2-D CS MRI Recovery

Random undersampling during CS MRI results in noise-like artefacts in the sparsifying domain. When dealing with k-space encoded biomedical imaging, such as MRI, the linear methods i.e., ZF or LR produces artefacts like Gaussian noise. The noise generated by subsampling depends on the under-sampling masks [99].

To reconstruct an image, CS MRI reconstruction transforms into an image noise removal problem, drawing a comparison between CS and noisy images. Initially, recovering the actual image involves estimating the noise, accomplished through the MAP estimation. The suggested method is reconstructing a 2-D CS real human brain MRI with dimensions  $256 \times 256$ . The original MRI was acquired through fully sampled k-space data. 1.5 Tesla GE – HDxt – MRI scanner at St. Mary's Hospital, London, England. The MRI is undersampled by retaining only 25% of the k-space data.

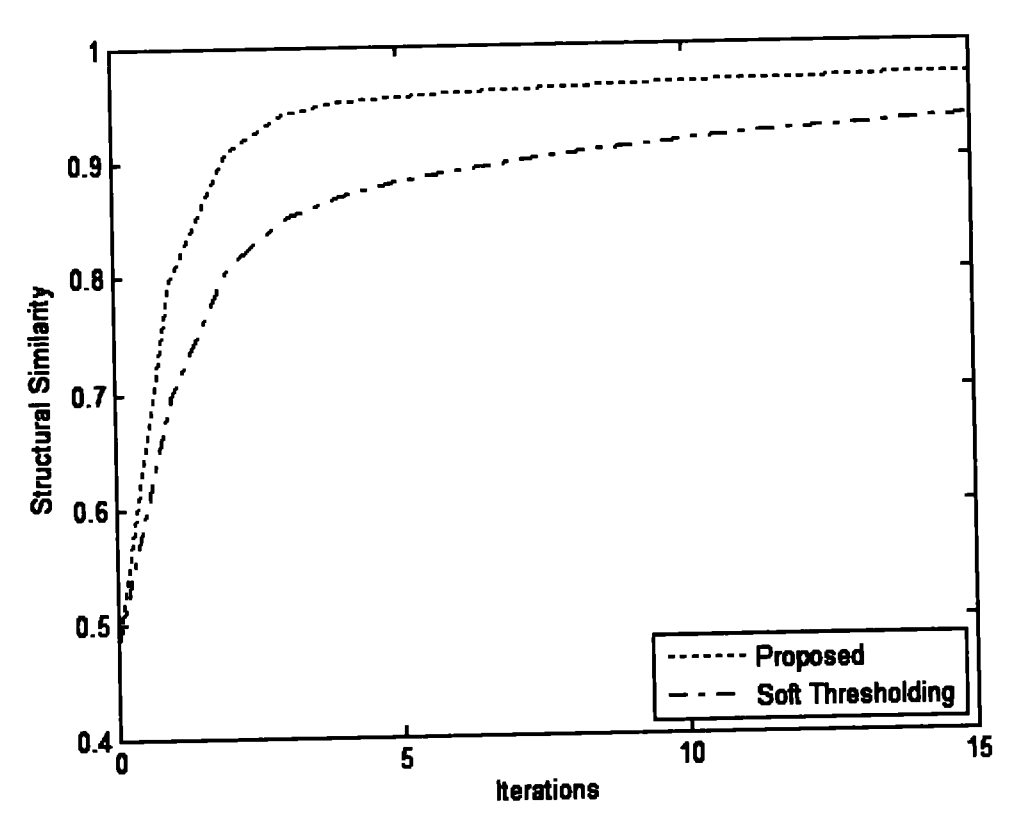


Figure 4-8: The SSIM between the soft-thresholding and proposed algorithm.

Figure 4-8 depicts the proficiency of the suggested algorithm in terms of SSIM. The suggested technique exhibits significantly better SSIM in comparison to the IST technique.

Figure 4-9 displays the achieved PSNR by the suggested technique. The proposed method outperforms the soft thresholding method in terms of PSNR.

Figure 4-10 depicts the subjective analysis of MRI: (a) the original 2D MRI of the human brain, (b) the recovered 2D MRI using conventional IST, (c) the 2D Brain MRI reconstructed from the under-sampled k-space data, (d) the difference between the ground truth image and the IST recovery, and (e) the error between the proposed recovery method image and the actual image. To enhance visibility, the scale of the difference is amplified by a factor of 1000.

Table 4-2 compares the performance of the conventional IST method and the suggested technique across various CR, ranging from 5% to 50% sub-sampling of the 2-D MRI. The results demonstrate that the suggested technique consistently outperforms the conventional soft thresholding method on performance metrics like SSIM and PSNR at different CR.

Table 4-3 comprehensively compares the performance between the proposed algorithm and IST in various performance metrics. After 15 iterations of IST and the suggested technique, the results demonstrate that the proposed method consistently achieves superior outcomes compared to IST.

In summary, both the visual representations in Figure 4-8 and Figure 4-9, along with the quantitative analysis in Table 4-2: The performance of both algorithms against varying CR., confirms that the proposed method outperforms the soft thresholding technique in terms of various performance measures.

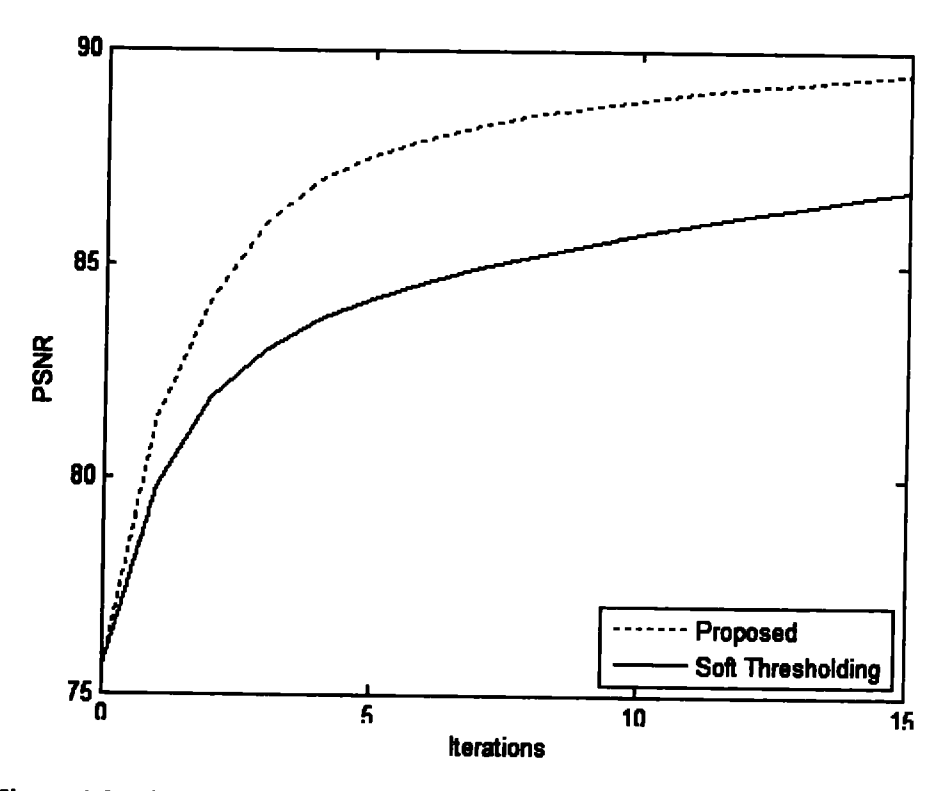


Figure 4-9: The correlation between the proposed *tanh* and the soft thresholding algorithm.

Table 4-2: The performance of both algorithms against varying CR.

Compression Ratio	Soft Thresholding		<b>Proposed Algorithm</b>	
	SSIM	PSNR	SSIM	PSNR
5 %	0.6843	75.9056	0.7048	76.1609
10%	0.7786	78.9320	0.8175	79.6580
20%	0.8994	82.0316	0.8472	83.7628
30%	0.9407	87.3535	0.9790	91.1620
40%	0.9724	91.2540	0.9920	96.1281
50%	0.9884	95.4245	0.9955	99.5496

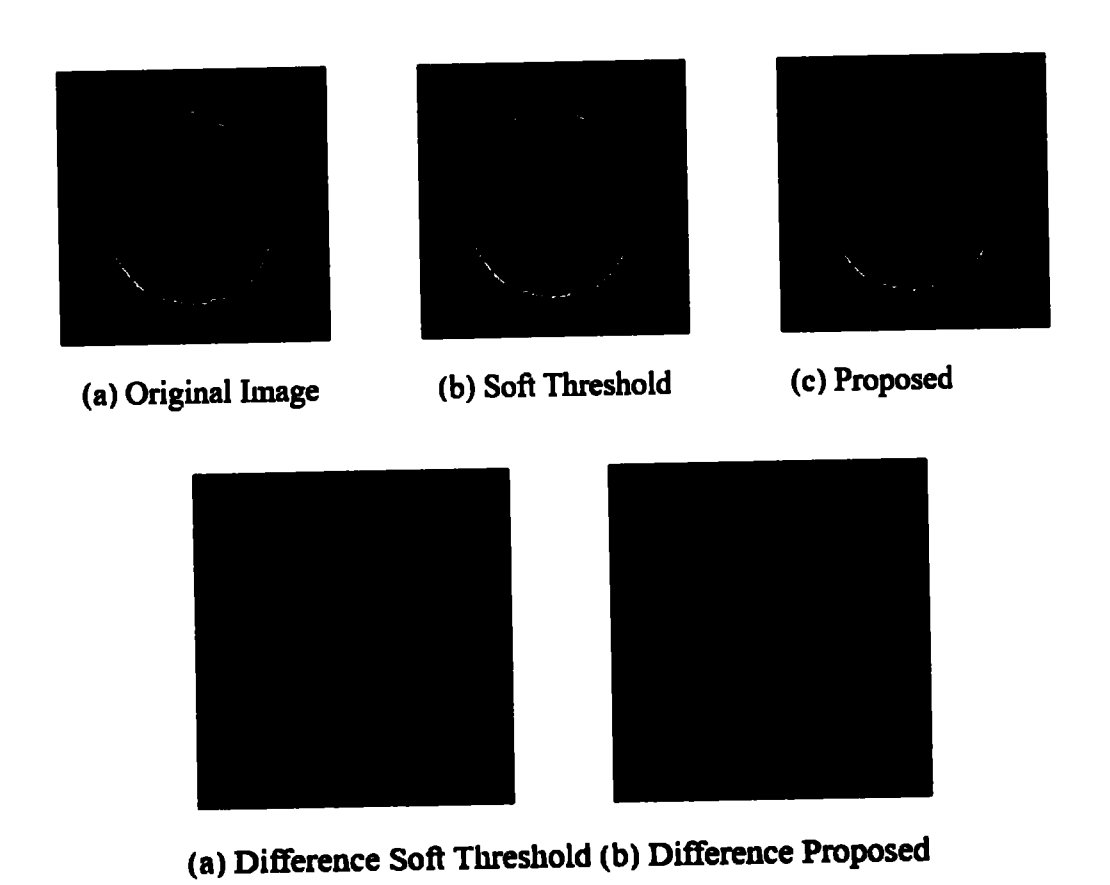


Figure 4-10: Depicts subjective analysis of MRI of recovered images

Table 4-3: The performance of various sparsity transforms is compared.

Performance Metrics	Soft Thresholding	Proposed Algorithm  0.73 x 10 - 4	
MSE	1.38 x 10 - 4		
PSNR	86.7195	89.4497	
ISNR	28.3832	31.1135	
SSIM	0.9346	0.9711	
SNR	26.0298	28.7491	
Correlation	0.9980	0.9989	

## 4.6.3 CS Cardiac Cine MRI Recovery

The suggested method is used for MRXCAT, which generates undersampled CC-MRI data acquired during breath-holding. The MRXCAT parameters were set as follows: recovery image size of  $256 \times 256$  with 24 cardiac phases, and an image resolution of  $1 \times 1 \times 1mm^3$ . The acquisition parameters for MRXCAT include a  $T_r$  of 3ms and  $T_E$  of 1.5ms. The proficiency of the suggested technique is evaluated using five different acceleration rates: R = (2, 4, 8, 12, 20).

For in vivo data, the values for different parameters are recovered matrix with dimension 256  $\times$  256, 25 cardiac phases, and FOV of 375mm. The TE is set to 1 ms,  $T_R$  is set to 3 ms, and the flip angle is 600. The proposed method is evaluated using the same five acceleration rates: R = (2, 4, 8, 12, 20).

The recovered MR images are compared to actual CC-MRI, depicted in Figure 4-11, here CC-MRIs are presented: (a) Short axis CC-MRI with an original diastolic frame, (b) The sparse representation CC-MRI diastolic frame using the temporal FFT  $(\Psi)$ , (c) Another sparsifying domain for CC-MR image (diastolic frame) by TV transform  $(\Psi)$ . All image reconstructions are performed using the proposed algorithm in MATLAB.

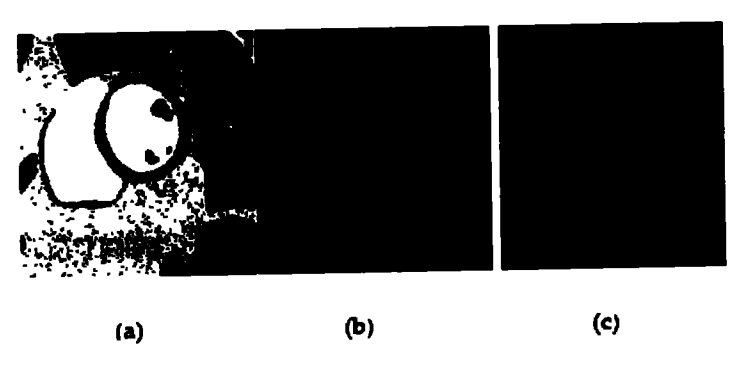


Figure 4-11: Recovered cardiac cine MRI with different sparsifying transforms

To assess the efficacy of the suggested method, the MRXCAT simulator software is used. This software is specifically developed for evaluating the performance of recovery algorithms in CC-MRI. Using MRXCAT, the proficiency of our suggested method is examined both objectively and subjectively.

This chapter employed various performance measures, including visual depictions of under-sampling artefacts, SSIM, PSNR, and RMSE.

For qualitative evaluation, we experimentally presented the reconstructed diastolic and systolic images using different (R=2,4,8,12,20). Additionally, the performance of the suggested technique was quantitatively assessed using PSNR, RMSE, and SSIM. An assessment was also conducted between the proposed and traditional IST methods.

In Figure 4-11, the performance of various sparsity transforms is compared based on the MSE in the sparse representation. Specifically, it is observed that the temporal FFT outperforms other sparsity transforms in the context of cardiac cine MRI.

Figure 4-12 illustrates the efficiency of the suggested method at different R in comparison to the IST method. The 1<sup>st</sup> column displays the diastolic images of CC-MRI at different R, while the second column represents the systolic frames of cine MRI. The upper row shows the findings of the IST method, whereas the lower row showcases the estimated images of the proposed method. In Figure 4-12 (a) A comparison between the suggested technique (lower row) and IST (upper row) at an R of 2. (b) The proficiency of the suggested technique at an R of 4, with an arrow indicating the presence of artefacts. (c) Results were obtained from both algorithms at an acceleration rate of 8, where the artefacts due to sub-sampling are more apparent in the IST results, as highlighted by an arrow. (d) Results were obtained when the R is set at 12, with both techniques exhibiting artefacts. However, these artefacts are more prominent in the IST results, as indicated by an arrow.

(e) A comparison between the degraded image quality of the IST and the proposed method, particularly highlighting the dominance of sub-sampling artefacts in the traditional IST results when the acceleration rate R is set to 20.

Table 4-4: Performance analysis of various sparsifying transform

<b>Acceleration Rate</b>	Spatial Domain	Total Variation	Temporal FFT
2	0.1096	0.1123	0.0728
4	0.2321	0.1849	0.0848
8	0.2810	0.2438	0.0948
12	0.3533	0.2684	0.1043
20	0.4756	0.2982	0.1150

The performance of various sparsity transforms is compared based on the MSE in the sparse representation. Specifically, it is observed that the temporal FFT outperforms other sparsity transforms in the context of cardiac cine MRI. The results show the squared errors averaged between the recovered and actual elements in sparse representation. The suggested technique, which utilises the *tanh* based approx. achieves notable accuracy in the FFT compared to other sparse representations. Specifically, at higher R, the proposed technique based on the tangent hyperbolic function demonstrates significantly improved recovery of compressed sensing (CS) images.

To quantitatively evaluate the recovered images, the Structural Similarity Index (SSIM) was used to compare the suggested method with the IST algorithm. Figure 4-13 demonstrates the efficiency of the suggested method using the SSIM index, showing a gradual degradation in SSIM as the acceleration rate increases compared to the IST algorithm, while the undersampled images exhibit noticeably poor quality.

At low R, the proficiency of the suggested method, and IST are comparable. However, as the R increases, it is apparent that IST-based recovery deteriorates more than the proposed method.

Figure 4-14 shows the iterations required for image recovery in both methods. The suggested technique achieves the solution in just 6 epochs, whereas, the IST method took 10 epochs to achieve near perfect solution. The findings here demonstrate the proficiency of the suggested method using data-consistency constraints.

To quantitatively assess the efficiency of our recovery algorithm, the recovery using PSNR at different R = (2, 4, 8, 12, 20) is examined. A comparison is made between our proposed technique and the traditional IST technique.

Figure 4-15 illustrates the efficiency of our proposed technique at various acceleration rates compared to the IST algorithm. The red line represents the results obtained from our method at different acceleration rates and the blue line depicts the PSNR values for the soft thresholding method and the undersampled data.

Performance analysis of the suggested technique and the IST method is presented in Figure 4-16 to examine the efficiency of the recovered frames by vivo dataset. The comparison is demonstrated across five different R = (2, 4, 8, 12, and 20). However, at higher R, the degrading artefacts in the IST reconstructed frames become further pronounced relative to the suggested method, as shown by arrows. In part (a) of the figure, the suggested method in comparison to IST at an R = 2, with the suggested method shown in the bottom row and IST in the top row. Part (b) displays the efficiency of the proposed method at an R of 4, with an arrow indicating the artefacts. Part (c) illustrates results at R = 8, where the artefacts because of sub-sampling gradually become pronounced in the IST findings, as indicated by an arrow. Part (d) shows the findings at R = 12, showing artefacts present in both techniques, but more prominent in IST as indicated by an arrow. Part (e) demonstrates the considerably low-quality image of IST when compared to the suggested method, particularly emphasizing the dominance of sub-sampling artefacts in the conventional IST results when the R = 20.

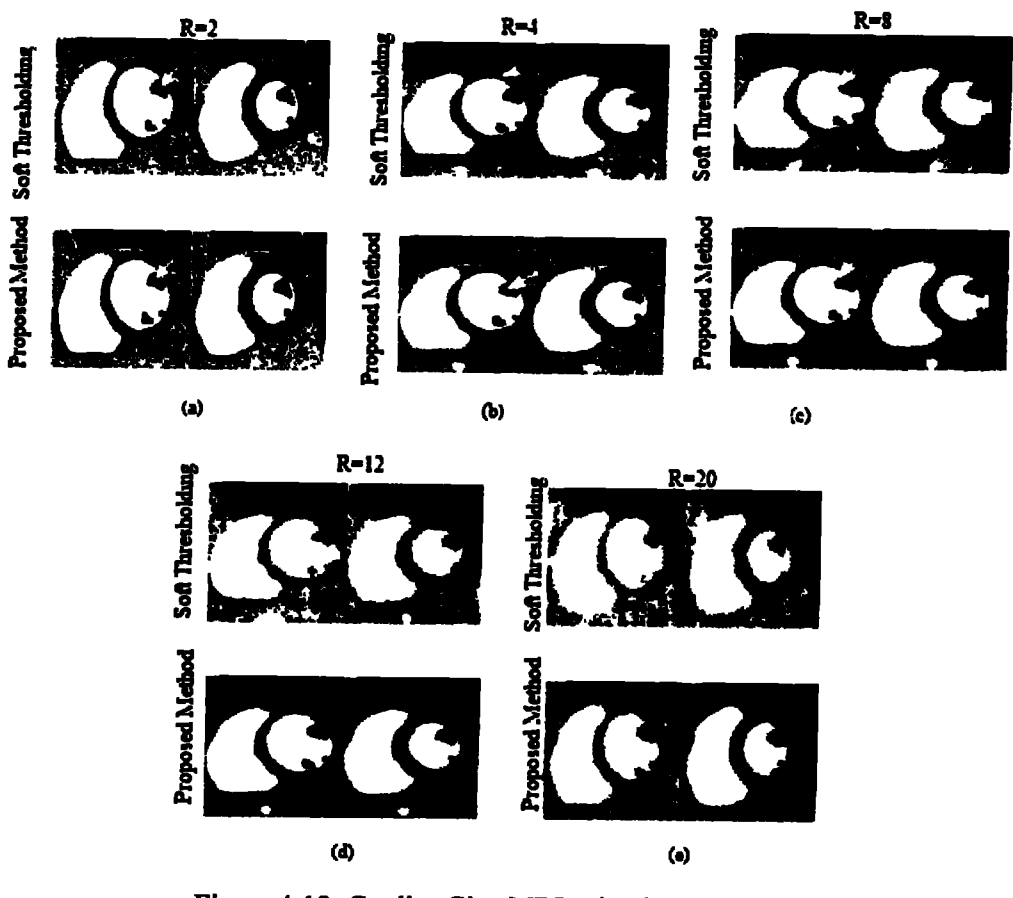


Figure 4-12: Cardiac Cine MRI using both algorithms

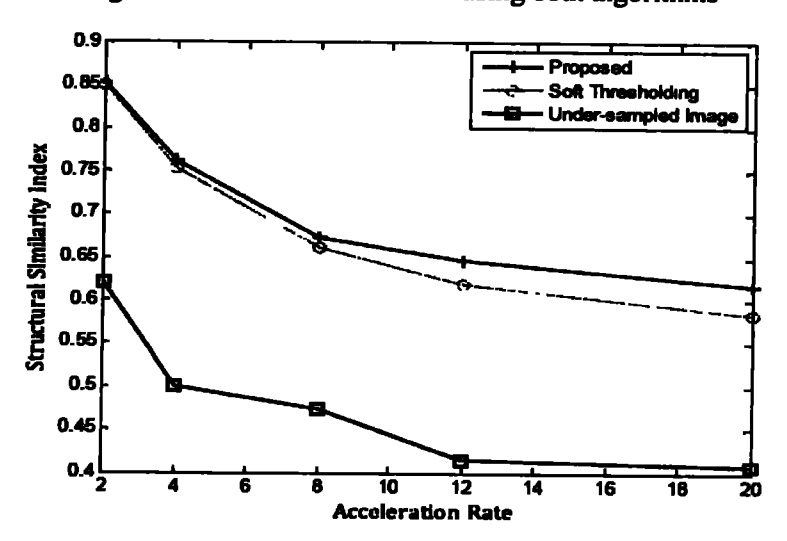


Figure 4-13: SSIM attained by various techniques at different acceleration rates

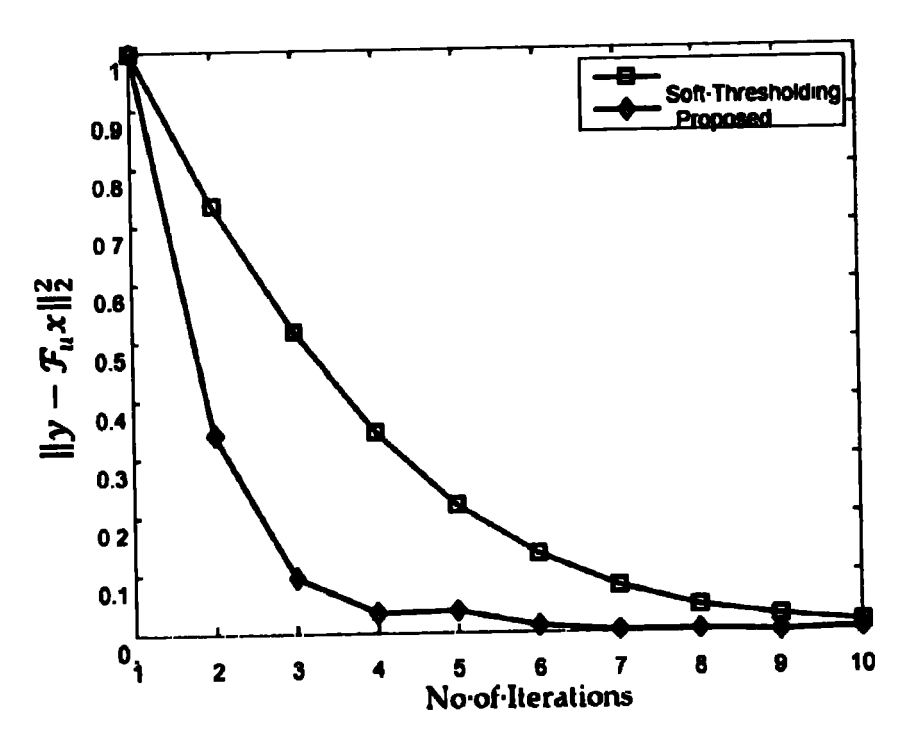


Figure 4-14: Fitness achieved by both methods for recovery of cardiac cine MRI

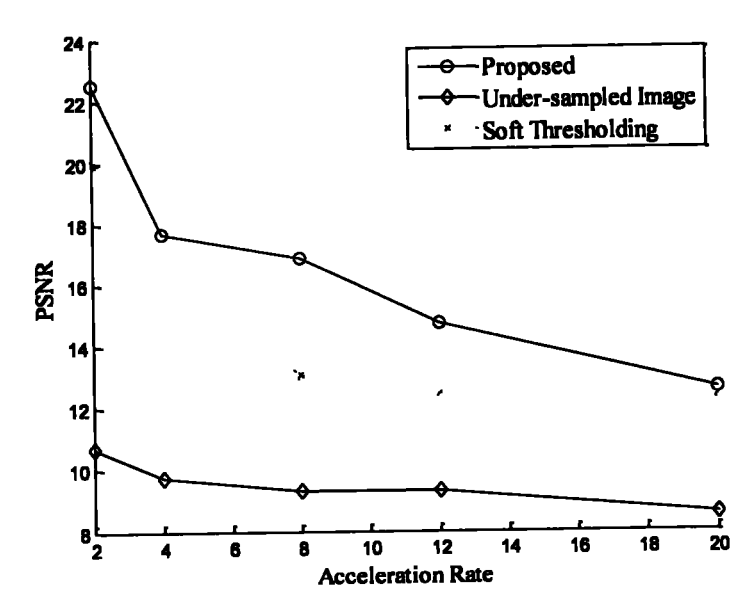


Figure 4-15: Our method outperforms the soft thresholding method in terms of PSNR at all acceleration rates.

Table 4-5: The performance comparison of conventional IST with proposed in terms of RMSE.

	Accelerat ion Rates	Undersampled image	Iterative Soft Thresholding	Proposed Method
2   4   8   12   20	2	0.081	0.0365	0.0353
	4	0.1218	0.0472	0.0372
	8	0.1498	0.0702	0.0419
	12	0.1583	0.0775	0.0485
	20	0.1782	0.0941	0.0606
In vivo Data	2	0.085	0.0099	0.0056
	4	0.106	0.0241	0.0172
	8	0.1170	0.0495	0.0206
	12	0.120	0.0567	0.0338
	20	0.1398	0.0585	0.0551

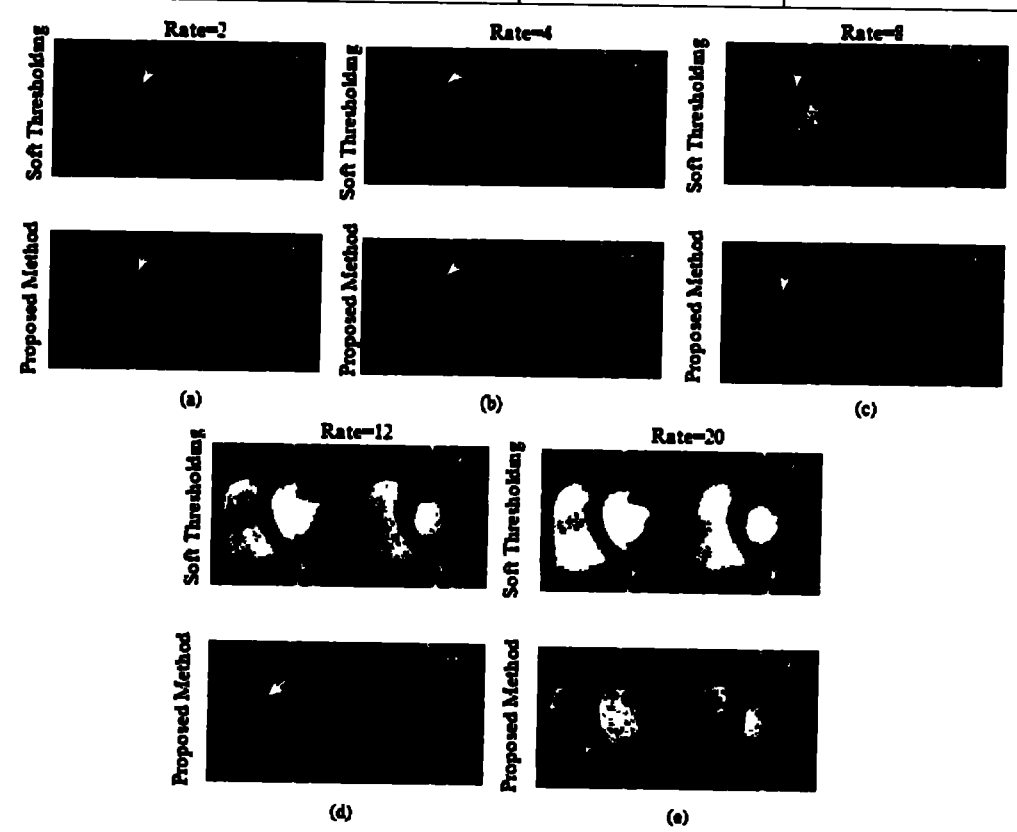


Figure 4-16: In real vivo data simulation results

## 4.7 Conclusion

This chapter proposed an innovative CS recovery algorithm for k-sparse signals and MRI. The suggested method has been tested in various scenarios, including 1-D k-sparse signals, 2-D MRI, and CC-MRI. The proposed technique introduces a tanh-based smooth estimate of the non-differentiable  $l_1$ -norm and the shrinkage method, resulting in improved performance compared to the conventional IST algorithm. Quantitative analysis based on several metrics demonstrates the superiority of our method in recovering sparse signals and MR images. Qualitative observations further highlight significant improvements, particularly at higher R, in the proposed method for CC-MRI.

#### **CHAPTER 5**

# CS MRI RECOVERY USING COMBINED SMOOTH $l_0$ AND $l_1$ RECOVERY

In this chapter, a novel method is proposed that combines smooth approximations of the  $l_0$  norm and  $l_1$  norm (SL01). The suggested approach introduces differentiable functions as smooth approximations, enabling the use of methods to solve  $l_0$  norm and  $l_1$  norm minimisation problems that involve gradient evaluations. To evaluate the proficiency of the SL01 algorithm, it is tested in recovering a 1-D signal and 2D MR image. The gradient ascent algorithm is deployed to reconstruct the k-sparse signal using the proposed algorithm. The performance of the SL01 is evaluated against smooth approximations of the  $l_0$  norm and  $l_1$  norm (SL01) in terms of metrics, such as SNR and MSE. The comparisons reveal that the proposed algorithm outperforms the smooth  $l_0$  norm approximation (SL0) and smooth  $l_1$  norm approximation (SL1) in terms of efficiency and accuracy in recovering compressively sampled sparse signals. Overall, the research demonstrates that the smooth approximations of the  $l_0$  norm and  $l_1$  norm yields a more efficient and effective method for recovering compressively sampled sparse signals, as evidenced by the comparative analysis using SNR and MSE metrics.

#### 5.1 Introduction

The sampling of acquired data in the CS framework is straightforward, but recovering a signal from CS measurements poses computational challenges due to its ill-posed nature. There can be infinitely many solutions to choose from. The CS framework has a special interest in the sparsest possible solution. Various techniques are developed for the reconstruction of sparse signals from undersampled data. The Basis Pursuit (BP) algorithm proposed in [92], replaces the non-convex  $l_0$ -norm with its convex approximation, the  $l_1$  norm. This substitution results in an analytically solvable convex optimisation problem, but the  $l_1$  norm gradient can't be evaluated origin. Consequently, the solutions that involve derivatives in loss function are not applicable to minimise  $l_1$ -norm problems [123].

Furthermore, BP can be ineffective for large datasets such as biomedical images, because of computational cost.

The IST methods have emerged as efficient computational techniques for recovering CS images to address these challenges. These algorithms employ matrix multiplications and shrinkage operations and minimise mixed  $l_1$   $l_2$  norms-based minimisation problems, making them suitable for large signals and images. By leveraging IST algorithms, we can overcome the limitations associated with the non-differentiability of the  $l_1$ -norm and the computational complexity of the BP algorithm, enabling more efficient recovery of sparse signals in CS applications.

In the decoding process of compressive sensing (CS), the objective is to efficiently reconstruct a k-sparse signal x from the dictionary matrix  $\Phi$  and observations vector y. This task of accurately recovering a CS k-sparse signal using limited measurements poses a challenge in CS decoding due to computational cost [4, 78]. The size of the sensing matrix  $\Phi$  is such that  $M \ll N$ , resulting in an under-determined system. This means that there are fewer equations than unknowns, leading to infinitely many potential solutions. Solving this under-determined system of linear equations alone will not yield the desired sparse solution, which is crucial in k-sparse signal reconstruction.

The optimisation problem defined in Eq. (5.1) must be solved to achieve sparsity in the estimated recovered signal. This optimisation problem involves finding the sparsest solution by promoting sparsity through the  $l_1$ -norm regularisation term. By solving this optimisation problem, we can obtain a solution that satisfies the under-determined system of linear equations and exhibits sparsity, thus fulfilling the goal of sparse signal recovery in CS.

minimize 
$$\|\mathbf{z}\|_0$$
 subject to  $\Phi \mathbf{z} = \mathbf{y}$  (5.1)

In the context of signal sparsity, the  $l_0$ -norm of a signal z, denoted as  $||z||_0$ , represents the count of non-zero components in the signal. Mathematically, it can be defined as the number of non-zero elements in the vector  $z = \{z_j\}_{j=1}^n$ . To incorporate this concept of sparsity into the optimisation problem, we can rewrite the  $l_0$ -norm in terms of an indicator function. The indicator function, denoted as r(i), is a mathematical construct that evaluates whether a certain condition is met. In this case, it determines whether the  $i^{th}$  element of the signal z is non-zero. By using the indicator function, the  $l_0$ -norm can be expressed as

the sum of the indicator function. By summing up the values of the indicator function for all elements of the signal, we obtain the count of non-zero components, representing the  $l_0$ -norm of the signal. This formulation allows us to quantify the sparsity of a signal in terms of the number of non-zero elements, providing a mathematical representation that guides the optimisation process towards finding the sparsest solution.

$$r(i) = \begin{cases} 1 & i \neq 0 \\ 0 & i = 0 \end{cases}$$
 (5.2)

$$\|\mathbf{z}\|_{0} = \sum_{i=1}^{n} r(z_{i})$$
 (5.3)

The  $l_0$  norm, as defined in Eq. (5.3), is a non-differentiable function. This means that it lacks a defined derivative at certain points, making it challenging to use gradient-based optimisation techniques.

Moreover, the  $l_0$  norm, as defined in Eq. (5.3), violates the homogeneity property of a norm. The homogeneity property states that scaling a vector by a constant should proportionally scale its norm. However, the  $l_0$  norm does not adhere to this property since total elements that are non-zero are counted, rather than considering their magnitudes.

Due to these properties, finding the solution to the  $l_0$ -norm optimisation problem becomes a non-tractable problem, meaning that it is computationally infeasible to solve directly. This non-tractability poses significant challenges when attempting to recover sparse signals or solving under-determined systems of equations in compressive sensing and sparse signal recovery applications.

The optimisation problem defined by equation (2) can be seen as an  $l_1$ -norm minimisation problem [2]. In this problem, the goal is to minimise the  $l_1$ -norm of the signal subject to the constraint imposed by the sensing matrix  $\Phi$  and measurements vector y.

The  $l_1$ -norm minimisation problem aims to find the solution that has the smallest  $l_1$ -norm among all solutions that satisfy the given constraints. This approach promotes sparsity in the solution by encouraging a larger number of zero or near-zero components in the signal. By framing the problem as an  $l_1$ -norm minimisation problem, it becomes tractable and amenable to efficient optimisation techniques. This contrasts with the non-tractable nature of the  $l_0$ -norm optimisation problem, which suffers from discontinuity and lack of differentiability. The  $l_1$ -norm minimisation approach has been widely adopted in

compressive sensing and sparse signal recovery due to its computational tractability and its ability to recover sparse solutions from under-determined systems of equations [4].

minimize 
$$\|\mathbf{z}\|_1$$
 subject to  $\Phi \mathbf{z} = \mathbf{y}$  (5.4)

The  $l_1$ -norm minimisation approach plays a significant role in promoting sparsity within a solution. By minimising the  $l_1$ -norm, the optimisation problem encourages a greater number of zero or near-zero components in the solution, effectively promoting sparsity. The optimisation problem defined by Eq. (5.4) is a convex problem, which means it possesses desirable mathematical properties that facilitate efficient solution finding. Convex problems can be solved using linear programming techniques, making them computationally tractable.

However, while  $l_1$ -norm minimisation is convex and can be solved using linear programming, it exhibits high computational complexity, especially when applied to high-dimensional datasets such as biomedical images. As the dimensionality of the dataset increases, the computational burden grows, leading to challenges in terms of time and resources required for the optimisation process. The high computational complexity of  $l_1$ -norm minimisation in high-dimensional datasets has prompted the exploration and development of alternative algorithms and techniques that can address this challenge and provide more efficient solutions for sparse signal recovery and compressive sensing applications [12, 130].

The unconstrained form of Eq. (5.4), incorporating the Lagrangian multiplier  $\lambda$ , can be expressed as follows:

$$minimize (\|\mathbf{y} - \mathbf{\Phi}\mathbf{z}\|_2^2 + \lambda \|\mathbf{z}\|_1)$$
 (5.5)

The mixed SL01 optimisation problem, as described in Eq. (5.5), is widely recognized as k-sparse. This approach is commonly known as IST algorithms. By iteratively applying the shrinkage operation, the IST methods progressively converge towards a solution that exhibits sparsity in the signal. These algorithms have been widely adopted due to their computational efficiency and effectiveness in recovering sparse signals, particularly in high-dimensional scenarios such as compressive sensing and sparse signal recovery applications.

The regularizing  $\lambda$  as a thresholding parameter, acting as the Lagrangian multiplier, is critical in determining the level of sparsity in the estimated solution of the CS recovery

problem. By adjusting the value of  $\lambda$ , one can control the trade-off between sparsity and accuracy in the recovered signal. A higher value of  $\lambda$  encourages a sparser solution by imposing stricter constraints on the magnitudes of the signal coefficients, resulting in more coefficients being set to zero. Conversely, a lower value of  $\lambda$  allows for a less sparse solution, enabling more non-zero coefficients in the estimated signal. The appropriate choice of  $\lambda$  depends on the specific application and desired balance between sparsity and fidelity in the recovered signal. It is often determined through cross-validation or other model selection techniques to achieve an optimal level of sparsity while preserving the essential features of the signal.

## 5.2 Proposed SL01 Algorithm

This section introduces a new approach that combines SL0 and SL1 to enhance the recovery of sparse signals. The SL01 algorithm leverages the complementary nature of both the smooth  $l_0$  norm and smooth  $l_1$  norm, which results in faster convergence compared to using either of them alone. By combining these two norms, the algorithm benefits from the advantages of the smooth  $l_0$  norm in promoting sparsity while also harnessing the advantages of the smooth  $l_1$  norm in facilitating differentiable optimisation. The hybrid approach strikes a balance between encouraging sparsity and enabling efficient optimisation, leading to improved performance in sparse signal recovery tasks. The proposed algorithm offers a promising solution for effectively addressing the challenges of recovering sparse signals in various applications. The SL01 aims to minimisation of the loss function defined by Eq. (5.7) that combines the  $l_0$  and  $l_1$  norm penalty simultaneously.

minimize 
$$f(z) = \frac{1}{2} ||y - \Phi \Psi^{H} z||_{2}^{2} + \alpha ||z||_{1} + \beta ||z||_{0}$$
 (5.6)

The non-differentiable  $l_0$  norm penalty, as defined in Eq. (5.2), can be substituted with its smooth and differentiable approximation, as defined in Eq. (5.7):

$$g_{\gamma}(z_j) = \exp\left(\frac{z^2}{2\gamma^2}\right) \tag{5.7}$$

The proposed function's parameter, which regulates the Gaussian kernel's width, is shown here. The function in Eq. (5.7) can be thought of as the indicator function's inverse, i.e.

$$\lim_{\gamma \to 0} g_{\gamma}(z_j) = \begin{cases} 1 & z_j = 0 \\ 0 & z_j \neq 0 \end{cases} \tag{5.8}$$

The function must fulfil two requirements to justify the  $g_{\gamma}(z_j)$  for the approximation of the  $l_0$ -norm.

Property-I:

$$\lim_{\gamma \to 0} g_{\gamma}(z_j) = 1 - r(z_j) \tag{5.9}$$

where (5.2) provides  $r(z_i)$ .

Property-II: Set up  $G_{\gamma}(z)$  as:

$$G_{\gamma}(\mathbf{z}) = \sum_{j=1}^{n} g_{\gamma}(z_j), \tag{5.10}$$

Then,

$$\lim_{\gamma \to \infty} G_{\gamma}(z) = \sum_{j=1}^{n} (1 - q(z_{j}))$$

$$= n - ||z||_{0}$$
(5.11)

Thus,  $||z||_0$  can be estimated by:

$$\|\mathbf{z}\|_{0} \cong n - \lim_{\mathbf{y} \to 0} G_{\mathbf{y}}(\mathbf{z}) \tag{5.12}$$

The crucial parameter, which determines the width of the Gaussian curve, is part of the smooth approximation of the  $l_0$  norm provided by Eq. (5.12). The  $l_0$  norm is accurately approximated when the width is less, but the function is less smooth. A smoother but less accurate approximation results from a wider width.

In Eq. (5.12), increasing  $G_{\gamma}$  is equivalent to decreasing the  $l_0$ -norm. The function  $G_{\gamma}$  with a smaller value is non-differentiable with numerous local maxima. The cost function grows smoother than increases, preventing local maxima. To attain precision and sparsity in solving a problem stated in Eq. (5.1), a large value of is used to avoid local maxima and a gradually decreasing value of is utilised to reduce inaccuracy.

The loss function has been maximised using the Steepest-Ascent-Algorithm (SAA). The next action updates the solution for each iteration.

$$\mathbf{z}_{k+1} \leftarrow \mathbf{z}_k + \mu_k \nabla G_{\nu}(\mathbf{z}_k) \tag{5.13}$$

Where  $\mu_k$  stands for the step size, which gets smaller with each iteration.  $G_{\gamma}$  varies with smaller value of  $\gamma$ . Therefore, a smaller step size is advised for stability. Back projection is used to enhance the solution in each repetition further.

The tangent hyperbola function, which is smooth and monotonically growing, and an analytically well-bounded function, is used to approximate the  $l_1$  norm smoothly. The angle of the curve at its beginning is adjustable [18]. Thus, the definition of our suggested approximation for the  $l_1$  norm in Eq. (5.14) is as follows:

$$\|\mathbf{z}\|_{1} \cong \sum_{i=1}^{n} z_{i} tanh(\alpha z_{i})$$
 (5.14)

Whereas:

$$f(z) = \frac{1}{2} ||y - z||_2^2 + \lambda \sum_{i=1}^n z_i \tanh(\alpha z_i)_1$$
 (5.15)

Vector differentiation cannot be used with the steepest descent algorithm. Therefore, we express (5.14) in element form to determine a partial derivative.

$$f(z) = \frac{1}{2} \sum_{i} (\boldsymbol{\Phi} z - y)_{i} (\boldsymbol{\Phi} z - y)_{i} + \lambda z_{i} \tanh(\gamma z_{i})$$
(5.16)

The element form of the partial derivative of Eq. (5.16) is thus written as:

$$\frac{\partial f(z)}{\partial z_l} = \sum_{ij} \mathbf{\Phi}_{ij} \mathbf{\Phi}_{il} z_j - \sum_{i} y_i \mathbf{\Phi}_{il} + \lambda \left( \tanh(\alpha z_l) + z_l \alpha \left( 1 - \tanh^2(\alpha z_l) \right) \right)$$
(5.17)

The following is the steepest descent algorithm for the  $l^{th}$  update:

$$(\Delta z)_l = -\eta \frac{\partial f(z)}{\partial x_l} \tag{5.18}$$

The steepest decent algorithm determines the answer using Eq. (5.17).

Once more, using the *tanh* as the foundation, A new thresholding strategy is suggested. The *tanh* is a suitable surrogate function for soft thresholding since it is bounded and has a variable slope at the origin. As a result, the mathematical equation for hyperbolic tangent-based soft thresholding is Eq. (5.19).

$$S_{\beta}(z) \cong \begin{cases} z tanh(\alpha(|z|-\beta)) & |z| > \beta \\ 0 & otherwise \end{cases}$$
 (5.19)

The proposed algorithm is described with detailed steps in Algorithm 5.1.

# Algorithm 5.1. Proposed Smoothed L01 Norm Approximation

#### Initialisation:

- 1. Initialise  $z_0$  by  $l_2$  approximate solution of  $\Phi z = y$ .
- 2. Set sequence of increasing  $\gamma$ ,  $[\gamma_1, \gamma_2, ..., \gamma_N]$

for 
$$k = 1, 2, ..., N$$
:

- 4. Set  $\gamma = \gamma_k$ .
- 5. Maximise  $G_{\gamma}$  using M iterations of the steepest ascent algorithm.
  - a. Initialise:  $z = q_{k-1}$
  - b. For i = 1, 2, ..., M

i. Set 
$$\Delta z = [z_1 g_{\gamma_k}(z_1), ..., z_n g_{\gamma_k}(z_n)]^T$$

- ii. Set  $\mathbf{z} \leftarrow \mathbf{z} \mu \Delta \mathbf{z}$
- iii. Project z back as  $z = z \Phi^T (\Phi \Phi^T)^{-1} (\Phi z y)$
- 6. Compute Gradient  $\nabla f(z_i)$  using Eq. (5.16)
- 7. Update the solution using Eq. (5.17) and Eq. (5.18)
- 4. Apply shrinkage operator using (5.19):  $\hat{\mathbf{z}}_{i+1} = S_{\beta}(\mathbf{z}_{i+1})$
- 8. Set  $q_k = z$

Final solution:  $\mathbf{z} = \mathbf{q}_{N}$ .

The above defined by algorithm 5.1 was further modified to recover CS MRI described below:

Algorithm 5.2. Modified SL01 for recovery of CS MRI

```
Initialise:
                Initialise X_0 = F_u^{-1}(Y), where Y is undersampled k – space data
         1.
         2.
                 Set \sigma as decreasing sequence for \sigma = [\sigma_1, \sigma_2, ..., \sigma_n]
 for i = 1, 2, ..., P:
         3.
                Set \sigma = \sigma_i
         4.
                Find Maxima for F_{\sigma}(x) in m iterations of the steepest ascent algorithm.
                  c. Initialise: X = X_{i-1}
                  d. For j = 1, 2, ..., Q
                          i. X_{sparse} = \Psi(X)
                         ii. Set \Delta X_{sparse} = X_{sparse}^T * f_{\sigma_i}(X_{sparse})
                        iii. Set X_{sparse} = X_{sparse} -
                      \mu \Delta X_{sparse}, where \mu is a step size
                        iv. X = \Psi^{-1}(X_{sparse})
         5.
                Data consistency: X \leftarrow F_u^{-1}(F_u(X) * (1 - M) + Y),
                           where M represents the undersampling mask
         6.
                Compute Gradient \nabla f(z_i) using Eq. (5.16)
         7.
                Update the solution using Eq. (5.17) and Eq. (5.18)
        8.
                Apply shrinkage operator using (5.19): \hat{X}_{i+1} = S_{\mathcal{B}}(X_{i+1})
        9.
                Set X_i = X
Final solution: X = X_p.
```

## 5.3 Experimental Results and Discussion

The proposed algorithm is employed to recover both 1-D sparse signals and 2-D MRI data that have been undersampled. To evaluate the performance of the algorithm, two commonly used metrics, SNR and MSE, are utilised. The results of the experiments clearly demonstrate that the proposed technique surpasses both the  $l_0$ -norm and l1-norm smooth approximations applied alone in terms of CS MRI recovery and 1-D sparse signal recovery. The higher SNR values and lower MSE values obtained indicate that the proposed algorithm achieves better accuracy and fidelity in reconstructing the original signals compared to the competing approaches defined in Chapter 3 and Chapter 4. This suggests that the proposed algorithm is more effective in recovering the underlying information

from undersampled observations, showcasing its potential for practical applications in sparse signal recovery and CS MRI reconstruction tasks.

## 5.3.1 Sparse Signal Recovery Application

MATLAB simulations are used to analyse the suggested algorithm's performance. Using a randomly generated Gaussian matrix with dimensions of  $m \times n$ , where m is the number of samples (set to 100) and n is the total length of the sparse signal (set to 256), the experimental setup entails undersampling a random 1-D sparse signal. To guarantee proper scaling, the columns are normalised.

The model used to produce the noisy observations is y = Az + w, where w stands for white Gaussian noise. This approach considers the existence of noise in the collected data. Through a gradient ascent loop that iterates three times (N = 3) for each iteration, the algorithm performance is assessed. A single value is used to execute the loop, enabling a systematic analysis of the algorithm performance under various parameter configurations. The algorithm may adjust and improve its performance for various conditions by changing.

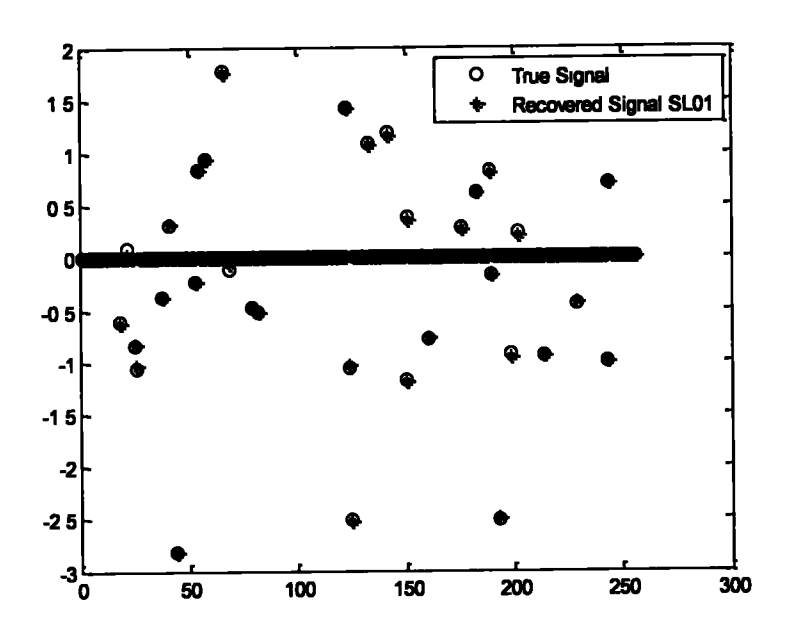


Figure 5-1: Ground Truth 'o' and Reconstructed Signal '\*'

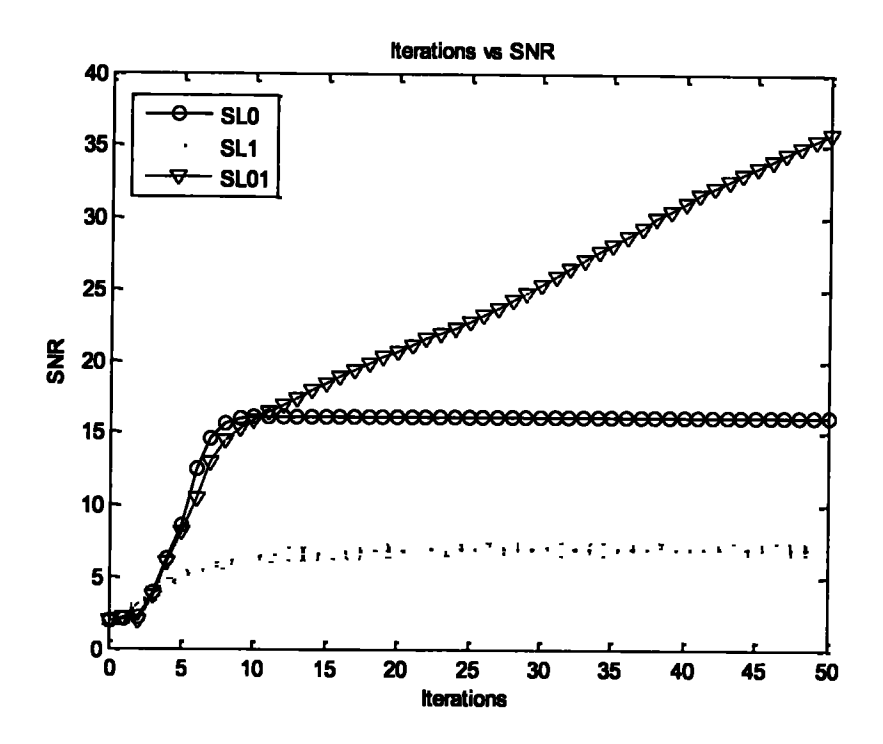


Figure 5-2: Recovered signal SNR at each iteration

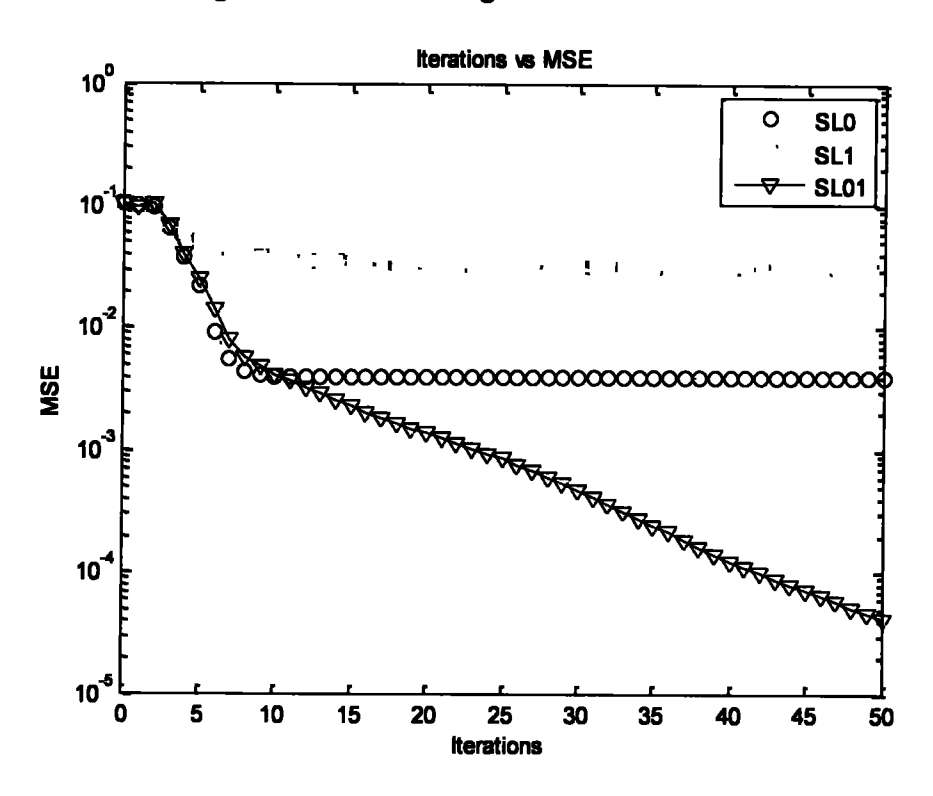


Figure 5-3: MSE of the recovered signal at each iteration

Both the original signal and the recovered signal are shown in Figure 5-1, which illustrates the precise recovery attained by the suggested technique for the 1D k-sparse signal. Figure 5-2 depicts a comparison between the suggested technique's SNR with the performance of the SL0 and SL1 algorithms proposed in Chapter 3 and Chapter 4. Notably, as compared to the other algorithms, the suggested technique achieves much higher SNR values. The suggested approach outperforms the competition by reaching the lowest MSE values, as seen in Figure 5-3's comparison of the algorithms' Mean Squared Error (MSE) results.

## 5.3.2 CS MRI Reconstruction Using Proposed Method

The SL01 technique is deployed to reconstruct CS MRI from its undersampled k-space data. Drawing a comparison between CS encoding and noisy images, compressed sensing recovery fundamentally transforms into an image-denoising task. Estimating the noise using the maximum a posteriori (MAP) estimator, is the first step in recovering the original image. A 2-D CS Brain MRI with dimensions of 256 x 256 is recovered using the suggested approach. The Brain MRI was scanned as a fully sampled image at St. Mary's Hospital in London, England. The MR image is compressively extracted in this instance by acquiring only 25% of the samples using the random mask.

Figure 5-4 provides a quantitative comparison of the proposed algorithm' combined Smooth approximation of  $l_0$  and  $l_1$  norm (SL01) performance with that of the Smooth approximation of  $l_0$  (SL0) and Smooth approximation of  $l_1$  norm (SL1) algorithms when applied to under-sampled MR data. The under-sampling process is conducted using a variable-density random sampling pattern.

In Figure 5-4(a), the improvement in SNR achieved by the proposed algorithm is depicted. It showcases the superiority of the proposed algorithm in terms of achieving higher SNR values compared to SL0 and SL1. The higher SNR values indicate better quality and fidelity in the recovered MRI.

Figure 5-4(b) illustrates the reduction in Mean Squared Error (MSE) achieved by the proposed algorithm compared to SL0 and SL1. A lower MSE value indicates a closer match between the recovered MR data and the original data. The significant decrease in MSE achieved by the proposed algorithm indicates its ability to achieve more accurate and reliable results than the other algorithms.

Overall, these comparisons highlight the quantitative advantages of the proposed algorithm over SL0 and SL1, as evidenced by the improvement in SNR and the decrease in MSE. These results further validate the effectiveness of the proposed algorithm for recovering under-sampled MR data.

Figure 5-5 presents the recovery of Compressed Sensing (CS) Magnetic Resonance Imaging (MRI) data that has been under-sampled using a variable density random sampling scheme. In Figure 5-5(a), the recovery results of the MRI using different algorithms, namely Zero Filling (ZF), Smooth approximation of  $l_0$  (SL0), Smooth approximation of  $l_1$  norm (SL1), and the proposed method (SL01), are displayed. Subjectively, the image recovered by the proposed method exhibits better visual quality than the other recovered images, indicating the effectiveness of the proposed algorithm.

Figure 5-5(b) illustrates the sampling pattern utilised by each algorithm. It visually represents how the different algorithms capture the under-sampled data. The sampling pattern reflects the spatial distribution of acquired measurements, which is crucial for accurate recovery.

Furthermore, Figure 5-5(c) focuses on the magnified difference between the original and recovered images. The zero-filling approach performs poorly, as the difference between the original and recovered images is more pronounced. On the other hand, the simple SL0 and SL1 algorithms exhibit higher error levels than the proposed method (SL01). The error in the proposed method is considerably lower than that of the other methods, indicating its superiority in achieving more accurate and faithful image recovery.

These findings highlight the advantages of the proposed algorithm (SL01) in terms of subjective image quality and reduced error when recovering under-sampled CS MRI compared to ZF, SL0, and SL1 algorithms.

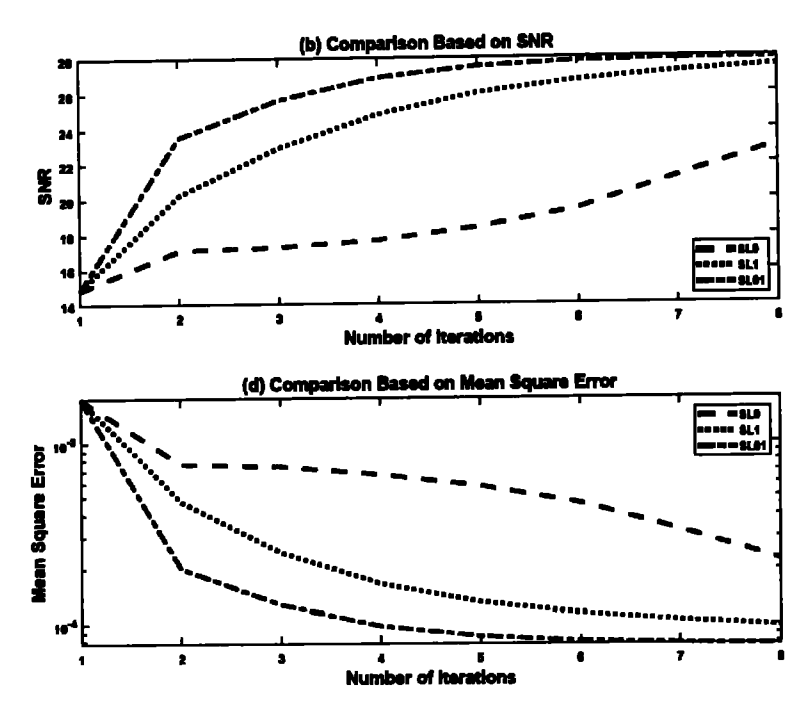


Figure 5-4: MSE and SNR curves for recovery of CS MRI

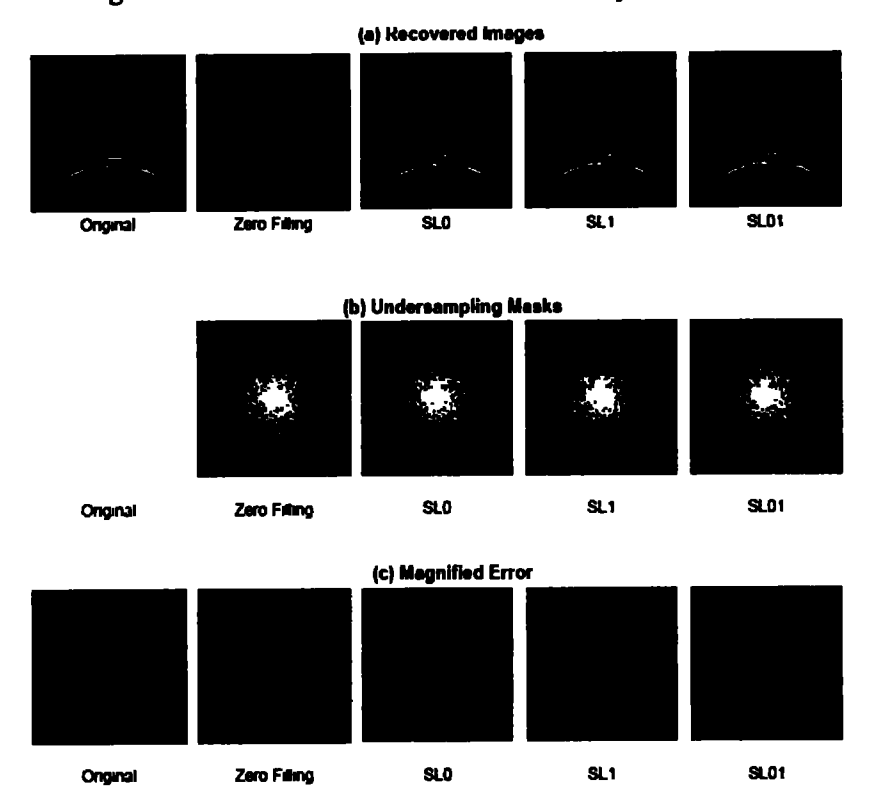


Figure 5-5: Illustration of proposed SL01 recovery from undersampled MRI (a) original and recovered images (b) masks for undersampling (c) Magnified (difference error x 1000) between original and recovered MRI.

#### 5.4 Conclusions

In compressive sensing, recovering compressively sampled sparse signals and MRI data from under-sampled k-space measurements is a computationally demanding task. In this chapter, we have addressed this challenge by proposing an efficient algorithm that leverages the combined power of smoothed  $l_0$  and smoothed  $l_1$  norms. These norms play a crucial role in promoting sparsity in the recovered signals.

To objectively evaluate the performance of the proposed algorithm, we conducted a comparative analysis with existing methods that utilised the smooth  $l_0$  norm and smooth  $l_1$  norm. We measured the performance using well-established metrics such as MSE and SNR. The results demonstrate the superiority of the proposed technique, as it consistently outperforms the other methods in terms of both MSE and SNR. This objective evaluation provides quantitative evidence of the improved performance achieved by our algorithm.

Furthermore, subjective analysis is conducted to assess the visual quality of the recovered MRI. The visual inspection revealed that our proposed technique produces images of higher visual fidelity than the other methods. This subjective evaluation further supports the effectiveness of our algorithm in accurately recovering compressively sampled sparse signals and MRI.

Overall, the combination of objective and subjective analyses confirms that the proposed algorithm offers a considerable improvement in performance compared to existing methods. The efficient recovery of compressively sampled sparse signals and MRI data achieved by our algorithm has the potential to benefit various applications in the field of compressive sensing.

#### **CHAPTER 6**

## **NATURE-INSPIRED IRLS FOR CS MRI RECOVERY**

This chapter introduces innovative approaches for recovering k-sparse signals and MR images from compressed measurements using nature-inspired evolutionary techniques, namely Particle Swarm Optimisation (PSO), in combination with a deterministic Iterative Reweighted Least Squares (IRLS)-based shrinkage algorithm. The proposed hybrid mechanisms incorporate appropriate regularisation constraints to enhance the convergence of the evolutionary algorithms and achieve accurate estimation k-sparse signal. Furthermore, the suggested algorithm is extended to address the specific challenge of recovering CS MRI from incomplete Fourier data in the context of Fourier-encoded MRI. This modified algorithm incorporates the combined principles of IRLS and evolutionary methods, particularly Genetic Algorithms (GA). The integration of these methodologies allows for efficient and effective recovery of biomedical images, even incomplete and under-sampled Fourier data. The presented algorithms offer notable advantages in accelerating convergence, precise estimation of sparse signals, and successful recovery of biomedical images from compressed measurements. These techniques contribute to the advancement of signal recovery methods, particularly in compressive sensing and Fourierencoded MR imaging.

## 6.1 Nature-Inspired Algorithms

Deterministic algorithms, known for their mathematical elegance, usually demand a well-defined initial solution and may not be user-friendly. Conversely, evolutionary algorithms like Genetic Algorithms (GA) and Particle Swarm Optimisation (PSO) offer simpler implementations but lack rigorous mathematical foundations [131]. Primarily utilised for unconstrained search problems, adapting these algorithms to constrained optimisation poses challenges [132-135]. Nevertheless, nature-inspired algorithms such as GA and PSO are ideal for tackling computationally complex problems that defy traditional approaches. These algorithms provide practical solutions, without strict mathematical modelling.

$$\hat{z} = \operatorname{agrmin} (\|\mathbf{y} - \mathbf{\Phi}\mathbf{z}\|_{2}^{2} \text{ subject to } \|\mathbf{z}\|_{0} \le k$$
(6.1)

However, a deterministic algorithm is needed to solve the  $l_0$  norm-based minimisation problem in Eq. (6.1) to hasten convergence [136].

## 6.2 Particle Swarm Optimisation

Particle Swarm Optimisation (PSO) is a probabilistic optimisation technique with a simple structure known as particle-based search optimisation [137-139]. In PSO, each particle's velocities are randomly assigned, allowing it to explore the search space. The velocities of the particles are updated iteratively based on their prior velocities and the distances between their local and global best solutions. [140] provides the velocity update equation for the PSO-based algorithm.

$$v_i = w \times v_{i-1} + c_1 r_1 (p_i - x_{i-1}) + c_2 r_2 (p_g - z_{i-1})$$
 (6.2)

Where  $r_1$  and  $r_2$  are two separate uniformly distributed random values in the range (0,1) and  $c_1$ ,  $c_2$  are problem-dependent constants. The scalar  $w \in [0,1]$  represents Inertial weight. The particle known as global best, or  $p_g$ , has the finest fitness across the board.  $p_i$  is the local best, which, according to the cost function, reflects the best prior position of the  $i^{th}$  particle. The algorithm's performance can be significantly impacted by changing the free parameters  $c_1$ ,  $c_2$ , and the inertia weight w [141].

The position  $z_i$  of the  $i^{th}$  particle is updated in the conventional PSO by its velocity:

$$\mathbf{z}_{l} = \mathbf{z}_{l-1} + \mathbf{v}_{l} \tag{6.3}$$

The Basic PSO algorithm begins with a random population of 20-50 particles, depending on the specific challenge. Particles move according to velocity iteratively, which is updated based on both local and global optimal positions.

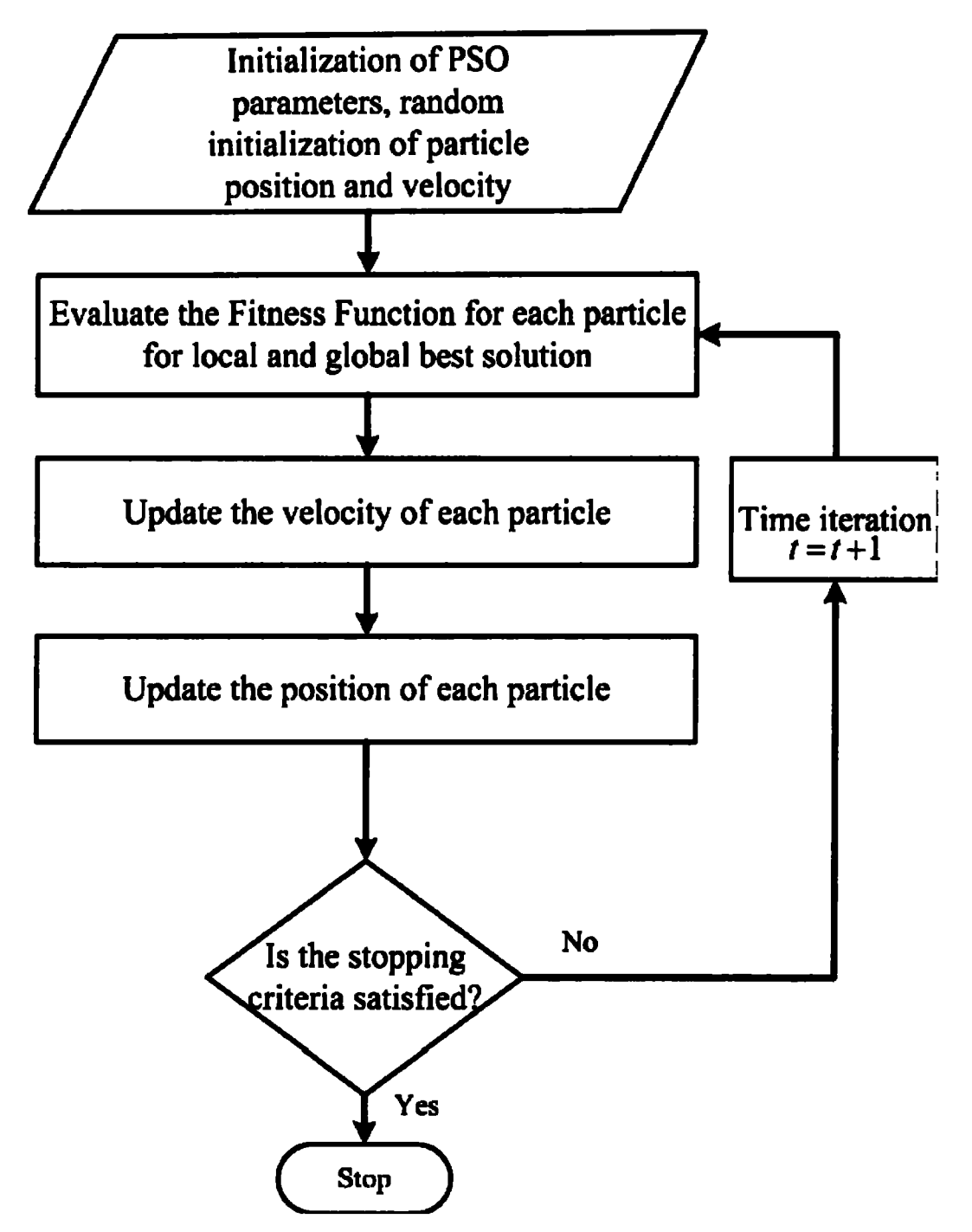


Figure 6-1: Basic PSO Flow Chart

## 6.3 Iterative Reweighted Least Square (IRLS)

The Iterative Reweighted Least Squares (IRLS) algorithm is effective for various optimisation problems [23]. Rather than directly minimising the  $l_1$ -norm, IRLS minimises a weighted residual at each iteration. IRLS can also find maximum likelihood solutions for generalized linear models [23]. For MRI reconstruction, IRLS transforms the non- $l_2$ -norm terms in Eq. (2.22) into weighted  $l_2$ -norms [21]. This allows rewriting the objective function as:

$$f(z) = \frac{1}{2} ||y - F_u z||_2^2 + \lambda \mathbf{1}^T \rho(\Psi z)$$
 (6.4)

where  $\mathbf{1}^T \rho(\Psi \mathbf{z})$  is replaced by  $0.5 \Psi \mathbf{z}^T \mathbf{W}^{-1}(\Psi \mathbf{z}) \Psi \mathbf{z}$ , where  $\mathbf{W}(\Psi \mathbf{z})$  is the diagonal matrix, having defined by Eq. (6.6) values in its diagonal of the matrix.

$$W[k,k] = \frac{0.5\Psi z[k]^2}{\rho(\Psi z[k])}$$
(6.5)

The loss function is given by:

$$f(z) = \frac{1}{2} \|y - F_u z\|_2^2 + \frac{\lambda}{2} \Psi z^T W^{-1} (\Psi z) \Psi z$$
 (6.6)

The following quadratic function is minimised to update the existing solution,  $x_0$  while assuming that **W** is fixed.

$$\nabla f(\mathbf{z}) = -\mathbf{F}_{\mathbf{u}}^{\mathsf{T}}(\mathbf{y} - \mathbf{F}_{\mathbf{u}}\mathbf{z}) + \lambda \, \mathbf{\Psi} \mathbf{z}^{\mathsf{T}} \mathbf{W}^{-1}(\mathbf{\Psi} \mathbf{z}) \mathbf{\Psi} \mathbf{z} = 0 \tag{6.7}$$

The next step for updating x is to take the inverse of the matrix  $\mathbf{F_u}^T \mathbf{F_u} + \lambda \mathbf{W}^{-1}$ . Then we update  $\mathbf{W}$  based on the updated solution z.

Standard IRLS performs poorly for high-dimensional signal recovery problems. To address this limitation, Adeyemi and Davies [23] modified the IRLS approach by adding and subtracting the term c.z in Eq. (2.24). This results in an iterative shrinkage algorithm where c is a relaxation constant chosen between 0 and  $\lambda_{max}(\mathbf{F_u}^T\mathbf{F_u})/2$  to ensure convergence. Here  $\lambda_{max}$  is the maximum eigenvalue of the matrix. The iterative update equation can then be written as:

$$\mathbf{z}_{k+1} = \left(\frac{\lambda}{c} \mathbf{W}^{-1} (\mathbf{\Psi} \mathbf{z}_k) + I\right)^{-1} \left(\frac{1}{c} \mathbf{F_u}^{\mathrm{T}} \mathbf{y} - \frac{1}{c} (\mathbf{F_u}^{\mathrm{T}} \mathbf{F_u} - c\mathbf{I}) \mathbf{z}_k\right)$$

$$= S. \left(\frac{1}{c} \mathbf{F_u}^{\mathrm{T}} (\mathbf{y} - \mathbf{F_u} \mathbf{z}_k) + \mathbf{\Psi} \mathbf{z}_k\right)$$
(6.8)

where diagonal matrix can be defined as:

$$S = \left(\frac{\lambda}{c} W^{-1}(\Psi z_k) + I\right)^{-1} = \left(\frac{\lambda}{c} I + W(\Psi z_k)\right)^{-1} W(\Psi z_k)$$
(6.9)

The above equation performs a shrinkage operation on the vector  $\frac{1}{c} \mathbf{F_u}^{\mathsf{T}} (\mathbf{y} - \mathbf{A} \mathbf{\Psi} \mathbf{z_k}) + \mathbf{\Psi} \mathbf{z_k}$ . Each entry in a vector is multiplied by the following scalar value.

$$\frac{0.5\Psi z_{k}[i]^{2}/\rho(\Psi z_{k}[i])}{\frac{\lambda}{c} + 0.5\Psi z_{k}[i]^{2}/\rho(\Psi z_{k}[i])} = \frac{\Psi z_{k}[i]^{2}}{\frac{2\lambda}{c}\rho(\Psi z_{k}[i]) + \Psi z_{k}[i]^{2}}$$
(6.10)

The shrinkage factor in the modified IRLS algorithm approaches one when the weighted norm  $\Psi z_k[i]$  is large and shrinks towards zero for smaller weighted norms. This provides the desired shrinkage effect. Initializing the IRLS solution to zero should be avoided since zeros will persist - causing the algorithm to get stuck in poor local minima. Instead, the initial guess should have nonzero values. Algorithm 6.1 outlines the iterative steps of the modified IRLS algorithm to recover an MR image from the undersampled partial Fourier k-space data while applying shrinkage to improve convergence.

Task: Find the value of image X that minimises the objective function:

$$f(X) = \underset{\mathbf{x}}{\operatorname{argmin}}(\|Y - \mathbf{F}_{\mathbf{x}}\mathbf{X}\|_{2}^{2} + \lambda \|\mathbf{x}\|_{1})$$

**Input:** Dictionary matrix  $F_u \in \mathbb{R}^{m \times n}$ ,

Measurement matrix  $Y \in \mathbb{R}^m$ ,

IRLS thresholding parameter  $\lambda$ .

Output:  $A K - sparse solution vector X \in \mathbb{R}^{n \times m}$ 

- 1) Initialisation: Initialise IRLS iteration number k=0Initial solution:  $X_0 = [x_1, x_2, ... ... x_{nxm}]$ , where each entry  $x_i \neq 0$ Initial residual:  $R_0 = Y X_0$
- 2) IRLS Main Iteration: Increment k by 1, and apply the following steps
  - a) Back Projection: Compute  $E = F_{u}^{T} X_{k-1}$
  - b) Shrink Update: Compute the diagonal matrix S by  $S[i,i] = \frac{x_k[i]^2}{\frac{2\beta}{\alpha} ||x||_1 + x_k[i]^2}$
  - c) Shrinkage: Compute  $E_s = S(X_{k-1} + \frac{e}{s})$
  - d) Solution Update: Compute  $X_k = X_{k-1} + (E_s X_{k-1})$
  - e) Residual Update: Compute  $R_k = y F_u X_k$
  - f) Stopping Rule: Go to step (2) until, either  $||X_k X_{k-1}||_2^2 <$ threshold value or maximum number of iterations criteria is met.
- 3) Output: The final value of x.

# 6.4 Nature Inspired Iterative Reweighted Least Square (NI-IRLS)

The proposed NI-IRLS algorithm introduces a combination of two different algorithms, namely PSO and Modified IRLS [12] that is inspired by POCS[59], to address the problem of recovering a k-sparse 1-D signal and performing CS MRI. The aim is to solve the constrained optimisation problem defined by Eq. (6.1).

To ensure the sparsity in the solution, all particles of the population are initialised and the technique applies soft thresholding based on the IRLS algorithm. Though, the particles after velocity update can lose sparsity. Therefore, after each position update, another round of soft thresholding based on IRLS is performed to maintain the sparsity constraint throughout the recovery process.

In situations where the fitness of the global best particle remains unchanged for a specified number of iterations, the modified IRLS algorithm is employed. This algorithm

updates the position of the second-best particle in the population using a specific strategy elaborated in *Algorithm 1*. This helps to improve the convergence and accuracy of the algorithm in finding the optimal solution. Overall, the proposed technique combined the strengths of PSO and modified IRLS to address the k-sparse 1-D signal and CS MRI recovery problem by ensuring sparsity and enhancing the optimisation process.

$$Z_{l} = S_{c,\beta} \left( \Psi \left( Z_{k-1} + \frac{E}{c} \right) \right) \tag{6.11}$$

Here  $S_{c,\beta}$  defines the shrinkage operation having a threshold defined by  $\beta$ . Where c is the random number,  $\Psi$  is a sparsifying domain, W is defined by Eq. (6.5) and E is the backpropagation error defined by Eq. (6.12)

$$\mathbf{E} = \mathbf{F_u}^{\mathsf{T}} (\mathbf{y} - \mathbf{\Phi} \mathbf{\Psi} \mathbf{z}_k) + \mathbf{\Psi} \mathbf{z}_k \tag{6.12}$$

In the proposed algorithm, the parameter  $\gamma$  is introduced to address varying compression ratios (CR) of the undersampled k-sparse signal. This adjustability empowers the algorithm to dynamically adapt to different degrees of data compression. By modifying  $\gamma$  based on the specific CR, the algorithm can effectively tailor its reconstruction approach, accommodating different levels of sparsity in the signal. The experimentation section provides evidence that the algorithm's flexibility yields promising results, showcasing its ability to handle varying CRs and consistently produce accurate reconstructions, making it a versatile and reliable solution for sparse signal recovery tasks across diverse data compression scenarios as shown in Figure 6-18 and Figure 6-19.

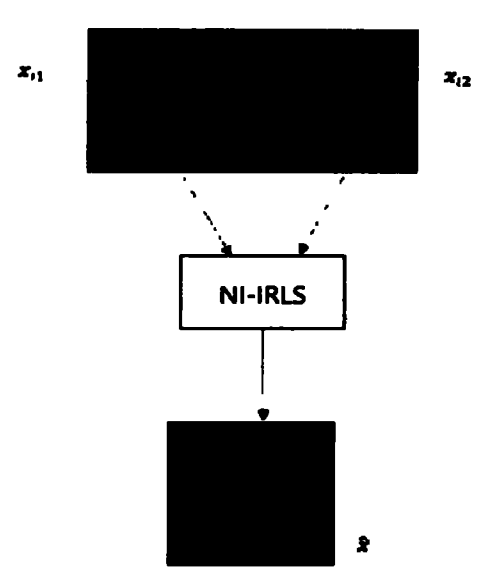
$$\gamma = 100 - compression \ ratio.$$
 (6.13)

The data consistency constraint in the frequency domain is a fundamental principle in Compressed Sensing Magnetic Resonance Imaging (CS MRI) recovery. It ensures that the actual samples acquired in the k-space domain remain constant throughout the recovery process. In other words, the measured data points in the frequency domain, which correspond to the acquired MRI measurements, are preserved, and not altered during the iterations of the recovery algorithm. The data consistency constraint is crucial because it guarantees that the recovered image remains consistent with the acquired data. It prevents the algorithm from introducing spurious information or modifying the original measurements, which could lead to erroneous results. By preserving the actual samples from the k-space domain, the algorithm ensures that the recovered image accurately represents the underlying structure of the imaged object, even with limited or under-

sampled data. The data consistency constraint in the frequency domain is a vital aspect of CS MRI recovery, as it maintains the integrity of the acquired data and helps achieve reliable and accurate image reconstruction.

$$\mathbf{Y}_{l}[j] = \mathbf{F}_{\mathbf{u}}(\mathbf{X}_{l}) \text{ (FFT of Estimated Image)}$$

$$\mathbf{Y}_{l}[j] = \begin{cases} \mathbf{y}_{l}[j] & \text{if } \mathbf{y}[j] = 0\\ \mathbf{y}[j] & \text{otherwie} \end{cases}$$
(6.14)



Recovery technique of proposed algorithm

Figure 6-2: Two Initial Inputs for NI-IRLS from ZF and LR and generated output from the proposed algorithm

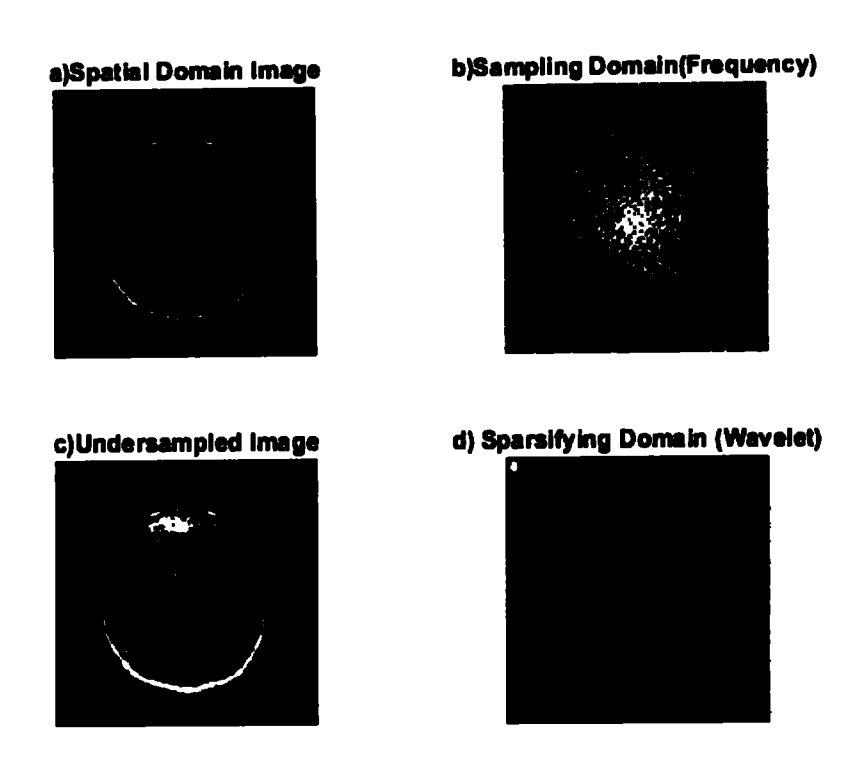


Figure 6-3: Different domains used in the proposed algorithm.

Figure 6-2 illustrates the two initializations used for the proposed algorithm, namely Low Resolution (LR) and Zero Filling (ZF), which are crucial for fitness comparison during optimisation. The LR initialization involves reconstructing the initial image from low-resolution measurements, providing a coarse estimation with limited details. On the other hand, the ZF initialization fills the missing k-space data with zeros, creating an initial image with potential artefacts. Both initializations are then evaluated based on fitness measures to determine which one better approximates the original image. The initialization with superior fitness serves as the global best solution, becoming the starting point for subsequent optimisation steps, enhancing the likelihood of achieving a high-quality reconstructed image through the algorithms' optimisation process.

In Figure 6-3, the proposed technique for image reconstruction is illustrated, showcasing different domains involved in the process (a) shows the original Image, this domain represents the original image, which serves as the reference for the entire reconstruction process. It contains the complete information about the image without any loss or compression. (b) depict the k-Space Sampling Domain, in this domain, the k-space data is generated by applying masks to the original image. The masks are applied for

undersampling the k-space data, meaning that only a subset of the k-space samples is acquired, reducing data acquisition time. (c) elaborates the effects of undersampling in the Spatial Domain, after undersampling in the k-space domain, the effects of this undersampling are depicted in the spatial domain. The spatial domain is the familiar domain where we perceive images with their pixel values. Due to undersampling, the reconstructed image in this domain will exhibit artefacts and degradation compared to the original image. (d) In the Sparsifying Domain i.e., Wavelet in our proposed method, the undersampled k-space data is processed through a sparsifying process that involves "shrinkage." Sparsifying transforms the k-space data into a sparse representation, where most coefficients are set to zero or close to zero, highlighting the sparsity of the data. Shrinkage, in this context, refers to reducing the magnitudes of non-zero coefficients, further enhancing the sparsity. This proposed technique aims to reconstruct the original image from undersampled k-space data using sparsity-promoting methods.

**Task:** Recovery of k- sparse signal  $z \in \mathbb{R}^n$  that minimises the objective function:

$$f(z) = \operatorname{argmin}(\|\mathbf{y} - \mathbf{F}_{\mathbf{u}}\mathbf{x}\|_{2}^{2} + \lambda \|\mathbf{z}\|_{1})$$

Input: Dictionary  $\Phi \in R^{m \times n}$ , Sparsity level k, Population size N, PSO parameters  $c_1, c_2$  and w Compressed Measurement  $\mathbf{y} \in R^m$ , IRLS thresholding parameter  $\lambda$ , constant  $\mu$ .

Output: A Recovered k – sparse signal  $z \in R^n$ 

1) Initialisation: Initialise IRLS iteration number k = 0

Initial solution:  $\mathbf{z}_0 = [\mathbf{z}_1, \mathbf{z}_2, \dots \dots \mathbf{z}_n]$ , where each entry  $\mathbf{z}_i \neq 0$  Initial residual:  $\mathbf{r}_0 = \mathbf{y} - \Phi \mathbf{z}_0$ ,  $\mathbf{V} = \mathbf{0}$ , velocity matrix Generate N particles randomly with desired sparsity  $\mathbf{Z} = [\mathbf{z}_1, \mathbf{z}_2, \dots \dots \mathbf{z}_n]$ , where  $\mathbf{z}_i \in \mathbb{R}^n$  and  $\|\mathbf{z}_i\|_0 \leq k \ \forall i \leq 1 \leq N$ 

2) Fitness Evaluation and Sorting:

$$f_{z} = fitness(z_{1}, z_{2}, ..., z_{N}) = [f_{1}, f_{2}, ..., f_{N}]$$
Where  $f_{j} = (\Phi z_{i} - y)^{T}(\Phi z_{i} - y)$ 

$$[f_{zz} index] = sort(f_{z}, descend)$$

$$f_{zz} = [f_{z1}, f_{z2}, ..., f_{zN}] \text{ with } f_{z1} \leq f_{z2} \leq ... \leq f_{zN}$$

3) Initial local and global best

$$\mathbf{P} = \mathbf{z_0}(index) = [p_1, p_2, ..., p_N]$$
 where  $p_i$  has fitness  $f_{zi}$   $\mathbf{p_z} = \mathbf{p_1}$  is the initial global best

- 4) NI-IRLS Main Iteration: Increment k by 1, and apply the following steps
  - a) Velocity and Position update: Velocity and position update of each particle defined by Eq. (6.2) and Eq. (6.3) respectively:

$$V = velocity(V, P, z_0, p_g, c_1, c_2, w)$$

$$= [v_1, v_2, ..., v_N]$$

$$Z = position(Z, V)$$

$$= [|z_1|_k, |z_2|_k, ..., |z_N|_k], \text{ where } z_i = z_{i-1} + v_i$$

- b) Back Projection: Compute  $e = \Phi^T r_{k-1}$
- c) Shrink Update: Compute the diagonal matrix S by  $S[i, i] = \frac{z_k[i]^2}{\frac{2\lambda}{c}||z_k[i]||_1 + z_k[i]^2}$
- d) Shrinkage: Compute  $e_s = S_{c,\beta} \left( z_{k-1} + \frac{e}{c} \right)$

Where c is a random number.

$$z_2 = rand \times (e_s - z_r) + z_1$$

where z, is a randomly selected from the population and CR is the compression ratio

e) Update local and global best based on fitness:

$$\begin{split} &f_{z2} = fitness(\mathbf{Z}) \\ &[f_{z2z} \ index] = sort(f_{2z}, descend) \\ &f_{z2z} = [f_{z21}, f_{z22}, \dots, f_{z2N}] \ with \ f_{z21} \leq f_{z22} \leq \dots \leq f_{z2N} \\ &\mathbf{Z}_2 = \mathbf{Z}(index) \\ &= [\mathbf{z}_{21}, \mathbf{z}_{22}, \dots, \mathbf{z}_{2N}] \ where \ \mathbf{z}_{2i} \ has \ a \ fitness \ f_{z2i} \\ &if \ f_{z21} \leq f_{z1}, then \ p_i = \mathbf{z}_{21} \ and \ f_{z1} = f_{z21}, (new \ global \ best) \\ &else \ if \ f_{z2i} \leq f_{zi}, then \ p_i = \mathbf{z}_{2i} \ and \ f_{zi} = f_{z2i}, \forall i \leq 1 \leq N \ (local \ best) \end{split}$$

- f) Solution Update: Compute  $z_k = p_i + \mu(e_s p_i)$
- g) Residual Update: Compute  $r_k = y \Phi z_k$
- h) Stopping Rule: Go to step (4) until, either  $||z_k z_{k-1}||_2^2 < threshold value or$  the maximum number of iterations criteria is met.
- 5) Output: The final estimated solution is  $z_k$

Task: Find the value of image X that minimises the objective function:

$$f(X) = \operatorname{argmin}(\|Y - F_{u}X\|_{2}^{2} + \lambda \|X\|_{1})$$

Input: Sampling Matrix  $F_u \in \mathbb{R}^{m \times n}$ , Sparsifying Transform  $\Psi$ , constant  $\mu$ ,

Measurement matrix (Undersampled) $Y \in R^m$ , IRLS thresholding parameter  $\lambda$ .

Output: A Recovered Image  $X \in R^{n\times m}$ 

- 6) Initialisation: Initialise IRLS iteration number k=0Initial solution:  $X_0=[x_1,x_2,....x_{nxm}]$ , where each entry  $x_i\neq 0$ Initial residual:  $R_0=Y-X_0$
- 7) Fitness Evaluation and Sorting:

$$[X_{1}, X_{2}, f_{1}f_{2}] = fitness(X_{i1}, X_{i2}, Y)$$
Where  $f_{j} = (F_{u}X_{ij} - Y)^{H}(F_{u}X_{ij} - Y), j = 1, 2$ 
With  $X_{1} = \begin{cases} X_{i1}, & \text{if } f_{1} \leq f_{2} \\ X_{i2}, & \text{otherwise} \end{cases}$ 

- 8) IRLS Main Iteration: Increment i by 1, and apply the following steps
  - a) Back Projection: Compute  $E = F_u^{-1}(y_{l-1} F_u x_{l-1})$
  - b) Shrink Update: Compute the diagonal matrix S by  $S[i, i] = \frac{x_k[i]^2}{\frac{2\beta}{6} ||x||_1 + x_k[i]^2}$
  - c) Shrinkage in Sparsifying domain:  $Compute\ E_s = \Psi^{-1}\left(S_{c\beta}\left(\Psi\left(X_{k-1} + \frac{E}{c}\right)\right)\right)$

Where c is a random number.

$$X_n = \gamma \times (E_s - X_r) + X_2$$

where  $X_r$  is a randomly selected from either  $X_1$  or  $X_2$ ,

and,  $\gamma = 100 - compression ratio$ 

d) Data Consistency in Fourier Domain

$$\begin{aligned} \mathbf{Y}_{l}[j] &= \mathbf{F}_{\mathbf{u}}(\mathbf{X}_{l}) \\ \mathbf{Y}_{l}[j] &= \begin{cases} \mathbf{y}_{l}[j] & \textit{if } \mathbf{y}[j] = 0 \\ \mathbf{y}[j] & \textit{otherwise} \end{cases} \end{aligned}$$

e) Reassignment as per fitness

$$X_t = F(X_n), f_t = (F_u X_t - Y)^H (F_u X_t - Y)$$
  
if  $f_t \le f_1, X_1 = X_t; X_2 = X_1;$   
else if  $f_t \le f_2, X_2 = X_1;$ 

- f) Solution Update: Compute  $X_i = X_{i-1} + \mu(E_s X_{i-1})$
- g) Residual Update: Compute  $R_i = Y F_u X_i$
- h) Stopping Rule: Go to step (2) until, either  $||X_i X_{i-1}||_2^2 < threshold value or$  the maximum number of iterations criteria is met.
- 9) Output: The final value of  $X_k$

## 6.5 Experimental Results for Recovery of 1-D Signal

The one-dimensional sparse signal is recovered using the proposed technique. In this experiment, MATLAB is used to generate a random sparse signal of length n=512, with K=85 non-zero elements serving as the sparse signal's support. With just m=256 measurements produced, a random measurement matrix  $\Phi \in \mathbb{R}^{256x512}$  is employed to compressively sample the random sparse signal.

In this chapter, various recovery algorithms were utilised to recover a sparse signal, including Least Square (LS), IRLS, PSO, PCD, SSF, and the novel Nature Inspired Iterative Reweighted Least Square (NI-IRLS),. Performance comparison was achieved through MSE, SNR, and Cost Function (CF) minimisation. The algorithms were evaluated based on their ability to reconstruct the original sparse signal, with MSE quantifying the mean squared difference, SNR, and, CF measuring the cost function's minimisation. These results offer valuable insights into the efficacy of the proposed NI-IRLS algorithm for sparse signal recovery.

In Figure 6-4, the recovered k-sparse 1D signal using the linear recovery method Least Square (LS) based on  $l_2$ -norm is depicted. However, the results reveal that LS fails to promote sparsity in the estimated solution, leading to inaccuracies in reconstructing sparse signals. This highlights the methods' limitations in effectively identifying and reconstructing sparse components, emphasizing the need for alternative approaches to handle sparsity in signal recovery.

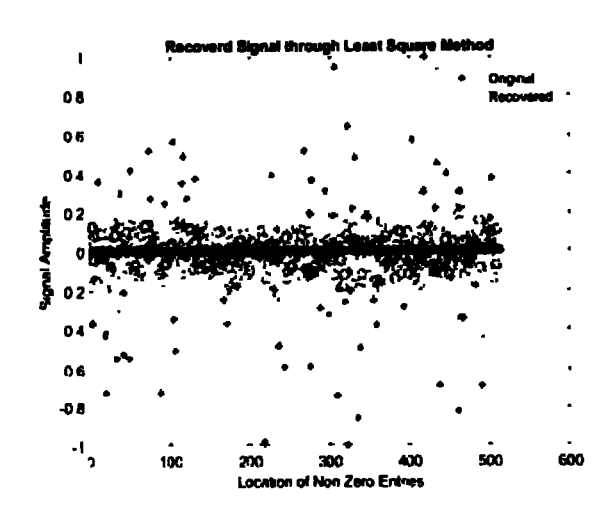


Figure 6-4: k-Sparse Signal Recovered through LS

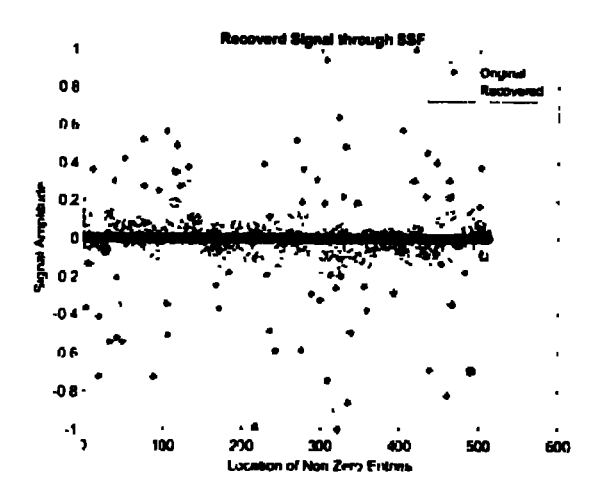


Figure 6-5: k-Sparse Signal Recovered through SSF

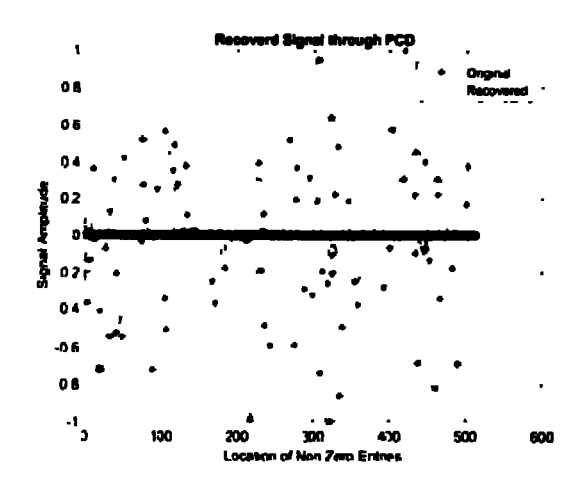


Figure 6-6: k-Sparse Signal Recovered through PCD

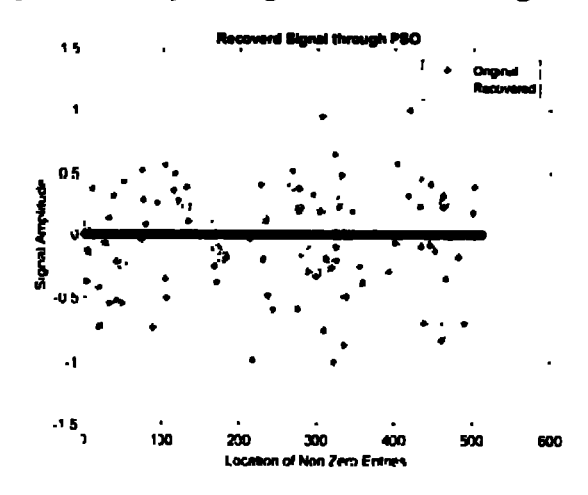


Figure 6-7: k-Sparse Signal Recovered through PSO

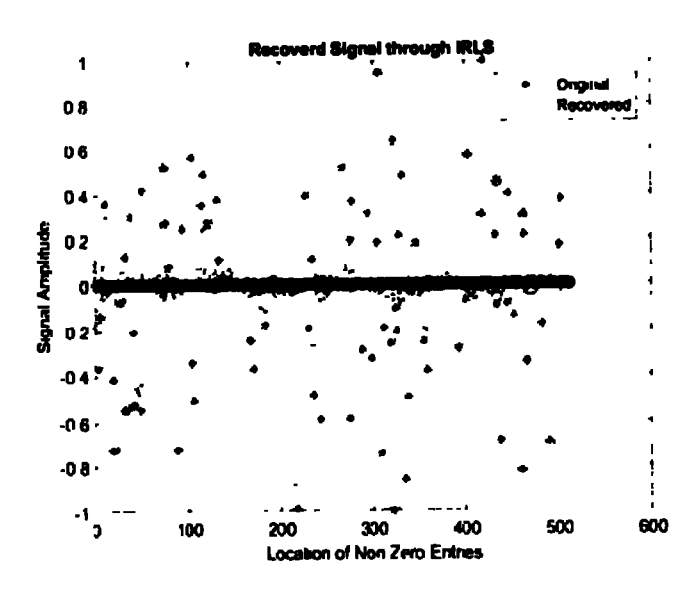


Figure 6-8: k-Sparse Signal Recovered through IRLS

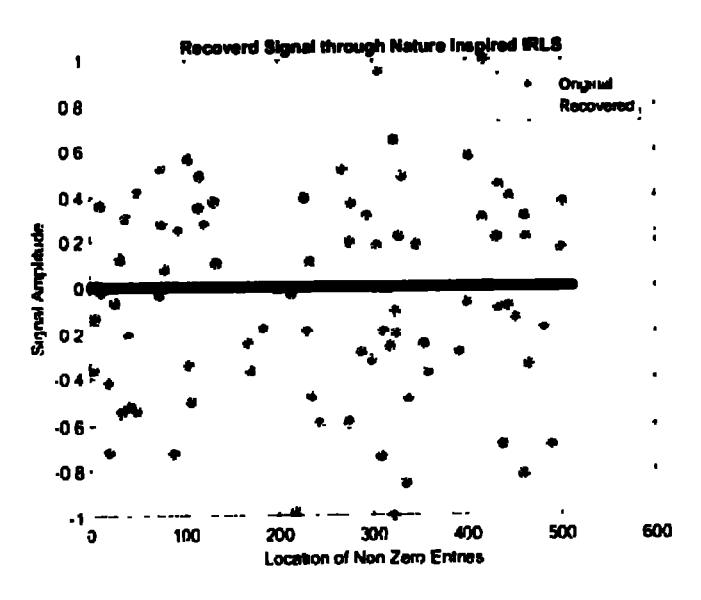


Figure 6-9: Recovered k-Sparse 1D Signal through Proposed Nature Inspired IRLS

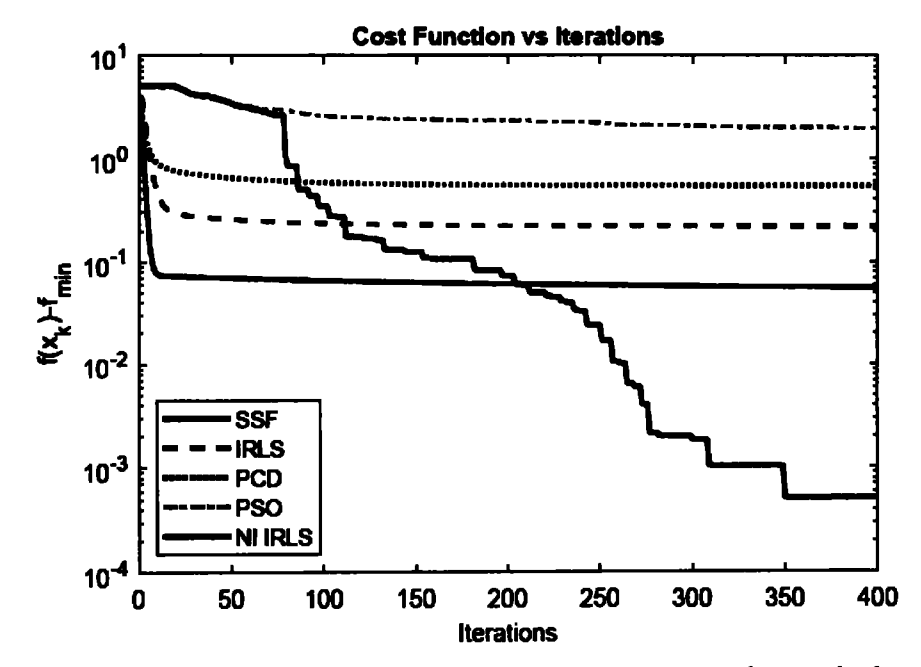


Figure 6-10: Cost Function minimisation by NI-IRLS vs other methods

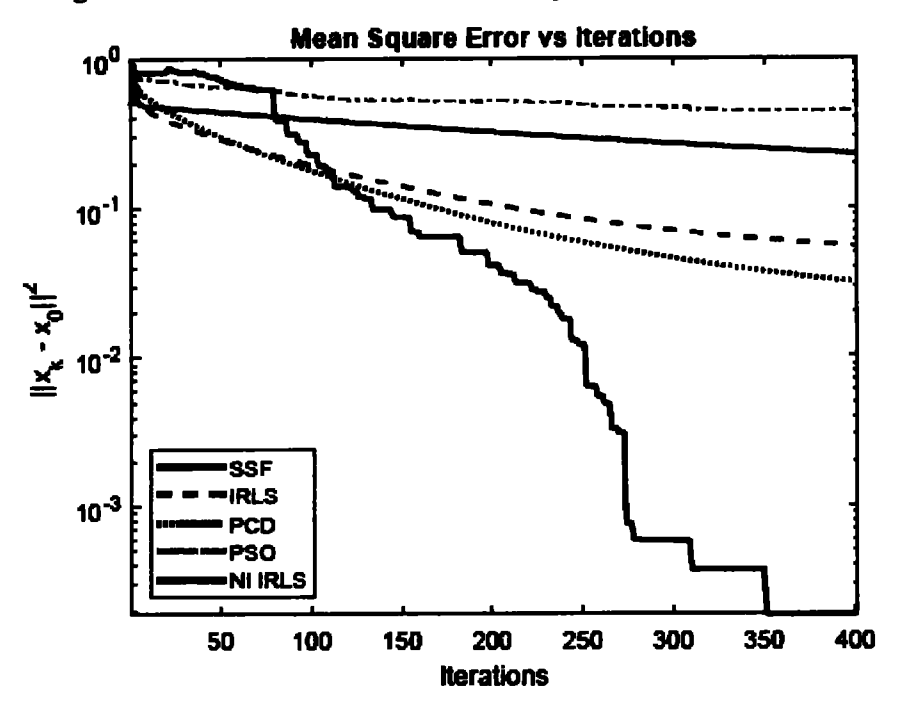


Figure 6-11: MSE minimised by proposed NI-IRLS vs other techniques

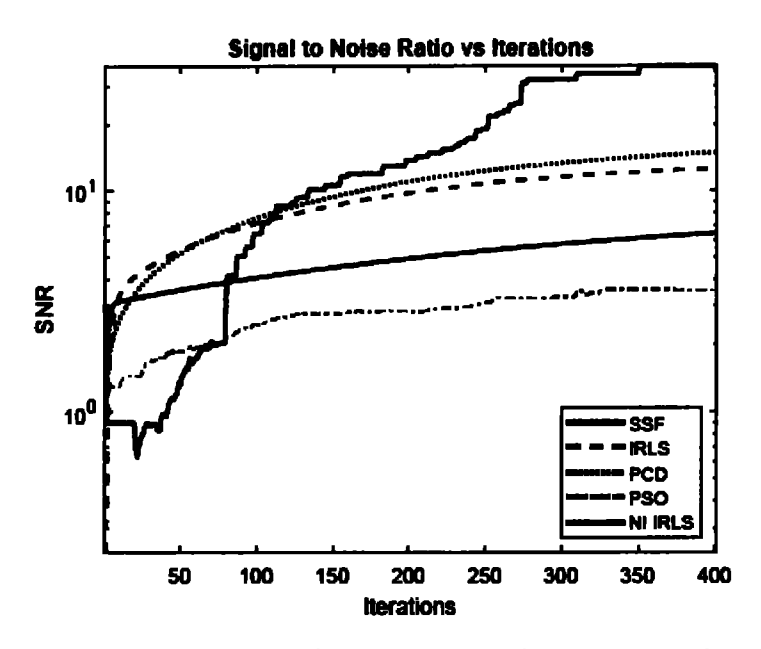


Figure 6-12: Maximum SNR achieved by proposed NI-IRLS vs other techniques

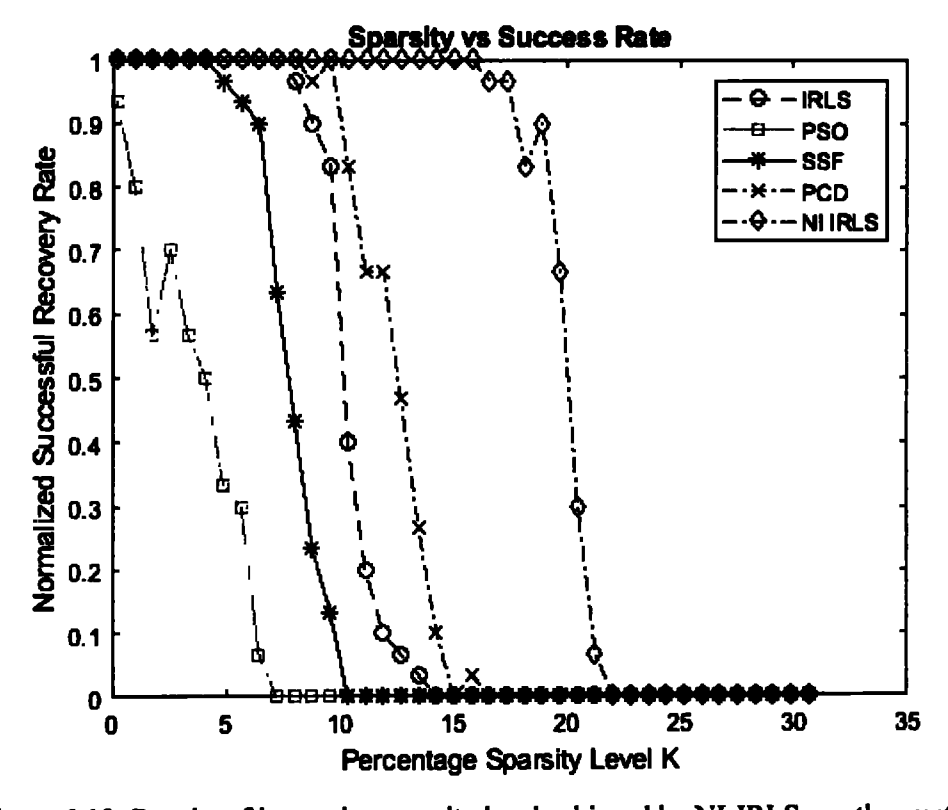


Figure 6-13: Results of increasing sparsity level achieved by NI-IRLS vs other methods

Figure 6-5 depicts the recovery of k-sparse 1D signal by SSF, which promotes sparsity but got stuck in local minima and failed to reach an optimal solution. Figure 6-6 shows the recovery by PCD as discussed in Chapter 2, which recovers the sparse signal with some accuracy, but fails to reach the desired accuracy. Figure 6-7 shows the recovered 1D sparse signal by PSO but could not achieve the desired recovery. Figure 6-8 shows the recovered signal from IRLS k-sparse signal from a limited set of observations.

Figure 6-9 depicts the recovered k-sparse signal from its undersampled data. The proposed Nature Inspired Iterative Reweighted Least Square (NI-IRLS) method achieves the best reconstruction. The figure demonstrates the effectiveness of the NI-IRLS algorithm in accurately estimating the sparsity level of the original signal and precisely recovering the amplitudes of the non-zero elements.

Figure 6-10 demonstrates the cost function minimisation process using the proposed Nature Inspired Iterative Reweighted Least Square (NI-IRLS) Method, revealing its advantages over other algorithms trapped in local minima. While traditional algorithms struggle to minimise the cost function and might become stuck in suboptimal solutions, the NI-IRLS method inherent randomness allows it to explore a broader solution space, effectively recovering from local minima and eventually reaching a near-optimal solution. This ability to escape local minima and explore diverse solutions enhances the algorithms' performance, making it more reliable and efficient in achieving better cost function minimisation during sparse signal recovery.

In Figure 6-11, the performance of different techniques is evaluated and compared to the NI-IRLS method in terms of MSE. The results indicate that the proposed NI-IRLS method outperforms the other techniques, achieving the minimum MSE. The lower MSE values obtained with NI-IRLS demonstrate its superior accuracy in reconstructing the sparse signal compared to the alternative methods. These findings validate the effectiveness of the NI-IRLS approach as a powerful and reliable technique for sparse signal recovery, making it a promising choice for applications requiring precise and efficient reconstruction of sparse signals.

In Figure 6-12, the performance of different methods is assessed and compared to the Nature Inspired Iterative Reweighted Least Square (NI-IRLS) algorithm in terms of SNR. The results reveal that the proposed NI-IRLS algorithm achieves the highest SNR among

all the methods under evaluation. The superior SNR NI-IRLS method achieves highlights its effectiveness and reliability in sparse signal recovery in a noisy environment.

Figure 6-13 shows the normalized successful recovery attained by each method while keeping by varying the percentage of sparsity levels in the test signal with a success criterion of MSE value at  $10^{-3}$ . Each method runs through 30 iterations, with the number of successes divided by the total number of iterations at each level of sparsity. The correct reconstruction of the original k-sparse signal using different recovery techniques is referred to in this context as successful recovery. The graphic illustration shows the efficiency of the proposed NI-IRLS method in successfully recovering the sparse signal, even in the presence of 20% non-zero elements only showcasing its efficacy to recover the compressively sampled 1D k-sparse signal.

The recovery process involves taking the undersampled data and applying the NI-IRLS method, which combines nature-inspired optimisation techniques and IRLS methods. Through this approach, the algorithm can intelligently adapt to the sparsity level of the signal, efficiently identifying the locations of the non-zero elements, and accurately reconstructing their amplitudes.

The successful recovery of the k-sparse signal shown above highlights the robustness and accuracy of the NI-IRLS method. It demonstrates that the proposed algorithm can handle sparse signals and effectively recover their essential components even from limited and undersampled data. The results emphasise the potential of the NI-IRLS technique for applications involving sparse signal recoveries, such as in medical imaging, signal processing, and data compression, where precise and efficient reconstruction is crucial.

## 6.6 Experimental Results and Discussion for CS MRI Recovery

Random sampling during CS image collection produces incoherent and noise-like effects in the sparsifying domain. The analytical recovery method, where un-sampled k-space data are substituted with zero and the resulting image is recovered using IFFT, causes artefacts that resemble additive Gaussian noise when applied to Fourier domain encoded biomedical imaging, such as MR imaging. The undersampling patterns determine what kind of noise is produced by sub-sampling [99].

Drawing a comparison between CS encoding and noisy images, compressed sensing recovery transforms into an image-denoising task. A real human brain MR image with

dimensions of 256 x 256 and a 2-D compressively sampled phantom MRI are recovered using the suggested approach. The St. Mary's Hospital in London provided both MRI data.

The results from the phantom MRI are presented first. The phantom MRI is compressively sampled by retaining only 25% of the samples using a random undersampling mask in k-space. The methods used for qualitative comparison of the proposed NI-IRLS algorithm are ZF, LR, SSF, POCS, IRLS, Modified IRLS, and PSO.

The proposed algorithm has outperformed all the methods, as evident from Figure 6-14. In Figure 6-14 (a), the recovered images along with the zoomed-in portion for further clarity by the proposed NI-IRLS method and other methods alongside the original image are shown. Evidently that the recovered image from NI-IRLS closely matches the original image. Figure 6-14 (b) shows the masks used for undersampling the original image. The original image is fully sampled, and LR uses the specific centric circle of the k-space. All other methods used the same random mask with only 25% values set as 1, while the remaining values are set to 0. In Figure 6-14 (c), the amplified difference between the original and recovered images by the factor of 1000 is depicted. Here it is visible that the proposed NI-IRLS method' recovered image is closer to the original image, and very few differences could be found. The LR method fails to recover the edges as only centric k-space data is acquired. The ZF method has introduced Gaussian noise-like artefacts in the recovered image. Other methods use the recovered image by ZF as the initial estimate of the image.

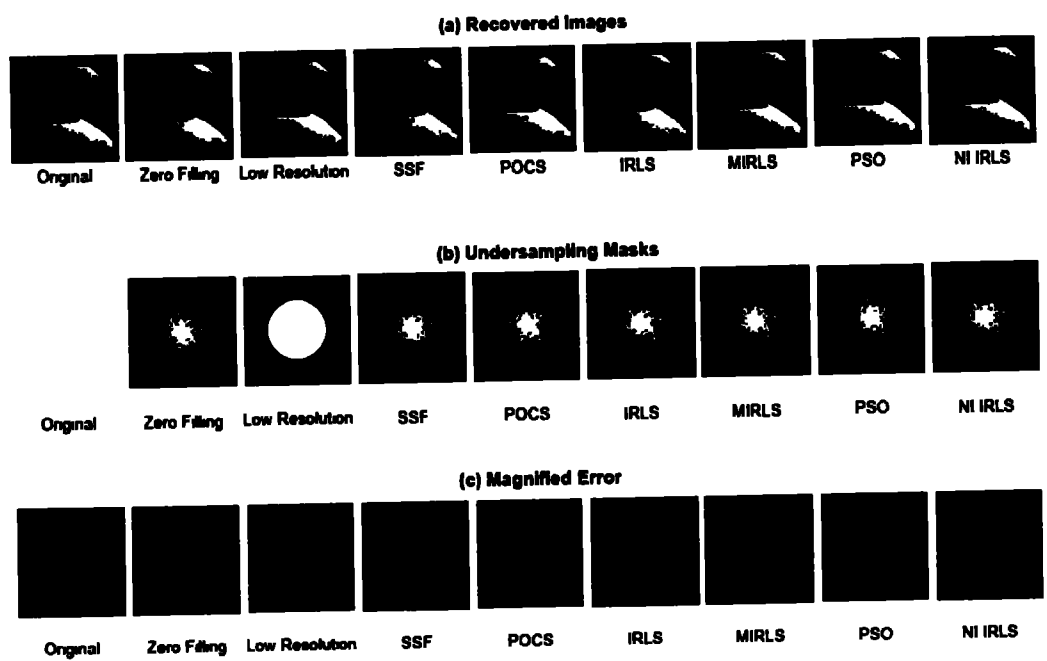


Figure 6-14: Illustrates (a) Zoomed-in recovered phantom MRI, (b) Masks for Undersampling, (c) Magnified Difference of Original and Recovered Phantom MRI.

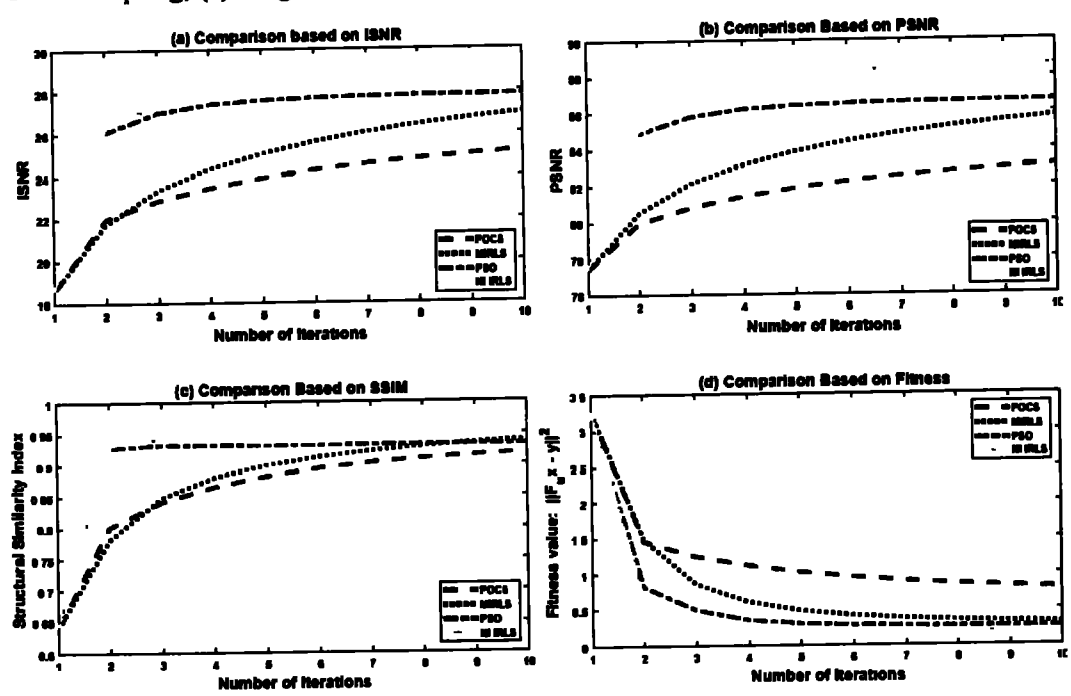


Figure 6-15: ISNR, PSNR, SSIM and Fitness achieved by NI-IRLS vs. other Methods for recovery of Phantom MRI.

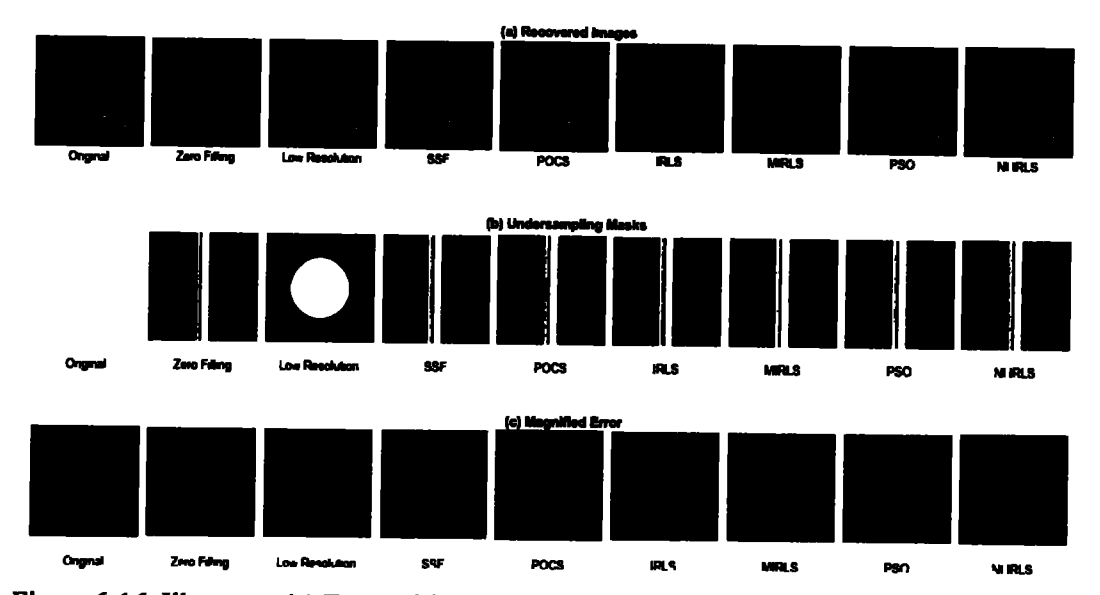


Figure 6-16: Illustrates (a) Zoomed-in recovered Brain MRI, (b) Masks for Undersampling, (c) Magnified Difference of Original and recovered Brain MRI Images.

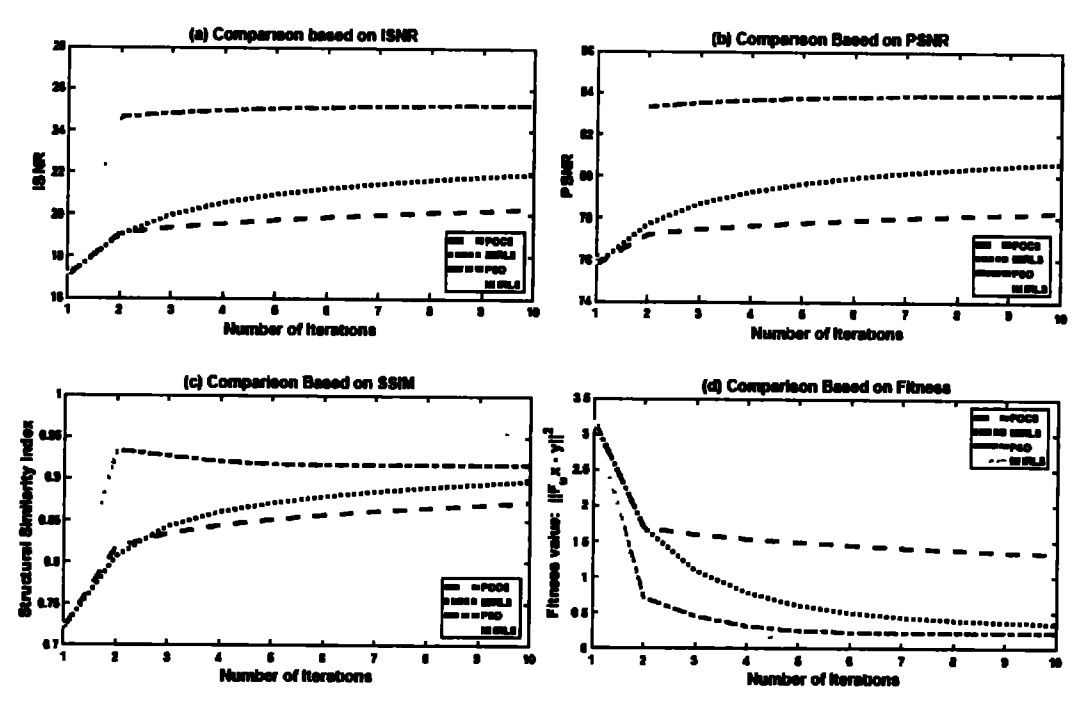


Figure 6-17: Comparison of ISNR, PSNR, SSIM and Fitness for recovery of CS Brain MRI at each iteration.

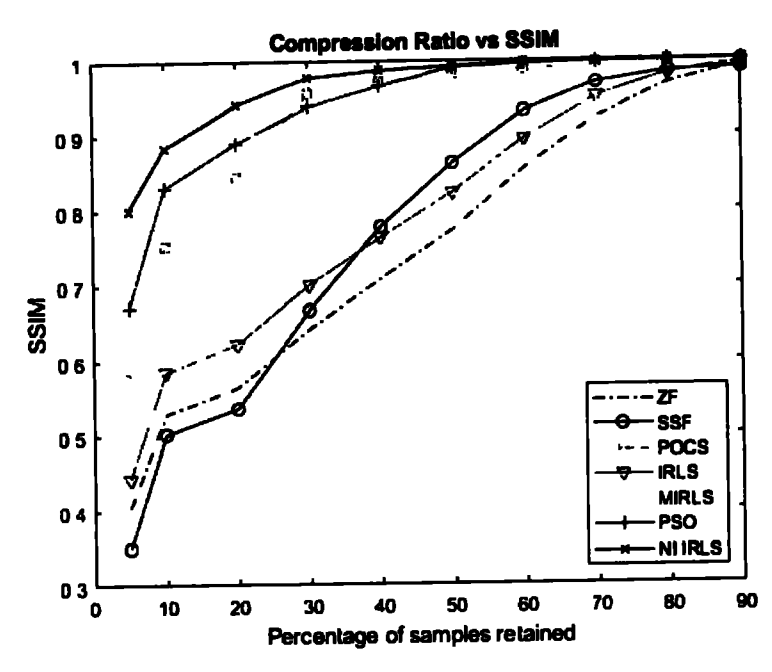


Figure 6-18: The SSIM achieved by varying compression ratio using NI-IRLS vs. other comparison methods.

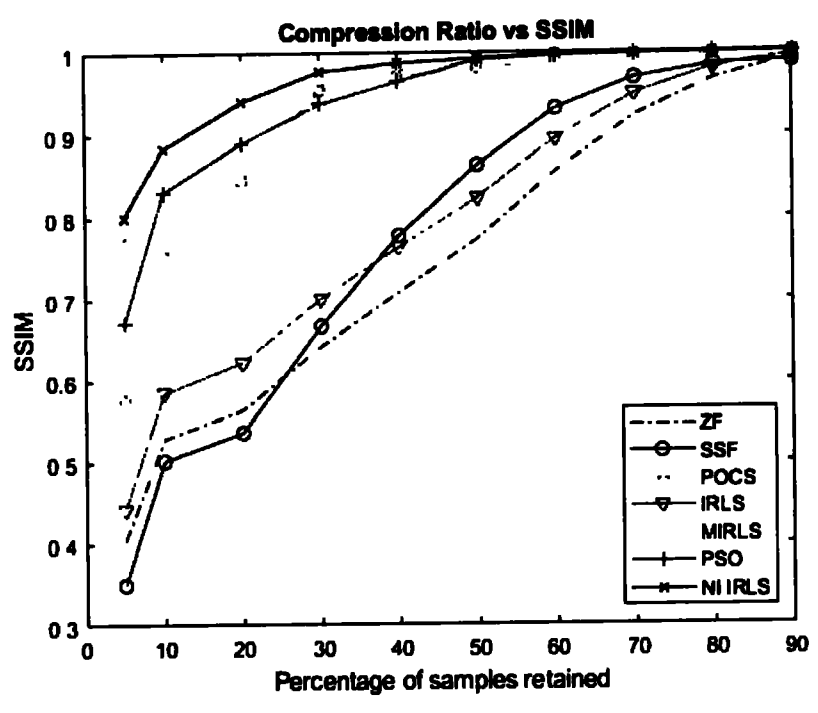


Figure 6-19: The PSNR achieved by varying compression ratio using NI-IRLS vs. other comparison methods.

Figure 6-15 quantitatively assesses the proposed NI-IRLS method's efficiency when applied to phantom MRI, comparing it with other techniques like POCS, Modified IRLS, and PSO. The evaluation is based on various metrics: ISNR, PSNR, SSIM, and Fitness. In Figure 6-15 (a), the ISNR comparison between POCS and the proposed NI-IRLS algorithm indicates that the proposed method improves ISNR. Similarly, Figure 6-15 (b) illustrates the improvement in PSNR achieved by using the proposed method. Furthermore, Figure 6-15(c) shows an increase in SSIM, denoting a better similarity between the recovered and original images when the proposed algorithm is applied. Lastly, Figure 6-15 (d) portrays a decrease in fitness, indicating that the proposed NI-IRLS algorithm outperforms other methods in terms of fitness during the signal CS MRI recovery process. These results collectively demonstrate the effectiveness and superiority of the proposed NI-IRLS method for enhancing the quality and accuracy of the reconstructed phantom MRI from undersampled k-space data.

The experimental results from Real Human Brain MRI are presented, where the MRI data is compressively sampled, retaining only 25% of the samples using a Cartesian undersampling mask in k-space. The proposed NI-IRLS algorithm is qualitatively compared with ZF, LR, SSF, POCS, IRLS, Modified IRLS, and PSO methods. Figure 6-16 shows that the proposed algorithm outperforms all other methods. In Figure 6-16 (a), the recovered images are shown alongside a zoomed-in portion for better clarity, illustrating the performance of NI-IRLS and other methods compared to the original image. The recovered image from NI-IRLS closely matches the original image. Figure 6-16 (b) depicts the masks used for undersampling the original image, with LR using specific centric ordered data of the k-space while all other methods use the same Cartesian mask with only 25% values set as 1, while the rest of the values are set as 0. Cartesian mask undersampling results in an aliasing artefact in recovered images. Figure 6-16 (c) amplifies the difference between the original image and the recovered image by a factor of 1000, clearly showing that NI-IRLS produces a recovered image closer to the original with minimal differences. The aliasing effect is clearly visible in the amplified error. The LR fails to recover edges due to limited data acquisition, and ZF introduces aliasing artefacts in the recovered image. Notably, the ZF-recovered image is used as the initial estimate for other methods. The results demonstrate the superiority of the proposed NI-IRLS algorithm in accurately

reconstructing real human brain MRI images even with significant undersampling, showcasing its potential for practical applications in medical imaging.

Figure 6-18 illustrates the Structural Similarity Index (SSIM) achieved in the reconstruction of Compressed Sensing (CS) Brain MRI for the proposed method and other techniques, with varying compression ratios ranging from 5% to 90%. The compression ratio represents the percentage of samples retained during k-space data acquisition, wherein higher percentages indicate more data is acquired, resulting in better recovery but longer MRI scanning time. The proposed NI-IRLS method consistently achieves the highest SSIM across different compression ratios. This demonstrates the algorithm's superior performance in accurately reconstructing CS Brain MRI images, even under various levels of data compression, making it an efficient and effective solution for achieving high-quality MRI reconstructions with reduced scanning time.

Figure 6-19 presents the PSNR achieved in the reconstruction of CS Brain MRI using the proposed method and other techniques. The compression ratios vary from 5% to 90%, representing the percentage of samples retained during k-space data acquisition, with higher ratios indicating more data is acquired, leading to better recovery at the cost of longer MRI scanning time. Importantly, the proposed NI-IRLS method consistently attains the highest PSNR across different compression ratios. This consistently high PSNR demonstrates the algorithm's exceptional performance in accurately reconstructing CS Brain MRI images, even under various levels of data compression. As a result, the NI-IRLS method proves to be an efficient and effective solution for achieving high-quality MRI reconstructions while reducing scanning time, making it a valuable approach for practical medical imaging applications.

#### 6.7 Conclusions

The proposed NI-IRLS method introduces an innovative approach to address the non-linear recovery challenges posed by Compressed Sensing (CS) through a fusion of deterministic and evolutionary techniques. The method underwent rigorous evaluation of 1D k-sparse signals, 2D phantom MRI, and real human brain MRI to validate its effectiveness. The subjective analysis of experimental results demonstrated the notable proficiency of the proposed method in accurately reconstructing 1D sparse signals and 2D MRI from their compressively sampled data, preserving critical image details. Moreover, the objective

analysis based on fitness, SNR, and MSE revealed the superiority of the NI-IRLS method over alternative recovery techniques when dealing with 1D signals, displaying its adaptability in handling varying sparsity levels. Quantitative assessments based on ISNR, PSNR, SSIM, and fitness for CS MRI reconstruction, both for phantom and real human brain MRI, clearly established the NI-IRLS method's superiority over other methods, indicating its capability to achieve high-quality and reliable MRI reconstructions. The Cartesian undersampling produces aliasing artefacts, while random undersampling introduces Gaussian noise-like artefacts. The proposed method could mitigate the effects of both these types of noises in the reconstructed image, showing the robustness of the proposed method under any type of noise. Even in scenarios with varying compression ratios, the NI-IRLS method consistently showcased excellent performance, solidifying its efficiency and reliability, making it a highly effective approach for practical medical imaging applications. The promising results of the proposed method open new possibilities for enhanced medical imaging technology and advanced diagnostic applications.

#### CHAPTER 7

# CS MRI RECOVERY USING HEURISTIC

# APPROXIMATION OF $l_1$ NORM

In this chapter, novel approaches are introduced for recovering k-sparse signals and MR images from compressed measurements, employing a combination of heuristic techniques such as Particle Swarm Optimisation (PSO) and deterministic smooth approximations of  $l_1$ -norm-based IST methods. The proposed framework, integrates suitable penalty to enhance the minimisation of the heuristic algorithm's loss function and accurately estimates the actual k-sparse signal. Additionally, the algorithm is extended to address the specific challenge of recovering CS MRI from incomplete k-space data in the context of Fourier-encoded MR images. This modified algorithm incorporates the principles of smooth  $l_1$  norm approximation by hyperbolic tangent and evolutionary computing techniques, specifically Genetic Algorithms. By integrating these methodologies, the proposed techniques facilitate efficient and effective recovery of biomedical images, using incomplete and under-sampled Fourier data. The presented algorithms offer distinct advantages in accelerating convergence, precise estimation of sparse signals, and successful recovery of biomedical images from compressed measurements. These advancements contribute significantly to signal recovery, particularly in the context of compressive sensing and Fourier-encoded MR imaging.

## 7.1 Heuristic Algorithms

Deterministic algorithms, renowned for their mathematical elegance, often require well-defined initial solutions, making them less user-friendly for various applications. On the other hand, evolutionary algorithms like PSO offer simpler implementations but may lack rigorous mathematical foundations [131]. While these algorithms are typically used for unconstrained search problems, applying them to constrained optimisation can be challenging [132-135]. However, heuristic algorithms like GA and PSO are well-suited for handling computationally complex problems that are not amenable to traditional

approaches. Despite the absence of strict mathematical modelling, these heuristic algorithms offer practical and efficient solutions.

$$2 = \operatorname{agrmin} (\|\mathbf{y} - \mathbf{\Phi}\mathbf{z}\|_{2}^{2} \text{ subject to } \|\mathbf{z}\|_{0} \le k$$
 (7.1)

However, a deterministic algorithm is needed to solve the  $l_0$  norm-based minimisation problem in Eq. (7.1) to hasten convergence [136].

### 7.2 l<sub>1</sub>-norm Approximation by Hyperbolic Tangent

Compressed sensing (CS) aims to reconstruct undersampled signals by minimising the  $l_1$ -norm of the solution, promoting sparsity where only a few elements are nonzero. This is particularly advantageous for naturally sparse signals, like MRI images on the appropriate basis, as it facilitates accurate and efficient reconstruction from limited data.

Consider a signal represented as a vector  $z \in \mathbb{R}^n$ . Let  $y \in \mathbb{C}^m$  be the undersampled measurements of the signal. The CS recovery function is written as follows:

$$f(x) = \frac{1}{2} \| y - \Phi \Psi^{H} z \|_{2}^{2} + \lambda \| z \|_{1}$$
 (7.2)

Here,  $\phi$  defines the sampling matrix for signal x, while  $\Psi$  is a sparsifying domain. The parameter  $\lambda$  in Eq. (7.2) is crucial parameter for the trade-off between fidelity and sparsity. The effectiveness of our algorithm depends on choosing the right threshold level. Depending on the signal size and its noise variance, we used the fixed value expression [115].

$$\lambda = \sigma_{\nu} \sqrt{2\ln\left(n\right)} \tag{7.3}$$

The noise standard variance is denoted by  $\sigma_v$ , and the length of the sparse signal is denoted by n. The tanh has many properties i.e., nonconvex, odd, analytical, smooth, monotonically increasing, bounded, and its curves at its origin are tuneable [123]. This is why we propose to use the tanh as an approximation for the  $l_1$ -norm in Eq. (7.2). The approximation is defined as follows:

$$\|\mathbf{z}\|_{1} \cong \sum_{i=1}^{n} z_{i} tanh(\gamma z_{i})$$
(7.4)

By selecting a relatively high value for the parameter  $\gamma$  to align with the tanh, the  $l_1$ -norm is smoothly approximated that is differentiable, resulting in the expression of Eq. (7.2):

$$f(z) = \frac{1}{2} \| y - \Phi \Psi^{H} z \|_{2}^{2} + \lambda \sum_{i=1}^{n} z_{i} \tanh(\gamma z_{i})$$
 (7.5)

To enable the application of the steepest descent algorithm, it is essential to rewrite the expression in element form, as depicted in Eq. (7.5), to facilitate the computation of partial derivatives. By introducing the notation,  $\mathbf{A} = \mathbf{\Phi} \mathbf{\Psi}^{\mathbf{H}}$ , we can express the element-wise equation as follows:

$$f(z) = \frac{1}{2} \sum_{l} (Az - y)_{i} (Az - y)_{l} + \lambda z_{i} \tanh(\gamma z_{l})$$
 (7.6)

By introducing the notation  $A = \phi \Psi^H$ , we can formulate the partial derivative of Eq. (7.5) in element form as follows. This formulation allows us to calculate the derivatives regarding each element individually:

$$\frac{\partial f(z)}{\partial z_l} = \sum_{ij} A_{ij} A_{il} z_j - \sum_{l} y_l A_{il} + \lambda \left( \tanh(\gamma z_l) + z_l \gamma \left( 1 - \tanh^2(\gamma z_l) \right) \right)$$
(7.7)

So, the proposed steepest descent algorithm scheme can be defined as for its  $l^{th}$  update is:

$$(\Delta z)_l = -\eta \frac{\partial f(z)}{\partial z_l} \tag{7.8}$$

The steepest descent algorithm is employed to find a solution using Eq. (7.8). The iterative update process towards the steepest descent, allows the algorithm to minimise the objective function by iteratively adjusting the solution based on gradient information.

The tanh offers the advantage of the adjustable slope near the origin and is a function that is bounded, making it a preferable choice as an estimation for soft thresholding (ST). Consequently, the mathematical description of tanh-based ST is represented as:

$$S_{\alpha,\beta}(q) \cong \begin{cases} cz(\tanh(\alpha(|q|-\beta))) & |q| > \beta \\ 0 & \text{otherwise} \end{cases}$$
 (7.9)

Eq. (4.38) encompasses a thresholding parameter,  $\beta$ , and a parameter  $\alpha$ , which governs the behaviour of the tanh. As  $\alpha$  tends to zero, the equation resembles a soft thresholding function, while approaching infinity transforms it into a hard thresholding function. Our proposed algorithm adopts an ST function initially, transitioning to a hard thresholding function in later iterations, leading to enhanced reconstruction compared to conventional soft thresholding methods [123].

### 7.3 Particle Swarm Optimisation (PSO)

PSO is a probabilistic optimisation technique with a simple structure known as particle-based search optimisation [137-139]. In PSO, each particle's velocities are randomly assigned, allowing it to traverse the search space. The velocity of the particles is updated at each iteration using their prior velocity. The gap between their local and global best solutions. [140] provides the velocity update equation for the PSO-based algorithm.

$$v_i = w \times v_{i-1} + c_1 r_1 (p_i - x_{i-1}) + c_2 r_2 (p_g - z_{i-1})$$
(7.10)

Where  $r_1$  and  $r_2$  are two separately uniformly distributed random values in the range (0,1) and  $c_1$ ,  $c_2$  are problem-dependent constants. Inertial weight is represented by the scalar  $w \in [0,1]$ . The particle known as the global best, or  $p_g$ , has the finest fitness across the board.  $p_i$  is the local best, which, according to the cost function, reflects the best prior position of the  $i^{th}$  particle. The algorithm's performance can be significantly impacted by changing the free parameters  $c_1$ ,  $c_2$ , and the inertia weight w [141].

The position  $z_i$  of the  $i^{th}$  particle is updated in the conventional PSO by its velocity:

$$z_l = z_{l-1} + v_l (7.11)$$

The Basic PSO algorithm begins with a random population of 20-50 particles, depending on the specific challenge. During each iteration, particles move according to their velocity, updated based on local and global optimal positions.

## 7.4 Heuristic Smooth Approximation of $l_1$ -norm (H-SL1)

The proposed H-SL1 algorithm introduces a combination of two different algorithms, namely PSO and smooth approximation of  $l_1$ -norm [12, 22] to address the problem of recovering a k-sparse 1-D signal and performing CS MRI. The aim is to solve the constrained optimisation problem defined by Eq. (7.2).

To ensure the sparsity in the solution, all particles of the population are initialised, and the technique applies soft thresholding based on the IRLS algorithm. Though, the particles after velocity update can lose sparsity. Therefore, after each position update, another round of soft thresholding defined by Eq. (7.9) is performed to maintain the sparsity constraint throughout the recovery process.

In situations where the fitness of the global best particle remains unchanged for a specified number of iterations, the SL1 is employed. This algorithm updates the position

of the second-best particle in the population, using a specific strategy elaborated in Algorithm 1 and Algorithm 2. This helps to improve the convergence and accuracy of the algorithm in finding the optimal solution. Overall, the proposed technique combines the strengths of PSO and smooth approximation of  $l_1$ -norm to address the k-sparse 1-D signal and CS MRI recovery problem by ensuring sparsity and enhancing the optimisation process.

The backpropagation error E is defined as Eq. (7.12).

$$\mathbf{E} = \mathbf{F_u}^{\mathsf{T}} (\mathbf{y} - \mathbf{\Phi} \mathbf{\Psi} \mathbf{z}_k) + \mathbf{\Psi} \mathbf{z}_k \tag{7.12}$$

The  $\gamma$  parameter is used to tackle the varying compression ratio of the MRI to be estimated defined by Eq.

$$\gamma = 100 - compression ratio.$$
 (7.13)

The parameter  $\gamma$  is introduced to address varying compression ratios (CR) of the undersampled k-sparse signal. This adjustability empowers the algorithm to dynamically adapt to different degrees of data compression. By modifying  $\gamma$  based on the specific CR, the algorithm can effectively tailor its reconstruction approach, accommodating different levels of sparsity in the signal. The experimentation section provides evidence that the algorithm's flexibility yields promising results, showcasing its ability to handle varying CRs and consistently produce accurate reconstructions, making it a versatile and reliable solution for sparse signal recovery tasks across diverse data compression scenarios as shown in Figure 7-17 and Figure 7-18.

The data consistency constraint in the frequency domain is a fundamental principle in CS MRI reconstruction defined by Eq. (7.14). It ensures that the actual samples acquired in the k-space domain remain constant throughout the recovery process. The measured data points in the frequency domain, which correspond to the acquired MRI measurements, are preserved, and not altered during the iterations of the recovery algorithm. The data consistency constraint is crucial because it guarantees that the recovered image remains consistent with the acquired data. It prevents the algorithm from introducing spurious information or modifying the original measurements, which could lead to erroneous results. By preserving the actual samples from the k-space domain, the algorithm ensures that the recovered image accurately represents the underlying structure of the imaged object, even with limited or under-sampled data. The data consistency constraint in the frequency

domain is a vital aspect of CS MRI recovery, as it maintains the integrity of the acquired data and helps achieve reliable and accurate image reconstruction.

$$\mathbf{Y}_{l}[j] = \mathbf{F}_{\mathbf{u}}(\mathbf{X}_{l}) \text{ (FFT of Estimated Image)}$$

$$\mathbf{Y}_{l}[j] = \begin{cases} \mathbf{y}_{l}[j] & \text{if } \mathbf{y}[j] = 0 \\ \mathbf{y}[j] & \text{otherwise} \end{cases}$$

$$\mathbf{x}_{l,1}$$

$$\mathbf{x}_{l,2}$$

$$\mathbf{x}_{l,2}$$
Recovery, technique of proposed algorithm

Figure 7-1: Two Initial Inputs for H-SL1 from ZF and LR and generated output from the proposed algorithm

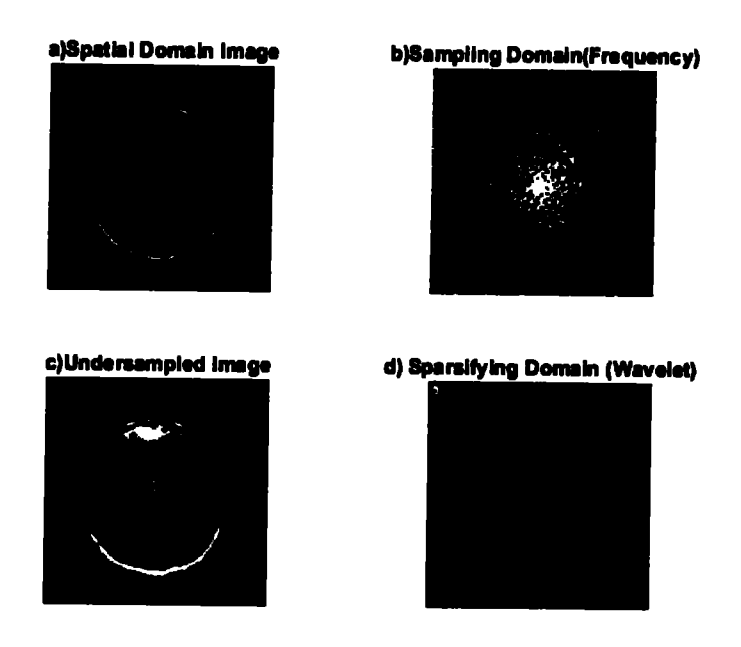


Figure 7-2: Different domains used in the proposed algorithm.

Figure 7-1 illustrates the two initializations used for the proposed algorithm Low Resolution (LR) and Zero Filling (ZF), which are crucial for fitness comparison during optimisation. The LR initialization involves reconstructing the initial image from low-resolution measurements, providing a coarse estimation with limited details. On the other hand, the ZF initialization fills the missing k-space data with zeros, creating an initial image with potential artefacts. Both initializations are then evaluated based on fitness measures to determine which better approximates the original image. The initialization with superior fitness is the global best solution, becoming the starting point for subsequent optimisation steps, enhancing the likelihood of achieving a high-quality reconstructed image through the algorithm's optimisation process.

In Figure 7-2, the proposed technique for image reconstruction is illustrated, showcasing different domains involved in the process (a) shows the original Image, this domain represents the original image, which serves as the reference for the entire reconstruction process. It contains complete information about the image without any loss or compression. (b) depict the k-space sampling domain, in this domain, the k-space data is generated by applying masks to the original image. The masks are applied for undersampling the k-space data, meaning that only a subset of the k-space samples is acquired, reducing data acquisition time. (c) elaborates the effects of undersampling in the Spatial Domain, after undersampling in the k-space domain, the effects of this undersampling are depicted in the spatial domain. The spatial domain is the familiar domain where we perceive images with their pixel values. Due to undersampling, the reconstructed image in this domain will exhibit artefacts and degradation compared to the original image. (d) In our proposed method, the Sparsifying Domain i.e., Wavelet, the undersampled k-space data is processed through a sparsifying process that involving shrinkage. Sparsifying transforms the k-space data into a sparse representation, where most coefficients are set to zero or close to zero, highlighting the sparsity of the data. Shrinkage, in this context, refers to reducing the magnitudes of non-zero coefficients, further enhancing the sparsity.

**Task:** Recovery of k – sparse signal  $z \in \mathbb{R}^n$  that minimises the objective function:

$$f(z) = \operatorname{argmin}_{z} \left(\frac{1}{2} \| \mathbf{y} - \Phi \Psi^{\mathsf{H}} \mathbf{z} \|_{2}^{2} + \lambda \sum_{i=1}^{n} z_{i} \tanh(\gamma z_{i})\right)$$

Input: Dictionary  $\Phi \in R^{m \times n}$ , Sparsity level k, Population size N, PSO parameters  $c_1, c_2$  and w Compressed Measurement  $y \in R^m$ , thresholding parameters:  $\alpha, \beta$ , constant  $\mu$ . Output: A Recovered k — sparse signal  $z \in R^n$ 

1) Initialisation: Initialise H - SL1 iteration number k = 0

Initial solution:  $\mathbf{z}_0 = [\mathbf{z}_1, \mathbf{z}_2, \dots, \mathbf{z}_n], \alpha = 1$ . Initial residual:  $\mathbf{r}_0 = \mathbf{y} - \Phi \mathbf{z}_0, V = 0$ , velocity matrix Generate N particles randomly with desired sparsity  $\mathbf{z} = [\mathbf{z}_1, \mathbf{z}_2, \dots, \mathbf{z}_n]$ , where  $\mathbf{z}_i \in \mathbf{R}^n$  and  $\|\mathbf{z}_i\|_0 \le k \ \forall i \le 1 \le N$ 

2) Fitness Evaluation and Sorting:

$$f_{z} = fitness(z_{1}, z_{2}, ..., z_{N}) = [f_{1}, f_{2}, ..., f_{N}]$$
Where  $f_{j} = (\Phi z_{i} - y)^{T}(\Phi z_{i} - y)$ 

$$[f_{zz} index] = sort(f_{z}, descend)$$

$$f_{zz} = [f_{z1}, f_{z2}, ..., f_{zN}] \text{ with } f_{z1} \leq f_{z2} \leq ... \leq f_{zN}$$

3) Initial local and global best

$$P = z_0(index) = [p_1, p_2, ..., p_N]$$
 where  $p_i$  has fitness  $f_{zi}$   $p_g = p_1$ , initial global best

- 4) H-SL1 Main Iteration: Increment k by 1, and apply the following steps
  - a) Velocity and Position update: Update Velocity and position defined by Eq. (7.10) and Eq. (7.11) respectively:  $V = velocity(V, P, z_0, p_g, c_1, c_2, w) = [v_1, v_2, ..., v_N]$   $Z = position(Z, V) = [[z_1]_k, [z_2]_k, ..., [z_N]_k], \text{ where } z_i = z_{i-1} + v_i$
  - b) Back Projection: Compute  $e = \Phi^T r_{k-1}$
  - c) Compute Gradient: Compute gradient by Eq. (7.7)
  - d) Steepest Descent Algorithm: Apply steepest descent algorithm using Eq. (7.8)
  - e) Shrinkage: Compute  $e_s = S_{\alpha,\beta}(e) \cong \begin{cases} cz(tanh(\alpha(|e|-\beta))) & |e| > \beta \\ 0 & otherwise \end{cases}$

Where c is a random number.

Update  $a_{k+1} = a_k * 1.5$  at each iteration (from soft to hard thresholding)  $z_2 = rand \times (e_s - z_r) + z_1$ 

where  $\mathbf{z}_{\tau}$  is a randomly selected from the population and CR is the compression ratio

f) Update local and global best based on fitness:

$$\begin{array}{l} f_{z2} = fitness(\mathbf{Z}) \\ [f_{z2s} \ index] = sort(f_{2s}, descend) \\ f_{z2s} = [f_{z21}, f_{z22}, ..., f_{z2N}] \ with \ f_{z21} \leq f_{z22} \leq ... \leq f_{z2N} \\ \mathbf{Z}_2 = \mathbf{Z}(index) \\ = [\mathbf{z}_{21}, \mathbf{z}_{22}, ..., \mathbf{z}_{2N}] \ where \ \mathbf{z}_{2i} \ has \ a \ fitness \ f_{x2i} \\ if \ f_{x21} \leq f_{z1}, then \ p_i = \mathbf{z}_{21} and \ f_{x1} = f_{x21}, (new \ global \ best) \\ else \ if \ f_{x2i} \leq f_{zi}, then \ p_i = \mathbf{z}_{2i} and \ f_{zi} = f_{z2i}, \forall i \leq 1 \leq N \ (local \ best) \end{array}$$

- g) Solution Update:  $Update z_k = p_l + \mu(e_s p_l)$
- h) Residual Update: Compute  $r_k = y \Phi z_k$
- i) Stopping Rule: Go to step (4) until, either  $||z_k z_{k-1}||_2^2 < threshold value or the maximum number of iterations criteria is met.$
- 5) Output: The final estimated solution is  $z_k$

### Algorithm 7.2: Proposed Algorithm for CS MR Image Recovery

Task: Find the value of image X that minimises the objective function:

$$f(X) = \underset{x}{\operatorname{argmin}}(\|Y - F_{w}X\|_{2}^{2} + \lambda \sum_{t=1}^{n} x_{t} tanh(\gamma x_{t}))$$

Input: Sampling Matrix  $\mathbf{F_u} \in R^{m \times n}$  , Sparsifying Transform  $\Psi$ , constant  $\mu$  ,

Measurement matrix (Undersampled)Y  $\in R^m$ , thresholding parameters:  $\alpha, \beta$ , constant  $\mu$ . Output: A Recovered Image X  $\in R^{nxm}$ 

- 1) Initialisation: Initialise IRLS iteration number k=0Initial solution:  $X_0=[x_1,x_2,.....x_{nxm}]$ Initial residual:  $R_0=Y-X_0$
- 2) Fitness Evaluation and Sorting:

$$[X_1, X_2, f_1 f_2] = fitness(X_{i1}, X_{i2}, Y)$$
  
Where  $f_j = (F_u X_{ij} - Y)^H (F_u x_{ij} - Y), j = 1, 2$   
With  $X_1 = \begin{cases} X_{i1}, & \text{if } f_1 \leq f_2 \\ X_{i2}, & \text{otherwise} \end{cases}$ 

- 3) H-SL1 Main Iteration: Increment i by 1, and apply the following steps
  - a) Back Projection: Compute  $E = F_u^{-1}(y_{i-1} F_u x_{i-1})$
  - b) Compute Gradient: Compute gradient by Eq. (7.7)
  - c) Steepest Descent Algorithm: Apply steepest descent algorithm using Eq. (7.8)
  - d) Shrinkage: Compute  $e_s = S_{\alpha,\beta}(e) \cong \begin{cases} cx(\tanh(\alpha(|e|-\beta))) & |e| > \beta \\ 0 & \text{otherwise} \end{cases}$

Where c is a random number.

Update  $a_{k+1} = a_k * 1.5$  at each iteration (from soft to hard thresholding) Where c is a random number.

$$X_n = \gamma \times (E_s - X_r) + X_2$$

where  $X_1$  is a randomly selected from either  $X_1$  or  $X_2$ ,

and y = 100 - compression ratio

e) Data Consistency in Fourier Domain

$$\begin{aligned} \mathbf{Y}_{t}[j] &= \mathbf{F}_{\mathbf{u}}(\mathbf{X}_{t}) \\ \mathbf{Y}_{t}[j] &= \begin{cases} \mathbf{y}_{t}[j] & \text{if } \mathbf{y}[j] = 0 \\ \mathbf{y}[j] & \text{otherwise} \end{cases} \end{aligned}$$

f) Reassignment as per fitness

$$X_t = F(X_n), f_t = (F_n X_t - Y)^H (F_n X_t - Y)$$
  
if  $f_t \le f_1, X_1 = X_t; X_2 = X_1;$   
else if  $f_t \le f_2, X_2 = X_1;$ 

- g) Solution Update: Compute  $X_i = X_{i-1} + \mu(E_s X_{i-1})$
- h) Residual Update: Compute  $R_i = Y F_{ii}X_i$
- i) Stopping Rule: Go to stp (2) until, either  $||X_l X_{l-1}||_2^2 < threshold value or the maximum number of iterations criteria is met.$
- 4) Output: The final value of  $X_k$

### 7.5 Experimental Results for Recovery of 1-D Signal

The one-dimensional sparse signal is recovered using the proposed technique. In this experiment, MATLAB is used to generate a random k-sparse signal of length n=512, with K=85 non-zero elements serving as the k-sparse signal's support. With just m=256 measurements taken, a random measurement matrix  $\Phi \in \mathbb{R}^{256x512}$  is employed to compressively sample the random sparse signal.

In this chapter, various recovery algorithms, including Least Square (LS), IRLS, PSO, PCD, SSF, and the novel Heuristic Smooth Approximation of  $l_1$ -norm (H-SL1), were utilised to recover a sparse signal. Performance comparison was achieved through MSE, SNR, and Cost Function (CF) minimisation. The algorithms were evaluated based on their potential to recover the 1D original k-sparse signal, with MSE quantifying the mean squared difference, SNR, and CF measuring the cost function's minimisation. These results offer valuable insights into the efficacy of the proposed H-SL1 algorithm for sparse signal recovery.

In Figure 7-3, the recovered k-sparse 1D signal using the linear recovery method Least Square (LS) based on  $l_2$ -norm is depicted. However, the results reveal that LS fails to promote sparsity in the estimated solution, leading to inaccuracies in reconstructing sparse signals. This highlights the methods' limitations in effectively identifying and reconstructing sparse components, emphasizing the need for alternative approaches to handle sparsity in signal recovery.

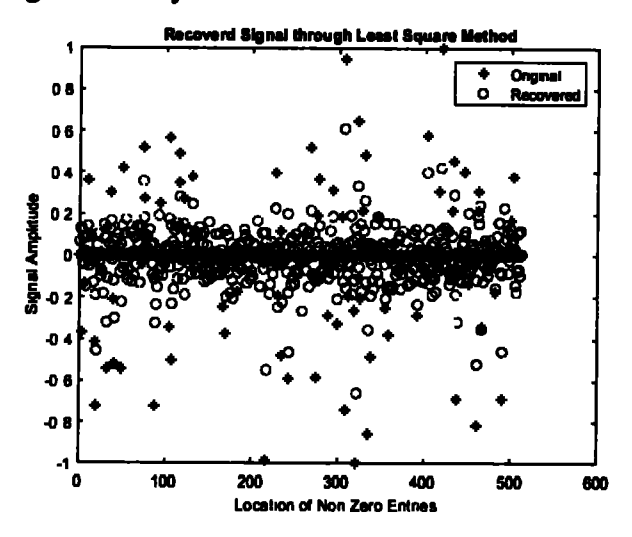


Figure 7-3: Recovered 1D k-sparse signal using LS

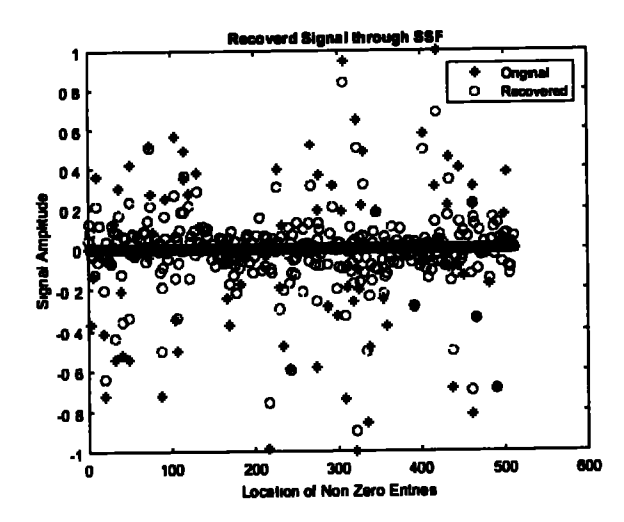


Figure 7-4: Recovered 1D k-sparse signal using SSF

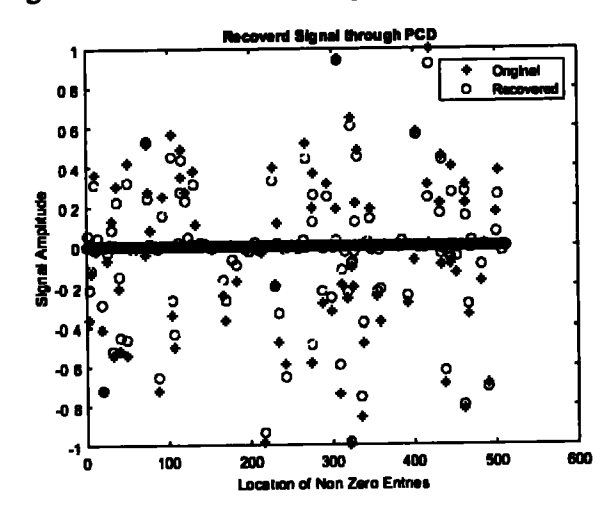


Figure 7-5: Recovered 1D k-sparse signal using PCD

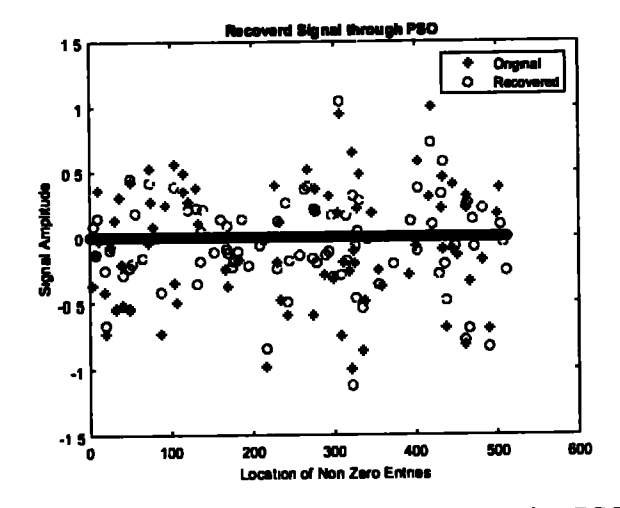


Figure 7-6: Recovered 1D k-sparse signal using PSO

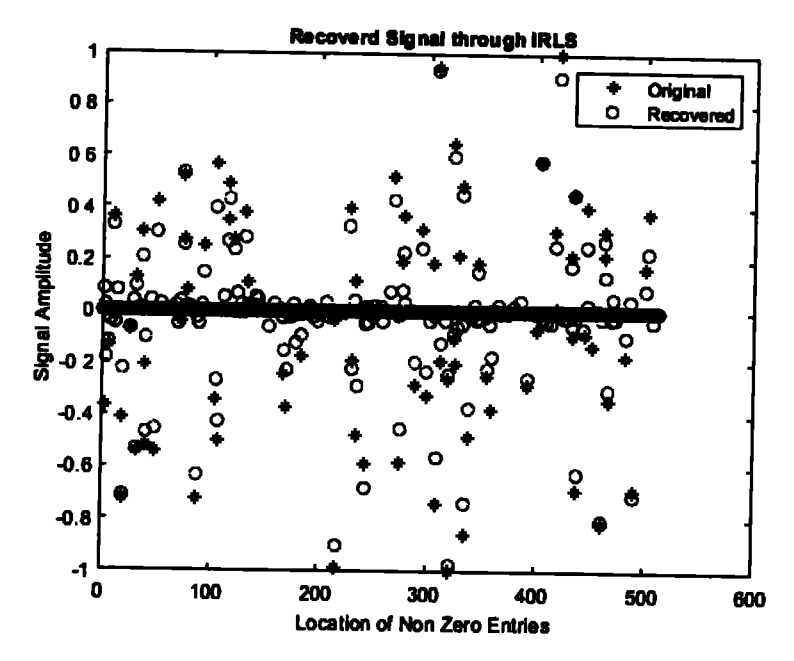


Figure 7-7: Recovered 1D k-sparse signal using IRLS

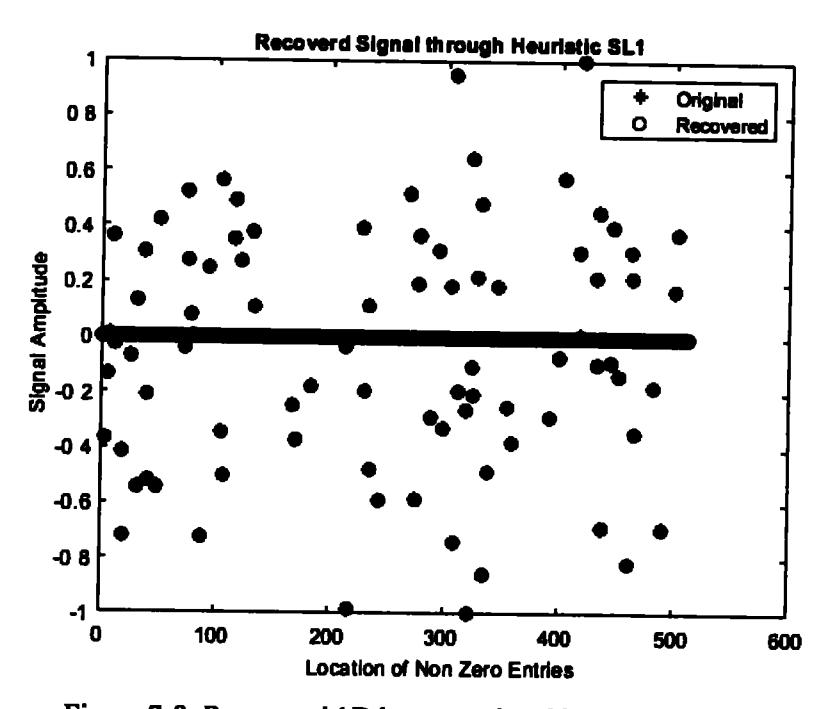


Figure 7-8: Recovered 1D k-sparse signal by Heuristic SL1

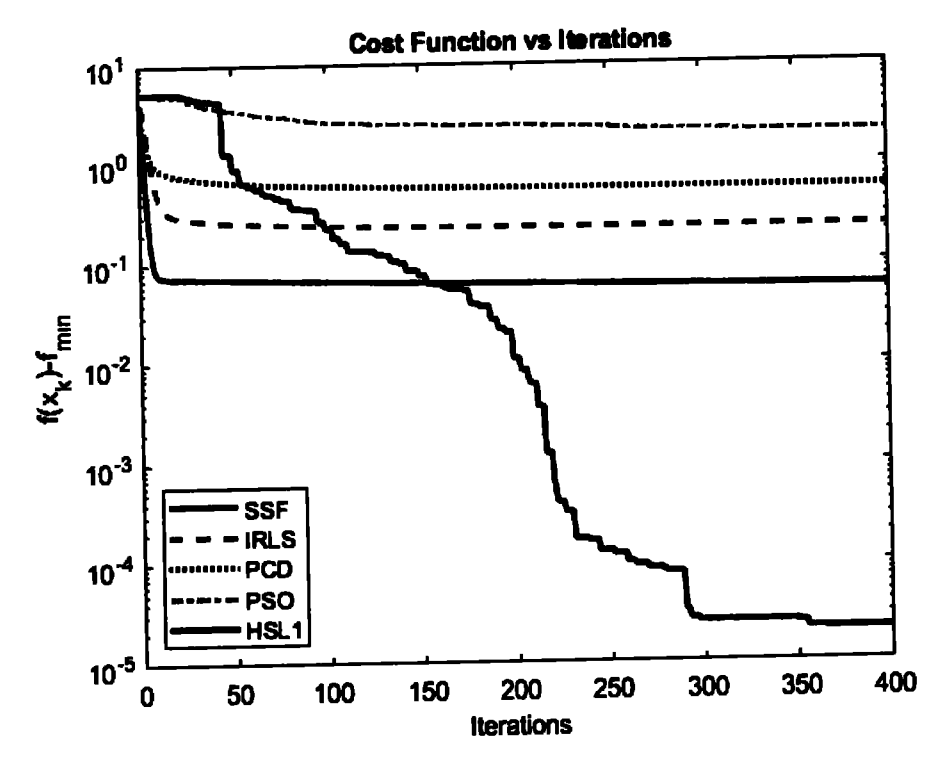


Figure 7-9: Cost Function minimised by H-SL1 vs. other methods

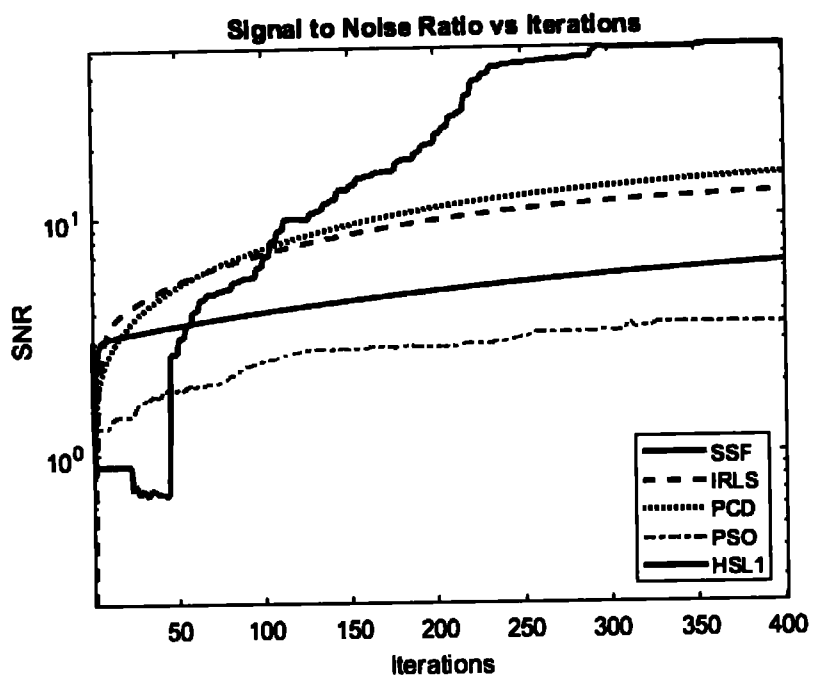


Figure 7-10: SNR achieved by H-SL1 vs. other methods

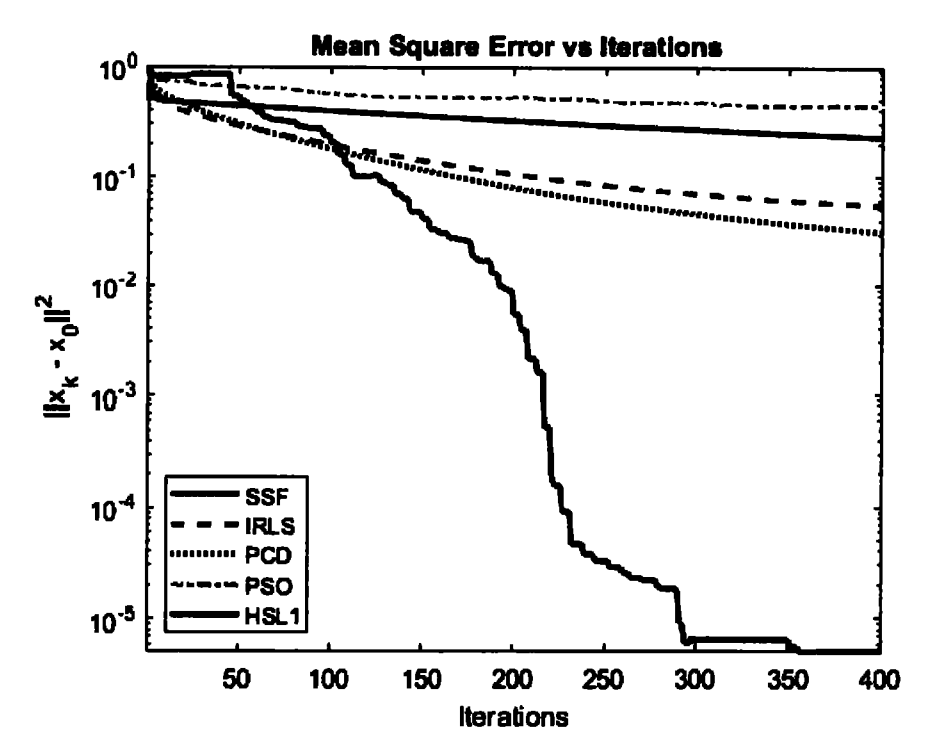


Figure 7-11: MSE minimised by proposed H-SL1 vs. other methods

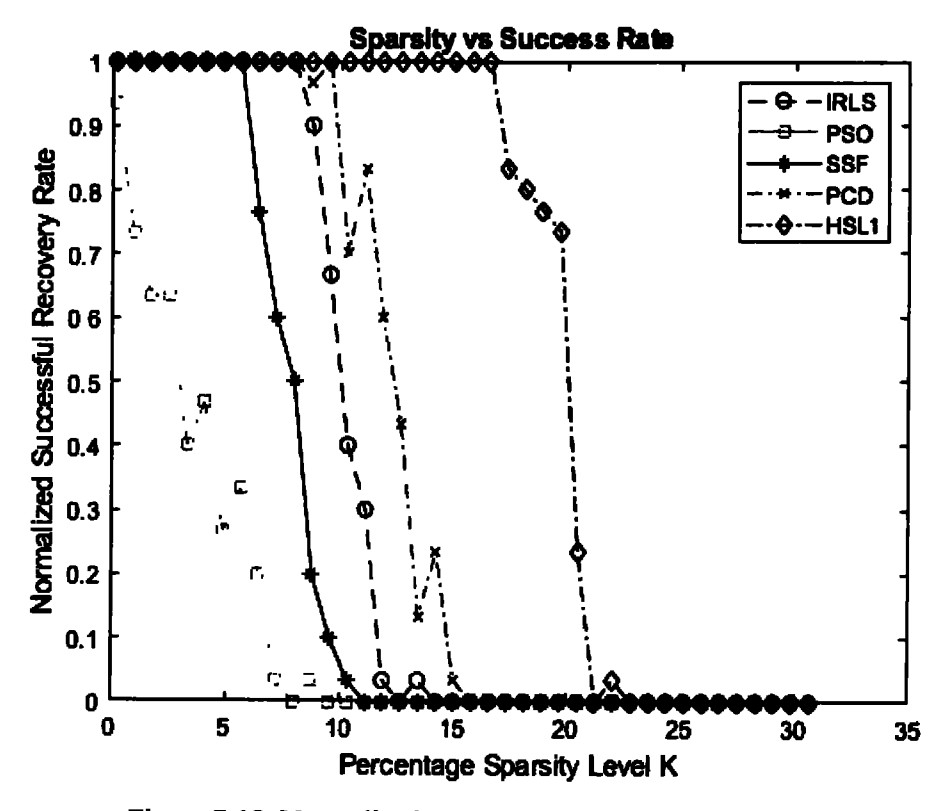


Figure 7-12: Normalized Success Rate by varying sparsity level

Figure 7-4 depicts the recovery of k-sparse 1D signal by SSF, which promotes sparsity but got stuck in local minima and failed to reach an optimal solution. Figure 7-5 shows the recovery by PCD, as discussed in Chapter 2, recovers the sparse signal with some accuracy, however, it fails to reach the desired accuracy. Figure 7-6 shows the recovered 1D sparse signal by PSO but the desired accuracy could not be achieved. Figure 7-7 shows the recovered signal from IRLS k-sparse signal from a limited set of observations.

In Figure 7-8, the recovered k-sparse signal from its undersampled data is depicted. The reconstruction is achieved using the proposed Heuristic Smooth approximation of  $l_1$ - norm (H-SL1) method. The figure demonstrates the effectiveness of the H-SL1 algorithm in accurately estimating the sparsity level of the original signal and precisely recovering the amplitudes of the non-zero elements.

Figure 7-9 demonstrates the cost function minimisation process using the proposed H-SL1 method, revealing its advantage over other algorithms that get trapped in local minima. While traditional algorithms struggle to minimise the cost function and might become stuck in suboptimal solutions, the H-SL1 method's inherent randomness allows it to explore a broader solution space, effectively recovering from local minima and eventually reaching a near-optimal solution. This ability to escape local minima and explore diverse solutions enhances the algorithm's performance, making it more reliable and efficient in improving cost function minimisation during sparse signal recovery.

In Figure 7-10, the performance of different methods is assessed and compared to the Proposed H-SL1 algorithm in terms of SNR. The results reveal that the proposed H-SL1 algorithm achieves the highest SNR among all the methods under evaluation. The superior SNR achieved by the proposed H-SL1 method highlights its effectiveness and reliability in sparse signal recovery in a noisy environment.

In Figure 7-11, the performance of different techniques is evaluated and compared to the H-SL1 method in terms of MSE. The results indicate that the proposed H-SL1 method outperforms the other techniques, achieving the minimum MSE. The lower MSE values obtained with H-SL1 demonstrate its superior accuracy in reconstructing the sparse signal compared to the alternative methods. These findings validate the effectiveness of the H-SL1 approach is a powerful and reliable technique for sparse signal recovery, making it a promising choice for applications requiring precise and efficient reconstruction of sparse signals.

Figure 7-12 shows the normalized successful recovery attained by each method while varying the percentage of sparsity levels in the test signal with a success criterion of MSE value at  $10^{-3}$ . Each method runs through 30 iterations, with the number of successes divided by the total number of iterations at each sparsity level. The correct reconstruction of the original k-sparse signal using different recovery techniques is referred to in this context as successful recovery. The graphic illustration shows the efficiency of the proposed H-SL1 method in successfully recovering the sparse signal, even in the presence of 20% non-zero elements showcasing its efficacy in faithfully recovering the compressively sampled 1D k-sparse signal.

The recovery process involves taking the undersampled data and applying the H-SL1 method, which combines heuristic optimisation techniques and smooth  $l_1$  norm methods. Through this approach, the algorithm can intelligently adapt to the sparsity level of the signal, efficiently identifying the locations of the non-zero elements and accurately reconstructing their amplitudes.

The successful recovery of the k-sparse signal shown above highlights the robustness and accuracy of the proposed H-SL1 method. It demonstrates that the proposed algorithm can handle sparse signals and recover their essential components even from limited and undersampled data. The results emphasize the potential of the H-SL1 technique for applications involving sparse signal recovery, such as in medical imaging, signal processing, and data compression, where precise and efficient reconstruction is crucial.

#### 7.6 Experimental Results and Discussion for CS MRI Recovery

Random sampling during CS image collection produces incoherent and noise-like effects in the sparsifying domain. The analytical recovery method, where missing k-space data is substituted with zero and the resulting recovered MRI is calculated using IFFT, causes artefacts that resemble additive Gaussian noise when applied to k-space encoded MRI. The undersampling patterns determine what kind of noise is produced by sub-sampling. [99].

Drawing a comparison between CS encoding and noisy images, compressed sensing reconstruction transforms into an image-denoising task. A Brain MRI with dimensions of  $256 \times 256$  and a 2-D compressively sampled phantom MRI are recovered using the suggested approach. The St. Mary's Hospital in London provided both the MRIs data.

The results from the phantom MRI are presented first. The phantom MRI is compressively sampled by retaining only 25% of the samples using a random undersampling mask in k-space. The methods used to qualitatively compare the proposed H-SL1 algorithm are ZF, LR, SSF, POCS, IRLS, Modified IRLS, and PSO.

The proposed algorithm has outperformed all the methods, as evident from Figure 7-13 for recovery of phantom CS MRI. In Figure 7-13 (a), the recovered images along with the zoomed-in portion for further clarity by the proposed H-SL1 method and other methods alongside the original image are shown. It is evident that the recovered image from H-SL1 closely matches the original image. Figure 7-13 (b) shows the masks the undersampled the original image. The original image is fully sampled, and LR uses the specific centric circle of the k-space. All other methods used the same random mask with only 25% values set as 1, while the remaining values are set to 0. In Figure 7-13 (c), the amplified difference between the original and recovered images by the factor of 1000 is depicted. Here it is visible that the proposed H-SL1 method recovered image is closer to the original image, and very few differences could be found. The LR method fails to recover the edges as only centric k-space data is acquired. The ZF method has introduced Gaussian noise-like artefacts in the recovered image. Other methods use the recovered image by ZF as the initial estimate of the image.

Figure 7-14 quantitatively assesses the proposed H-SL1 method efficiency when applied to phantom MRI, comparing it with other techniques like POCS, Modified IRLS, and PSO. The evaluation is based on various metrics, namely ISNR, PSNR, SSIM, and Fitness. In Figure 7-14 (a), the ISNR comparison between POCS and the proposed H-SL1 algorithm indicates that the proposed method improves ISNR. Similarly, Figure 7-14 (b) illustrates the improvement in PSNR achieved by using the proposed method. Furthermore, Figure 7-14 (c) shows an increase in SSIM, denoting a better similarity between the recovered and original images when the proposed algorithm is applied. Lastly, Figure 7-14 (d) portrays a decrease in fitness, indicating that the proposed H-SL1 algorithm outperforms other methods in terms of fitness during the signal CS MRI recovery process. These results collectively demonstrate the effectiveness and superiority of the proposed H-SL1 method for enhancing the quality of the reconstructed phantom MRI from undersampled k-space data.

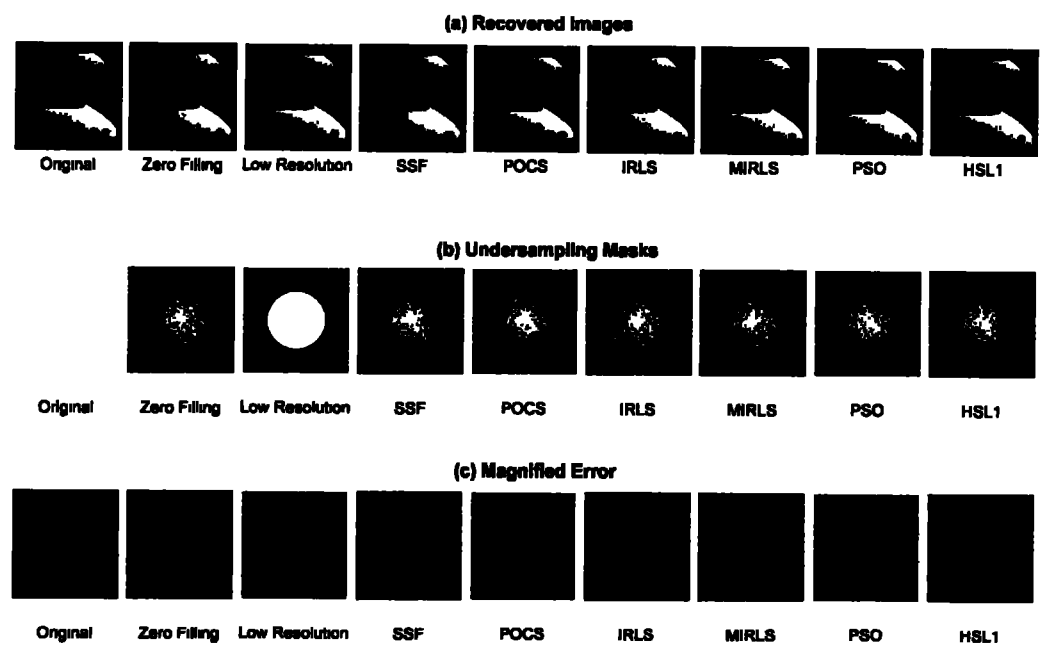


Figure 7-13: Illustrates (a) Zoomed-in recovered phantom MRI, (b) Masks for Undersampling, (c) Magnified Difference of Original and Recovered Phantom MRI.

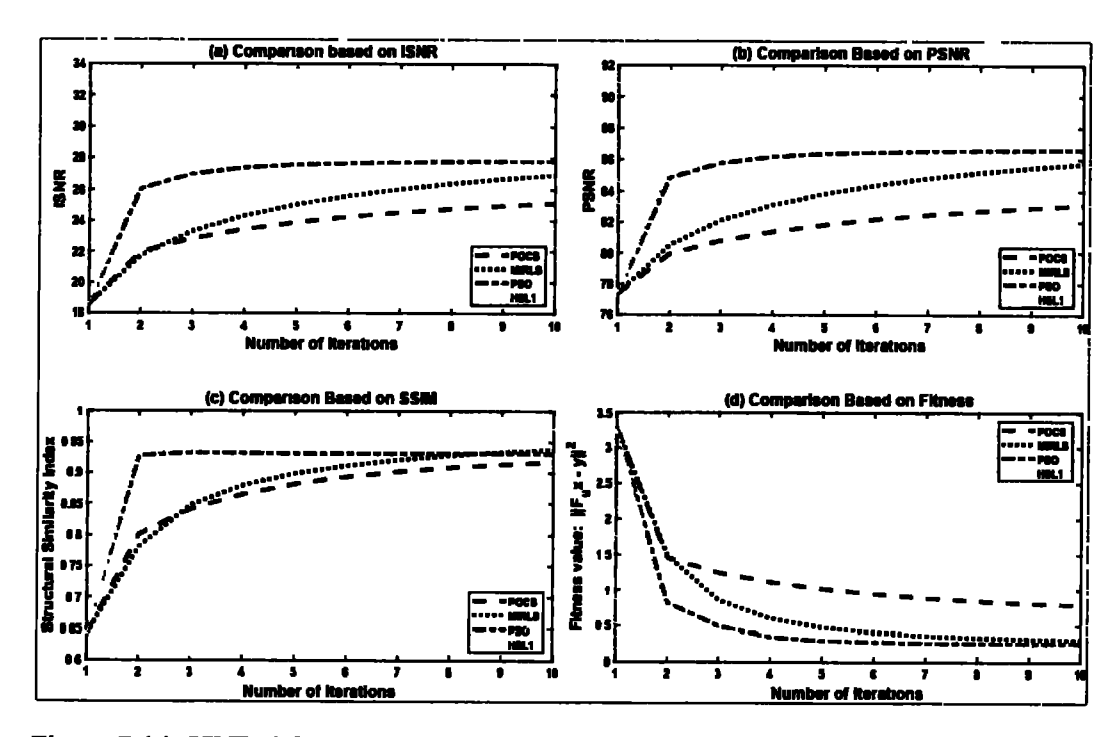


Figure 7-14: ISNR, PSNR, SSIM and Fitness achieved by H-SL1 vs. other Methods for recovery of Phantom MRI.

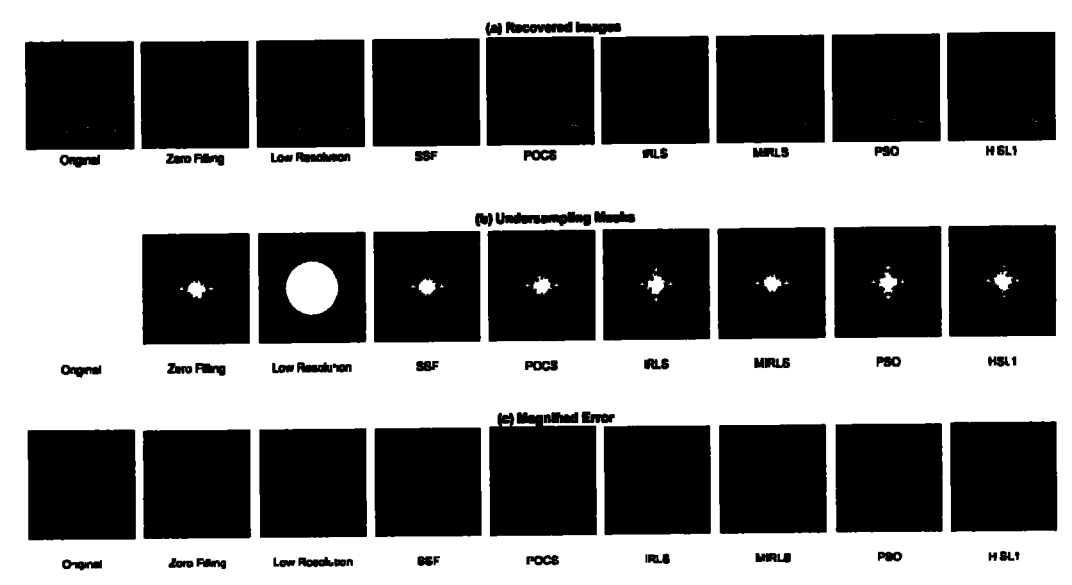


Figure 7-15: Illustrates (a) Zoomed-in recovered Brain MRI, (b) Masks for Undersampling, (c) Magnified Difference of Original and recovered Brain MRI Images.

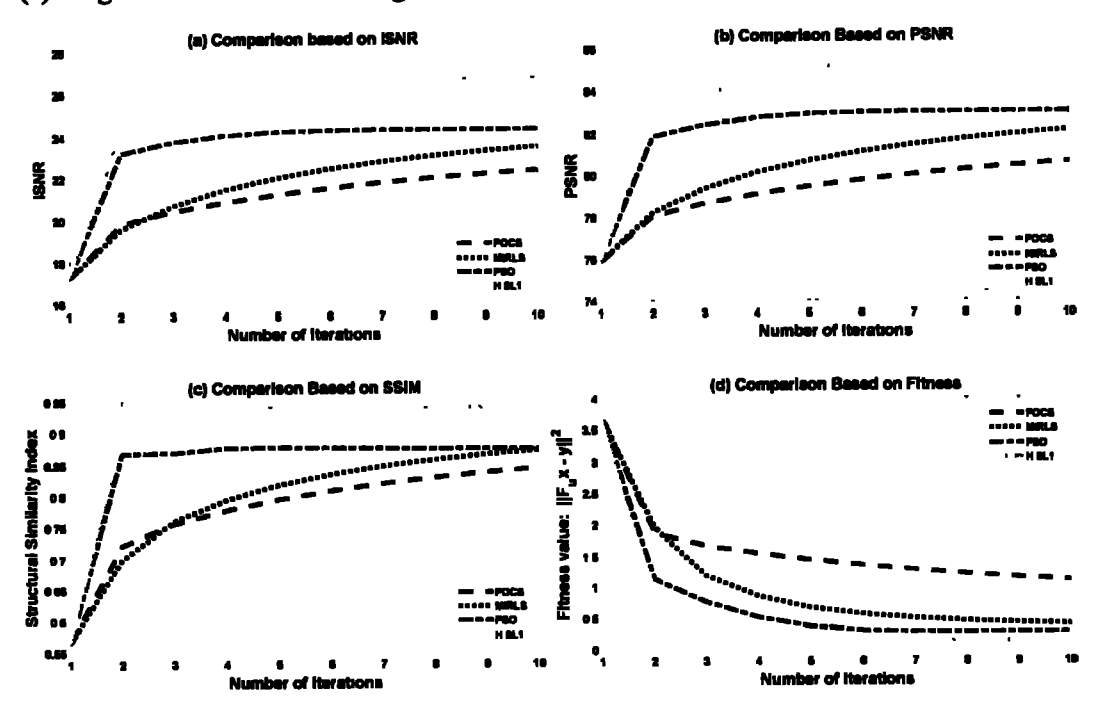


Figure 7-16: Comparison of ISNR, PSNR, SSIM and Fitness for recovery of CS Brain MRI at each iteration.

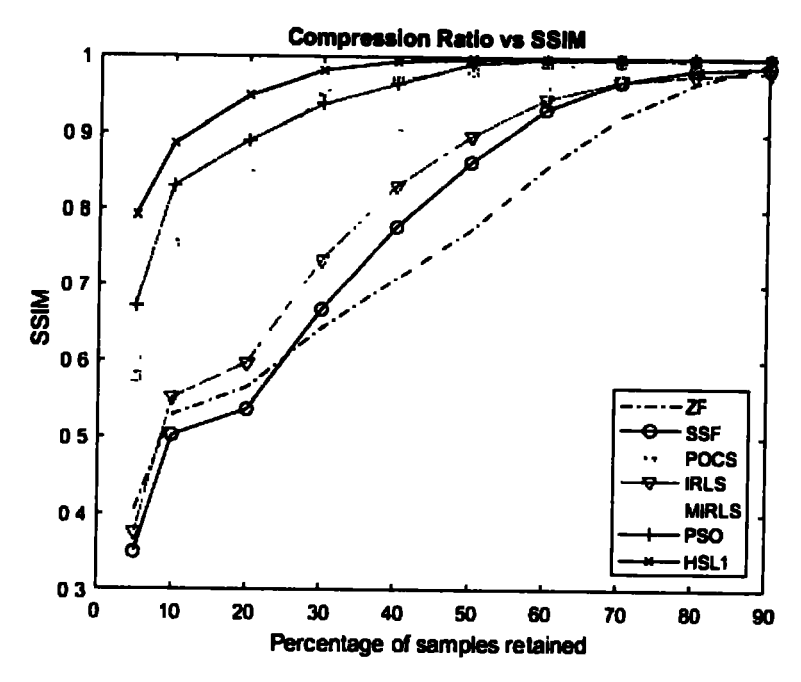


Figure 7-17: The SSIM achieved by varying compression ratio using H-SL1 vs. other comparison methods.

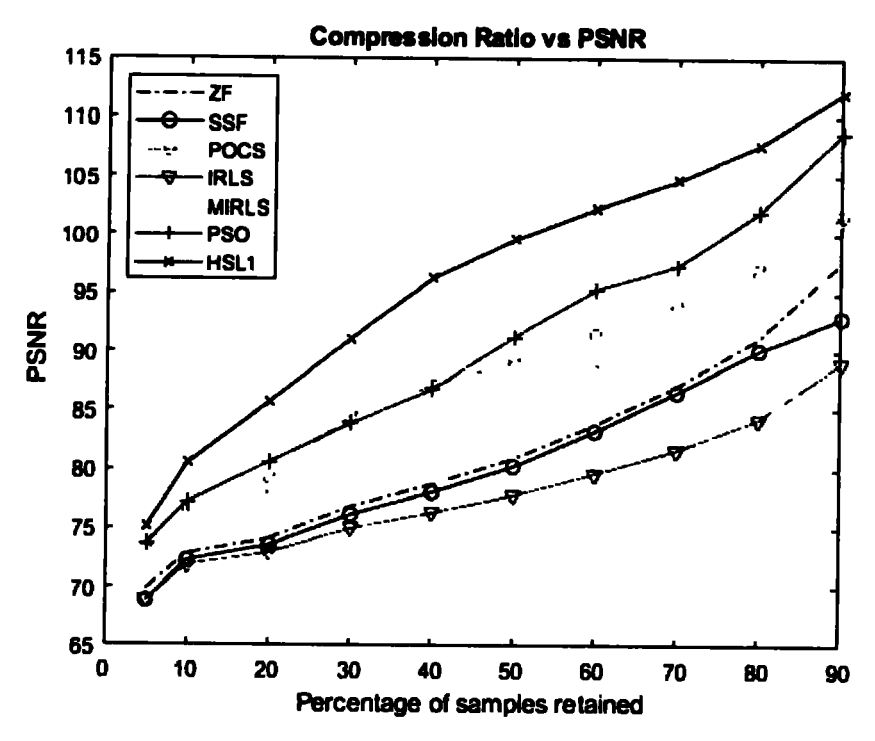


Figure 7-18: The PSNR achieved by varying compression ratio using H-SL1 vs. other comparison methods.

The experimental results from Real Human Brain MRI are presented, where the MRI data is compressively sampled, retaining only 25% of the samples using radial lines undersampling mask in k-space. The proposed H-SL1 algorithm is qualitatively compared with ZF, LR, SSF, POCS, IRLS, Modified IRLS, and PSO methods. Figure 7-16 shows that the proposed algorithm outperforms all other methods. In Figure 7-16 (a), the recovered images are shown alongside a zoomed-in portion for better clarity, illustrating the performance of H-SL1 and other methods compared to the original image. The recovered image from H-SL1 closely matches the original image. Figure 7-16 (b) depicts the masks used for undersampling the original image, with LR using specific centric ordered data of the k-space while all other methods use the same radial line mask with only 25% values set as 1, while the rest of the values are set as 0. Radial mask undersampling results in a Gaussian-like noise effect in recovered images. Figure 7-16 (c) amplifies the difference between the original image and the recovered image by a factor of 1000, clearly showing that H-SL1 produces a recovered image closer to the original with minimal differences. The LR fails to recover edges due to limited data acquisition, and ZF introduces Gaussian noise-like artefacts in the recovered image. Notably, the ZF-recovered image is used as the initial estimate for other methods. The results demonstrate the superiority of the proposed H-SL1 algorithm in accurately reconstructing real human brain MRI images even with significant undersampling, showcasing its potential for practical applications in medical imaging.

Figure 7-17 illustrates the Structural Similarity Index (SSIM) achieved in the reconstruction of Compressed Sensing (CS) Brain MRI for the proposed method and other techniques, with varying compression ratios ranging from 5% to 90%. The compression ratio represents the percentage of samples retained during k-space data acquisition, wherein higher percentages indicate more data is acquired, resulting in better recovery but longer MRI scanning time. The proposed H-SL1 method consistently achieves the highest SSIM across different compression ratios. This demonstrates the algorithm's superior performance in accurately reconstructing CS Brain MRI images, even under various levels of data compression, making it an efficient and effective solution for achieving high-quality MRI reconstructions with reduced scanning time.

Figure 7-18 presents the PSNR achieved in the reconstruction of CS Brain MRI using the proposed method and other techniques. The compression ratios vary from 5% to 90%,

### **CHAPTER 8**

**DISTA-CSNet: DEEP LEARNING-BASED CS MRI** 

#### RECOVERY

In this chapter, a novel deep learning model is introduced called "Deep Iterative Shrinkage Thresholding Algorithm Compressed Sensing Network" (DISTA-CSNet) designed for efficient recovery of CS MRI. Our model can be easily trained on various datasets and achieves impressive results with just 20 epochs. By incorporating dropouts into the model, we ensure its robustness across diverse datasets, as verified during testing. The trained DISTA-CSNet performs remarkably in recovering CS MRI from different datasets by using dropouts. In comparison to several advanced deep learning techniques used for CS MRI recovery with changing compression ratios, our proposed model consistently outperforms them. We observed significant improvements in both PSNR and SSIM metrics, reaffirming the efficacy of our approach.

#### 8.1 Introduction

Recently, there has been a growing interest in utilizing deep learning (DL) methods to enhance the reconstruction of CS MRI images from sparsely sampled data. Among these techniques, CNN has the potential to capture intricate patterns and structures in images, making them well-suited for producing high-quality MR images. Researchers have devised deep learning architectures to cater specifically to CS MRI reconstruction. These networks are trained to map undersampled input data and fully sampled MRI. Leveraging extensive datasets containing paired undersampled and fully sampled MR images, these models aim to grasp the underlying image structures and thus enhance the accuracy of reconstructions [29-31].

A prevalent approach in CS MRI recovery with deep learning is to adopt an end-to-end learning framework. This entails the network taking undersampled data as input and directly generating the fully sampled image as output, eliminating the need for intermediate

representing the percentage of samples retained during k-space data acquisition, with higher ratios indicating more data is acquired, leading to better recovery at the cost of longer MRI scanning time. Importantly, the proposed H-SL1 method consistently attains the highest PSNR across different compression ratios. This consistently high PSNR demonstrates the algorithm's exceptional performance in accurately reconstructing CS Brain MRI images, even under various levels of data compression. As a result, the H-SL1 method is an efficient and effective solution for achieving high-quality MRI reconstructions while reducing scanning time, making it a valuable approach for practical medical imaging applications.

### 7.7 Conclusions

The proposed H-SL1 method introduces an innovative approach to address the non-linear recovery challenges posed by Compressed Sensing (CS) through a fusion of deterministic and evolutionary techniques. The method underwent rigorous evaluation on 1D k-sparse signals, 2D phantom MRI, and real human brain MRI to validate its effectiveness. The subjective analysis of experimental results demonstrated the notable proficiency of the proposed method in accurately reconstructing 1D sparse signal and 2D MRIs from their compressively sampled data, preserving critical image details. Moreover, the objective analysis based on fitness, SNR, and MSE revealed the superiority of the H-SL1 method over alternative recovery techniques when dealing with 1D signals, displaying its adaptability in handling varying sparsity levels. Quantitative assessments based on ISNR, PSNR, SSIM, and fitness for CS MRI reconstruction, both for phantom and real human brain MRI, clearly established the H-SL1 method's superiority over other methods. indicating its capability to achieve high-quality and reliable MRI reconstructions. Even in scenarios with varying compression ratios, the H-SL1 method consistently showcased excellent performance, solidifying its efficiency and reliability, making it an invaluable and highly effective approach for practical medical imaging applications. The promising results obtained by the proposed method open new possibilities for enhanced medical imaging technology and advanced diagnostic applications.

# 8.2 Iterative Shrinkage Methods and Deep Learning

The iterative sparse coding algorithm idea was first put forth in [152], and it serves as the foundation for the discriminative learning techniques explored here. These techniques incorporate concepts from trained models to DL methodologies. One iteration in these methods is comparable to a conventional CNN-based training approach. In contrast to conventional CNNs, these frameworks can learn the necessary mapping during the training phase by increasing the number of iterations without introducing additional parameters. As a result, network depth can be expanded without suffering the parameter costs associated with conventional CNNs. Adler and Ktem [153] developed a primal-dual learning technique where proximal operators were replaced with a CNN, drawing inspiration from primal-dual hybrid gradient approaches.

To achieve convergence under specific circumstances, Gupta et al. [154] introduced a relaxed version of projected gradient descent that enforced measurement consistency between the reconstructed pictures and their related measurements. Our method produced better results for the reconstruction of sparse-view computed tomography (CT). Hammernik et al. unrolled gradient descent method for reconstructing knee MR images with a 4 undersampling factor included a variational model [155]. With the use of a single graphics card, this work showed increased computational performance for undersampled reconstruction. A deep CNN was used to replace the denoising operator in each iteration of the learned-AMP method created by Metzler et al. [156] and is known as the unrolled approximate message passing (D-AMP) algorithm [157].

Building on their earlier work in [158] and [29], they suggested a CS reconstruction approach for MR and natural image recovery using an unrolled alternate direction method of multipliers (ADMM) algorithm [158]. This model's discriminatively learned CS recovery and ADMM parameters produce good results on real-valued natural pictures and complex-valued MR images.

An IST approach for CS recovery of natural and MR images was proposed in [30] and is based on an unfolded neural architecture. They recovered real images from undersampled observations using an iterative thresholding technique (ISTA) [30]. These proposed ISTA-Nets utilise the advantages of both optimisation-based and network-based computer science methods, and they are designed with a well-structured topology for

steps like iterative reconstruction. As a result, the end-to-end approach improves efficiency and reduces computational complexity [32].

However, a common challenge arises from the limited training data available. Researchers have explored various data augmentation techniques to artificially expand the training dataset to tackle this issue. These techniques include applying random transformations, patch extraction, and simulated undersampling patterns. Additionally, regularisation techniques, like incorporating sparsity or total variation constraints, have enhanced the generalisation and reconstruction quality of deep learning models [33, 34].

In recent years, deep learning techniques successfully addressed the inverse image processing challenges [142], [143]. For instance, the ImageNet dataset was used in [144] to rebuild natural images. A CNN framework for recovering CS videos was presented in [145] [6]. Some of these methods, meanwhile, have limitations due to fixed measurement matrices and image sizes.

K.H. Jin et al. suggested a CNN-based technique to overcome these limitations[143]. This algorithm learned mappings from CS reconstructions to highly efficient reconstructions. GANs have been developed more recently for CS-MRI reconstruction to attain higher quality CS reconstruction [35, 37]. These CNNs use MSE as their cost function. To enhance the calibre of MR image reconstructions, A DL framework with the Bayesian method was proposed in [146] by leveraging the probability of priors as a training loss.

Other researchers have also been investigated Novel frameworks. To more accurately predict CT images, J.M. Wolterink et al. presented a CNN-based framework in addition to adversarial CNN [147]. To maintain texture and edges in the reconstructed CS image, the DAGAN method combined was proposed [148]. To obtain improved performance and a quick reconstruction time, a GAN-based framework with dictionary learning frameworks combining pixel-wise mapping was proposed in [149].

The DL method using patch-based CS jointly improved the dictionary and non-linear recovery operator, leading to enhanced proficiency compared to cutting-edge approaches [150]. A self-supervised training approach for MRI recovery with undersampled data in cases where fully sampled datasets are not readily available [151].

improved CS image reconstruction. A key aspect of ISTA-Nets is their interpretable nature, enabling a clear understanding of their operations. Unlike traditional methods, all parameters in ISTA-Nets are end-to-end discriminatively learned, ensuring efficient utilisation of the network's potential for image reconstruction. By combining the strengths of optimisation-based and network-based approaches and incorporating interpretability, ISTA-Nets represent a promising advancement in CS image recovery.

The ML-CSC system for CS-MRI restoration [31], employing iterative thresholding techniques to extract nonlinear mapping parameters from CS MRI k-space data. MRI-CS framework effectively learns the appropriate mapping from CS measurements for knee and brain MRI. The CS reconstruction results showed improvement with a relatively small increase in the number of learnable parameters in the deep neural network.

# 8.3 DISTA-CSNet Model

Deep learning architectures are frequently trained using heuristic methods, which call for theoretical analysis to improve feature learning and provide precise answers to inverse problems, particularly in biological images. For doctors to diagnose patients correctly, biomedical imaging reconstruction quality cannot be compromised. These frameworks must first undergo substantial training on unique datasets before being used in real-world situations. There is a need for a universal framework that is robust to varied datasets to encourage the incorporation of machine learning technologies in MRI scanning. The test/restore methodology must also be easily used in clinical situations once the model parameters have been learned to ensure wider applicability.

The effectiveness of the iterative shrinkage-based methods is applied to the inverse problem of CS-MRI, demonstrating its suitability in deep learning. Recently, this theory has been used to explain the theoretical basis of deep learning, showcasing its efficiency in addressing CS-MRI reconstruction challenges. The DISTA-CSNet approach leverages CNN unfolding, allowing for increased network depth without adding parameters or computational complexity, distinguishing it from the conventional DL approach based on CNNs. As a result, the reconstruction performance is significantly enhanced, as confirmed by experiments conducted on diverse datasets, validating its ability to produce high-quality reconstructions.

Three benchmark datasets are utilised to train a generalised framework, and images are restored using this adaptable approach. To demonstrate its versatility and practicality, the framework is thoroughly tested on both GPU and CPU computers, demonstrating respectable restoration times and yielding high PSNR/SSIM metrics for MR image reconstruction. This comprehensive evaluation affirms the framework's potential for real-world application in medical imaging scenarios, showcasing its ability to reconstruct MR images with high fidelity and accuracy efficiently.

The proposed CS-MRI restoration paradigm in the study incorporates new findings from theoretical deep-learning research [159]. This approach, which combines an ISTA-based global iterative process with a multi-layered convolutional neural network, aims to effectively train to quickly map fully sampled MR images and matching CS MRI k-space. The primary benefit of DISTA-CSNet is its ability to train quickly (i.e., 20 epochs) and global pursuit, which enables the framework to learn the mapping more effectively.

The DISTA-CSNet model was trained using a GPU processor during the training phase, allowing us to achieve rapid training times and effectively learn the model parameters. Once the model has been learned, it may be used to restore CS-MR images using a variety of CS ratios and random masks. The approach demonstrates flexibility and sturdiness by generating accurate reconstructions for various undersampling conditions.

The capacity of our suggested framework to perform test set reconstructions on a CPU without relying on GPUs is a noteworthy advantage. This method permits suitable restoration times, illuminating the effectiveness of the trained parameters. As a result, the framework is useful for practical applications in clinical settings where GPUs might not always be available, offering a successful method for CS-MRI restoration with significant timesaving capabilities.

In general, the iterative shrinkage thresholding-based algorithms in the context of CS MRI recovery aim to minimise the cost function defined by the following equation.

$$f(x) = \underset{x}{\operatorname{argmin}} \frac{1}{2} \| y - \Phi \Psi^{H} x \|_{2}^{2} + \lambda \| x \|_{1}$$
(8.1)

The layered iterative shrinkage methods proposed by [30] and [160] attempt to unfold neural networks by simultaneously minimising the above-cost function by iterative thresholding methods. This approach is aimed at achieving a global multilayer sparse

model, where it is not attainable. Instead, the focus is on obtaining representation estimates that describe the local layer defined by Eq. (8.2).

$$f(x_i) = \underset{x_i}{\operatorname{argmin}} \frac{1}{2} \| y_i - \Phi \Psi^{\mathsf{H}} x_{i-1} \|_2^2 + \lambda_i \| x_{i-1} \|_1$$
 (8.2)

Where  $x_i$  represents the current layer of the model.

# 8.4 DISTA-CSNet Training Model

The suggested approach processes images in k-space with related CS measurements using multi-layer ISTA. The proposed DISTA-CSNet aims to effectively train to quickly map fully sampled MR images and matching CS MRI k-space and store these mappings as model parameters. The model trains with only 20 epochs while achieving better PSNR and SSIM than other state-of-the-art algorithms, as evident from experimental results. The testing module then reconstructs test images using the trained ML-ISTA learning parameters and computes the recovered images' PSNR and SSIM. For all layers, it uses Xavier initialisation to initialise the dictionaries.

Algorithm-8.1 presents the multi-layered basis pursuit algorithm, which uses the iterative thresholding process. To train the model parameters, the framework collects ground truth images, k-space data, and masks for under-sampling. Without additional parameters, the learning process, Algorithm-8.1, uses ML-ISTA unfolding to deepen the learning framework. The model was trained separately on the Brain MR image and Knee MR image. Both models were tested for CS MRI recovery based on PSNR and SSIM.

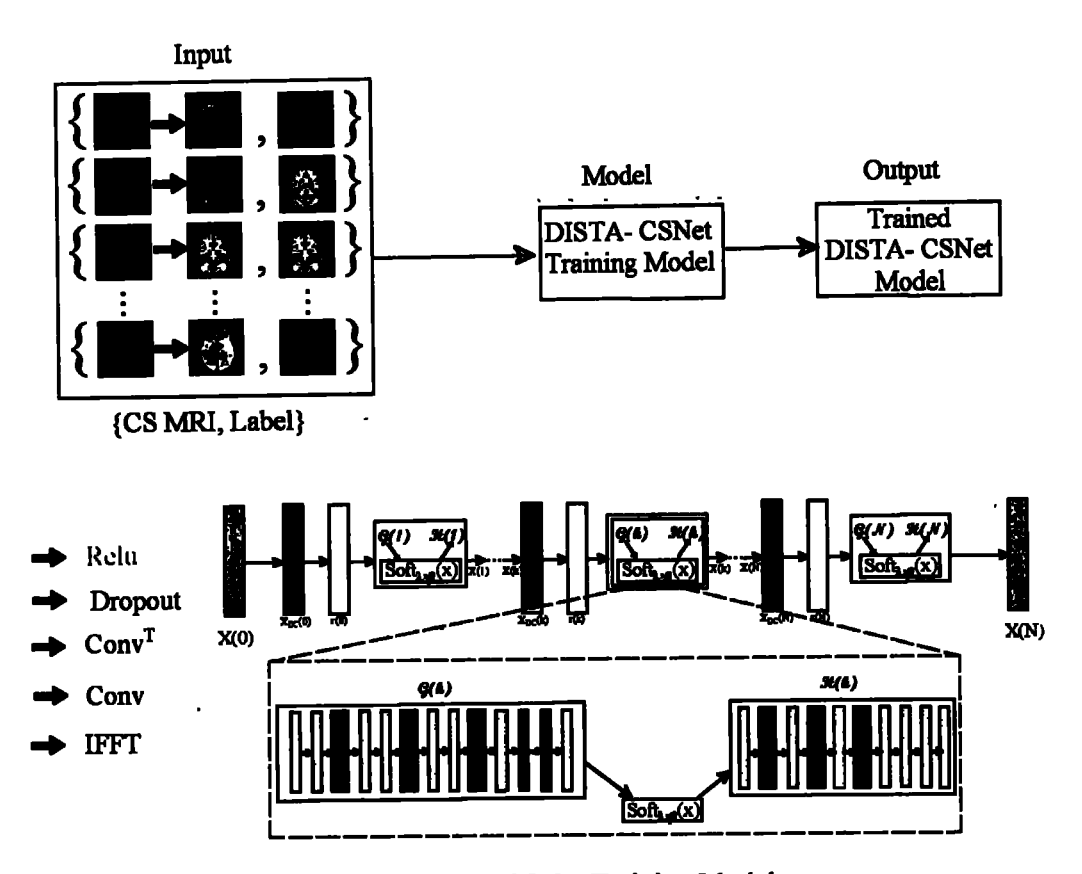


Figure 8-1: DISTA-CSNet Training Model

### 8.4.1 Training /Testing Datasets

The first dataset comes from earlier work [30], and it comprises 850 brain MRIs that were captured in the sagittal and axial planes as a pair of (CS MRI, Label (Ground Truth Image) (Dataset 1). 621 Knee MRIs from patients comprise the second dataset used to train the CS-MRI framework. These Knee MRIs are fully sampled of the coronal view with PD fat saturation and were taken using a 1.5T imaging device (Siemens MAGNETOM Symphony) at the Hospital Kuala Lumpur (HKL) (Dataset 2). A certified radiologist classified the MRIs into three categories: full tear, partial tear, and normal knee. The images were collected to diagnose anterior cruciate ligament (ACL) damage. The performance was evaluated using a test set of 50 and 21 MRIs randomly from both datasets, respectively. The third dataset comprises 123 slices thick, 256 × 256 size MRIs of ageingnormal brains in the coronal plane [161] (Dataset 3), this dataset was used for testing

purposes only. It was tested by using the model trained on the first dataset. The Harvard Medical School's AANLIB database makes this dataset accessible to the public.

Algorithm 8.1. Training of DISTA-CSNet

Task: Training of DISTA - CS Net with CS MRI data along with its fully sampled labels

$$f(x) = \underset{x}{\operatorname{argmin}} \left(\frac{1}{2} \|y - F_u \Psi^H x\|_2^2 + \lambda \sum_{i=1}^n x_i \tanh(\gamma x_i)\right)$$

Input:

Training Data (CS MRI along with labels), Dictionary  $\Phi \in \mathbb{R}^{m \times n}$ , Masks for Undersampling , Thresholding parameter  $\lambda$ ,  $\beta$ . Adams Optimizer learning rate  $\mu$ , undersampled data  $\gamma$ , Output: Trained DISTA — CSNet Model for CS — MRI Recovery

1) Initialisation: Initialise Wieghts and Conv filters using Xavier Initialisation Set thresholding  $\lambda$  and  $\beta$  to a learnable parameter.

Initial residual:  $r_0 = x_0 - \alpha F_{\pi}^{-1}(y_0 - F_{\pi}x_0)$ 

- 2) DISTA CS-Net Main Iteration: Increment i by 1, and apply the following steps
  - a) Residual: Compute  $r_i = F_{ii}^{-1}(y_{i-1} F_{ii}x_{i-1})$
  - b) Data Consistency in Fourier Domain

$$\begin{aligned} \mathbf{X}[j] &= \mathbf{F}_{\mathbf{u}}(\mathbf{X}_{l}) \\ \mathbf{X}_{\mathbf{DC}}[j] &= \begin{cases} \mathbf{x}_{l}[j] & \textit{if } \mathbf{x}[j] = 0 \\ \mathbf{x}[j] & \textit{otherwise} \end{cases} \end{aligned}$$

- c) Convolutions: Perform convolutions as shown in Figure 8-1
- d) Dropouts: Perform Dropouts as shown in Figure 8-1
- e) Convolution Transpose: Apply convolution Transpose as shown in Figure 8-1
- f) ReLU: Apply Relu as shown in Figure 8-1
- g) Shrinkage: Compute  $x_i = S_{\lambda,\beta}(x) \cong \begin{cases} x_i(\tanh(\lambda(|x_i| \beta))) & |x| > \beta \\ 0 & \text{otherwise} \end{cases}$
- h) Use Adam Optimisation: Compute updated  $x_i$  using learning rate  $\mu$
- i) Residual Update: Compute  $r_{l+1} = y F_u x_l$
- j) Stopping Rule: Go to step (2) until the maximum number of epochs criteria is met.
- 3) Output: Trained DISTA CSNet Model

## 8.4.2 Mote Carlo Dropouts

The introduction of Monte Carlo (MC) Dropout has certainly made the proposed model more robust as evidenced by performance on varying datasets by avoiding over-fitting. Dropout, originally proposed by Yarin et al. [162], is a practical and computationally efficient method to estimate model uncertainty in deep neural networks. It involves applying dropout during both training and inference, allowing for the computation of prediction uncertainty, and addressing overconfidence in deep learning models. MC Dropout introduces variability in predictions by performing dropout multiple times during inference, leading to improved reliability and performance of deep neural networks.

MC Dropout is a technique used during training in a deep neural network, where dropout is applied to certain neurons with probability p, resulting in a set of predictions  $(y_1, y_2, ..., y_n)$  obtained by sampling the output multiple times with different dropout masks. The final prediction for an input data point x is calculated as the average of these sampled predictions, allowing for prediction uncertainty estimation and improved model performance.

$$y_{final} = \left(\frac{1}{n}\right) * \Sigma(y_i) from i = 1 to n$$
 (8.3)

MC Dropout is a technique that utilises dropout during both training and inference to enhance model performance, estimate prediction uncertainty effectively, and improve the robustness and accuracy of deep neural network architectures in various tasks by estimating prediction uncertainty from the variance of the sampled predictions.

### 8.4.3 Soft Thresholding

Using a new thresholding method based on the *tanh* was used for training. The *tanh* offers the advantage of an adjustable slope near the origin and is a bounded function, making it a preferable choice as an estimation for soft thresholding (ST). Consequently, the mathematical description of *tanh*-based ST is represented as:

$$Soft_{\lambda,\beta}(x) \cong \begin{cases} tanh(\beta(|x|-\lambda)) & |x| > \lambda \\ 0 & otherwise \end{cases}$$
 (8.4)

The equation above includes a thresholding parameter,  $\lambda$ , and a parameter  $\beta$  that controls the shape of the tanh. When  $\beta$  is close to zero, Eq. (8.4) approximates the behaviour of a soft thresholding function. As  $\beta$  approaches infinity, Eq. (8.4) transforms into a hard thresholding function. Both  $\lambda$  and  $\beta$  are learnable parameters.

# 8.4.4 Data Consistency Constraints

The data consistency constraint (DCC) is introduced in the training model which significantly improves the learning rate of the training model. DCC in the frequency domain is a fundamental principle in CS MR recovery. It ensures that the samples acquired in the k-space domain remain constant throughout the recovery process. In other words, the measured data points in the frequency domain, which correspond to the acquired MRI measurements, are preserved, and not altered during the iterations of the recovery algorithm. The data consistency constraint is crucial because it guarantees that the

recovered MRI stay consistent with sampled data. It prevents the algorithm from introducing spurious information or modifying the original measurements, which could lead to erroneous results. By preserving the actual samples from the k-space domain, the algorithm ensures that the recovered image accurately represents the underlying structure of the imaged object, even with limited or under-sampled data. The data consistency constraint in the frequency domain is a vital aspect of CS MRI recovery, as it maintains the integrity of the acquired data and helps achieve reliable and accurate image reconstruction.

$$X[j] = F_{u}(X_{l}) \text{ (FFT of Estimated Image)}$$

$$X_{DC}[j] = \begin{cases} X_{l}[j] & \text{if } X[j] = 0 \\ X[j] & \text{otherwise} \end{cases}$$
(8.5)

#### 8.4.5 Convolution

In deep neural networks, convolutions are a fundamental operation used in convolutional layers to process and extract features from input data. A filter or kernel is slid across the input data during the convolutional procedure, and element-wise multiplication is done between the filter and kernel and the corresponding local input region. The result is then summed to produce a single value in the output feature map. Mathematically, the 2D convolution operation for a single channel (grey scale) input image can be represented as follows:

$$Y(i,j) = \sum_{m=0}^{M-1} \sum_{n=0}^{N-1} X(i+m,j+n).H(m,n)$$
 (8.6)

Here:

- Y(i,j) represents the value at position (i,j) in the output feature map.
- X(i+m,j+n) represents the value at position (i+m,j+n) in the input image.
- H(m,n) represents the value at position (m,n) in the filter/kernel while M and N are the dimensions of the filter.

Convolutional layers employ several filters to extract distinct features from the input data, producing several feature maps that capture the different patterns and traits of the input. For tasks like image identification, object detection, and natural language processing, the use of convolutions in deep neural networks is essential because it enables the network to learn hierarchical representations from the input data effectively.

## 8.4.6 Convolution Transpose

Convolution transpose, also known as deconvolution or up-sampling, is an operation used in deep neural networks for tasks like image segmentation and image generation. It is the opposite of standard convolution and is used to increase the spatial dimensions of the feature maps. Mathematically, the 2D convolution transpose operation for a single channel (grey scale) input feature map can be represented as follows:

$$Y(i,j) = \sum_{m=0}^{M-1} \sum_{n=0}^{N-1} X(i-m,j-n).H(m,n)$$
 (8.7)

Where:

- Y(i,j) is the output representing the value at position (i,j) in the output feature map.
- X(i-m,j-n) represents the value at position (i-m,j-n) in the input feature map.
- H(m,n) represents the value at position (m,n) in the filter/kernel while M and N are the dimensions of the filter.

Convolution transpose is commonly used in up-sampling layers of neural networks to recover spatial resolution lost during down-sampling, allowing the network to generate high-resolution images or perform tasks requiring detailed spatial information.

# 8.4.7 Rectified Linear Unit (ReLU)

ReLU is an activation function commonly used in deep neural networks to introduce non-linearity. It returns the input if it is positive and zero otherwise. Mathematically, the ReLU activation function can be represented as follows:

$$ReLU(x) = \max(0, x) \tag{8.8}$$

Where:

- -x is the input to the ReLU function.
- ReLU(x) is the output of the ReLU function, which is equal to x if x is positive and zero if x is negative or zero.

#### 8.4.8 Xavier Initialisation

Xavier or Glorot Initialisation, is a weight initialisation technique used in deep neural networks. It sets the initial weights of the neurons to random values drawn from a specific distribution, designed to help with better training convergence.

Xavier Initialisation was first proposed by Glorot et al. [163]. The technique is widely used to initialise weights in neural network layers, especially in networks using the ReLU activation function, as it helps in maintaining signal variance and promoting stable and efficient training.

### 8.4.9 Adam optimizers

The optimisation approach used in training the DISTA model is Adam (Adaptive Moment Estimation) which is frequently used in deep learning to update the weights of a neural network while it is being trained. To adapt the learning rate for each parameter based on their historical gradients and second moments, it utilises the advantages of both the RMSprop and momentum methods. Adam dynamically adjusts the learning rate, which makes it ideal for training complicated, high-dimensional neural networks and promotes faster convergence and improved performance across a range of deep learning applications.

#### 8.4.10 Cost Function

In optimisation in deep learning, the cost or objective function plays a crucial role in guiding the training process of a neural network. The objective function represents the measure of how well the model performs on a given task, and the optimisation process aims to minimise this cost function to improve model performance. The cost or objective function comprises two components: the discrepancy loss and the constraint loss. These two components are combined to form the total loss that the optimisation algorithm aims to minimise during training.

The discrepancy loss measures the difference between the predicted outputs of the neural network and the true target values. It quantifies how well the model's predictions match the ground truth for the given task. Common discrepancy loss functions include mean squared error (MSE) for regression tasks and cross-entropy loss for classification tasks.

The constraint loss incorporates additional constraints or regularization terms to guide the model's behaviour during training. In the training model, the  $l_1$  or  $l_2$  norm regularization terms can be added to the constraint loss to encourage sparsity in the model's weights, promoting a simpler and more interpretable model.

By combining the discrepancy loss and constraint loss, the total loss function represents a trade-off between fitting the training data well (minimising discrepancy loss) and satisfying additional constraints or regularization requirements (minimising constraint loss). During optimisation, the neural network parameters are adjusted to minimise this total loss, resulting in a model that performs well on the task while adhering to specific constraints or regularization preferences.

$$L_T = L_d + \gamma L_c \tag{8.9}$$

$$L_d = \frac{1}{N_d N} \sum_{i=1}^{N_d} \left\| x_i^{N_p} - x_i \right\|_2^2$$
 (8.10)

$$L_{C} = \frac{1}{N_{d}N} \sum_{l=1}^{N_{d}} \sum_{k=1}^{N_{p}} \left\| G^{k} \left( H^{k}(x_{l}) \right) - x_{l} \right\|_{2}^{2}$$
 (8.11)

Where  $L_T$ ,  $L_d$  and  $L_c$  are a total loss, discrepancy loss and constraint loss, respectively. N,  $N_d$ ,  $N_p$  and  $\gamma$  are the size of each block  $x_l$ , total training blocks, total phases, and regularisation constraint respectively. All these three losses during the training process by our model are depicted in Figure 8-2 and Figure 8-3. Figure 8-2 shows the convergence of all the losses with respect to Epochs when the compression ratio (CR) is set to only 20%. Whereas Figure 8-3 shows the convergence of the above-mentioned losses when 2-fold CR is applied.

During the training process of our model, three losses are considered: the discrepancy loss, the constraint loss, and the total loss. These losses are illustrated in Figure 8-2 and Figure 8-3. In Figure 8-2, we observe the convergence of all losses concerning the number of training epochs when the compression ratio (CR) is set to 20%. On the other hand, Figure 8-3 depicts the convergence of the mentioned losses when a 2-fold compression ratio is applied. These figures show how the losses change over the training epochs, providing valuable insights into the model performance and convergence behaviour for different compression ratios.

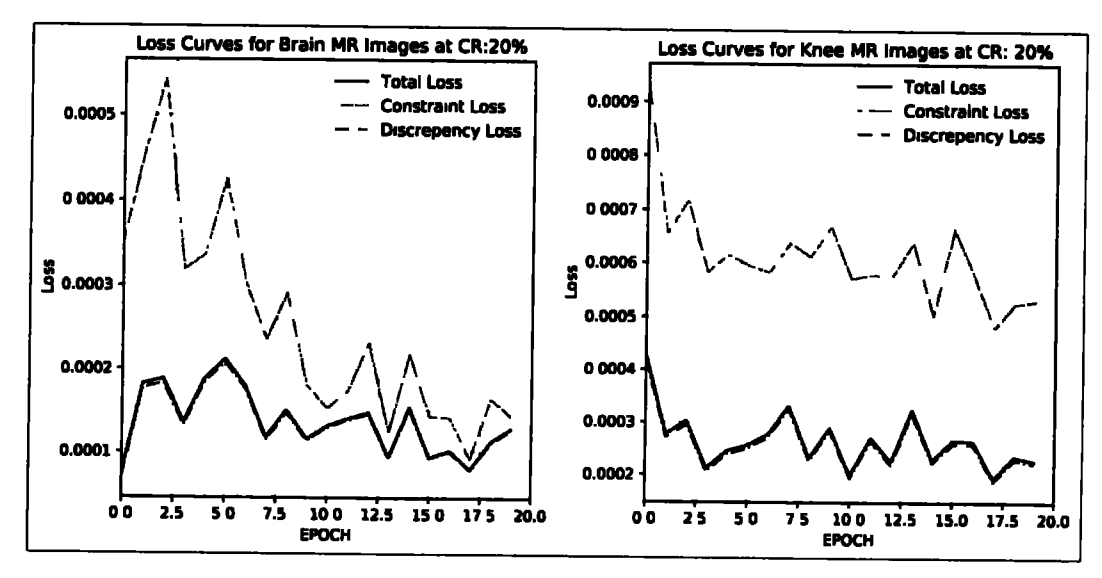


Figure 8-2: Loss functions vs Epochs for 5-fold compression of Brain and Knee MRIs

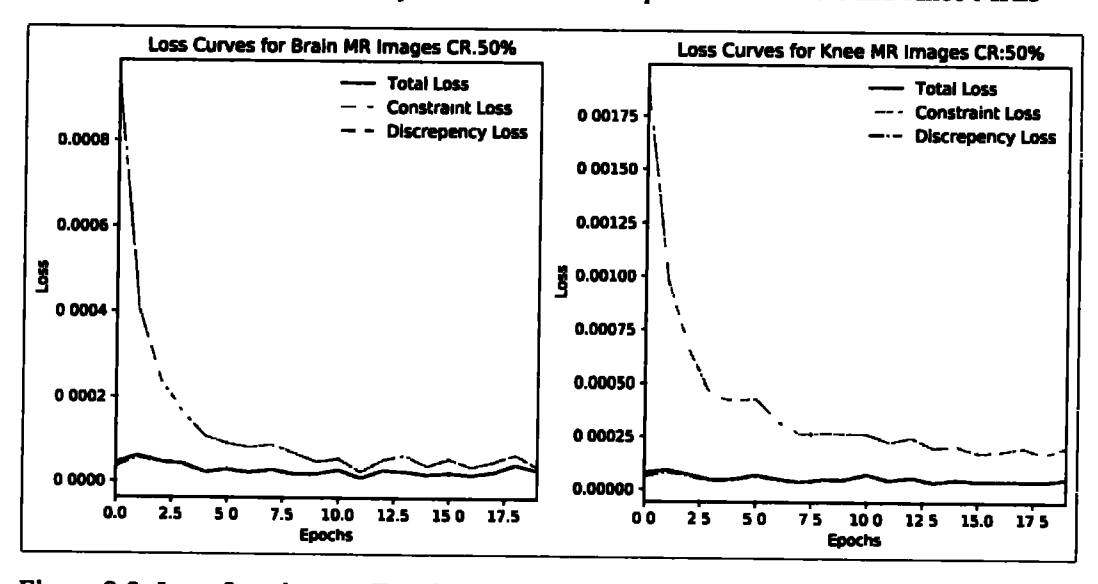


Figure 8-3: Loss functions vs Epochs for 2-fold compression of Brain and Knee MRIs

# 8.5 DISTA-CSNet Testing Model

After training two separate DISTA-CSNet models for Compressed Sensing MRI reconstruction of Brain and Knee MRIs. The testing phase evaluated the models' accuracy by reconstructing MRIs from three test datasets: Brain MRI (50 slices), Knee MRI (21 images), and an additional Brain MRI dataset (123 slices). The trained models performed with great accuracy regarding PSNR and SSIM, demonstrating their ability to produce high-quality MRI estimates from compressed measurements. Overall, the DISTA-CSNet models proved effective in accurately reconstructing MRIs, showcasing their potential for

practical medical imaging applications. The process of testing the model is illustrated in Figure 8-4. Algorithm 8.2 describes the testing process.

# **Model Testing**

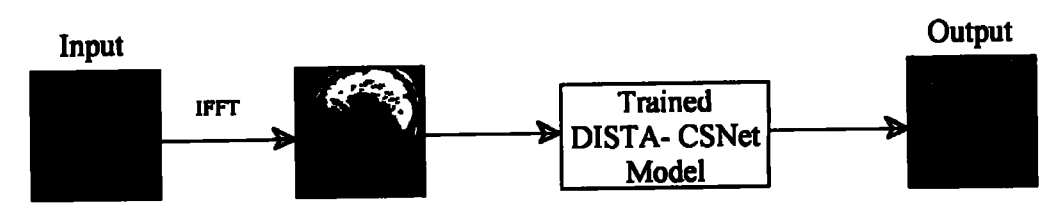


Figure 8-4: DISTA-CSNet Testing Model

# Algorithm 8.2: Testing DISTA-CSNet Process

Task: Test the Trained DISTA - CS Net for CS MRI Reconstruction

Input: Trained Model,

Test MR images,

Undersampling Mask

Output: Reconstructed MRI from CS - MRI

PSNR of the reconstructed image

SSIM of the reconstructed image

Recovery time by GPU/CPU

- 1) Initialisation: Initialize Wieghts and Conv filters using Xavier Initialisation Set thresholding  $\lambda$  and  $\beta$  to a learnable parameter.

  Initial residual:  $\mathbf{r_0} = \mathbf{x_0} \alpha \mathbf{F_u}^{-1}(\mathbf{y_{t-1}} \mathbf{F_u}\mathbf{x_{t-1}})$
- 2) Loading Model: Load pre trained DISTA CSNet
- 3) DISTA CS-Net Main Iteration: For every CS MRI in the test dataset
  - a) Loading Model: Load pre trained learnt dictionary
  - b) Masking: Apply masking to input MRI at appropriate CR in k-space
  - c) Reconstruction: Apply a pre trained model for MRI reconstruction
  - d) Calculate Performance Measures: Calculate PSNR and SSIM of the recovered image
  - e) Stopping Rule: If all images are tested in dataset go to Step 4 otherwise go to Step 3a.
- 4) Output: Reconstructed Image, Recovery time, PSNR and SSIM in comparison to Ground Truth

# 8.6 DISTA-CSNet Model Testing Results and Discussion

In the evaluation phase, the DISTA-CSNet Model was subjected to testing using three distinct datasets: the first dataset consisted of Brain MRIs with 50 slices [30], the second dataset included 21 Knee MR images, and the third dataset contained 123 Brain MRI slices [161]. To assess the performance of the proposed algorithm, the reconstructed images were

compared to their respective ground truth images using two key metrics: PSNR and SSIM. By measuring the PSNR and SSIM values, the experiments aimed to quantitatively evaluate how accurately the DISTA-CSNet Model reconstructed the MRIs compared to the original ground truth images, providing insights into the algorithm's efficacy and potential for medical imaging applications.

The training and testing of the proposed model were performed on the Lambda ( $\lambda$ ) Quad AI Workstation with a single Nvidia GeForce RTX 3090 GPU using JupyterLab platform. The batch size was set to 4 for training for Brain and Knee MRI training datasets.

Figure 8-5 presents a selection of randomly recovered images, which were obtained during the testing phase using three distinct datasets. These datasets were subjected to a 5-fold compression in the sampling process, resulting in a significant 5-time reduction in scanning time compared to conventional methods. The PSNR / SSIM of the recovered images are also shown. The visual evidence from the recovered images indicates that they meet the required standards for clinical treatment. The reconstructed images demonstrate high quality and accuracy, making them suitable for practical medical applications with confidence.

Table 8-1 presents the effectiveness of the proposed DISTA-CSNet model that was trained on 800 Brain MR images, showcasing its superior performance in terms of PSNR and SSIM across various compression ratios. Even at a 5-fold compression, the model achieves an impressive average SSIM value of 0.9634, indicating its proficiency in producing high-quality reconstructions. During testing, the computational efficiency of the model demonstrated significant improvements when executed on a GPU, with computation times in the sub-second range. However, even on a CPU, the computational time has been reduced, making it feasible to test the model without relying on a GPU. Moreover, the training time for the DISTA-CSNet model was substantially reduced when trained on Dataset 1, requiring only 20 epochs and approximately 16 minutes to reach a near-optimal performance level. This observation highlights the fast-learning capability of the proposed method compared to other state-of-the-art approaches, further solidifying its potential for practical and time-efficient applications in medical image reconstruction.

Table 8-2 illustrates the effectiveness of the proposed DISTA-CSNet model, which was trained on a dataset containing 600 Brain MR images, showcasing its superior performance in terms of PSNR and SSIM across various compression ratios. Remarkably, even at a 5-

fold compression, the model achieves an impressive average SSIM value of 0.9395, demonstrating its proficiency in generating high-quality reconstructions. The model's computational efficiency during testing was notably improved when utilizing a GPU, resulting in computation times within the sub-second range. Nevertheless, the computational time on a CPU has also been significantly reduced, making it viable to test the model without relying on a GPU. Additionally, the training time for the DISTA-CSNet model on Dataset 2 showed substantial reductions, requiring only 20 epochs and approximately 12 minutes to achieve near-optimal performance. The reduced training time compared Brain MRI training time was mainly due to fewer MR images being available for training i.e., 600 instead of 800 MRIs. This observation emphasizes the proposed method's fast-learning capability compared to other state-of-the-art approaches, further validating its potential for practical and time-efficient medical image reconstruction applications at clinical standards.

Table 8-3 demonstrates the effectiveness of the proposed DISTA-CSNet model, which was tested using Dataset 3 on the same model that was trained on a dataset comprising 800 Brain MR images, showcasing its exceptional performance concerning PSNR and SSIM across different compression ratios and robustness against varying test data. Even at a 5-fold compression, the model achieves remarkable average SSIM and PSNR scores, underscoring its ability to generate high-quality reconstructions. Notably, during testing, the model exhibited significant improvements in computational efficiency when employed on a GPU, achieving computation times in the sub-second range. However, the computational time on a CPU has also been reduced, making it feasible to test the model without relying solely on a GPU. These finding highlights the proposed method's adaptability and robustness mainly by introducing dropouts, compared to other state-of-the-art approaches, further reinforcing its potential for practical and time-efficient applications in medical image reconstruction.

In Figure 8-6, the performance of the trained DISTA-CSNet model is depicted when it was tested on Dataset 1, which consisted of 50 slices of Brain MRI used for testing. The graph shows the PSNR and SSIM values achieved by the model at different compression ratios. Notably, the red dotted line highlights the average PSNR and SSIM attained by the

proposed model when the compression ratio was set at only 20%. This emphasises the efficacy of the proposed model in recovering Compressed Sensing (CS) MRI data. Even at a relatively low compression ratio of 20%, the model achieves high PSNR and SSIM values, indicating its ability to produce accurate and high-quality MRI reconstructions. This result demonstrates the robustness and effectiveness of the DISTA-CSNet model in handling CS MRI recovery tasks, making it a promising solution for medical imaging applications that involve compressed data.

Figure 8-7 illustrates the performance of the trained DISTA-CSNet model during testing on Dataset 2, comprising 21 MRIs of Knee MRI used for evaluation. The graph showcases the PSNR and SSIM values achieved by the model at various compression ratios. The red dotted line highlights the average PSNR and SSIM obtained by the proposed model when the compression ratio was set to just 20%. This emphasizes the model's effectiveness in recovering Compressed Sensing (CS) MRI data. Even at a relatively 5-fold compression, the model can produce accurate and high-quality MRI reconstructions with better PSNR and SSIM. These results underscore the robustness and efficacy of the DISTA-CSNet model in handling CS MRI recovery tasks, rendering it a promising solution for medical imaging applications that deal with compressed data.

Figure 8-8 presents the performance of the trained DISTA-CSNet model during testing on Dataset 3, which consists of 123 slices of Brain MRIs used for evaluation. The graph showcases the PSNR and SSIM values achieved by the model at different compression ratios. Of particular significance is the red dotted line, indicating the average PSNR and SSIM obtained by the proposed model at a compression ratio of 20%. This highlights the model's effectiveness in recovering Compressed Sensing (CS) MRI data. Even at a relatively high 5-fold compression, the model can produce accurate and high-quality MRI reconstructions, with improved PSNR and SSIM values. These results underscore the robustness and efficacy of the DISTA-CSNet model in handling CS MRI recovery tasks, making it a promising solution for medical imaging applications that involve compressed k-space data.

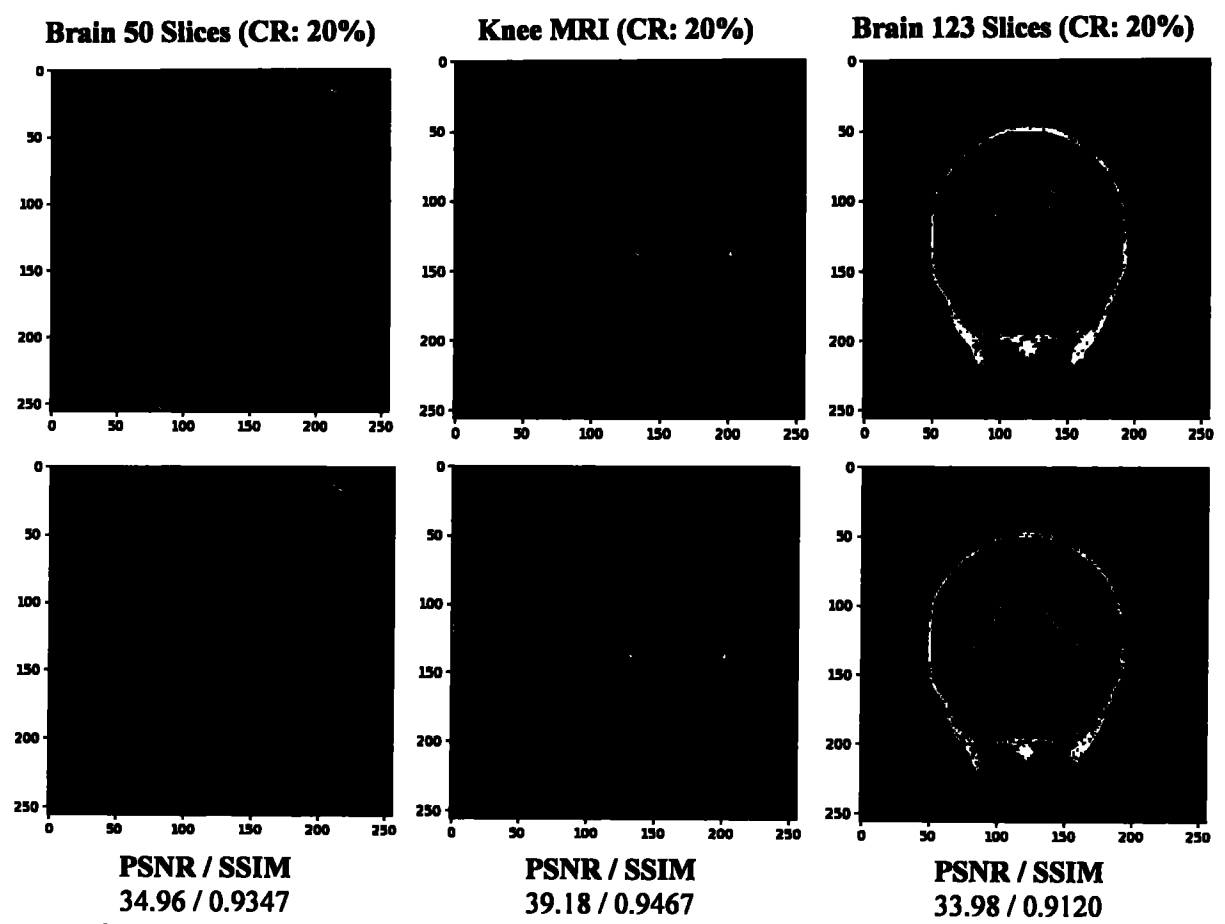


Figure 8-5: Sample Recovered Images from Testing with Different Datasets

Table 8-1: Brain MRI with 50 Slices Testing Results

Algorithms		GPU/CPU		$\Gamma$			
	20% PSNR/SSIM	30% PSNR/SSIM	40% PSNR/SSIM	50% PSNR/SSIM	Testing Time (Sec)	Training Time	Epochs
ADMM-	37.17/	39.84/	41.56/	43.00/	0.9535 <i>s</i>		<del>                                     </del>
Net	0.9374	0.9526	0.9664	0.9734	/5.2s	03: 31: 23	200
ISTA-Net+	38.70/	40.97/	42.65/	44.12/	0.1437 <i>s</i>	02: 38: 15	200
	0.9484	0.9639	0.9729	0.9792	/4.8s		
ML-CSC	39.25/	41.50/	43.66/	45.96/	0.0688s		
ML-CSC	0.9551	0.9689	0.9774	0.9855	/ 2.8s	01: 09: 22	50
DISTA-	40.36/	42.67/	45.24/	47.51/	0.0114s	00: 16 <sup>.</sup> 18	20
CSNet	0.9634	0.9755	0.9839	0. 9899	/1.36s		

Table 8-2: Knee MRI Dataset Testing Results with 21 MR Images

Algorithms		GPU/CPU		$\overline{}$			
	20% PSNR/SSIM	30% PSNR/SSIM	40% PSNR/SSIM	50% PSNR/SSIM	Testing Time (Sec)	Training Time	Epochs
ADMM-	34.30/	38.29/	40.78/	41.33/	0.8935s	02: 38. 27	200
Net	0.8987	0.9385	0.9665	0.9775	/ 2,32s		
ISTA-Net+	33.51/	36.23/	39.42/	41.86/	0.1261s	01: 58: 07	200
	0.8533	0.9089	0.9502	0.9723	/2.05 <i>s</i>		
ML-CSC	36.93 /	39.68/	42.04 /	43.44 /	0.0538s	00: 49: 35	50
	0.9262	0.9569	0.9738	0.9824	/ 2.18s		
DISTA-	38.06 /	41.04/	43.42/	46.21/	0.01125	00: 12: 15	20
CSNet	0. 9395	0.9661	0.9799	0.9898	/ 1.34s		

Table 8-3: Testing results of Brain MR images with 123 slices

Algorithms	20% PSNR/SSIM	30% PSNR/SSIM	40% PSNR/SSIM	50% PSNR/SSIM	GPU/CPU Testing Time	
ADMM-Net	29.29/	33.00/	36,02/	38.95/	0 9730s /5.4s	
ADMM-Net	0.84386	0.89599	0.92406	0 94158		
ICTA No.1	30.50/	33.94/	36.96/	39 96/	0.1528s /4 94s	
ISTA-Net+	0.8786	0.9214	0 9483	0.9661		
ML-CSC	31 68/	35 21/	38 35/	41.60/	0.0732s/3 79s	
ML-CSC	0.8782	0.9234	0 9554	0 9724		
DIST-CSNet	33.32 /	37.9 /	41.37/	44.50/	0.0429s/1.40s	
nia i -Canet	0.8975	0.9522	0.9749	0.9863		

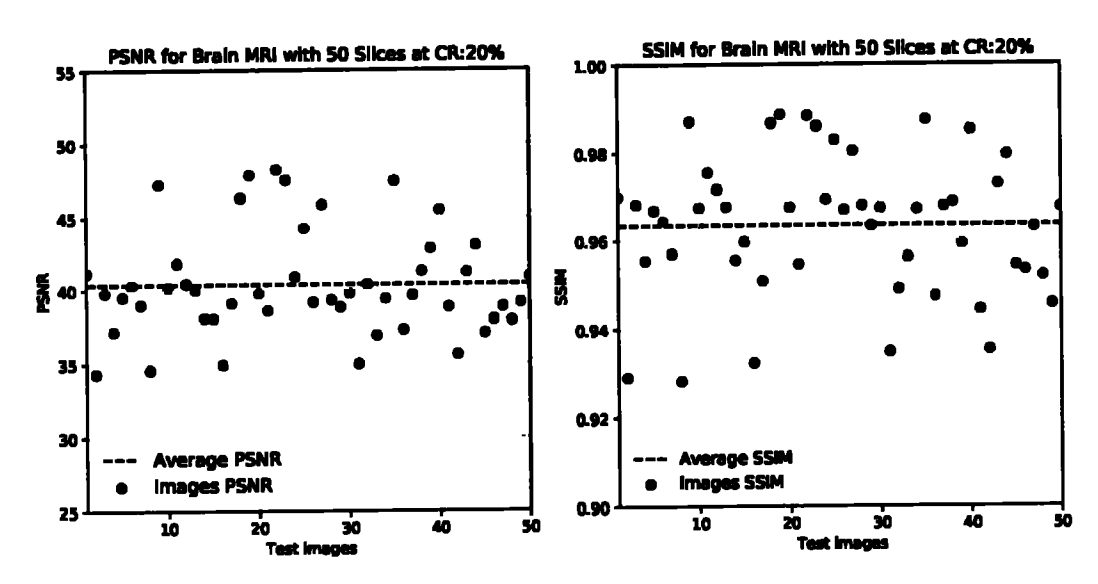


Figure 8-6: PSNR and SSIM for Brain MRI of 50 slices at a compression ratio of 20 %

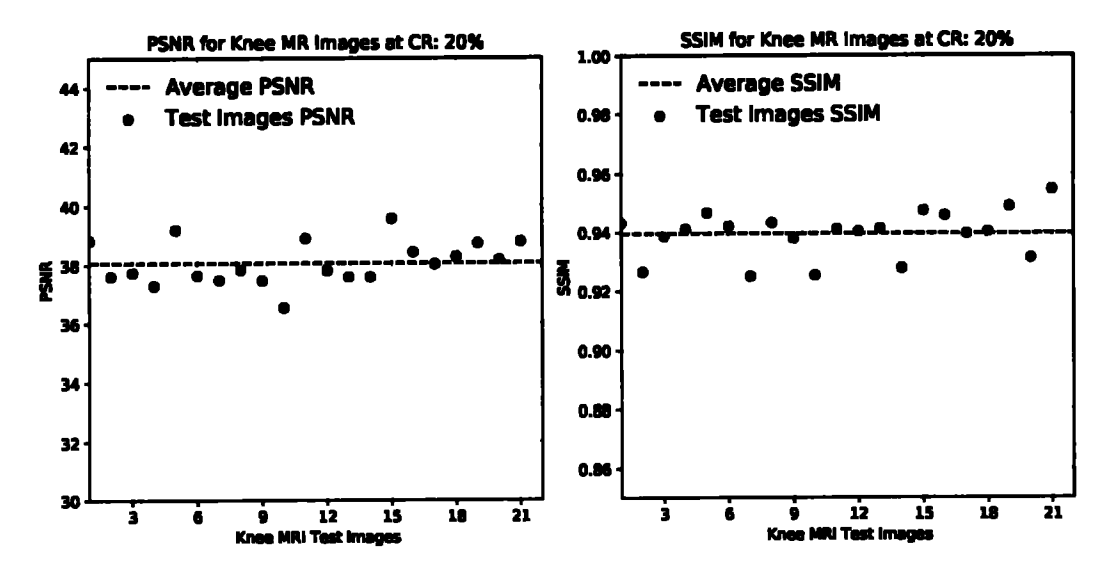


Figure 8-7: PSNR and SSIM for Knee MR Images at 5-fold compression

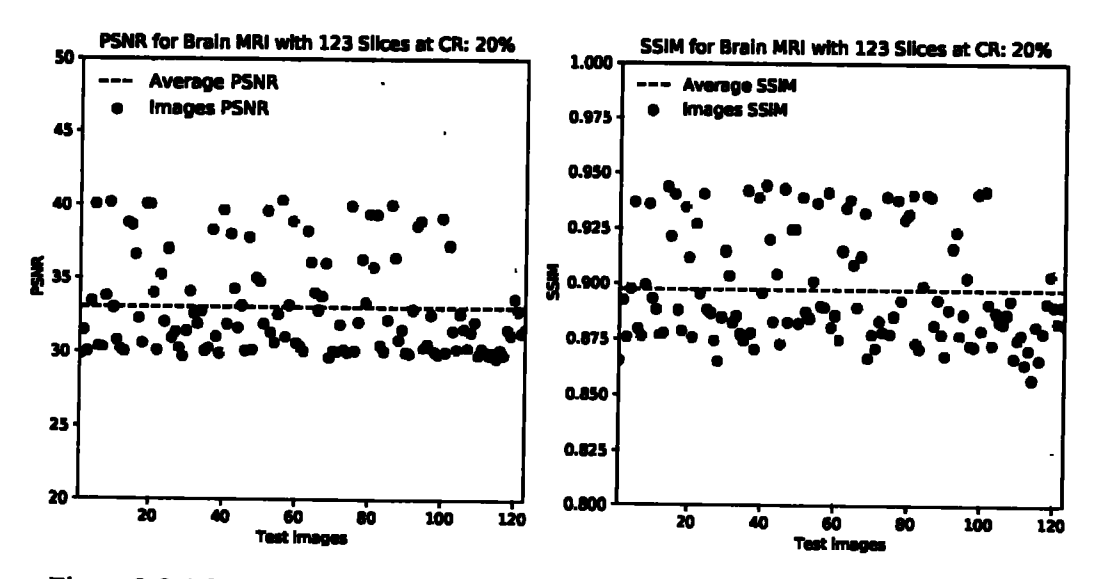


Figure 8-8: PSNR and SSIM for Brain MRI with 123 slices with 5-fold compression

### 8.7 Conclusions

The proposed DISTA-CSNet model has introduced data consistency constraints and a flexible *tanh*-based shrinkage technique, leading to remarkable advancements in terms of reduced training time, requiring only 20 epochs to adapt to different datasets for specific applications efficiently. Despite the reduced training time, the model's testing performance significantly improves in both SSIM and PSNR values. Moreover, incorporating dropouts in the proposed model has demonstrated its robustness when confronted with varying datasets. This resilience is evident from the testing results on Brain MRI with 123 slices, where the proposed model outperforms other state-of-the-art methods in recovering Compressed Sensing MRI data. These findings highlight the effectiveness and versatility of the DISTA-CSNet model, making it a promising and competitive solution for medical image reconstruction tasks.

#### CHAPTER 9

# **CONCLUSIONS**

# 9.1 Summary of Thesis

Compressed sensing is a cutting-edge acquisition procedure created to function at low sample rates. It has the benefit of shortening acquisition times in biomedical applications including computed tomography (CT), microwave imaging (MWI), and magnetic resonance imaging (MRI). This is especially useful when conventional acquisition techniques take a long time or subject patients to harmful radiation for an extended length of time. Compressed sensing in biomedical imaging has considerably decreased the amount of raw data needed and slashed acquisition times. The lengthened processing time during image recovery is a downside, though. The nonlinear CS recovery problem was solved using convex optimisation-based techniques in early CS attempts. However, these generic reconstruction algorithms frequently proved slow and ineffective for high-dimensional biomedical images, necessitating lengthy computations.

This dissertation's main objective is to provide a new set of algorithms that may effectively reconstruct Fourier-encoded biological images from sub-sampled observations to address this issue. To increase the overall efficacy and efficiency of CS MRI recovery, these suggested algorithms estimate the missing Fourier samples by using data consistency in the Fourier domain and shrinkage in the sparsity domain. The efficacy of different sparsity-promoting norms, such as  $l_0$ -norm and  $l_1$ -norm was evaluated and novel approaches to estimate sparsifying transforms were evaluated.

Table 9.1 summarises the compressively sampled MRI recovery through various proposed methods in terms of SSIM. The SSIM attained by the proposed methods highlights their effectiveness in recovering the MR images even with only 25% and 20% of the sampled, accelerating the MRI scanning process by 4 to 5 times respectively. The DISTA-CSNet has a clear advantage over other methods as it achieved similar accuracy with 5-fold compression and was tested on 50 different Brain MRIs, while other CS MRI

recovery algorithms were applied on a single Brain MRI, and still achieving competitive results.

Table 9-1: Summary of SSIM attained proposed methods to recover CS MRI.

Proposed Methods	Structural Similarity Index	CR 25%	
Smooth l <sub>0</sub> norm	0.9665		
Smooth l <sub>1</sub> norm	0.9567	25%	
Hybrid Smooth $l_0$ and $l_1$ norm	0.9696	25%	
Nature Inspired IRLS	0.9664	25%	
Heuristic Smooth l <sub>1</sub> -norm	0.9641	25%	
DISTA-CSNet Model	0.9634	20%	

The main conclusions from the thesis are covered as follows:

- The dissertation proposed a novel Kronecker Delta function for smooth approximation of  $l_0$  norm that efficiently recovered the undersampled 1D signal sparse signal and CS MRI, as compared to previous techniques.
- In-depth performance analysis of different Kronecker Delta functions to approximate sparsity promoting l<sub>0</sub> norm for recovery of CS MRI and undersampled 1D sparse signal was presented, highlighting the better-suited approximations based on their application.
- This thesis introduced a novel cost function that combines smooth approximations
  of l<sub>0</sub> and l<sub>1</sub> norm for recovery of undersampled 1D sparse signal and MRI from
  fewer observations in k-space. The proposed method achieved high accuracy in CS
  MRI recovery.
- A novel method that approximates l<sub>1</sub>norm and shrinkage with tanh. The proposed smooth approximation in loss function allowed us to apply gradient descent-based optimisation techniques to find the near-optimal solutions to the inverse problems posed by CS MRI recovery efficiently.
- The nature-inspired algorithm i.e., Particle Swarm Optimisation (PSO) was combined with Iterative Reweighted Least Square (IRLS) method to recover CS MRI from undersampled k-space data and the 1D k-sparse signal from fewer observations. The proposed method was evaluated with a comprehensive

- experiment to recover the 1D sparse signal and MRI accurately from undersampled data as compared to existing techniques.
- The heuristic smooth approximation of the l<sub>1</sub> norm was proposed to recover CS MRI from undersampled k-space data and the 1D sparse signal. The proposed method was assessed with extensive experimentation to recover 1D sparse signal and MRI accurately from undersampled data as compared to existing techniques.
- The main contribution of this thesis was developing a novel deep neural network dubbed DISTA-CSNet that trains the model to efficiently recover MRI from undersampled k-space data in significantly reduced time as compared to state-of-the-art methods that exist in literature. The data consistency constraint and tank-based shrinkage significantly improved the learning rate while training in only 20 Epochs. The dropouts introduced in the proposed DNN as a regularisation method made the trained model more robust to different datasets while testing it to three different datasets. The DISTA-CSNet not only recovered MR images more computationally efficiently in the testing phase but also improved the accuracy of the recovered CS MRI.

## 9.2 Future Directions

There can be several ways and enhancements for future research work that can take the lead from the ideas presented in this thesis.

- The focus of this work can be broadened to incorporate dynamic MR imaging,
   which entails quick data collection to track swift changes in signal strength.
- The proposed algorithms are appropriate for usage in conjunction with parallel imaging methods due to their computational simplicity.
- This thesis utilised analytical sparsifying transforms (dictionary), but it is suggested that incorporating an adaptive dictionary learning mechanism could enhance recovery results.
- The suggested CS reconstruction methods are promising for recovering video from compressed data, but an intelligent sensing mechanism might be required to fully take advantage of the strong correlation in a video sequence.

- The proposed CS recovery can be expanded to patch-based CS reconstruction in place of recovering the complete biological image in one go. It is envisaged that the reconstruction quality will increase as global modelling gives way to local and adaptive modelling.
- In a deep learning context, the transfer learning in this thesis can be expanded to create more universal CS recovery-based models that can adapt to other datasets without requiring initial training.
- The proposed DISTA-CSNet model can be implemented using multiple GPUs to enhance its training efficacy.
- The proposed DISTA-CSNet model can be modified to classify biomedical images under the CS framework.

# REFERENCES

- [1] J. Romberg, "Imaging via compressive sampling," *IEEE Signal Processing Magazine*, vol. 25, no. 2, pp. 14-20, 2008.
- [2] D. L. Donoho, "Compressed sensing," *IEEE Transactions on Information Theory*, vol. 52, no. 4, pp. 1289-1306, 2006, doi: 10.1109/TIT.2006.871582.
- [3] E. J. Candès, J. Romberg, and T. Tao, "Robust uncertainty principles: Exact signal reconstruction from highly incomplete frequency information," *IEEE Transactions on information theory*, vol. 52, no. 2, pp. 489-509, 2006.
- [4] E. J. Candes and M. B. Wakin, "An Introduction To Compressive Sampling," *IEEE Signal Processing Magazine*, vol. 25, no. 2, pp. 21-30, 2008, doi: 10.1109/MSP.2007.914731.
- [5] E. J. Candès, "Compressive sampling," in *Proceedings of the international congress of mathematicians*, 2006, vol. 3: Madrid, Spain, pp. 1433-1452.
- [6] X. Chai, J. Bi, Z. Gan, X. Liu, Y. Zhang, and Y. Chen, "Color image compression and encryption scheme based on compressive sensing and double random encryption strategy," *Signal Processing*, vol. 176, p. 107684, 2020/11/01/ 2020, doi: <a href="https://doi.org/10.1016/j.sigpro.2020.107684">https://doi.org/10.1016/j.sigpro.2020.107684</a>.
- [7] M. Wang, Q. Wang, J. Chanussot, and D. Hong, "lo-l1 Hybrid Total Variation Regularization and its Applications on Hyperspectral Image Mixed Noise Removal and Compressed Sensing," *IEEE Transactions on Geoscience and Remote Sensing*, vol. 59, no. 9, pp. 7695-7710, 2021, doi: 10.1109/TGRS.2021.3055516.
- [8] A. Pradhan, V. Amalladinne, A. Vem, K. R. Narayanan, and J. F. Chamberland, "A Joint Graph Based Coding Scheme for the Unsourced Random Access Gaussian Channel," in 2019 IEEE Global Communications Conference (GLOBECOM), 9-13 Dec. 2019 2019, pp. 1-6, doi: 10.1109/GLOBECOM38437.2019.9013278.
- [9] S. U. Khan, I. M. Qureshi, H. Haider, F. Zaman, and B. Shoaib, "Diagnosis of Faulty Sensors in Phased Array Radar Using Compressed Sensing and Hybrid IRLS-SSF Algorithm," Wireless Personal Communications, vol. 91, no. 1, pp. 383-402, 2016/11/01 2016, doi: 10.1007/s11277-016-3466-7.
- [10] O. Kerdjidj, N. Ramzan, K. Ghanem, A. Amira, and F. Chouireb, "Fall detection and human activity classification using wearable sensors and compressed sensing," *Journal of Ambient Intelligence and Humanized Computing*, vol. 11, no. 1, pp. 349-361, 2020/01/01 2020, doi: 10.1007/s12652-019-01214-4.
- [11] A. Raj, Y. Li, and Y. Bresler, "GAN-Based Projector for Faster Recovery With Convergence Guarantees in Linear Inverse Problems," in 2019 IEEE/CVF International Conference on Computer Vision (ICCV), 27 Oct.-2 Nov. 2019 2019, pp. 5601-5610, doi: 10.1109/ICCV.2019.00570.
- [12] H. Haider, J. A. Shah, I. M. Qureshi, H. Omer, and K. Kadir, "Compressively Sampled MRI Recovery Using Modified Iterative-Reweighted Least Square Method," *Applied Magnetic Resonance*, vol. 47, no. 9, pp. 1033-1046, 2016/09/01 2016, doi: 10.1007/s00723-016-0810-8.

- [13] J. Shah, I. Qureshi, H. Omer, and A. Khaliq, "A modified POCS-based reconstruction method for compressively sampled MR imaging," *International Journal of Imaging Systems and Technology*, vol. 24, no. 3, pp. 203-207, 2014/09/01 2014, doi: 10.1002/ima.22095.
- [14] M. Lustig, D. Donoho, and J. M. Pauly, "Sparse MRI: The application of compressed sensing for rapid MR imaging," Magnetic Resonance in Medicine, vol. 58, no. 6, pp. 1182-1195, 2007/12/01 2007, doi: 10.1002/mrm.21391.
- [15] M. Lustig, D. L. Donoho, J. M. Santos, and J. M. Pauly, "Compressed Sensing MRI," *IEEE Signal Processing Magazine*, vol. 25, no. 2, pp. 72-82, 2008, doi: 10.1109/MSP.2007.914728.
- [16] M. Lustig, Sparse mri. Stanford University, 2008.
- [17] J. A. Fessler, "Model-based image reconstruction for MRI," *IEEE Signal Processing Magazine*, vol. 27, no. 4, pp. 81-89, 2010.
- [18] J. Huang, S. Zhang, and D. Metaxas, "Efficient MR image reconstruction for compressed MR imaging," *Medical Image Analysis*, vol. 15, no. 5, pp. 670-679, 2011.
- [19] M. Doneva, Advances in compressed sensing for magnetic resonance imaging. 2010.
- [20] I. Daubechies, M. Defrise, and C. De Mol, "An iterative thresholding algorithm for linear inverse problems with a sparsity constraint," *Communications on pure and applied mathematics*, vol. 57, no. 11, pp. 1413-1457, 2004.
- [21] M. Elad, "From exact to approximate solutions," in Sparse and Redundant Representations: Springer, 2010, pp. 79-109.
- [22] H. Haider, J. A. Shah, K. Kadir, and N. Khan, "Sparse Reconstruction Using Hyperbolic Tangent as Smooth 11-Norm Approximation," *Computation*, vol. 11, no. 1, p. 7, 2023. [Online]. Available: <a href="https://www.mdpi.com/2079-3197/11/1/7">https://www.mdpi.com/2079-3197/11/1/7</a>.
- [23] T. Adeyemi and M. Davies, "Sparse representations of images using overcomplete complex wavelets," in *IEEE/SP 13th Workshop on Statistical Signal Processing*, 2005, 17-20 July 2005 2005, pp. 865-870, doi: 10.1109/SSP.2005.1628715.
- [24] J. A. Shah, "Applications of Compressed Sensing to Biomedical Imaging," 2015.
- [25] J. A. Shah, I. M. Qureshi, H. Omer, A. A. Khaliq, and Y. Deng, "Compressively sampled magnetic resonance image reconstruction using separable surrogate functional method," *Concepts in Magnetic Resonance Part A*, vol. 43, no. 5, pp. 157-165, 2014/09/01 2015, doi: 10.1002/cmr.a.21314.
- [26] S. Kremer et al., "Brain MRI Findings in Severe COVID-19: A Retrospective Observational Study," Radiology, vol. 297, no. 2, pp. E242-E251, 2020, doi: 10.1148/radiol.2020202222.
- [27] A. Wadhwa, A. Bhardwaj, and V. Singh Verma, "A review on brain tumor segmentation of MRI images," *Magnetic Resonance Imaging*, vol. 61, pp. 247-259, 2019/09/01/2019, doi: <a href="https://doi.org/10.1016/j.mri.2019.05.043">https://doi.org/10.1016/j.mri.2019.05.043</a>.
- [28] R. M. Mann, N. Cho, and L. Moy, "Breast MRI: State of the Art," *Radiology*, vol. 292, no. 3, pp. 520-536, 2019, doi: 10.1148/radiol.2019182947.
- [29] Y. Yang, J. Sun, H. Li, and Z. Xu, "ADMM-CSNet: A Deep Learning Approach for Image Compressive Sensing," *IEEE Transactions on Pattern Analysis and Machine Intelligence*, vol. 42, no. 3, pp. 521-538, 2020, doi: 10.1109/TPAMI.2018.2883941.

- [30] J. Zhang and B. Ghanem, "ISTA-Net: Interpretable Optimization-Inspired Deep Network for Image Compressive Sensing," in 2018 IEEE/CVF Conference on Computer Vision and Pattern Recognition, 18-23 June 2018 2018, pp. 1828-1837, doi: 10.1109/CVPR.2018.00196.
- [31] A. Wahid, J. A. Shah, A. U. Khan, M. Ahmed, and H. Razali, "Multi-Layer Basis Pursuit for Compressed Sensing MR Image Reconstruction," *IEEE Access*, vol. 8, pp. 186222-186232, 2020, doi: 10.1109/ACCESS.2020.3028877.
- Q. Huang et al., "Dynamic MRI reconstruction with end-to-end motion-guided network," Medical Image Analysis, vol. 68, p. 101901, 2021/02/01/ 2021, doi: https://doi.org/10.1016/j.media.2020.101901.
- P. Chlap, H. Min, N. Vandenberg, J. Dowling, L. Holloway, and A. Haworth, "A review of medical image data augmentation techniques for deep learning applications," *Journal of Medical Imaging and Radiation Oncology*, vol. 65, no. 5, pp. 545-563, 2021, doi: <a href="https://doi.org/10.1111/1754-9485.13261">https://doi.org/10.1111/1754-9485.13261</a>.
- [34] Z. Fabian, R. Heckel, and M. Soltanolkotabi, "Data augmentation for deep learning based accelerated MRI reconstruction with limited data," presented at the Proceedings of the 38th International Conference on Machine Learning, Proceedings of Machine Learning Research, 2021. [Online]. Available: <a href="https://proceedings.mlr.press/v139/fabian21a.html">https://proceedings.mlr.press/v139/fabian21a.html</a>.
- [35] M. Yaqub et al., "GAN-TL: Generative Adversarial Networks with Transfer Learning for MRI Reconstruction," Applied Sciences, vol. 12, no. 17, p. 8841, 2022. [Online]. Available: <a href="https://www.mdpi.com/2076-3417/12/17/8841">https://www.mdpi.com/2076-3417/12/17/8841</a>.
- [36] F. Knoll, K. Hammernik, E. Kobler, T. Pock, M. P. Recht, and D. K. Sodickson, "Assessment of the generalization of learned image reconstruction and the potential for transfer learning," *Magnetic Resonance in Medicine*, vol. 81, no. 1, pp. 116-128, 2019, doi: <a href="https://doi.org/10.1002/mrm.27355">https://doi.org/10.1002/mrm.27355</a>.
- [37] J. Lv et al., "Transfer learning enhanced generative adversarial networks for multichannel MRI reconstruction," Computers in Biology and Medicine, vol. 134, p. 104504, 2021, doi: <a href="https://doi.org/10.1016/j.compbiomed.2021.104504">https://doi.org/10.1016/j.compbiomed.2021.104504</a>.
- [38] C. E. Shannon, "Communication in the Presence of Noise," *Proceedings of the IRE*, vol. 37, no. 1, pp. 10-21, 1949, doi: 10.1109/JRPROC.1949.232969.
- [39] H. J. Landau, "Necessary density conditions for sampling and interpolation of certain entire functions," *Acta Mathematica*, vol. 117, no. 1, pp. 37-52, 1967/07/01 1967, doi: 10.1007/BF02395039.
- [40] E. J. Candes and T. Tao, "Near-Optimal Signal Recovery From Random Projections: Universal Encoding Strategies?," *IEEE Transactions on Information Theory*, vol. 52, no. 12, pp. 5406-5425, 2006, doi: 10.1109/TIT.2006.885507.
- [41] E. Candes and J. Romberg, "11-magic: Recovery of sparse signals via convex programming," *URL*: www. acm. caltech. edu/l1magic/downloads/l1magic. pdf, vol. 4, no. 14, p. 16, 2005.
- [42] E. J. Candes and T. Tao, "Decoding by linear programming," *IEEE Transactions on Information Theory*, vol. 51, no. 12, pp. 4203-4215, 2005, doi: 10.1109/TIT.2005.858979.
- [43] J. C. Emmanuel and K. R. Justin, "Signal recovery from random projections," in Proc.SPIE, 2005, vol. 5674, pp. 76-86, doi: 10.1117/12.600722. [Online]. Available: <a href="https://doi.org/10.1117/12.600722">https://doi.org/10.1117/12.600722</a>

- [44] M. A. Bernstein, K. F. King, and X. J. Zhou, *Handbook of MRI pulse sequences*. Elsevier, 2004.
- [45] R. W. Brown, Y.-C. N. Cheng, E. M. Haacke, M. R. Thompson, and R. Venkatesan, *Magnetic resonance imaging: physical principles and sequence design*. John Wiley & Sons, 2014.
- [46] P. C. Lauterbur, "Image Formation by Induced Local Interactions: Examples Employing Nuclear Magnetic Resonance," *Nature*, vol. 242, no. 5394, pp. 190-191, 1973/03/01 1973, doi: 10.1038/242190a0.
- [47] G. H. Glover and J. M. Pauly, "Projection reconstruction techniques for reduction of motion effects in MRI," (in eng), *Magn Reson Med*, vol. 28, no. 2, pp. 275-89, Dec 1992, doi: 10.1002/mrm.1910280209.
- [48] C. B. Ahn, J. H. Kim, and Z. H. Cho, "High-speed spiral-scan echo planar NMR imaging-I," (in eng), *IEEE Trans Med Imaging*, vol. 5, no. 1, pp. 2-7, 1986, doi: 10.1109/tmi.1986.4307732.
- [49] J. G. Pipe, "Motion correction with PROPELLER MRI: application to head motion and free-breathing cardiac imaging," (in eng), *Magn Reson Med*, vol. 42, no. 5, pp. 963-9, Nov 1999, doi: 10.1002/(sici)1522-2594(199911)42:5<963::aid-mrm17>3.0.co;2-1.
- [50] K. Scheffler and J. Hennig, "Frequency resolved single-shot MR imaging using stochastic k-space trajectories," (in eng), *Magn Reson Med*, vol. 35, no. 4, pp. 569-76, Apr 1996, doi: 10.1002/mrm.1910350417.
- [51] D. C. Noll, D. G. Nishimura, and A. Macovski, "Homodyne detection in magnetic resonance imaging," *IEEE transactions on medical imaging*, vol. 10 2, pp. 154-63, 1991.
- [52] R. S. Likes, "Moving gradient zeugmatography," United States Patent US patent document 4,307,343/A/ Patent Appl. Bibliographic information available from INIS: <a href="http://inis.iaea.org/search/search.aspx?orig\_q=RN:13692214">http://inis.iaea.org/search/search.aspx?orig\_q=RN:13692214</a> U.S. Commissioner of Patents, Washington, D.C. 20231, USA, \$.50, 1981. [Online]. Available: <a href="http://inis.iaea.org/search/search.aspx?orig\_q=RN:13692214">http://inis.iaea.org/search/search.aspx?orig\_q=RN:13692214</a>
- [53] M. Doneva, P. Börnert, H. Eggers, C. Stehning, J. Sénégas, and A. Mertins, "Compressed sensing reconstruction for magnetic resonance parameter mapping," *Magnetic Resonance in Medicine*, vol. 64, no. 4, pp. 1114-1120, 2010, doi: https://doi.org/10.1002/mrm.22483.
- [54] S. Mallat, A Wavelet Tour of Signal Processing, Third Edition: The Sparse Way, 3rd ed. USA: Academic Press Inc., 2008.
- [55] B. A. Chronik and B. K. Rutt, "Simple linear formulation for magnetostimulation specific to MRI gradient coils," *Magnetic Resonance in Medicine*, vol. 45, no. 5, pp. 916-919, 2001, doi: <a href="https://doi.org/10.1002/mrm.1121">https://doi.org/10.1002/mrm.1121</a>.
- [56] M. K. Stehling, R. Turner, and P. Mansfield, "Echo-Planar Imaging: Magnetic Resonance Imaging in a Fraction of a Second," *Science*, vol. 254, no. 5028, pp. 43-50, 1991, doi: doi:10.1126/science.1925560.
- [57] D. K. Sodickson and W. J. Manning, "Simultaneous acquisition of spatial harmonics (SMASH): fast imaging with radiofrequency coil arrays," (in eng), *Magn Reson Med*, vol. 38, no. 4, pp. 591-603, Oct 1997, doi: 10.1002/mrm.1910380414.
- [58] D. C. Noll, D. G. Nishimura, and A. Macovski, "Homodyne detection in magnetic resonance imaging," (in eng), *IEEE Trans Med Imaging*, vol. 10, no. 2, pp. 154-63, 1991, doi: 10.1109/42.79473.

- [59] K. P. Pruessmann, M. Weiger, M. B. Scheidegger, and P. Boesiger, "SENSE: sensitivity encoding for fast MRI," (in eng), *Magn Reson Med*, vol. 42, no. 5, pp. 952-62, Nov 1999.
- [60] P. J. Koopmans and V. Pfaffenrot, "Enhanced POCS reconstruction for partial Fourier imaging in multi-echo and time-series acquisitions," *Magnetic Resonance in Medicine*, vol. 85, no. 1, pp. 140-151, 2021, doi: https://doi.org/10.1002/mrm.28417.
- [61] Y. Li, H. Yang, D. Xie, D. Dreizin, F. Zhou, and Z. Wang, "POCS-Augmented CycleGAN for MR Image Reconstruction," *Applied Sciences*, vol. 12, no. 1, p. 114, 2022. [Online]. Available: https://www.mdpi.com/2076-3417/12/1/114.
- [62] S. Chen et al., "Highly accelerated multi-shot intravoxel incoherent motion diffusion-weighted imaging in brain enabled by parametric POCS-based multiplexed sensitivity encoding," NMR in Biomedicine, vol. n/a, no. n/a, p. e5063, doi: https://doi.org/10.1002/nbm.5063.
- [63] I. Koshelev and S. Lefkimmiatis, "Iterative Reweighted Least Squares Networks With Convergence Guarantees for Solving Inverse Imaging Problems," arXiv preprint arXiv:2308.05745, 2023.
- [64] K. Liang and M. J. Clay, "Iterative re-weighted least squares algorithm for lp-minimization with tight frame and 0 Linear Algebra and its Applications, vol. 581, pp. 413-434, 2019/11/15/ 2019, doi: https://doi.org/10.1016/j.laa.2019.07.029.
- [65] M. L. de Leeuw den Bouter, M. B. van Gijzen, and R. F. Remis, "Conjugate gradient variants for \$\${\ell}\_{p}\$\$-regularized image reconstruction in low-field MRI," SN Applied Sciences, vol. 1, no. 12, p. 1736, 2019/11/30 2019, doi: 10.1007/s42452-019-1670-2.
- [66] I. Daubechies, M. Defrise, and C. De Mol, "An iterative thresholding algorithm for linear inverse problems with a sparsity constraint," Communications on Pure and Applied Mathematics: A Journal Issued by the Courant Institute of Mathematical Sciences, vol. 57, no. 11, pp. 1413-1457, 2004.
- [67] A. H. Ahmed, I. M. Qureshi, J. A. Shah, and H. Omer, "Efficient Reconstruction of Free Breathing Under-Sampled Cardiac Cine MRI," arXiv preprint arXiv:1904.04615, 2019.
- [68] M. Elad, "Optimized projections for compressed sensing," *IEEE Transactions on Signal Processing*, vol. 55, no. 12, pp. 5695-5702, 2007.
- [69] Y. K. Cheung, R. J. Cole, and Y. Tao, "Parallel Stochastic Asynchronous Coordinate Descent: Tight Bounds on the Possible Parallelism," *SIAM Journal on Optimization*, vol. 31, no. 1, pp. 448-460, 2021, doi: 10.1137/19m129574x.
- [70] J. Glaubitz, A. Gelb, and G. Song, "Generalized Sparse Bayesian Learning and Application to Image Reconstruction," *SIAM/ASA Journal on Uncertainty Quantification*, vol. 11, no. 1, pp. 262-284, 2023/03/31 2023, doi: 10.1137/22M147236X.
- [71] C. Zhang, "Next Generation CT Image Reconstruction via Synergy of Human Wisdom and Machine Intelligence," The University of Wisconsin-Madison, 2023.
- [72] A. Beck and M. Teboulle, "A fast iterative shrinkage-thresholding algorithm for linear inverse problems," *SIAM journal on imaging sciences*, vol. 2, no. 1, pp. 183-202, 2009.

- [73] S. Babapour, M. Lakestani, and A. Fatholahzadeh, "AFISTA: Accelerated FISTA for sparse signal recovery and compressive sensing," *Multimedia Tools and Applications*, vol. 80, no. 13, pp. 20707-20731, 2021/05/01 2021, doi: 10.1007/s11042-021-10701-w.
- [74] Q. Huang, D. Yang, J. Yi, L. Axel, and D. Metaxas, "FR-Net: Joint Reconstruction and Segmentation in Compressed Sensing Cardiac MRI," in *Functional Imaging and Modeling of the Heart*, Cham, Y. Coudière, V. Ozenne, E. Vigmond, and N. Zemzemi, Eds., 2019// 2019: Springer International Publishing, pp. 352-360.
- [75] J. Lang, K. Gang, and C. Zhang, "Adjustable shrinkage-thresholding projection algorithm for compressed sensing magnetic resonance imaging," *Magnetic Resonance Imaging*, vol. 86, pp. 74-85, 2022/02/01/ 2022, doi: <a href="https://doi.org/10.1016/j.mri.2021.11.013">https://doi.org/10.1016/j.mri.2021.11.013</a>.
- [76] L. Xin, D. Wang, and W. Shi, "FISTA-CSNet: a deep compressed sensing network by unrolling iterative optimization algorithm," *The Visual Computer*, vol. 39, no. 9, pp. 4177-4193, 2023/09/01 2023, doi: 10.1007/s00371-022-02583-2.
- [77] S. G. Mallat and Z. Zhang, "Matching pursuits with time-frequency dictionaries," *IEEE Transactions on signal processing*, vol. 41, no. 12, pp. 3397-3415, 1993.
- [78] J. A. Tropp and A. C. Gilbert, "Signal recovery from random measurements via orthogonal matching pursuit," *IEEE Transactions on information theory*, vol. 53, no. 12, pp. 4655-4666, 2007.
- [79] D. L. Donoho, Y. Tsaig, I. Drori, and J.-L. Starck, "Sparse solution of underdetermined systems of linear equations by stagewise orthogonal matching pursuit," *IEEE transactions on Information Theory*, vol. 58, no. 2, pp. 1094-1121, 2012.
- [80] D. Needell and R. Vershynin, "Uniform uncertainty principle and signal recovery via regularized orthogonal matching pursuit," *Foundations of computational mathematics*, vol. 9, pp. 317-334, 2009.
- [81] D. Needell and J. A. Tropp, "CoSaMP: Iterative signal recovery from incomplete and inaccurate samples," *Applied and computational harmonic analysis*, vol. 26, no. 3, pp. 301-321, 2009.
- [82] S. Ament and C. Gomes, "On the Optimality of Backward Regression: Sparse Recovery and Subset Selection," in ICASSP 2021 2021 IEEE International Conference on Acoustics, Speech and Signal Processing (ICASSP), 6-11 June 2021 2021, pp. 5599-5603, doi: 10.1109/ICASSP39728.2021.9415082.
- [83] X. Zhang, Y. Liu, and X. Wang, "A Sparsity Preestimated Adaptive Matching Pursuit Algorithm," *Journal of Electrical and Computer Engineering*, vol. 2021, p. 5598180, 2021/04/30 2021, doi: 10.1155/2021/5598180.
- [84] Q. Deng et al., "Compressed sensing for image reconstruction via back-off and rectification of greedy algorithm," Signal Processing, vol. 157, pp. 280-287, 2019/04/01/2019, doi: <a href="https://doi.org/10.1016/j.sigpro.2018.12.007">https://doi.org/10.1016/j.sigpro.2018.12.007</a>.
- [85] D. W. Turner, "Parallelisation of greedy algorithms for compressive sensing reconstruction," University of Cambridge, 2019.
- [86] M. V. R. Manimala, C. D. Naidu, and M. N. Giri Prasad, "Dictionary Learning-Based MR Image Reconstruction in the Presence of Speckle Noise: Greedy Versus Convex," in *Soft Computing and Signal Processing*, Singapore, J. Wang, G. R. M. Reddy, V. K. Prasad, and V. S. Reddy, Eds., 2019// 2019: Springer Singapore, pp. 537-546.

- [87] J. Li, P. Chow, Y. Peng, and T. Jiang, "FPGA Implementation of an Improved OMP for Compressive Sensing Reconstruction," *IEEE Transactions on Very Large Scale Integration (VLSI) Systems*, vol. 29, no. 2, pp. 259-272, 2021, doi: 10.1109/TVLSI.2020.3030906.
- [88] J. F. De Boer, B. Cense, B. H. Park, M. C. Pierce, G. J. Tearney, and B. E. Bouma, "Improved signal-to-noise ratio in spectral-domain compared with time-domain optical coherence tomography," *Optics letters*, vol. 28, no. 21, pp. 2067-2069, 2003.
- [89] Q. Huynh-Thu and M. Ghanbari, "Scope of validity of PSNR in image/video quality assessment," *Electronics Letters*, vol. 44, no. 13, pp. 800-801.
- [90] G. H. Mohimani, M. Babaie-Zadeh, and C. Jutten, "Fast Sparse Representation Based on Smoothed £0 Norm," in *Independent Component Analysis and Signal Separation*, Berlin, Heidelberg, M. E. Davies, C. J. James, S. A. Abdallah, and M. D. Plumbley, Eds., 2007// 2007: Springer Berlin Heidelberg, pp. 389-396.
- [91] I. F. Gorodnitsky and B. D. Rao, "Sparse signal reconstruction from limited data using FOCUSS: a re-weighted minimum norm algorithm," *IEEE Transactions on Signal Processing*, vol. 45, no. 3, pp. 600-616, 1997, doi: 10.1109/78.558475.
- [92] S. S. Chen, D. L. Donoho, and M. A. Saunders, "Atomic Decomposition by Basis Pursuit," *SIAM Review*, vol. 43, no. 1, pp. 129-159, 2001, doi: 10.1137/s003614450037906x.
- [93] S. P. Boyd and L. Vandenberghe, *Convex optimization*. Cambridge university press, 2004.
- [94] D. L. Donoho, "For most large underdetermined systems of equations, the minimal ?1-norm near-solution approximates the sparsest near-solution," *Communications on Pure and Applied Mathematics*, vol. 59, no. 7, pp. 907-934, 2006, doi: https://doi.org/10.1002/cpa.20131.
- [95] J. Xiang, H. Yue, X. Yin, and G. Ruan, "A Reweighted Symmetric Smoothed Function Approximating L0-Norm Regularized Sparse Reconstruction Method," Symmetry, vol. 10, no. 11, p. 583, 2018. [Online]. Available: <a href="https://www.mdpi.com/2073-8994/10/11/583">https://www.mdpi.com/2073-8994/10/11/583</a>.
- [96] C. Zhang, D. Hao, C. Hou, and X. Yin, "A New Approach for Sparse Signal Recovery in Compressed Sensing Based on Minimizing Composite Trigonometric Function," *IEEE Access*, vol. 6, pp. 44894-44904, 2018, doi: 10.1109/ACCESS.2018.2855958.
- [97] G. H. Mohimani, M. Babaie-Zadeh, and C. Jutten, "Complex-valued sparse representation based on smoothed & 0 norm," in 2008 IEEE International Conference on Acoustics, Speech and Signal Processing, 2008: IEEE, pp. 3881-3884.
- [98] L. Xu, C. Lu, Y. Xu, and J. Jia, "Image smoothing via L 0 gradient minimization," in *Proceedings of the 2011 SIGGRAPH Asia Conference*, Hong Kong, China, 2011 2011, vol. 30, ACM: ACM, 6 ed., 2011, pp. 1-12, doi: 10.1145/2070781.2024208.
- [99] J. Jin, B. Yang, K. Liang, and X. Wang, "General image denoising framework based on compressive sensing theory," *Computers & Graphics*, vol. 38, pp. 382-391, 2014/02/01/2014, doi: <a href="https://doi.org/10.1016/j.cag.2013.11.011">https://doi.org/10.1016/j.cag.2013.11.011</a>.
- [100] H. Zayyani and M. Babaie-Zadeh, "Thresholded smoothed-lo(SL0) dictionary learning for sparse representations," in 2009 IEEE International Conference on Acoustics, Speech and Signal Processing, 19-24 April 2009 2009, pp. 1825-1828, doi: 10.1109/ICASSP.2009.4959961.

- [101] J. Liu, W. Zhou, and F. H. Juwono, "Joint Smoothed le-Norm DOA Estimation Algorithm for Multiple Measurement Vectors in MIMO Radar," (in eng), Sensors (Basel), vol. 17, no. 5, May 8 2017, doi: 10.3390/s17051068.
- [102] G. Gui, W. Peng, Q. Wan, and F. Adachi, "A Fast Compressive Channel Estimation with Modified Smoothed L0 Algorithm," arXiv preprint arXiv:1005.2267, 2010.
- [103] W. Tang, Z. Shi, and Z. Duren, "Sparse hyperspectral unmixing using an approximate L0 norm," *Optik*, vol. 125, no. 1, pp. 31-38, 2014/01/01/ 2014, doi: <a href="https://doi.org/10.1016/j.ijleo.2013.06.073">https://doi.org/10.1016/j.ijleo.2013.06.073</a>.
- [104] J. Portilla and L. Mancera, "L0-based sparse approximation: two alternative methods and some applications," in *Optical Engineering + Applications*, 2007, vol. 6701: SPIE, p. 15.
- [105] H. Xue, L. Sun, and G. Ou, "Speech reconstruction based on compressed sensing theory using smoothed L0 algorithm," in 2016 8th International Conference on Wireless Communications & Signal Processing (WCSP), 13-15 Oct. 2016 2016, pp. 1-4, doi: 10.1109/WCSP.2016.7752443.
- [106] C. Zhang, S. Song, X. Wen, L. Yao, and Z. Long, "Improved sparse decomposition based on a smoothed L0 norm using a Laplacian kernel to select features from fMRI data," *Journal of Neuroscience Methods*, vol. 245, pp. 15-24, 2015/04/30/ 2015, doi: <a href="https://doi.org/10.1016/j.jneumeth.2014.12.021">https://doi.org/10.1016/j.jneumeth.2014.12.021</a>.
- [107] J. A. Shah, H. Haider, K. A. Kadir, and S. Khan, "Sparse signal reconstruction of compressively sampled signals using smoothed £0-norm," in 2017 IEEE International Conference on Signal and Image Processing Applications (ICSIPA), 12-14 Sept. 2017 2017, pp. 61-65, doi: 10.1109/ICSIPA.2017.8120580.
- [108] D. A. Auger et al., "Imaging left-ventricular mechanical activation in heart failure patients using cine DENSE MRI: Validation and implications for cardiac resynchronization therapy," *Journal of Magnetic Resonance Imaging*, vol. 46, no. 3, pp. 887-896, 2017/09/01 2017, doi: 10.1002/jmri.25613.
- [109] J. Liu et al., "Highly-accelerated self-gated free-breathing 3D cardiac cine MRI: validation in assessment of left ventricular function," Magnetic Resonance Materials in Physics, Biology and Medicine, vol. 30, no. 4, pp. 337-346, 2017.
- [110] J. F. P. van Amerom et al., "Fetal cardiac cine imaging using highly accelerated dynamic MRI with retrospective motion correction and outlier rejection," Magnetic Resonance in Medicine, vol. 79, no. 1, pp. 327-338, 2018/01/01 2018, doi: 10.1002/mrm.26686.
- [111] W. J. Paulus et al., "How to diagnose diastolic heart failure: a consensus statement on the diagnosis of heart failure with normal left ventricular ejection fraction by the Heart Failure and Echocardiography Associations of the European Society of Cardiology," European Heart Journal, vol. 28, no. 20, pp. 2539-2550, 2007, doi: 10.1093/eurheartj/ehm037.
- [112] U. Gamper, P. Boesiger, and S. Kozerke, "Compressed sensing in dynamic MRI," *Magnetic Resonance in Medicine*, vol. 59, no. 2, pp. 365-373, 2008/02/01 2008, doi: 10.1002/mrm.21477.
- [113] J. Yerly et al., "A phantom study to determine the theoretical accuracy and precision of radial MRI to measure cross-sectional area differences for the application of coronary endothelial function assessment," *Magnetic Resonance in Medicine*, vol. 79, no. 1, pp. 108-120, 2018/01/01 2018, doi: 10.1002/mrm.26646.

- [114] A. H. Ahmed, I. M. Qureshi, J. A. Shah, and M. Zaheer, "Motion correction based reconstruction method for compressively sampled cardiac MR imaging," *Magnetic Resonance Imaging*, vol. 36, pp. 159-166, 2017/02/01/ 2017, doi: https://doi.org/10.1016/j.mri.2016.10.008.
- [115] D. L. Donoho, "De-noising by soft-thresholding," *IEEE Transactions on Information Theory*, vol. 41, no. 3, pp. 613-627, 1995, doi: 10.1109/18.382009.
- [116] J. A. Tropp, M. B. Wakin, M. F. Duarte, D. Baron, and R. G. Baraniuk, "Random Filters for Compressive Sampling and Reconstruction," in 2006 IEEE International Conference on Acoustics Speech and Signal Processing Proceedings, 14-19 May 2006 2006, vol. 3, pp. III-III, doi: 10.1109/ICASSP.2006.1660793.
- [117] W. Yin, S. Osher, D. Goldfarb, and J. Darbon, "Bregman Iterative Algorithms for \$\ell\_1\$-Minimization with Applications to Compressed Sensing," *SIAM Journal on Imaging Sciences*, vol. 1, no. 1, pp. 143-168, 2008/01/01 2008, doi: 10.1137/070703983.
- [118] M. A. Khajehnejad, W. Xu, A. S. Avestimehr, and B. Hassibi, "Weighted &leinf>1</inf>minimization for sparse recovery with prior information," in 2009 IEEE International Symposium on Information Theory, 28 June-3 July 2009 2009, pp. 483-487, doi: 10.1109/ISIT.2009.5205716.
- [119] C. He, J. Xing, J. Li, Q. Yang, and R. Wang, "A New Wavelet Thresholding Function Based on Hyperbolic Tangent Function %J Mathematical Problems in Engineering," vol. 2015, p. 10, 2015, Art no. 528656, doi: 10.1155/2015/528656.
- [120] L. Jing-yi, L. Hong, Y. Dong, and Z. Yan-sheng, "A New Wavelet Threshold Function and Denoising Application %J Mathematical Problems in Engineering," vol. 2016, p. 8, 2016, Art no. 3195492, doi: 10.1155/2016/3195492.
- [121] M. Bilal, J. A. Shah, I. M. Qureshi, and K. Kadir, "Respiratory Motion Correction for Compressively Sampled Free Breathing Cardiac MRI Using Smooth 1(1)-Norm Approximation," *International journal of biomedical imaging*, vol. 2018, pp. 7803067-7803067, 2018, doi: 10.1155/2018/7803067.
- [122] J. Shah, I. M. Qureshi, Y. Deng, and K. Kadir, "Reconstruction of Sparse Signals and Compressively Sampled Images Based on Smooth 11-Norm Approximation," *Journal of Signal Processing Systems*, vol. 88, no. 3, pp. 333-344, 2017.
- [123] J. A. Shah, I. M. Qureshi, H. Omer, A. A. Khaliq, and Y. Deng, "Compressively sampled magnetic resonance image reconstruction using separable surrogate functional method," *Concepts in Magnetic Resonance Part A*, vol. 43, no. 5, pp. 157-165, 2014/09/01 2014, doi: 10.1002/cmr.a.21314.
- [124] M. Schmidt, G. Fung, and R. Rosales, "Fast Optimization Methods for L1 Regularization: A Comparative Study and Two New Approaches," in *Machine Learning: ECML 2007*, Berlin, Heidelberg, J. N. Kok, J. Koronacki, R. L. d. Mantaras, S. Matwin, D. Mladenič, and A. Skowron, Eds., 2007// 2007: Springer Berlin Heidelberg, pp. 286-297.
- [125] T. Blumensath and M. E. Davies, "Iterative hard thresholding for compressed sensing," *Applied and Computational Harmonic Analysis*, vol. 27, no. 3, pp. 265-274, 2009/11/01/2009, doi: https://doi.org/10.1016/j.acha.2009.04.002.
- [126] S. G. Chang, Y. Bin, and M. Vetterli, "Spatially adaptive wavelet thresholding with context modeling for image denoising," *IEEE Transactions on Image Processing*, vol. 9, no. 9, pp. 1522-1531, 2000, doi: 10.1109/83.862630.

- [127] J. Prinosil, Z. Smekal, and K. Bartusek, "Wavelet Thresholding Techniques in MRI Domain," in 2010 International Conference on Biosciences, 7-13 March 2010 2010, pp. 58-63, doi: 10.1109/BioSciencesWorld.2010.14.
- [128] M. Nasri and H. Nezamabadi-pour, "Image denoising in the wavelet domain using a new adaptive thresholding function," *Neurocomputing*, vol. 72, no. 4, pp. 1012-1025, 2009/01/01/2009, doi: <a href="https://doi.org/10.1016/j.neucom.2008.04.016">https://doi.org/10.1016/j.neucom.2008.04.016</a>.
- [129] L. Sendur and I. W. Selesnick, "Bivariate shrinkage functions for wavelet-based denoising exploiting interscale dependency," *IEEE Transactions on Signal Processing*, vol. 50, no. 11, pp. 2744-2756, 2002, doi: 10.1109/TSP.2002.804091.
- [130] H. Haider, J. A. Shah, and U. Ali, "Comparative analysis of sparse signal recovery algorithms based on minimization norms," in *World Congress on Sustainable Technologies (WCST-2014)*, 2014: IEEE, pp. 72-76.
- [131] E. Gopi, Algorithm collections for digital signal processing applications using Matlab. Springer Science & Business Media, 2007.
- [132] B. Craenen, A. Eiben, and E. Marchiori, "How to handle constraints with evolutionary algorithms," *Practical Handbook Of Genetic Algorithms:* Applications, pp. 341-361, 2001.
- [133] G. T. Pulido and C. A. C. Coello, "A constraint-handling mechanism for particle swarm optimization," in *Proceedings of the 2004 Congress on Evolutionary Computation (IEEE Cat. No. 04TH8753)*, 2004, vol. 2: Ieee, pp. 1396-1403.
- [134] Y. Wang, Z. Cai, Y. Zhou, and Z. Fan, "Constrained optimization based on hybrid evolutionary algorithm and adaptive constraint-handling technique," *Structural and Multidisciplinary Optimization*, vol. 37, pp. 395-413, 2009.
- [135] G. Coath and S. K. Halgamuge, "A comparison of constraint-handling methods for the application of particle swarm optimization to constrained nonlinear optimization problems," in *The 2003 Congress on Evolutionary Computation*, 2003. CEC'03., 2003, vol. 4: IEEE, pp. 2419-2425.
- [136] J. A. Shah, I. Qureshi, A. A. Khaliq, and H. Omer, "Sparse signal recovery based on hybrid genetic algorithm," *Research journal of recent sciences*, vol. 2277, p. 2502, 2013.
- [137] J. Kennedy and R. Eberhart, "Particle swarm optimization," in *Proceedings of ICNN'95-international conference on neural networks*, 1995, vol. 4: IEEE, pp. 1942-1948.
- [138] Y. Shi, "Particle swarm optimization," *IEEE connections*, vol. 2, no. 1, pp. 8-13, 2004.
- [139] R. Poli, J. Kennedy, and T. Blackwell, "Particle swarm optimization: An overview," Swarm intelligence, vol. 1, pp. 33-57, 2007.
- [140] M. Clerc, Particle swarm optimization. John Wiley & Sons, 2010.
- [141] E. RC, "Shi Y. Particle swarm optimization: developments, applications and resources," in *Proc. Congress on evolutionary computation*, 2001, pp. 81-6.
- [142] K. Zhang, W. Zuo, Y. Chen, D. Meng, and L. Zhang, "Beyond a gaussian denoiser: Residual learning of deep cnn for image denoising," *IEEE transactions on image processing*, vol. 26, no. 7, pp. 3142-3155, 2017.
- [143] K. H. Jin, M. T. McCann, E. Froustey, and M. Unser, "Deep convolutional neural network for inverse problems in imaging," *IEEE transactions on image processing*, vol. 26, no. 9, pp. 4509-4522, 2017.

- [144] A. Mousavi, A. B. Patel, and R. G. Baraniuk, "A deep learning approach to structured signal recovery," in 2015 53rd annual allerton conference on communication, control, and computing (Allerton), 2015: IEEE, pp. 1336-1343.
- [145] M. Iliadis, L. Spinoulas, and A. K. Katsaggelos, "Deep fully-connected networks for video compressive sensing," *Digital Signal Processing*, vol. 72, pp. 9-18, 2018.
- [146] G. Luo, N. Zhao, W. Jiang, E. S. Hui, and P. Cao, "MRI reconstruction using deep Bayesian estimation," *Magnetic resonance in medicine*, vol. 84, no. 4, pp. 2246-2261, 2020.
- [147] J. M. Wolterink, T. Leiner, M. A. Viergever, and I. Išgum, "Generative adversarial networks for noise reduction in low-dose CT," *IEEE transactions on medical imaging*, vol. 36, no. 12, pp. 2536-2545, 2017.
- [148] G. Yang et al., "DAGAN: Deep de-aliasing generative adversarial networks for fast compressed sensing MRI reconstruction," *IEEE transactions on medical imaging*, vol. 37, no. 6, pp. 1310-1321, 2017.
- [149] M. Mardani et al., "Deep generative adversarial neural networks for compressive sensing MRI," *IEEE transactions on medical imaging*, vol. 38, no. 1, pp. 167-179, 2018.
- [150] A. Adler, D. Boublil, and M. Zibulevsky, "Block-based compressed sensing of images via deep learning," in 2017 IEEE 19th International Workshop on Multimedia Signal Processing (MMSP), 2017: IEEE, pp. 1-6.
- [151] B. Yaman, S. A. H. Hosseini, S. Moeller, J. Ellermann, K. Uğurbil, and M. Akçakaya, "Self-supervised physics-based deep learning MRI reconstruction without fully-sampled data," in 2020 IEEE 17th International Symposium on Biomedical Imaging (ISBI), 2020: IEEE, pp. 921-925.
- [152] K. Gregor and Y. LeCun, "Learning fast approximations of sparse coding," in Proceedings of the 27th international conference on international conference on machine learning, 2010, pp. 399-406.
- [153] J. Adler and O. Öktem, "Learned primal-dual reconstruction," *IEEE transactions on medical imaging*, vol. 37, no. 6, pp. 1322-1332, 2018.
- [154] H. Gupta, K. H. Jin, H. Q. Nguyen, M. T. McCann, and M. Unser, "CNN-based projected gradient descent for consistent CT image reconstruction," *IEEE transactions on medical imaging*, vol. 37, no. 6, pp. 1440-1453, 2018.
- [155] K. Hammernik et al., "Learning a variational network for reconstruction of accelerated MRI data," Magnetic resonance in medicine, vol. 79, no. 6, pp. 3055-3071, 2018.
- [156] C. Metzler, A. Mousavi, and R. Baraniuk, "Learned D-AMP: Principled neural network based compressive image recovery," Advances in neural information processing systems, vol. 30, 2017.
- [157] C. A. Metzler, A. Maleki, and R. G. Baraniuk, "From denoising to compressed sensing," *IEEE Transactions on Information Theory*, vol. 62, no. 9, pp. 5117-5144, 2016.
- [158] J. Sun, H. Li, and Z. Xu, "Deep ADMM-Net for compressive sensing MRI," Advances in neural information processing systems, vol. 29, 2016.
- [159] J. Sulam, A. Aberdam, A. Beck, and M. Elad, "On multi-layer basis pursuit, efficient algorithms and convolutional neural networks," *IEEE transactions on pattern analysis and machine intelligence*, vol. 42, no. 8, pp. 1968-1980, 2019.

- [160] C. Murdock, M. Chang, and S. Lucey, "Deep component analysis via alternating direction neural networks," in *Proceedings of the European Conference on Computer Vision (ECCV)*, 2018, pp. 820-836.
- [161] J. A. B. Keith A. Johnson. *The whole brain Atlas*, 1995-1999. [Online]. Available: <a href="https://www.med.harvard.edu/aanlib/">https://www.med.harvard.edu/aanlib/</a>
- Y. Gal and Z. Ghahramani, "Dropout as a bayesian approximation: Representing model uncertainty in deep learning," in international conference on machine learning, 2016: PMLR, pp. 1050-1059.
- [163] X. Glorot and Y. Bengio, "Understanding the difficulty of training deep feedforward neural networks," in *Proceedings of the thirteenth international conference on artificial intelligence and statistics*, 2010: JMLR Workshop and Conference Proceedings, pp. 249-256.

